Electrical and thermal properties of silicon nanowire arrays

Sofia Rodichkina

▶ To cite this version:

Sofia Rodichkina. Electrical and thermal properties of silicon nanowire arrays. Electronics. Université de Lyon; Université Lomonossov (Moscou), 2019. English. ⟨NNT : 2019LYSEI129⟩. ⟨tel-02900516⟩

HAL Id: tel-02900516

https://theses.hal.science/tel-02900516v1

Submitted on 16 Jul 2020

HAL is a multi-disciplinary open access archive for the deposit and dissemination of scientific research documents, whether they are published or not. The documents may come from teaching and research institutions in France or abroad, or from public or private research centers.

L'archive ouverte pluridisciplinaire **HAL**, est destinée au dépôt et à la diffusion de documents scientifiques de niveau recherche, publiés ou non, émanant des établissements d'enseignement et de recherche français ou étrangers, des laboratoires publics ou privés.

HAL Authorization

Faculty of Physics
M.V.Lomonosov Moscow State University

N°d'ordre NNT : 2019LYSEI129

THESE de DOCTORAT DE L'UNIVERSITE DE LYON

opérée au sein de

Institut national des sciences appliquées de Lyon

et délivré en partenariat international avec

Université d'État Lomonossov de Moscou

Ecole Doctorale N° 34
Matériaux

Spécialité de doctorat : Nanomatériaux

Soutenue publiquement/à huis clos le 10/12/2019, par :

Sofia Rodichkina

Electrical and thermal properties of silicon nanowire arrays

Devant le jury composé de :

Nom, prénom grade/qualité établissement/entreprise Président.e (à préciser après la soutenance)

LERONDEL Gilles/ Professeur des Universités, Université de Technologie de Troyes	Rapporteur
GAUTIER Gael/ Professeur des Universités, Université de Tours	Rapporteur
LE DANTEC Ronan/ Professeur des Universités, Université de Savoie	Examinateur
GOMES Séverine/ Directrice de Recherche, CNRS	Examinatrice
TIMOSHENKO Victor/ Professeur des Universités, MSU (Russie)	Directeur de thèse
LYSENKO Vladimir/ Chargé de recherche, CNRS (France)	Directeur de thèse
NYCHYPORUK Tetyana/ Maître de conférences, INSA Lyon (France)	Co-directrice de thèse

Cette thèse est accessible à l'adresse : http://theses.insa-lyon.fr/publication/2019LYSEI129/these.pdf
© [S. Rodichkina], [2019], INSA de Lyon, tous droits réservés

Département FEDORA – INSA Lyon - Ecoles Doctorales – Quinquennal 2016-2020

SIGLE	ECOLE DOCTORALE	NOM ET COORDONNEES DU RESPONSABLE
CHIMIE	**CHIMIE DE LYON** **http://www.edchimie-lyon.fr** Sec. : Renée EL MELHEM Bât. Blaise PASCAL, 3e étage **secretariat@edchimie-lyon.fr** INSA : R. GOURDON	**M. Stéphane DANIELE** Institut de recherches sur la catalyse et l'environnement de Lyon IRCELYON-UMR 5256 Équipe CDFA 2 Avenue Albert EINSTEIN 69 626 Villeurbanne CEDEX **directeur@edchimie-lyon.fr**
E.E.A.	**ÉLECTRONIQUE, ÉLECTROTECHNIQUE, AUTOMATIQUE** **http://edeea.ec-lyon.fr** Sec. : M.C. HAVGOUDOUKIAN **ecole-doctorale.eea@ec-lyon.fr**	**M. Gérard SCORLETTI** École Centrale de Lyon 36 Avenue Guy DE COLLONGUE 69 134 Écully Tél : 04.72.18.60.97 Fax 04.78.43.37.17 **gerard.scorletti@ec-lyon.fr**
E2M2	**ÉVOLUTION, ÉCOSYSTÈME, MICROBIOLOGIE, MODÉLISATION** **http://e2m2.universite-lyon.fr** Sec. : Sylvie ROBERJOT Bât. Atrium, UCB Lyon 1 Tél : 04.72.44.83.62 INSA : H. CHARLES **secretariat.e2m2@univ-lyon1.fr**	**M. Philippe NORMAND** UMR 5557 Lab. d'Ecologie Microbienne Université Claude Bernard Lyon 1 Bâtiment Mendel 43, boulevard du 11 Novembre 1918 69 622 Villeurbanne CEDEX **philippe.normand@univ-lyon1.fr**
EDISS	**INTERDISCIPLINAIRE SCIENCES-SANTÉ** **http://www.ediss-lyon.fr** Sec. : Sylvie ROBERJOT Bât. Atrium, UCB Lyon 1 Tél : 04.72.44.83.62 INSA : M. LAGARDE **secretariat.ediss@univ-lyon1.fr**	**Mme Sylvie RICARD-BLUM** Institut de Chimie et Biochimie Moléculaires et Supramoléculaires (ICBMS) - UMR 5246 CNRS - Université Lyon 1 Bâtiment Curien - 3ème étage Nord 43 Boulevard du 11 novembre 1918 69622 Villeurbanne Cedex Tel : +33(0)4 72 44 82 32 **sylvie.ricard-blum@univ-lyon1.fr**
INFOMATHS	**INFORMATIQUE ET MATHÉMATIQUES** **http://edinfomaths.universite-lyon.fr** Sec. : Renée EL MELHEM Bât. Blaise PASCAL, 3e étage Tél : 04.72.43.80.46 **infomaths@univ-lyon1.fr**	**M. Hamamache KHEDDOUCI** Bât. Nautibus 43, Boulevard du 11 novembre 1918 69 622 Villeurbanne Cedex France Tel : 04.72.44.83.69 **hamamache.kheddouci@univ-lyon1.fr**
Matériaux	**MATÉRIAUX DE LYON** **http://ed34.universite-lyon.fr** Sec. : Stéphanie CAUVIN Tél : 04.72.43.71.70 Bât. Direction **ed.materiaux@insa-lyon.fr**	**M. Jean-Yves BUFFIÈRE** INSA de Lyon MATEIS - Bât. Saint-Exupéry 7 Avenue Jean CAPELLE 69 621 Villeurbanne CEDEX Tél : 04.72.43.71.70 Fax : 04.72.43.85.28 **jean-yves.buffiere@insa-lyon.fr**
MEGA	**MÉCANIQUE, ÉNERGÉTIQUE, GÉNIE CIVIL, ACOUSTIQUE** **http://edmega.universite-lyon.fr** Sec. : Stéphanie CAUVIN Tél : 04.72.43.71.70 Bât. Direction **mega@insa-lyon.fr**	**M. Jocelyn BONJOUR** INSA de Lyon Laboratoire CETHIL Bâtiment Sadi-Carnot 9, rue de la Physique 69 621 Villeurbanne CEDEX **jocelyn.bonjour@insa-lyon.fr**
ScSo	**ScSo*** **http://ed483.univ-lyon2.fr** Sec. : Véronique GUICHARD INSA : J.Y. TOUSSAINT Tél : 04.78.69.72.76 **veronique.cervantes@univ-lyon2.fr**	**M. Christian MONTES** Université Lyon 2 86 Rue Pasteur 69 365 Lyon CEDEX 07 **christian.montes@univ-lyon2.fr**

Cette thèse est accessible à l'adresse : http://theses.insa-lyon.fr/publication/2019LYSEI129/these.pdf
© [S. Rodichkina], [2019], INSA de Lyon, tous droits réservés

*ScSo : Histoire, Géographie, Aménagement, Urbanisme, Archéologie, Science politique, Sociologie, Anthropologie

Résumé

Les nanofils de silicium (SiNWs) attirent l'attention particulière en raison de leurs applications thermoélectriques prometteuses. La faible conductivité thermique et les propriétés électriques proches du Si massif en font un nanomatériau thermoélectrique idéal dans le concept de "verre à phonons - cristal à électrons". Théoriquement, les valeurs du facteur de mérite thermoélectrique (ZT) pour SiNW peuvent atteindre 3 à la température ambiante. ZT = 0,7 a été déjà obtenu expérimentalement pour des SiNW individuels, ce qui est proche de ZT pour les chalcogénures de bismuth (ZT = 0,8 -1,0) qui sont couramment utilisés. De point de vue pratique, il faut savoir fabriquer des réseaux de SiNWs à faible coût.

Dans cette thèse, nous avons cherché: (i) à adapter des technologies existantes pour la fabrication des SiNWs fortement dopés, (ii) à développer des méthodes de caractérisation sans contact et non destructive des propriétés électriques et thermiques de réseaux de SiNWs, (iii) à fabriquer et caractériser des réseaux de SiNWs à haute conductivité électrique et faible conductivite thermique.

Les résaux des SiNW ayant la morphologie et le niveau de dopage nécessaires pour obtenir un ZT maximal ont été fabriquées par gravure chimique assistée par métaux de substrats de silicium. Une procédure de dopage post-fabrication a été développée en utilisant la diffusion thermique d'atomes de dopant à partir de solutions de dopage (via un dépôt spin-on). En particulier, les réseaux de nanofils de silicium ayant un diamètre typique de 100 nm, une longueur de 10 μm, une morphologie de type "cœur crystallin/ surface rugueuse" et un niveau de dopage de 10^{20} cm^{-3}, presque uniforme le long des nanofils, ont été obtenus. Des techniques de spectroscopie infrarouge et Raman ont été développées pour estimer la concentration en porteurs de charge libre dans SiNWs. Sur la base des valeurs de la concentration de porteurs, la résistivité électrique des SiNWs a été estimée par des mesures électriques à deux sondes. La méthode de spectroscopie Raman et la modélisation du transport de chaleur ont été développées pour déterminer la conductivité thermique des SiNWs. Les réseaux de SiNWs fabriqués ont eu une résistivité électrique d'environ 1-5 mΩ*cm et une conductivité thermique d'environ 1 W/(m*K).

Il a été démontré que le gradient de température le long des nanofils dans les réseaux de SiNWs à chauffage photo-induit existe à une profondeur d'environ 10 μm, ce qui limite la longueur maximale des nanofils dans les réseaux de SiNWs pour des applications thermoélectriques. Il a été démontré que la contrainte mécanique induite par le gradient de température

Cette thèse est accessible à l'adresse : http://theses.insa-lyon.fr/publication/2019LYSEI129/these.pdf
© [S. Rodichkina], [2019], INSA de Lyon, tous droits réservés

/

dans SiNWs était responsable de la transformation du réseau cristallin cubique-en-hexagonal diamant dans SiNWs sous forte photoexcitation.

La thèse aboutit à 3 articles publiés, 1 article en cours de révision et 1 article qui sera soumis prochainement.

Mots-clés: nanofils de silicium, conductivité thermique, conductivité électrique, caractérisation optique, thermoélectricité.

Cette thèse est accessible à l'adresse : http://theses.insa-lyon.fr/publication/2019LYSEI129/these.pdf
© [S. Rodichkina], [2019], INSA de Lyon, tous droits réservés

Abstract

Silicon nanowires (SiNWs) attract growing attention in view of their promising thermoelectric applications. Low thermal conductivity and bulk-like electrical properties make them a perfect candidate as a thermoelectric material in framework of the concept "phonon-glass/ electron-crystal". Theoretically, the values of figure of merit (ZT) for SiNWs as high as three can be achieved at room temperature, and experimentally ZT = 0.7 were already observed for individual SiNWs, which is close to ZT for commonly used bismuth chalcogenides (ZT = 0.8-1.0). For practical application of SiNWs, the low-cost fabrication methods for SiNWs arrays with high ZT should be achieved.

In this thesis we aimed: (i) to adapt available semiconductor technology for fabrication of highly-doped SiNWs arrays, (ii) to develop contactless methods for non-destructive characterization of electrical and thermal properties of the SiNWs arrays, (iii) to fabricate and characterize SiNWs arrays with high electrical and low thermal conductivities.

The arrays of SiNWs with the morphology and doping level necessary for maximum ZT were fabricated using metal-assisted chemical etching of silicon wafers and post-fabrication doping procedure, which consisted of the thermal diffusion of dopant atoms from spin-on dopant solutions. In particular, the arrays of silicon nanowires with a typical diameter of 100 nm, length of 10 μm, bulk core/rough surface morphology and doping level of 10^{20} cm^{-3}, nearly uniform along nanowires, were obtained. The infrared and Raman scattering techniques were developed to probe free charge carrier concentration in SiNWs. Being based on the determined values of free charge carrier concentration, the electrical resistivity of SiNWs was estimated and verified by two-probe electrical measurements for SiNWs arrays. The Raman spectroscopy method and heat transport modeling were developed to determine thermal conductivity of SiNWs. Fabricated SiNWs array exhibited the electrical resistivity of about 1-5 mΩ*cm and the thermal conductivity of about 1 W/(m*K).

It was shown, that the temperature gradient along nanowires in SiNWs arrays under photo-induced heating exists to a depth about 10 μm, which limits the maximum nanowire length in SiNWs arrays for thermoelectric applications. The temperature gradient induced mechanical stresses in SiNWs were shown to be responsible for the cubic-to-hexagonal diamond crystalline lattice transformation in SiNWs under the strong photoexcitation.

The PhD work results in 3 published articles, 1 article under review and 1 article to be

Cette thèse est accessible à l'adresse : http://theses.insa-lyon.fr/publication/2019LYSEI129/these.pdf
© [S. Rodichkina], [2019], INSA de Lyon, tous droits réservés

/

submitted.

Keywords: silicon nanowires, thermal conductivity, electrical conductivity, optical characterization, thermoelectricity

Cette thèse est accessible à l'adresse : http://theses.insa-lyon.fr/publication/2019LYSEI129/these.pdf
© [S. Rodichkina], [2019], INSA de Lyon, tous droits réservés

Acknowledgments

The work on this PhD thesis was performed at Faculty of Physics, Lomonosov Moscow State University and Institut des Nanotechnologies de Lyon, INSA Lyon under the supervision of Prof. V.Yu. Timoshenko and Dr. V. Lysenko. I wish to express my gratitude to Prof. V.Yu. Timoshenko for the help in choosing the research problem and overall management of the project. I sincerely appreciate the guidance of Dr. V. Lysenko throughout my PhD work, his help in formulation and solving the research problems, as well as for his help in my installation in France. The constant interest of both my supervisors in the issue of nanomaterials, their scientific experience and fruitful discussions inspired me throughout our cooperation and made a great contribution to the success of this PhD work. I also would like to thank my co-supervisor at INSA Lyon Dr. T. Nychyporuk for her help with the sample fabrication and characterization. Her contribution helped us to obtain the nanostructures with desired properties, and it was important for achieving the global goal of the PhD work.

This work would not have been possible without collaboration with our colleagues from Lomonosov Moscow State University, INSA Lyon, Universite de Lorraine, Taras Shevchenko National University of Kyiv. I am deeply grateful to all my co-authors duiring the PhD work: A.V. Pavlikov, A. Belarouci, M. Isaiev, A. Pastushenko, I. Bezverkhnyy, R. Chassagnon. Their scientific experience and experimental skills made the results of our research more valuable and reliable, and allowed us to publish the high-level articles. I express my appreciation to B. Canut, J.-M. Bluet, F. Mandorlo, A. Belarouci from INSA Lyon and V.V. Pryadun, V.M. Senyavin from MSU for the help with measurements of SiNWs. Thanks to my colleagues, I was able to expand the number of my scientific contacts and feel integrated into the scientific community.

I sincerely appreciate Prof. G. Lerondel, Prof. G. Gautier, Prof. R. Le Dantec, Dr. S. Gomes for taking the responsibility of being the rapporteurs and examiners of this PhD thesis.

I wish to acknowledge the entire research group of the Department of Low Temperature Physics and Superconductivity, Faculty of Physics, MSU and Institut des Nanotechnologies, INSA Lyon, working near you has made the PhD journey more pleasant and interesting. Special thanks to the technical and engineering staff of both the LTP and INL laboratories for their contribution to the maintenance of the laboratories, as well as to the administrative staff of the doctoral schools, in which I was enrolled.

Heartfelt thanks to my family who supported me in my PhD work and my friends from

Cette thèse est accessible à l'adresse : http://theses.insa-lyon.fr/publication/2019LYSEI129/these.pdf
© [S. Rodichkina], [2019], INSA de Lyon, tous droits réservés

/

Moscow and Lyon who made me not to think about it too much.

Finally, I acknowledge the Campus France team for their support in my accommodation in France. I am sincerely grateful to Lomonosov Moscow State University, Institut National des Sciences Appliquées de Lyon and "Vernadski" scholarship program of the Embassy of France in Russia for making possible this joint PhD program and financial support.

Cette thèse est accessible à l'adresse : http://theses.insa-lyon.fr/publication/2019LYSEI129/these.pdf
© [S. Rodichkina], [2019], INSA de Lyon, tous droits réservés

Contents

General introduction **29**

1 State of the art: fabrication and properties of silicon nanowires (SiNWs) **30**

1.1 Fabrication of SiNWs arrays, their morphology and structural properties 30

1.1.1 Common fabrication techniques 30

1.1.2 Metal-assisted chemical etching 32

1.1.3 Vapour-liquid-solid growth 40

1.1.4 Hexagonal diamond silicon and other polymorphs 42

1.2 Impact of doping on structural properties of SiNWs 45

1.2.1 In-situ doping during VLS growth 45

1.2.2 Etching of highly-doped c-Si wafers 46

1.2.3 Ex-situ doping of silicon nanowires 47

1.3 Thermal properties of SiNWs 53

1.3.1 Thermal transport in bulk crystalline silicon (c-Si) 53

1.3.2 Effect of nanoscale boundaries 56

1.3.3 Dependence on temperature 59

1.3.4 Effect of free charge carriers 60

1.3.5 Role of surface roughness 62

1.4 Electrical properties of SiNWs 64

1.4.1 Electrical transport in c-Si 64

1.4.2 Free charge carrier concentration 66

1.4.3 Free charge carrier mobility 68

1.4.4 Electrical resistivity 72

1.5 Thermoelectric performance of SiNWs 77

1.6 Thermal and electrical properties of hexagonal diamond silicon 83

1.7 Conclusions to the state of the art 85

1.8 Statement of the research tasks for PhD thesis 89

Cette thèse est accessible à l'adresse : http://theses.insa-lyon.fr/publication/2019LYSEI129/these.pdf
© [S. Rodichkina], [2019], INSA de Lyon, tous droits réservés

2 Materials and methods **91**
2.1 Fabrication of silicon nanowires 91
2.1.1 Metal-assisted chemical etching 91
2.1.2 Post-fabrication doping 92
2.1.3 Investigated samples 92
2.2 Characterization of silicon nanowires 93
2.2.1 Scanning electron microscopy 93
2.2.2 Transmission electron microscopy 94
2.2.3 Infrared spectroscopy 95
2.2.4 Raman spectroscopy 96
2.2.5 Photoluminescence spectroscopy 97
2.2.6 Electrical resistance measurements 98

3 Structural properties of silicon nanowires **99**
3.1 Fabrication of SiNWs arrays by metal-assisted chemical etching 99
3.1.1 Morphology and crystalline structure of initial SiNWs 99
3.1.2 Structural properties of additionally doped SiNWs 104
3.2 Photo-induced formation of hexagonal diamond phase in SiNWs 105
3.2.1 Evolution of Raman spectra of SiNWs with laser power 105
3.2.2 Temperature gradient induced mechanical stresses 106
3.2.3 Cubic-to-hexagonal polytype transformation 108
3.3 Conclusions to Chapter 3 112

4 Contactless diagnostics of free charge carriers **114**
4.1 Infrared spectroscopy 114
4.1.1 Modeling of infrared spectra for nanostructured media 114
4.1.2 Infrared diagnostics of isotropic nanostructured layers 120
4.1.3 IR-ATR diagnostics of anisotropic SiNWs arrays 126
4.2 Raman scattering spectroscopy 129
4.2.1 Raman spectra of highly p-type doped SiNWs 129
4.2.2 Dependence of Fano effect on free charge carrier concentration 134
4.2.3 In-depth profiles of doping level for SiNWs arrays 136
4.3 Comparison of IR-ATR and Raman techniques 137

Cette thèse est accessible à l'adresse : http://theses.insa-lyon.fr/publication/2019LYSEI129/these.pdf
© [S. Rodichkina], [2019], INSA de Lyon, tous droits réservés

4.3.1 p-type SiNWs arrays 138
4.3.2 n-type SiNWs arrays 139
4.4 Conclusions to Chapter 4 142

5 In-depth doping of silicon nanowire arrays 144
5.1 Influence of doping procedure parameters 144
5.1.1 Dilution of dopant solution 144
5.1.2 Thickness of dopant layer 147
5.1.3 Annealing time and temperature 149
5.2 Influence of SiNWs surface roughness on doping efficiency 150
5.3 Conclusions to Chapter 5 151

6 Electrical and thermal transport in silicon nanowires 153
6.1 Electrical resistivity of SiNWs 153
6.1.1 Estimation based on the free hole concentration 153
6.1.2 Two-probe electrical measurements 154
6.2 Thermal conductivity of SiNWs 157
6.2.1 Thermal conductivity by Raman spectroscopy 157
6.2.2 Thermal conductivity of low- and highly-doped SiNWs 164
6.3 Conclusions to Chapter 6 167

General conclusions 171

Appendix A 174

Bibliography 174

Cette thèse est accessible à l'adresse : http://theses.insa-lyon.fr/publication/2019LYSEI129/these.pdf
© [S. Rodichkina], [2019], INSA de Lyon, tous droits réservés

List of Figures

1.1 SiNWs production steps for top-down and bottom-up approaches [1] 31

1.2 Illustration of Ag deposition during the first step of MACE. Due to the facile Ag^+/Ag reaction and ohmic interfacial electron exchange between silicon and silver, Ag nanoparticle dynamically reorganize to their lowest energy state [2]. . 33

1.3 Illustration of the etching mechanism of Si in HF and H_2O_2 solution. Pathway I involves the direct reaction of H_2O_2 with Si and is kinetically not favored. Pathway II is the preferred Si oxidation reaction, which involves Ag/Ag^+, leading to nanowire formation. Pathway III shows the diffusion of holes from the Ag/Si interface, which leads to general porous silicon formation. HF is not shown in the diagram, but implied [2]. 34

1.4 SEM images of SiNWs arrays, fabricated by MACE of (a) p-type and (b) n-type c-Si (100) wafers with the specific resistivity of 0.2–1.0 Ω*cm Si(100) wafers [3]. 35

1.5 SiNWs formed in the Ag/H_2O_2 system. Porous silicon is seen at the base of the nanowires and is presumed to cover the nanowires as well. Areas where Ag nanoparticles are "missing" show terminated etching and a clear accumulation of porous silicon [2]. 36

1.6 Cross-sectional and top-view SEM images of SiNWs arrays, fabricated by MACE of n-type c-Si (100) with $\rho = 0.008 - 0.2$ Ω*cm in etchant solutions composed of 4.8 M HF and 0.3 M H_2O_2. $AgNO_3$ concentration for the deposition of Ag nanoparticles was of (a-b) 5 mM, (c-d) 10 mM. The scale bars in (a,c) and (b,d) are 20 and 10 μm. Adapted from [4]. 37

Cette thèse est accessible à l'adresse : http://theses.insa-lyon.fr/publication/2019LYSEI129/these.pdf
© [S. Rodichkina], [2019], INSA de Lyon, tous droits réservés

1.7 SEM and TEM images of SiNWs, fabricated by MACE with increasing concentration of H_2O_2. Substrates: n-type c-Si (100) with $\rho = 0.008 - 0.02$ Ω*cm. HF concentration was of 4.8 M. H_2O_2 concentration was of: (A-D) 0.1 M, (E-H) 0.15 M, (I-L) 0.2 M, (M-P) 0.3 M. The etching time for left-sided and right-sided images was of 30 and 60 min, respectively. The scale bars for SEM and TEM images is 10 μm and 60 nm, respectively [5]. 37

1.8 HRTEM and TEM (insets) images of MACE-SiNWs, fabricated on p-type c-Si wafers with the doping concentrations of (b) 10^{14}, (c) 10^{16}, and (d) 10^{18} cm^{-3}. The scale bars for HRTEM and inset TEM images are 5 and 200 nm, respectively. Adapted from [6]. 38

1.9 (a) SEM image of MACE-SiNWs array. (b) TEM image of MACE-SiNWs. The surface roughness is clearly seen. The SAED pattern (inset) indicates that SiNWs are single crystalline all along the length. (c) HRTEM image of MACE-SiNWs. The roughness is evident at the interface between the crystalline Si core and the amorphous native oxide at the surface, and at undulations of the alternating light/dark thickness fringes near the edge. (d) HRTEM of VLS-SiNWs. Scale bars for a–d are 10 μm, 20 nm, 4 nm and 3 nm, respectively [7]. 39

1.10 Raman spectra of low-doped MACE-SiNWs at different excitation laser power. The inset shows the dependence of the Raman peak position on laser power [8]. 39

1.11 a) Schematic illustration of the VLS growth mechanism [9]. (b) Tilted SEM view of a Cu-catalyzed VLS-grown SiNWs array [10]. Adapted from [9]. . . . 41

1.12 Schematic overview of silicon high pressure phases (red) and low pressure low energy allotropes that can potentially be stabilized at ambient conditions. Structures known to exist at ambient conditions are marked in blue. Theoretically proposed but not yet observed structures are shown in green. Violet denotes structures proposed for the still elusive Si-IX and Si-XIII phases [11]. 43

1.13 Switch from the twinned cubic phase to the 2H hexagonal phase in SiNWs, grown by VLS method, associated with a change in the growth direction. The schematic shows that the relationship between the two phases is close to epitaxial [12]. 44

Cette thèse est accessible à l'adresse : http://theses.insa-lyon.fr/publication/2019LYSEI129/these.pdf
© [S. Rodichkina], [2019], INSA de Lyon, tous droits réservés

1.14 Typical Raman spectra for lapped silicon wafer surfaces. (a) cub-Si at 521 cm^{-1} and a-Si at ~ 470 cm^{-1} and ~ 150 cm^{-1}, (b) hex-Si at 508 cm^{-1}. Adapted from [13]. 44

1.15 (a) Cross-section SEM micrograph of the VLS-grown p-doped SiNWs array. TEM micrographs of (b) tip and (c) base segment of an as-grown TMB-doped Si nanowire grown using $SiCl_4$. Both images reveal a single crystalline Si core surrounded by a 1 nm thick native oxide shell. Diffraction pattern (inset) confirms that the [111] orientation of as-grown nanowire [14]. 46

1.16 Typical TEM images of SiNWs (a) before ion implantation, and after ion implantation with a dose of (b) $1*10^{16}$ B^+/cm^2, (c) $5*10^{15}$ B^+/cm^2, (d) $1*10^{16}$ P^+/cm^2. The activation annealing of dopant atoms was performed at 900 ^{0}C after implantation. The scale bar is 5 nm. (e) Illustration of ion implantation for SiNWs. (f) Depth profiles of B and P as estimated by simulation of transport of ions in matter [15]. 48

1.17 (a) Raman spectra of SiNWs, which show the Si optical phonon peak and B local vibrational peak, after B ion implantation with a dose of $1*10^{16}$ B^+/cm^2 and subsequent activation annealing. (b) Magnified image of (a). (c) Raman spectra of SiNWs after P ion implantation with a dose of $1*10^{16}$ P^+/cm^2 and subsequent activation annealing. (d) Raman spectrum of SiNWs before and after the ion implantation doping with P. Adapted from [15]. 49

1.18 Solid solubility for common dopants in silicon [16] (summarized from [17, 18]). 51

1.19 SIMS profiles of boron in doped oxide and in the silicon substrate after RTA at 1060 ^{0}C for: (a) 30 s, (b) 1 min, and (c) 3 min. The solid solubility of boron in silicon at the given temperature of $1.6*10^{20}$ cm^{-3} [19] is shown as the dotted horizontal lines [20]. 51

1.20 High-resolution TEM micrographs of (a) undoped SiNWs and (b) doped SiNWs using the annealing at 950 ^{0}C. The high magnification images show the nanowire section near the surface along with the surface oxide layer of 23 nm for the undoped SiNWs and somewhat thicker oxide layer of 5-6 nm after the doping. The $< 111 >$ axis lies along the growth direction [21]. 52

Cette thèse est accessible à l'adresse : http://theses.insa-lyon.fr/publication/2019LYSEI129/these.pdf
© [S. Rodichkina], [2019], INSA de Lyon, tous droits réservés

1.21 Phonon scattering rates in bulk Si and Si nanowire with diameter of 20 nm due to the different scattering mechanisms as functions of the phonon frequency. The results are shown for the three-phonon Umklapp, mass-difference, phonon-electron, and boundary scattering at $T = 300$ K [22]. 55

1.22 Accumulated contributions to the thermal conductivity of the phonon modes in bulk c-Si with respect to their frequency at $T = 300$ K (solid line), 200 K (dashed line) and 100 K (dotted line). The results are obtained for lightly doped n-type silicon. Adapted from [23]. 56

1.23 Lattice thermal conductivity of bulk Si and SiNW with $D = 20$ nm at room temperature as a function of specular phonon-boundary scattering fraction p. Adapted from [22]. 57

1.24 Nanowire thermal conductivity vs diameter 6 nm $<$ d $<$ 500 nm. The experimental results (up triangles) of Li et al. (Ref. [24]) are compared to Monte-Carlo simulation data (squares) of Lacroix et al. (Ref. [25]), kinetic theory results (circles) of Chantrenne et al. (Ref. [26]), molecular dynamic results (diamonds) of Volz and Lemonnier (Ref. [27]), kinetic theory+molecular dynamic results (stars) of Mingo (Ref. [28]), and kinetic theory with modified dispersion curves (down triangles) of Zou and Balandin (Ref. [22]) [25]. 59

1.25 Experimental (solid line) and theoretical (dashed line) dependencies of the thermal conductivity coefficient on temperature for bulk c-Si. Varoius dashed line correspond to the thermal conductivity values, obtained theoretically considering particular scattering mechanisms [29]. 60

1.26 Low temperature experimental data on the thermal conductivity of SiNWs with different diameter, grown by VLS technique. The T^3, T^2, and T^1 curves are shown for comparison [24]. 60

1.27 Thermal conductivities of p-type bulk c-Si samples with different doping concentrations as a function of temperature. Adapted from [30]. 61

Cette thèse est accessible à l'adresse : http://theses.insa-lyon.fr/publication/2019LYSEI129/these.pdf
© [S. Rodichkina], [2019], INSA de Lyon, tous droits réservés

1.28 (a) The temperature-dependent thermal conductivity of VLS- (black squares; reproduced from Ref. [24]) and MACE-SiNWs (red squares). (b) Temperature-dependent thermal conductivity of MACE-SiNWs etched from wafers of different resistivities: 10 Ω*cm (red squares), 10^{-1} Ω*cm and doped post-synthesis to 10^{-3} Ω*cm (green squares), and 10^{-2} Ω*cm (blue squares). For the purpose of comparison, the k of bulk amorphous silica is plotted with open squares. The highly doped MACE-SiNWs have a k approaching that of insulating glass, suggesting an extremely short phonon mean free path [7]. 62

1.29 (a) Predicted effect of roughness rms on the thermal conductivity of 115 and 56 nm NW at $T = 300$ K, roughness autocorrelation length is of 6nm. (b) Effect of roughness rms on the dependence of NW thermal conductivity on equivalent circular diameter [31]. 63

1.30 Resistivity as a function of the impurity concentration for bulk Si at 300 K. Ref. [32], adapted from [33]. 65

1.31 Electrical resistivities of p-type bulk Si samples with different doping concentrations as a function of temperature. Adapted from [30]. 66

1.32 Ratio of the average electron concentration to the dopant concentration (N/N_D) as a function of the dopant concentration for various SiNWs diameters and the interface trap level density of 10^{12} $eV^{-1}cm^{-2}$. Dopant is P with a bulk ionization energy of 45 meV; $T = 300$ K. Adapted from [34]. 68

1.33 Calculated surface-roughness-limited (a), surface-roughness and Coulomb-limited (b), phonon-limited (c), and total (d) electron mobility as a function of the effective field ranging from 0.05 to 1 MV/cm and silicon body diameter ranging from 3 to 14 nm [35]. 69

1.34 (a) Low-field electron mobility as a function of temperature for 4-nm silicon nanowires with and without diamond coating. Dotted line shows electron mobility for pure bulk silicon. (b) Enhancement of low-field electron mobility for coated 4-nm silicon nanowires in comparison with the free-standing nanowire[36]. 71

Cette thèse est accessible à l'adresse : http://theses.insa-lyon.fr/publication/2019LYSEI129/these.pdf
© [S. Rodichkina], [2019], INSA de Lyon, tous droits réservés

1.35 Electrical characterization of silicon nanowires: (A) I-V characterstics of silicon nanowires (length of 40 μm, thickness of 50 nm, width of 80, 130, 300 nm) before (blue lines) and after (red lines) thermal annealing, the insets show the magnification view of the I-V curves for SiNWs before annealing; (B) (i) electrical conductance and (iii) electrical conductivity of silicon nanowires before and after the thermal annealing as a function of their width, (ii) ratio between the electrical conductances of SiNWs before and after the thermal annealing as a function of their width [37]. 72

1.36 Ohmic current to voltage characteristic of n- and p-type silicon nanowire with diameter of 50 nm. The extracted resistivity is of 1.1 and 1.2 mΩ*cm for n- and p-type silicon nanowires, correspondingly [38]. 74

1.37 Theoretical electrical conductivity of n-type silicon nanowires as a function of the nanowire width (triangular cross section), normalized with respect to the bulk electrical conductivity [39]. 74

1.38 Experimental dependence of electrical resistivity of SiNWs on their radius for different donor densities [40]. 75

1.39 Si nanowire resistivity as a function of the silane to dopant precursor ratio during CVD synthesis [34]. 76

1.40 Illustrative plot of the dependence of Seebeck coefficient S, electrical conductivity σ, thermal conductivity k and thermoelectric figure of merit ZT on free charge carrier concentration in the materials [41]. 78

1.41 (a) Seebeck coefficient of medium- and highly-doped p- and n-type c-Si as a function of temperature. Dashed lines show the results of the Seebeck coefficient calculation for n- and p-type c-Si with $N = 1 * 10^{19}$ cm^{-3} from Ref. [42]. (b) Calculated ZT values of medium- and highly-doped p- and n-type c-Si as a function of temperature [30]. 80

1.42 Seebeck coefficient (red dashed lines, refer to left scale, red units) and power factor (blue solid lines, refer to right scale, blue units) for electron-doped silicon in dependence on the doping level. The doping dependence of the electrical conductivity is given as a dashed–dotted line in arbitrary units. The maxima of the power factor are marked by black open circles [42]. 81

Cette thèse est accessible à l'adresse : http://theses.insa-lyon.fr/publication/2019LYSEI129/these.pdf
© [S. Rodichkina], [2019], INSA de Lyon, tous droits réservés

1.43 Seebeck voltage as a function of temperature difference. (a) Seebeck coefficient and power factor are of -0.13 mV/K and 1.46 mW·m^{-1}·K^{-2}, respectively for n-type SiNWs. (b) Seebeck coefficient and power factor are of 0.14 mV/K and 1.66 mW·m^{-1}·K^{-2}), respectively for p-type SiNWs [38]. 82

1.44 Single SiNWs power factor (red squares) of 48 nm nanowire and calculated ZT (blue squares) using the measured k of 52 nm nanowire [7]. 83

1.45 (a) Thermal conductivity of bulk cub-Si (circles) and hex-Si (diamonds) as a function of temperature. (b) Thermal conductivity of cun-Si (black lines) and hex-Si (red lines) SiNWs as a function of their diameter at $T = 200$, 300 and 400 K. Insets: ratio of the thermal conductivity between hexagonal and cubic NWs [43]. 84

3.1 Cross-sectional and top-view (insets) images of SiNWs (series B), fabricated on c-Si wafers with the specific resistivity of (a) 40-50 Ω*cm, (b) 1-20 Ω*cm and (c) 0.1-0.2 Ω*cm. Images (d,g) show the magnified view of (a); (e,h) show the magnified view of (b); (f,i) show the magnified view of (c). The scale bars for (a-c) are 10 μm, for the instes in (a-c) are 500 nm, for (d-i) are 2 μm. 100

3.2 (a) Cross-section SEM image of SiNWs (series A) with the length of 22 μm, (b) TEM image of an individual nanowire, (c) HRTEM image of a SiNW, (d) Fourier transform of the HRTEM image, shown in (c). 102

3.3 (a) Cross-sectional SEM image of initial SiNWs (SiNWs-A series) with the length of 15 μm (b) Cross-sectional SEM image of the same SiNWs after the additional doping with boron. The insets show the top-view images of the corresponding samples. (c) Normalized Raman spectra of SiNWs with different length and c-Si substrate. (d) Normalized Raman spectra of additionally boron-doped SiNWs with different length. The laser wavelength used for the Raman measurements was 632.8 nm. 103

3.4 Top-view SEM image of a por-Si (series A) sample prepared for the etching time of 5 min, the inset shows a cross-sectional view of this sample. 104

Cette thèse est accessible à l'adresse : http://theses.insa-lyon.fr/publication/2019LYSEI129/these.pdf
© [S. Rodichkina], [2019], INSA de Lyon, tous droits réservés

3.5 Normalized Raman spectra of low doped SiNWs (circles), obtained at excitation laser intensity of 0.015 (black), 7 (blue) and 15 kW/cm^2 (red). No observable laser-induced heating occurs at the laser intensity of 0.015 kW/cm^2. Additional Raman peaks (B and C) appear at laser excitation intensities $>$ 4 kW/cm^2. The dashed lines visualize the peaks A, B, C after the deconvolution of the Raman spectra by Lorentzians. The solid lines correspond to the sum of the Lorentzian peaks and fit well the experimental data. 105

3.6 Calculated heating profile along SiNWs for the laser excitation intensities of 4 and 10 kW/cm^2, required for the LO-TO phonon splitting and hex-Si phase formation, respectively. The dashed lines show the linear $\Delta T \sim z$ dependence. . 107

3.7 (a) Raman spectra at the high laser intensity of 15 kW/cm^2 for SiNWs samples with the c-Si substrate at room temperature (upper spectrum) and heated to 450 K (bottom spectrum). (b) Dependence of the spectral position of the Raman peaks of SiNWs as a function of a distance between the c-Si substrate and the heated part of SiNWs. The dependence was measured both at low (15 W/cm^2, black crosses) and high (15 kW/cm^2) laser intensity. 107

3.8 Spectral positions of the Raman peaks of SiNWs as function of laser intensity. Black and blue squares correspond to the Raman peaks A and B (stressed and heated cub-Si phase of SiNWs). Hexagons correspond to peak C (hex-Si phase of SiNWs). 108

3.9 Relation between spectral position (Ω) and width (Γ) of the Raman peak A of cub-Si and SiNWs for the case of homogeneous thermal heating (blue squares and black circles, correspondingly) and of SiNWs under photoexcitation (red circles). 109

3.10 Relative integrated intensity of the Raman peaks of SiNWs as a function of the laser intensity. 110

Cette thèse est accessible à l'adresse : http://theses.insa-lyon.fr/publication/2019LYSEI129/these.pdf
© [S. Rodichkina], [2019], INSA de Lyon, tous droits réservés

3.11 (a) Normalized PL spectra of SiNWs, obtained at the high laser excitation intensity (> 10 kW/cm^2). Arrows indicate the spectral position of PL maximum. The inset shows the dependence of the PL maximum intensity, divided to the laser intensity, on the laser intensity. Dashed line illustrates the threshold of hex-Si phase formation in SiNWs. (b) Normalized Raman spectra Raman of SiNWs obtained at the same point for different excitation laser intensities. Dashed lines show the Raman peaks A,B and C after deconvolution of the spectra by Lorentzians, solid lines correspond to the sum of the Lorentzian peaks. The correlation between the observed PL and peak C can be observed. 112

4.1 Illustration to the problem of calculating the reflectance from an anisotropic medium. Orange arrows show the chosen coordinate system. Light falls from the transparent medium (upper half-space, $z < 0$), while the sample is placed in the lower half-space ($z > 0$). z-axis coincides with the optical axis of the sample and is perpendicular to the sample surface. Red arrows illustrate the incident (0), reflected (1) and transmitted ordinary (o) and extraordinary (e) light waves. . . 117

4.2 (a) Calculated ATR spectra for s-polarized (dash-dotted line), p-polarized (dashed line) and non-polarized (blue solid line) incident light for the anisotropic medium (SiNWs), as well as for non-polarized light for the isotropic medium (por-Si, black solid line) (b) calculated spectra of the absorption coefficient for ordinary (dash-dotted line) and extraordinary (dashed line) ray for the anisotropic medium, as well as the absorption coefficient for the porous (por-Si, black solid line) and non-porous (c-Si, red solid line) isotropic medium. The sample parameters, used for calculations, are the same for SiNWs and por-Si: $p = 0.75$, $\omega_p = 2000$ cm^{-1}, $g_0 = 500$ cm^{-1}, $g_1 = 1000$ cm^{-1}, $N = 1.6 * 10^{19}$ cm^{-3}. 119

4.3 Calculated effective light penetration depth for s-polarized (dash-dotted line), p-polarized (dashed line) incident light for SiNWs and for natural incident light for doped (black solid line) and undoped (red solid line) por-Si. 119

4.4 Spectra of specular reflectance for n-type (blue circles) and p-type (red circles) c-Si wafers. Lines show their fit using the Drude model (see Eqs. (4.1)-(4.5)). . 121

4.5 Spectra of specular reflectance for low- and highly-doped c-Si wafers (black and red dotted lines, respectively), initial (black line) and doped (red line) macroporous Si samples, prepared for the etching time of 5 min. 122

Cette thèse est accessible à l'adresse : http://theses.insa-lyon.fr/publication/2019LYSEI129/these.pdf
© [S. Rodichkina], [2019], INSA de Lyon, tous droits réservés

4.6 ATR spectra for the initial (circles) and doped (lines) por-Si layers prepared for the etching time of 5 (blue), 20 (red) and 60 min (black). 123

4.7 (a) Experimental (points) and theoretical (lines) spectra of $-ln(R_{ATR})$, where R_{ATR} are the relative ATR values for additionally doped por-Si layers etched for different time. (b) Calculated spectra of the absorption coefficient (α) for the same por-Si layers. 123

4.8 Absorption spectrum of por-Si layer (5 min etching) obtained from the ATR data (circles) and modeling results, where the fitting parameter ω_p is varied (lines). . 125

4.9 (a) ATR spectra for powder of initial (close circles) and doped (open circles) por-Si. (b) Spectra of $-ln(R_{ATR})$ for powder of doped por-Si. Line corresponds to the fit of experimental spectra with the theoretical model assuming $p = 0.9$ and electron concentration of about $2 * 10^{19}$ cm^{-3}. 125

4.10 Spectrum of $-ln(R_{ATR})$ for highly-doped SiNWs with the length of 4 μm (black line) and its fitting using the anisotropic model with (magenta line) and without (black line) surface scattering of charge carriers, and isotropc model with (red line) and without (blue line) surface scattering of charge carriers. The inset shows the ATR spectra for this SiNWs sample before (red line) and after (black line) the additional doping. 127

4.11 Experimental spectra (points) and fitting (lines) of the ATR signal ($-ln(R_{ATR})$) for p-type SiNWs with different length. The fitting was done using Eqs. (4.6)-(4.11), (4.3)-(4.5) considering $g_1 \neq 0$. 129

4.12 Raman spectra of initial and additionally doped SiNWs (length of 8 μm) and corresponding c-Si wafer under excitation with laser wavelength of 632.8 nm. Solid lines are fits of the spectra according to Eq.(4.13). 130

4.13 Raman spectra of highly doped SiNWs with the length of 8 μm for different laser wavelengths of 473, 514.5 and 632.8 nm. Solid lines are fits of the spectra according to Eq. (4.13). 132

Cette thèse est accessible à l'adresse : http://theses.insa-lyon.fr/publication/2019LYSEI129/these.pdf
© [S. Rodichkina], [2019], INSA de Lyon, tous droits réservés

4.14 Raman spectra for SiNWs array on c-Si substrate (triangles) and detached SiNWs (circles). SiNWs length is of 15 μm. Solid lines represent fits of the spectra by Eq.(4.13). Contribution of c-Si substrate and fit of the total Raman spectrum of SiNWs on c-Si substrate are given by dash-dotted and dashed lines, correspondingly. The inset shows dependence of the relative integrated intensity of c-Si substrate peak in the total Raman spectrum for doped SiNWs on nanowire's length, solid line represents the fit of this dependence with Eq.(4.14). Laser wavelength is 632.8 nm. 134

4.15 Dependence of the Raman line half-width (Γ) on the free hole concentration for c-Si (open squares, circles and triangles) and SiNWs (blue triangles). Line is a fit by Eq.(4.15) with $C_1 = -1.8$ cm^{-1} and $C_2 = 3.8$. 136

4.16 Profiles of the free charge carrier concentration in arrays of doped SiNWs (length of 10 μm). The doping was done using the standard spin-on dopant (solid circles) and 50% diluted one with acetone (open circles). The inset illustrates the Raman mapping technique. 137

4.17 Normalized Raman spectra for SiNWs with different length (circles). Blue lines correspond to the Raman peaks for doped SiNWs (solid lines) and c-Si substrate (dash-dotted lines). Black lines show the total fit of the Raman spectra for SiNWs samples. Excitation wavelength is of 632.8 nm. 138

4.18 (a) Experimental spectra (points) and fitting (lines) of the ATR signal ($-ln(R_{ATR})$) for n-type SiNWs with different length. The fitting was done using Eqs. (4.6)-(4.11), (4.3)-(4.5) considering $g_1 \neq 0$. (b) Normalized Raman spectra for highly-doped n-type SiNWs and of initial c-Si substrate. 140

5.1 In-depth profile of the free hole concentration in SiNWs array after the additional doping using the standard spin-on dopant (black points) and one, fourfold diluted with ethanol, applied to SiNWs four times before the annealing (red points). The RTA annealing for 15 s with a maximum temperature of about 950 ^{0}C was used for both samples. The lines are to guide the eye, z is the depth coordinate with $z = 0$ at SiNWs top and $z = L$ at SiNWs/c-Si interface. 145

5.2 Free hole concentration in the top layer of SiNWs array for diluted SOD solution (acetone) as a function of the dissolution degree. The annealing temperature was about 900 ^{0}C. The line is to guide the eye. 146

Cette thèse est accessible à l'adresse : http://theses.insa-lyon.fr/publication/2019LYSEI129/these.pdf
© [S. Rodichkina], [2019], INSA de Lyon, tous droits réservés

5.3 Dependence of the free hole concentration for the top layer of SiNWs array on the number of spin-coating and pre-baking procedures. SOD fourfold diluted with acetone was used. The annealing temperature was about 900 ^{0}C. The line is to guide the eye. 146

5.4 In-depth profile of the free hole concentration in SiNWs array after the additional doping using the thin (open circles) and thick (solid circles) layer of deposited spin-on dopant, obtained by using the spin-coating procedure and without it, correspondingly. The annealing was performed for 25 s using the RTA device with maximal temperature of about 1000 ^{0}C. The lines are to guide the eye. . . 147

5.5 In-depth profile of the free hole concentration in SiNWs array after the additional doping using the thin (open circles) and thick (solid circles) layer of deposited spin-on dopant, obtained by using the spin-coating procedure and without it, correspondingly. The annealing was performed for 5 min using the oven at about 1000 ^{0}C. The lines are to guide the eye. 148

5.6 (a) Free hole concentration for the top layer of SiNWs array as a function of maximal temperature in the RTA chamber for the standard SOD (black squares) and one diluted 3 times with isopropanol (blue squares). Blue line shows the linear fit of the corresponding dependence, black dashed line is to guide the eye. (b) Temperature in the RTA chamber as a function of time for the different annealing time. 149

5.7 (a) Photoluminescence spectra of initial (red circles) and doped (blue) SiNWs, the line shows the Gauss fit of PL spectrum for doped SiNWs, (b) Dependence of the free hole concentration in doped SiNWs on the PL intensity of initial ones. The line is a guide for eye. 151

6.1 (a) Electrical resistance of the initial and additionally doped samples versus thickness of the PS layer; (b) "specific resistivity" of the initial ad additionally doped PS/c-Si structures measured by the standard 4-probe setup versus thickness of the PS layer. (c) Dependence of the electrical resistance on the distance between electrodes (d) for 5μm sample. (d) Schematic illustration of the configuration used for electrical measurements. 155

Cette thèse est accessible à l'adresse : http://theses.insa-lyon.fr/publication/2019LYSEI129/these.pdf
© [S. Rodichkina], [2019], INSA de Lyon, tous droits réservés

6.2 (a) Dependence of the electrical resistance on the distance between electrodes for doped SiNWs samples with length of 25 and 10 μm. Electrical contact area is of 2 and 1.4 mm^2 for 25 and 10 μm sample, correspondingly. The free hole concentration in both samples, determined using the Raman spectroscopy, is of about $1.6*10^{20}$ cm^{-3}. 156

6.3 Raman spectra of low doped c-Si wafer under oven heating at different temperatures. 158

6.4 Dependence of the spectral position (a) and width (b) of the Raman peak for low doped c-Si on temperature. The red lines in (a,b) show the linear fit of the corresponding dependencies. The linear fits are given by: $\Omega = 528.2$ [cm^{-1}] $-$ 0.025 [cm^{-1}/K] $*T$; $\Gamma = 1.9$ [cm^{-1}] $+ 0.0083$ [cm^{-1}/K] $*T$, where T is the absolute temperature given in [K]. 158

6.5 Normalized Raman spectra for SiNWs at low laser intensities. The inset shows the dependence of integrated Raman peak intensity for SiNWs on the laser intensity. 160

6.6 Heating of SiNWs at the center of the laser spot, calculated from the Raman peak position (blue rectangles) and width (red rectangles) as a function of excitation laser intensity. 161

6.7 Illustration of the theoretical model used for calculations of the temperature distribution in SiNWs. The color indicates the SiNWs temperature, accordingly to the scale on the right. 162

6.8 Experiment dependence (circles) of the photo-induced heating of SiNWs on their length. Lines show the fits of the experimental dependence, calculated assuming the three-dimensional (black line) and one-dimensional (red line) heat transport in SiNWs array. 163

6.9 Heating of SiNWs, determined from the broadening of the one-phonon Raman peak, as a function of the laser power for (a) initial and (b) doped SiNWs. Lines show the linear fits of the above dependencies. Insets: (points) Raman spectra of SiNWs at different laser power, (lines) fit of the Raman spectra with Fano resonance function. The free hole concentration in doped SiNWs is of 15.7 ± 0.7 cm^{-3}. Laser wavelength is 632.8 nm. 165

Cette thèse est accessible à l'adresse : http://theses.insa-lyon.fr/publication/2019LYSEI129/these.pdf
© [S. Rodichkina], [2019], INSA de Lyon, tous droits réservés

6.10 Effective thermal conductivity coefficient of SiNWs array as a function of the free hole concentration. SiNWs length is 10 and 25 μm. Lines show the least squares linear fit of the above dependence. 166

Cette thèse est accessible à l'adresse : http://theses.insa-lyon.fr/publication/2019LYSEI129/these.pdf
© [S. Rodichkina], [2019], INSA de Lyon, tous droits réservés

List of Tables

1.1 Different characteristics of SiNWs, fabricated by VLS, MACE and RIE methods. Adapted from [44]. 32

1.2 Comparison of thermoelectric properties of metals, semiconductors and insulators at $T = 300$ K. Adapted from [45]. 80

2.1 The parameters of MACE procedure used to obtain high aspect ratio SiNWs. . 91

2.2 Investigated samples, their morphology and doping parameters. D is the diameter and L is the length of nanowires in SiNWs array, N is the free charge carrier concentration. MACE column refers to the MACE procedure from Table 2.1, used for SiNWs fabrication. 93

4.1 Sample parameters obtained from the experimental data and from the modeling of IR-ATR spectra for por-Si. 124

4.2 Sample parameters obtained from the experimental data and from modeling of IR-ATR spectra for SiNWs using the isotropic and anisotropic effective medium approximation. 128

4.3 Raman line shape parameters for c-Si wafers, initial and doped SiNWs (length of 8 μm) for different laser wavelengths, obtained by fitting the Raman spectra with Eq.(4.13) 131

4.4 Free charge carrier concentration in p-type SiNWs of different length obtained from the modeling of the IR-ATR spectra of SiNWs considering the anisotropic effective medium and $g_1 \neq 0$, as well as from the Raman spectra using the Fano peak half-width. 139

Cette thèse est accessible à l'adresse : http://theses.insa-lyon.fr/publication/2019LYSEI129/these.pdf
© [S. Rodichkina], [2019], INSA de Lyon, tous droits réservés

List of abbreviations

SiNWs	silicon nanowires
por-Si	porous silicon
c-Si	bulk crystalline silicon
MACE	metal-assisted chemical etching
SOD	spin-on dopant
RTA	rapid thermal annealing
IR	infrared (spectroscopy)
ATR	attenuated total reflectance
PL	photoluminescence
SEM	scanning electron microscopy
TEM	transmission electron microscopy
HRTEM	high-resolution transmission electron microscopy
L	length of SiNWs
D	diameter of SiNWs
Γ	half-width of the Raman peak
Ω	phonon frequency
N	free charge carrier concentration
μ	free charge carrier mobility
T	temperature
ρ	electrical resistivity
σ	electrical conductivity
k	thermal conductivity

Cette thèse est accessible à l'adresse : http://theses.insa-lyon.fr/publication/2019LYSEI129/these.pdf
© [S. Rodichkina], [2019], INSA de Lyon, tous droits réservés

General introduction

Thermal energy conversion is one of the critical issues in modern energy technology due to the increasing demand in waste heat utilization and ecological power sources. Thermoelectric (TE) generators, which use temperature difference to create an electric current, are attracting increasing attention due to numerous advantages, such as direct energy conversion, absence of moving parts and long service life. For years, TE generators were mainly developed to generate electrical power in severe conditions, e.g. in space, due to their extreme reliability. Low efficiency and relatively high cost of current TE materials does not allow the widespread use of TE generators.

The capability of TE material to efficiently produce thermoelectric power is described by its TE figure of merit

$$ZT = \frac{S^2 \sigma T}{k} \quad (1)$$

where S is the Seebeck coefficient, σ is the electrical conductivity, k is the thermal conductivity, T is the absolute temperature. The figure of merit of TE material is related to the efficiency of TE generator. The optimal TE material should have thermal properties like that of a glass, and electrical properties like that of a single-crystal. Slack G.A. (1995) has described the perfect material for TE applications within the concept of "phonon-glass electron-crystal". Such a material possesses a low thermal conductivity and a good electrical conductivity, which enhances its TE performance.

Silicon nanowires (SiNWs) represent a promising thermoelectric material within the framework of the concept "phonon-glass electron-crystal". Rough SiNWs exhibit low thermal conductivity close to that of amorphous silicon and bulk-like electrical properties. For the optimal doping level ($\sim 10^{20}$ cm^{-3}), ZT in SiNWs can reach the value of three at room temperature, which exceeds the current values for commercial thermoelectric materials. The highest experimentally observed value of ZT for individual SiNWs at $T = 300$ K is of about 0.7 [7], which is close to that for commonly used bismuth chalcogenides (ZT = 0.8-1.0).

The actual problems on the way to creating efficient SiNWs-based TE devices include the

Cette thèse est accessible à l'adresse : http://theses.insa-lyon.fr/publication/2019LYSEI129/these.pdf
© [S. Rodichkina], [2019], INSA de Lyon, tous droits réservés

lack of low-cost, large-area and simple fabrication methods for highly-doped SiNWs arrays. While the thermal and electrical conductivity of individual SiNWs have been studied in sufficient detail, there are few relevant data for low- and highly-doped SiNWs arrays. The characterization of SiNWs arrays is challenging, and the contactless, nondestructive methods for characterization of SiNWs arrays are of high importance.

We have carried out the systematic research of thermal and electrical properties of SiNWs arrays, fabricated by wet chemical etching, followed by additional thermo-diffusional doping. We developed optical methods for express-diagnostics of thermal and electrical properties of SiNWs arrays. We have shown that fabricated highly-doped SiNWs possess the low thermal and high electrical conductivity, which is essential for TE applications.

PhD thesis consists of six chapters:

- First chapter represents the literature review, and it provides the state of the art on fabrication and doping of SiNWs, their structural, thermal and electrical properties. The optimal morphology and doping level of SiNWs for thermoelectric applications is discussed, and the strategy for fabrication of SiNWs arrays with optimal properties is chosen.
- Second chapter provides a summary of the methods used for fabrication and doping of SiNWs arrays, as well as of the used characterization techniques. An overview of the investigated samples, including the fabrication conditions, morphology, doping type and level, is given.
- Third chapter describes the fabrication of low-doped SiNWs arrays by metal-assisted chemical etching (MACE), and he morphology and crystallinity of SiNWs fabricated on c-Si substrates with different doping type and level is studied. Further, the reversible photo-induced formation of hex-Si phase in initially cubic diamond MACE-fabricated SiNWs is reported. A key role of mechanical stresses in SiNWs due to temperature gradient along nanowires is emphasized to be responsible for the hex-Si phase formation, that should be taken into account for TE applications of SiNWs
- Fourth chapter is devoted to studying the effectiveness of the post-fabrication doping of SiNWs using the the thermally activated diffusion of dopant atoms from the spin-on dopant solutions. The contactless methods based on infrared spectroscopy and Raman scattering spectroscopy are developed to monitor the free charge carrier concentration in highly-doped SiNWs arrays.
- Fifth chapter investigates in detail the in-depth doping of SiNWs arrays, i.e. the influence

Cette thèse est accessible à l'adresse : http://theses.insa-lyon.fr/publication/2019LYSEI129/these.pdf
© [S. Rodichkina], [2019], INSA de Lyon, tous droits réservés

of the dilution degree of dopant solution, annealing time and temperature on the in-depth profiles of the free charge carrier concentration in SiNWs, as well as the influence of morphology of SiNWs on the doping efficiency.

– In sixth chapter the electrical and thermal conductivity of highly-doped SiNWs arrays is estimated using the Raman scattering spectroscopy technique. The obtained data are used to evaluate the potential of fabricated SiNWs arrays as a thermoelectric material.

This work aims to provide a reader with information on fabrication of highly-doped SiNWs arrays, their contactless diagnostics, thermal and electrical conductivity. The obtained data will be useful for application of highly-doped MACE-SiNWs arrays in thermoelectric, nano-electronic and sensor devices. The developed techniques for SiNWs characterization will allow us the express-diagnostics of Si nanostructured materials of various morphology and doping. We hope that the conducted research will stimulate further investigation of highly-doped MACE-SiNWs arrays, in particular, their Seebeck coefficient, and creation of efficient ecological and low-cost TE devices.

Cette thèse est accessible à l'adresse : http://theses.insa-lyon.fr/publication/2019LYSEI129/these.pdf
© [S. Rodichkina], [2019], INSA de Lyon, tous droits réservés

Chapter 1
State of the art: fabrication and properties of silicon nanowires (SiNWs)

1.1 Fabrication of SiNWs arrays, their morphology and structural properties

This section describes the controlled fabrication and structural properties of SiNWs. The common top-down method of metal-assisted chemical etching (MACE) of c-Si wafers and bottom-up method of vapour-liquid-solid (VLS) growth of SiNWs are described, and the mechanisms of SiNWs formation in both methods are explained. Both the above methods are versatile, and the control of the morphology of formed SiNWs by varying the fabrication conditions is reported. In addition, the possibility of the VLS growth of hexagonal diamond SiNWs is shown and discussed in the perspective of their thermoelectric applications.

1.1.1 Common fabrication techniques

Fig. 1.1 illustrates the common fabrication techniques of SiNWs. They include different approaches, such as wet chemical etching [46], reactive ion etching (RIE) [47, 48], combined with different lithographic techniques [49, 50], as well as vapour–liquid–solid (VLS) method implemented by chemical vapour deposition [51], laser ablation [52], molecular beam epitaxy [53]. All the fabrication procedures can be classified under two main categories: (a) the top-down approaches and (b) the bottom-up approaches [1].

The top-down approaches consist in the removal of the material from initial c-Si wafers. Standard etching process to remove silicon are the wet chemical etching and RIE, which can produce highly uniform vertical SiNWs arrays on c-Si wafers [1]. Besides, they are commonly used to fabricate horizontal SiNWs on silicon-on-insulator substrates [37, 38]. The lithographic techniques, such as the electron-beam [49] or the extreme ultra-violet interference lithography

Cette thèse est accessible à l'adresse : http://theses.insa-lyon.fr/publication/2019LYSEI129/these.pdf
© [S. Rodichkina], [2019], INSA de Lyon, tous droits réservés

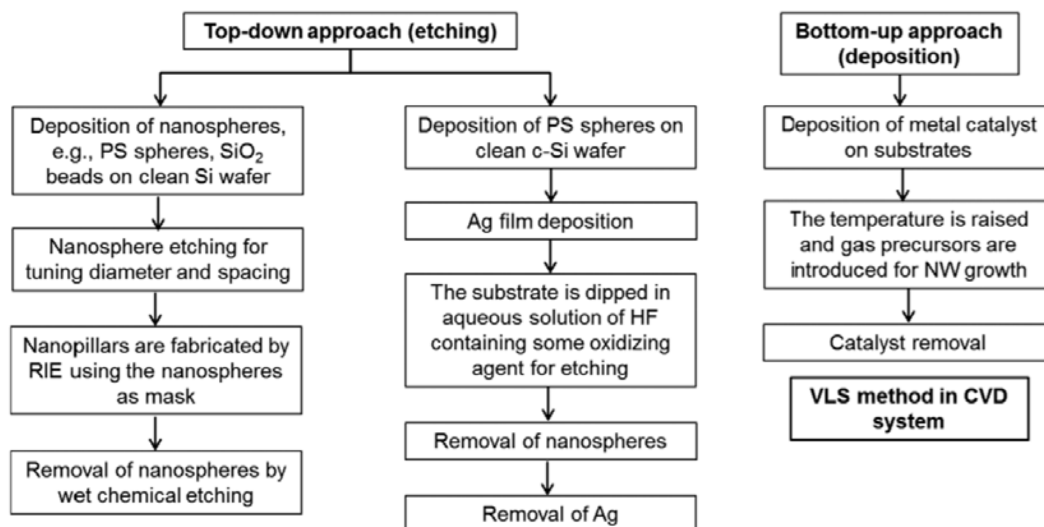

Figure 1.1: SiNWs production steps for top-down and bottom-up approaches [1]

[50], can be used to create an etching mask and define the etching pattern. The role of the etching mask is to protect certain areas of the wafer, which can also be easily achieved by patterning using the nanosphere assembly or nano-imprint lithography [1]. The nanosphere assembly approach involves silica (SiO_2) or polymer spheres deposited on the wafer using the spin coating, dip coating, roll coating or the Langmuir–Blodgett methods [47, 48]. The deep reactive ion etching (DRIE) technique was developed to obtain high aspect-ratio SiNWs [48]. The SiNWs length and diameter can be controlled by the RIE time and the silica nanosphere diameter. Highly oriented SiNW arrays can also be produced by metal-assisted chemical etching (MACE) of c-Si wafers [46]. The etching mask can be produced by immersing the wafer in a HF–$AgNO_3$ solution [54]. Also, to create the etching mask, the annealing of the Ag film was used to obtain spherical Ag particles on c-Si wafer, which served as the inverse pattern. Then the Au layer was deposited on c-Si wafer with Ag spheres with subsequent liftoff of Ag to create the Au etching mask [55]. MACE is performed in an aqueous solution containing HF and oxidizing agents, e.g. H_2O_2 or $Fe(NO_3)_3$ [46]. Highly ordered SiNWs arrays with controlled diameter can be obtained by the combination of lithography techniques and MACE [1, 46]. The crystalline structure and morphology of SiNWs, fabricated by top-down approach, is determined by those of the initial c-Si substrate [46, 48].

The most common bottom-up approach to synthesize SiNWs is based on the VLS mechanism [1]. Wagner et al. were the first to use this method to grow SiNWs epitaxially on c-Si (111) substrates using Au as a catalyst [51]. The VLS method works well over a wide range of nanowire lengths ($\sim$ 100 nm $\div$ 100 μm) and diameters ($\sim$ 1 nm $\div$ 1 μm) [1]. This process also

Cette thèse est accessible à l'adresse : http://theses.insa-lyon.fr/publication/2019LYSEI129/these.pdf
© [S. Rodichkina], [2019], INSA de Lyon, tous droits réservés

offers the advantage of in-situ doping by introducing dopant gases (e.g. PH_3 or B_2H_6) in order to achieve n-type or p-type doping [56, 57]. The porous anodic aluminum oxide templates were used in the VLS growth method to obtain highly-ordered SiNWs arrays [58]. The VLS nanowire growth methods have been demonstrated by various techniques [44], such as chemical vapor deposition [51], plasma-enhanced chemical vapour deposition [59], molecular beam epitaxy [60], laser ablation [52]. Due to the nature of VLS mechanisms, the choice of precursors and catalysts plays a significant role in the nanowire synthesis [9]. Especially, the oxide assisted growth mechanism, an approach to grow SiNWs without the presence of metal catalysts, is favorable for high performance device without metal contamination [44].

Table 1.1: Different characteristics of SiNWs, fabricated by VLS, MACE and RIE methods. Adapted from [44].

Method	Diameter	Length	Morphology	Defects	Cost
VLS	1 nm - 1 μm	0.1 - 100 μm	bulk core/ smooth surface	Metal contamination or twin fault	High
MACE	5 nm - 1 μm	0.1 - 100 μm	bulk or porous core/ rough (Ag, Au) or smooth (Au) surface	None	Low
RIE	determined by template	0.1 - 10 μm	bulk core/ surface defects	Surface defects	High

Table 1.1 shows the overview of advantages and drawbacks of common SiNWs fabrication techniques. It is important to note that SiNWs arrays, especially those fabricated using MACE, can represent non-one-dimensional structures, since SiNWs in the array can be interconnected. In this case the SiNWs array is a quasi-one-dimensional structure, in which the lateral thermal and electrical transport is strongly suppressed compared to the one along SiNWs. The following sections discuss the MACE and VLS mechanisms in detail as the most commonly used for fabrication of SiNWs with high thermoelectric performance.

1.1.2 Metal-assisted chemical etching

a) Mechanism

Metal-assisted chemical etching (MACE) is a low-cost top-down method, which allows to fabricate large-area vertically aligned SiNWs arrays with high uniformity. In this method, noble metal mask is formed on a silicon substrate and then the silicon underneath the metal is etched off, leaving behind arrays of SiNWs. MACE process requires two fundamental components:

Cette thèse est accessible à l'adresse : http://theses.insa-lyon.fr/publication/2019LYSEI129/these.pdf
© [S. Rodichkina], [2019], INSA de Lyon, tous droits réservés

(i) an oxidant, which can oxidize the metal nanoparticles and (ii) an etchant to dissolve the ionic silicon. The metal plays a role of a local catalyst of the etching reaction, and provides the anisotropic etching of Si wafer. MACE allows versatile control of SiNWs morphology (diameter, length, surface roughness), crystalline orientation and density of SiNWs array by varying the c-Si wafer, noble metal, type and concentration of oxidant and etchant [46].

To fabricate SiNWs arrays with the diameter of about 100 nm and length of 10-100 μm for thermoelectric applications, Ag (silver) assisted MACE is usually used, performed in two steps. The following mechanisms take place [2]:

(a) 1 step: Ag deposition. In this step, Si wafers are immersed in $AgNO_3$-containing aqueous solution. Ag^+ ions from the solution are reduced at Si surface by taking electron from Si wafer and from Ag nanoparticles at Si surface. Thus, the thickness of the deposited Ag layer increases with the immersing time and electron concentration in Si wafer. Fig. 1.2 shows the illustration of the mechanism of the Ag deposition on a Si wafer.

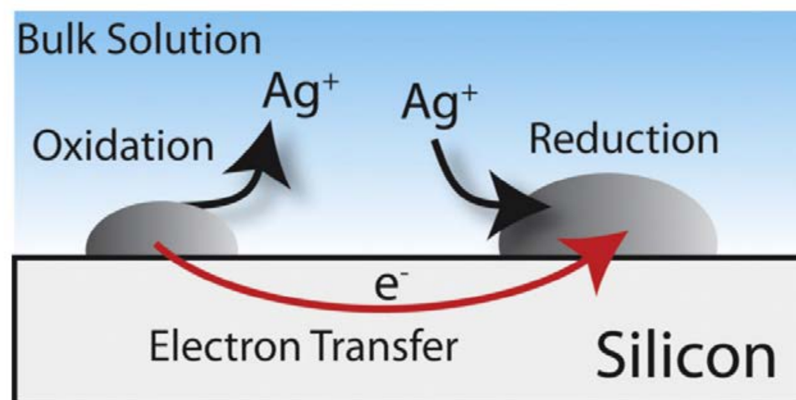

Figure 1.2: Illustration of Ag deposition during the first step of MACE. Due to the facile Ag^+/Ag reaction and ohmic interfacial electron exchange between silicon and silver, Ag nanoparticle dynamically reorganize to their lowest energy state [2].

(b) 2 step: etching of Si substrates. In this step, Ag-covered Si wafers are immersed in aqueous solution containing H_2O_2 and HF, which leads to several simultaneous chemical reactions:

1. Ag nanoparticles are oxidized at Si surface by H_2O_2: $Ag^0 \rightarrow Ag^+$.
2. Ag nanoparticles are reduced by taking an electron from Si wafer:
   $Ag^+ \rightarrow Ag^0$; $Si^0 \rightarrow Si^+$. This step is similar to the Ag deposition on Si substrate from the solution.
3. Si^+ is dissolved in HF.

Fig. 1.3 shows an illustration of the mechanism of Ag-assisted etching of Si wafer. Depending

Cette thèse est accessible à l'adresse : http://theses.insa-lyon.fr/publication/2019LYSEI129/these.pdf
© [S. Rodichkina], [2019], INSA de Lyon, tous droits réservés

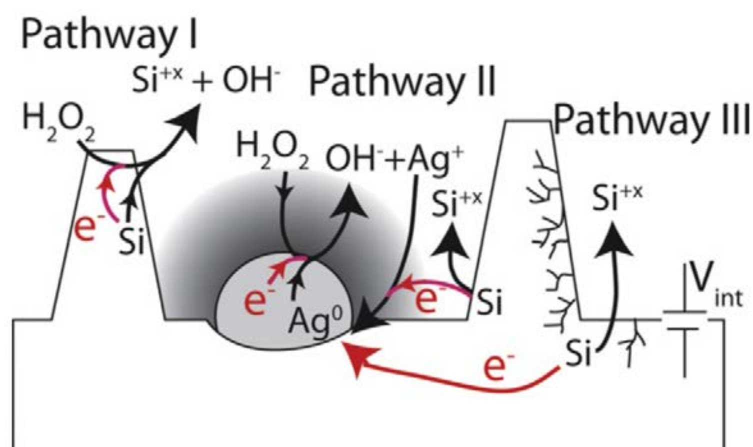

Figure 1.3: Illustration of the etching mechanism of Si in HF and H_2O_2 solution. Pathway I involves the direct reaction of H_2O_2 with Si and is kinetically not favored. Pathway II is the preferred Si oxidation reaction, which involves Ag/Ag^+, leading to nanowire formation. Pathway III shows the diffusion of holes from the Ag/Si interface, which leads to general porous silicon formation. HF is not shown in the diagram, but implied [2].

on the etching conditions, bulk core/rough surface and porous SiNWs, as well as por-Si can be formed. The pore formation in SiNWs during the etching is mainly due to two reasons. First, Ag is known to be dissolved in HF via oxidation and formation of Ag^+ ions [61]. If the rate of Ag^0 oxidation is higher than the rate of Ag^+ reduction, the formed Ag^+ ions go into the solution and then redeposit in other places of SiNWs, where pores in Si are later formed [62]. Secondly, the holes in Si wafer can diffuse away from the metal-coated area and cause the dissolution of Si by HF [63]. The latter fact explains the formation of porous SiNWs or even por-Si on highly-doped Si wafers. Also, the stain etching of Si due to direct oxidation of Si by H_2O_2 or due to holes in Si wafer also increases the surface roughness of SiNWs, at that, the etching rate for MACE is considerably higher than that for the stain etching [64]. Fig. 1.3 illustrates the mechanism of the pore formation in SiNWs due to hole diffusion and stain etching. Note, that to exclude the influence of Ag redeposition during the etching, other metals, such as Pt or Au, which are not dissolved by H_2O_2, can be used [65, 66].

b) Role of substrate doping type

Fig. 1.4 shows the typical SEM image of SiNWs arrays fabricated by Ag-assisted etching of p- and n-type low-doped (100) c-Si substrates. Samples represent arrays of vertically aligned nanowires on a c-Si substrate with nearly uniform diameter along nanowires. The etching time for the samples was 2 h, and the length both for p- and n-type SiNWs is of about 20 μm. The insensitivity of MACE to the doping type of c-Si was previously reported (see Ref. [64] and

Cette thèse est accessible à l'adresse : http://theses.insa-lyon.fr/publication/2019LYSEI129/these.pdf
© [S. Rodichkina], [2019], INSA de Lyon, tous droits réservés

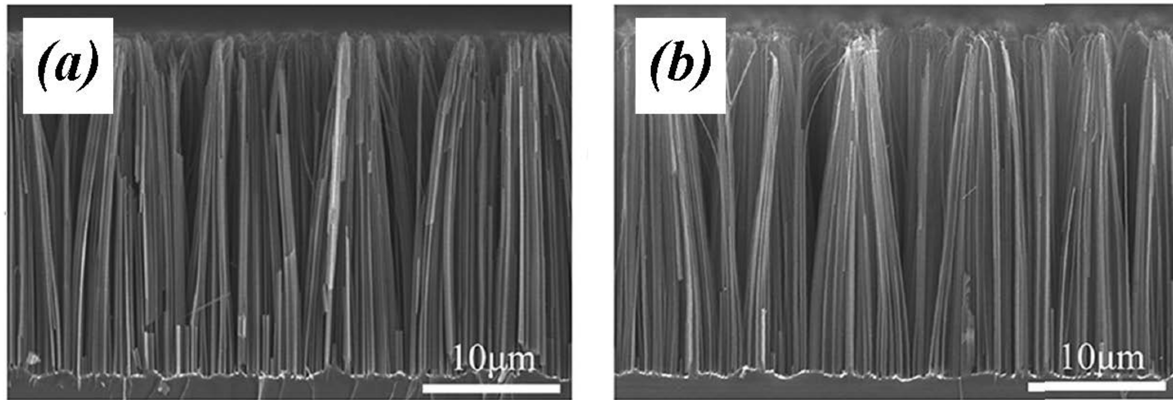

Figure 1.4: SEM images of SiNWs arrays, fabricated by MACE of (a) p-type and (b) n-type c-Si (100) wafers with the specific resistivity of 0.2–1.0 Ω*cm Si(100) wafers [3].

references therein), and it was explained by the independence of the Si valence band energy at Ag/Si interface on doping type of c-Si, which determines the rate of Ag^+ ion reduction for the c-Si substrate with a given Fermi level [64].

c) Role of substrate crystalline orientation

The etching of Si substrates in the MACE method is anisotropic and occurs mainly in $< 100 >$ crystallographic direction. By etching (100) c-Si substrates, vertically oriented nanowires perpendicular to the substrate are formed [67]. For the substrates with a different crystallographic orientation, the etching in most cases occurs at an inclination to the substrate surface, in one of the directions equivalent to $< 100 >$ [46]. For example, MACE of (100) and (110) oriented low-doped c-Si substrates resulted in vertically and slantingly SiNWs, respectively, which was explained by etching anisotropy along $< 100 >$ direction [68]. Despite the etching anisotropy, for the substrates with a crystallographic orientation other than (100), there were developed methods that allow to obtain vertically oriented nanowires [46, 68].

d) Ag redeposition during MACE

Accordingly to the above, Ag nanoparticles are dissolved in HF via oxidation, and Ag^+ ions redeposit on SiNWs walls [61]. Fig. 1.5 shows SiNWs array with the length of about 10 μm, formed by Ag-assisted MACE on (100) p-type, 5–50 Ω*cm wafer. Porous silicon is formed at the bottom of SiNWs array and is presumed to cover the nanowires as well. At SiNWs/c-Si interface, the Ag nanoparticles can be seen. Several areas is devoid of Ag nanoparticles, which is explained by the loss of electronic contact between Ag nanopartcile and Si and consequent dissolution of Ag nanoparticle, which terminates nanowire formation in that area, and allows the

Cette thèse est accessible à l'adresse : http://theses.insa-lyon.fr/publication/2019LYSEI129/these.pdf
© [S. Rodichkina], [2019], INSA de Lyon, tous droits réservés

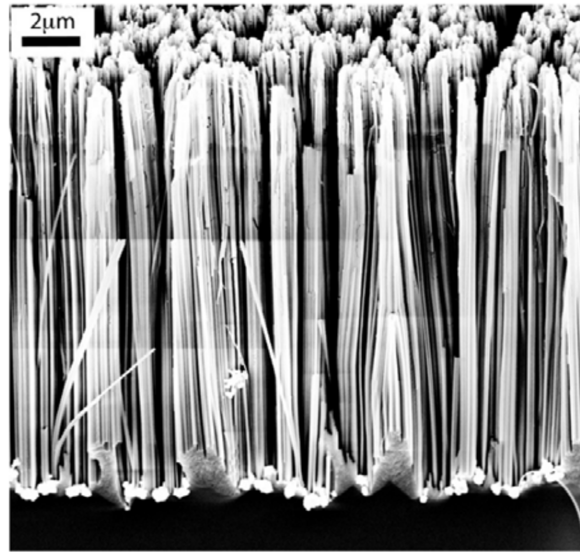

Figure 1.5: SiNWs formed in the Ag/H_2O_2 system. Porous silicon is seen at the base of the nanowires and is presumed to cover the nanowires as well. Areas where Ag nanoparticles are "missing" show terminated etching and a clear accumulation of porous silicon [2].

Ag^+ to diffuse away and react at more remote sites [62], thereby creating a general bulk etching effect.

e) Morphology of MACE-SiNWs

MACE method allows to control various parameters of SiNWs, such as cross-sectional shape, diameter, length, orientation, porosity and doping level. The diameter and cross-sectional shape of SiNWs obtained by MACE is determined by the shape of the metal layer before etching. For example, using the metal films containing identical ordered pores, ordered arrays of SiNWs with the same cross-sectional shape and equal diameters can be formed [46]. The length of SiNWs is increases with the etching time and is proportional to the etching rate. The etching rates of about 0.4-1 μm/min can be expected for Ag-assisted MACE [4].

Fig. 1.6 shows cross-sectional and top-view images of high aspect ratio SiNWs arrays, fabricated by Ag-assisted MACE. The details of the MACE procedure are: at the first step Ag nanoparticles were deposited on Si surface in $HF/AgNO_3$ solution with $AgNO_3$ concentrations of 0.005 M or 0.01 M for 1 min, at the second step c-Si wafers were etched in the solution containing of 4.8 M HF and 0.3 M H_2O_2. The length of SiNWs are about 70 μm, and their diameter is ranged from 100 nm to 1 μm. As one can see, the SiNWs diameter increases with $AgNO_3$ concentration in the first step, which is explained by the different morphology of the deposited Ag layer.

Cette thèse est accessible à l'adresse : http://theses.insa-lyon.fr/publication/2019LYSEI129/these.pdf
© [S. Rodichkina], [2019], INSA de Lyon, tous droits réservés

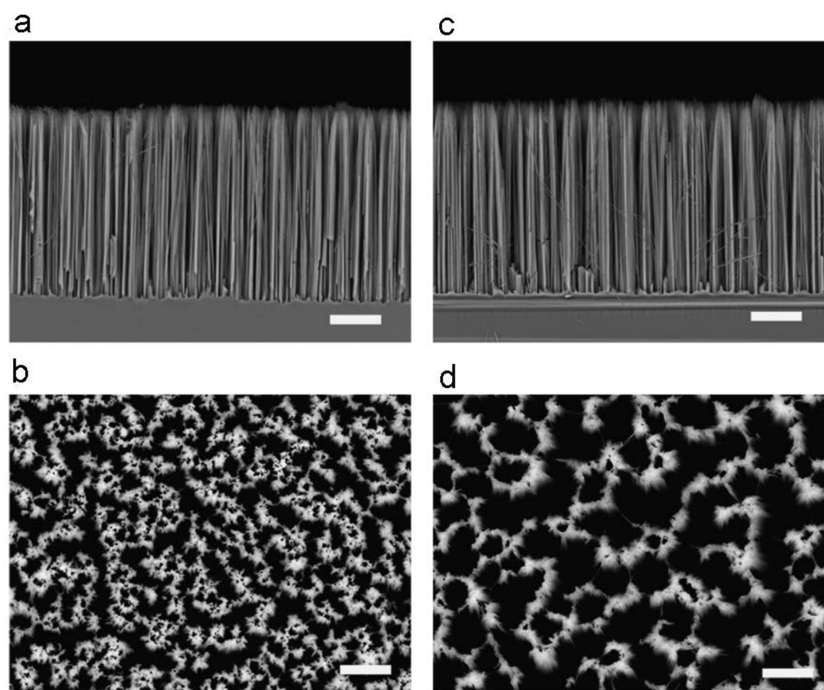

Figure 1.6: Cross-sectional and top-view SEM images of SiNWs arrays, fabricated by MACE of n-type c-Si (100) with $\rho = 0.008 - 0.2$ Ω*cm in etchant solutions composed of 4.8 M HF and 0.3 M H_2O_2. $AgNO_3$ concentration for the deposition of Ag nanoparticles was of (a-b) 5 mM, (c-d) 10 mM. The scale bars in (a,c) and (b,d) are 20 and 10 μm. Adapted from [4].

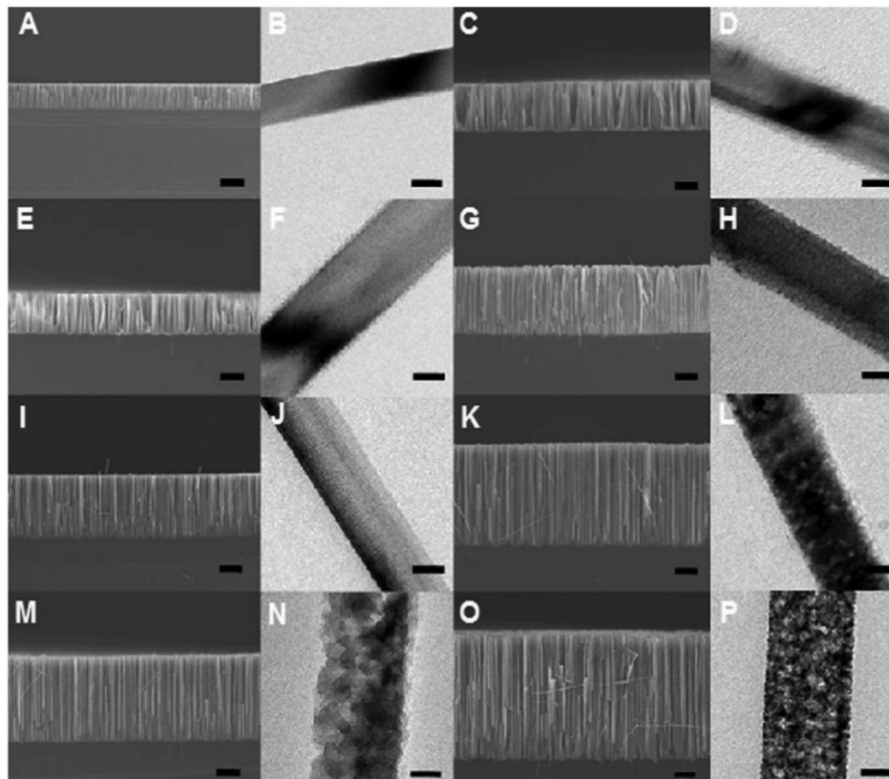

Figure 1.7: SEM and TEM images of SiNWs, fabricated by MACE with increasing concentration of H_2O_2. Substrates: n-type c-Si (100) with $\rho = 0.008 - 0.02$ Ω*cm. HF concentration was of 4.8 M. H_2O_2 concentration was of: (A-D) 0.1 M, (E-H) 0.15 M, (I-L) 0.2 M, (M-P) 0.3 M. The etching time for left-sided and right-sided images was of 30 and 60 min, respectively. The scale bars for SEM and TEM images is 10 μm and 60 nm, respectively [5].

Cette thèse est accessible à l'adresse : http://theses.insa-lyon.fr/publication/2019LYSEI129/these.pdf
© [S. Rodichkina], [2019], INSA de Lyon, tous droits réservés

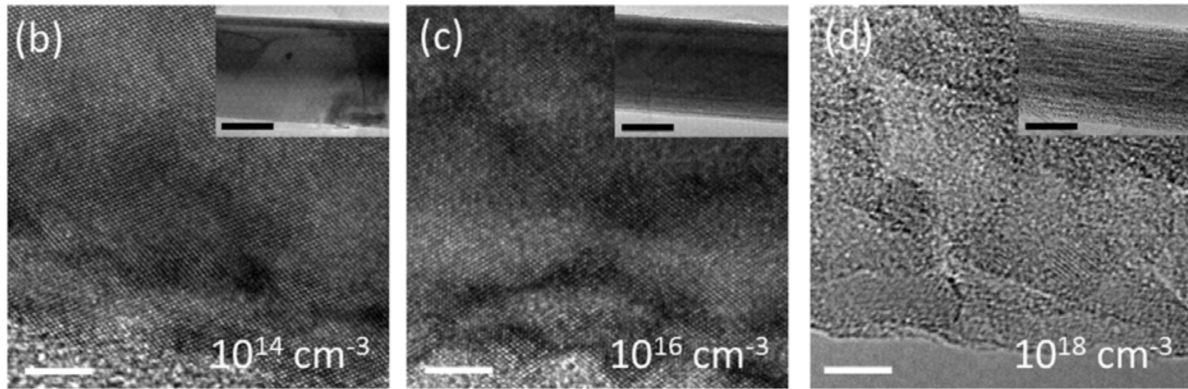

Figure 1.8: HRTEM and TEM (insets) images of MACE-SiNWs, fabricated on p-type c-Si wafers with the doping concentrations of (b) 10^{14}, (c) 10^{16}, and (d) 10^{18} cm^{-3}. The scale bars for HRTEM and inset TEM images are 5 and 200 nm, respectively. Adapted from [6].

Fig. 1.7 shows the evolution of SiNWs morphology with increasing oxidant concentration in the etching solution. The etching solution contained of 4.8 M HF and 0.1-0.3 M H_2O_2. The increase in the porosity of SiNWs with H_2O_2 concentration can be seen, which can be explained by the increase in the rate of Ag redeposition due to enhanced Ag oxidation by H_2O_2, as well as by the increase in the stain etching rate. In general case, the influence of the parameter $\rho_{etch} = [\mathrm{HF}]/([\mathrm{HF}] + [\mathrm{H_2O_2}])$ on the morphology of MACE-SiNWs was thoroughly studied, however the contradictory results were obtained [3, 4, 64, 69, 70].

The type and doping level of SiNWs obtained by MACE are determined by the values of these parameters for the c-Si substrate. However, the substrate doping level also affects the morphology of the formed nanowires. It was established that with an increase in the doping level of the substrate, SiNWs with more rough walls are formed [71]. Fig. 1.8 shows the TEM images of SiNWs, fabricated on p-type boron-doped c-Si with different doping level by Ag-assisted MACE using the pre-deposited 50 nm Ag film and 4.8 M HF/ 0.3 M H_2O_2 etching solution. The increase in surface roughness with c-Si doping level from 10^{14} to 10^{16} cm^{-3} can be seen, while porous SiNWs are formed on 10^{18} cm^{-3} substrates. The formation of mesoporous SiNWs on p-type c-Si wafers with doping level of 10^{19} cm^{-3} was reported [72]. It is important to note, that in contrast to the smooth nanowire surfaces, typical for VLS-grown SiNWs, the surface of SiNWs produced by MACE is much rougher (see Fig. 1.9). The mean roughness height of MACE-SiNWs nanowires is usually of about $1-5$ nm with a roughness period of the order of several nanometres [7].

Cette thèse est accessible à l'adresse : http://theses.insa-lyon.fr/publication/2019LYSEI129/these.pdf
© [S. Rodichkina], [2019], INSA de Lyon, tous droits réservés

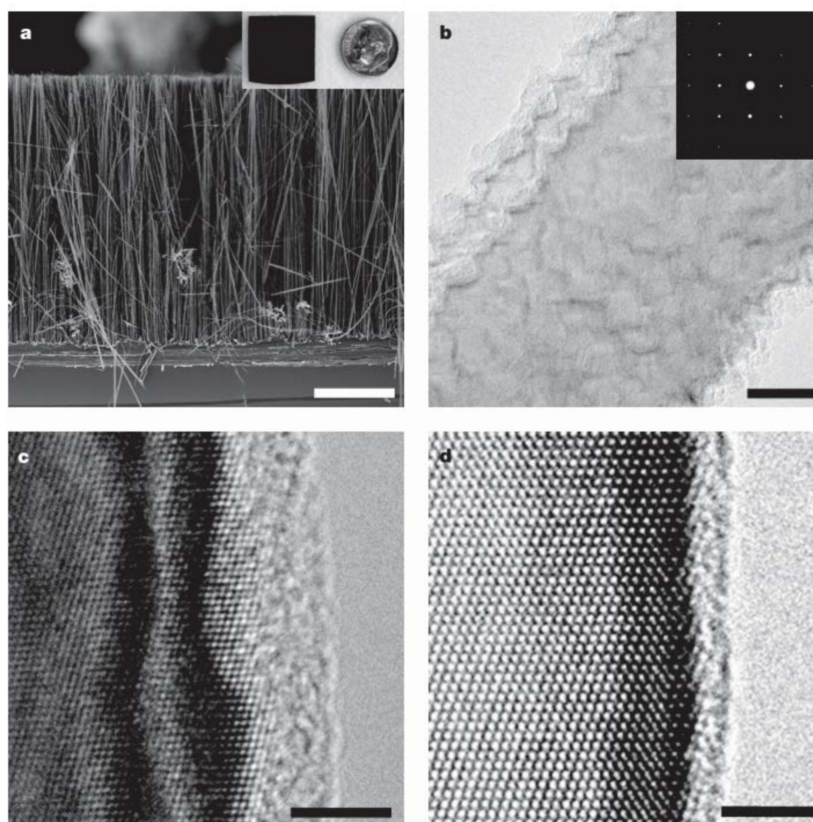

Figure 1.9: (a) SEM image of MACE-SiNWs array. (b) TEM image of MACE-SiNWs. The surface roughness is clearly seen. The SAED pattern (inset) indicates that SiNWs are single crystalline all along the length. (c) HRTEM image of MACE-SiNWs. The roughness is evident at the interface between the crystalline Si core and the amorphous native oxide at the surface, and at undulations of the alternating light/dark thickness fringes near the edge. (d) HRTEM of VLS-SiNWs. Scale bars for a–d are 10 μm, 20 nm, 4 nm and 3 nm, respectively [7].

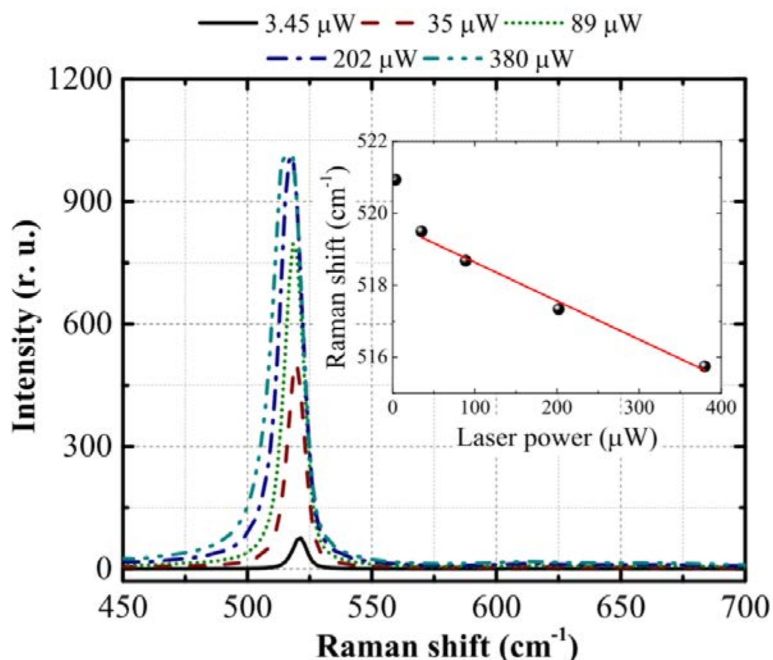

Figure 1.10: Raman spectra of low-doped MACE-SiNWs at different excitation laser power. The inset shows the dependence of the Raman peak position on laser power [8].

Cette thèse est accessible à l'adresse : http://theses.insa-lyon.fr/publication/2019LYSEI129/these.pdf
© [S. Rodichkina], [2019], INSA de Lyon, tous droits réservés

f) Crystalline structure of MACE-SiNWs

Fig. 1.9 shows the TEM and electron diffraction images of MACE-SiNWs. The B-doped p-type (100) Si wafers were used, and the etching was performed in aqueous solution of 0.02M $AgNO_3$ and 5M HF at 50 ^{0}C. Both the electron diffraction and HRTEM images of SiNWs show that SiNWs are single crystalline, they have a cubic diamond lattice, the same as the original c-Si wafers. The rough surface of MACE-SiNWs can be seen, in contrast to smooth surface of VLS-SiNWs, which is explained by the etching of SiNWs walls during the MACE procedure. Fig. 1.8 shows that MACE-SiNWs with both bulk and porous morphology are single crystalline, which was also proved by selected area electron diffraction (SAED) measurements [72].

The crystalline structure of SiNWs can be also studied by the Raman spectroscopy. Fig. 1.10 shows the Raman spectrum for low-doped MACE-SiNWs array. SiNWs length is of 35 μm and the diameter is about 150 nm. At low excitation laser intensity the one-phonon Raman spectrum of SiNWs coincides with the one for c-Si, which implies the same crystalline structure of SiNWs and initial c-Si wafers. Note, the quantum confinement of phonons, which leads to the asymmetric low-frequency broadening of the Raman peak for SiNWs [73], takes place for SiNWs diameter below 10 nm [35, 74]. The low-frequency shift and broadening of the Raman peak of SiNWs with increasing laser power is related to the photo-induced heating of SiNWs [8].

1.1.3 Vapour-liquid-solid growth

a) Mechanism

Let us consider the synthesis of SiNWs by bottom-up methods. The main problem for obtaining nanowires using the bottom-up method is to provide the anisotropic crystal growth. A widely used method for the growth of nanowires of various materials is the vapour-liquid-crystal (VLS) method. In this method, anisotropic crystal growth is facilitated by the presence of the border liquid melt/crystal. SiNWs are usually grown from Si vapors using Au (gold) particles as a solvent at high temperature [75]. The growth of nanowires in the VLS method is explained by the fact that, based on the phase diagram of Si-Au, Si and Au form a liquid melt at a temperature above the eutectic point (363 ^{0}C). The liquid surface of the melt has a large coefficient of accommodation, therefore, the Si atoms from the vapor are deposited mainly on it. After the liquid melt is saturated with silicon, the growth of Si nanowires begins due to precipitation at the liquid-crystal surface [24].

Cette thèse est accessible à l'adresse : http://theses.insa-lyon.fr/publication/2019LYSEI129/these.pdf
© [S. Rodichkina], [2019], INSA de Lyon, tous droits réservés

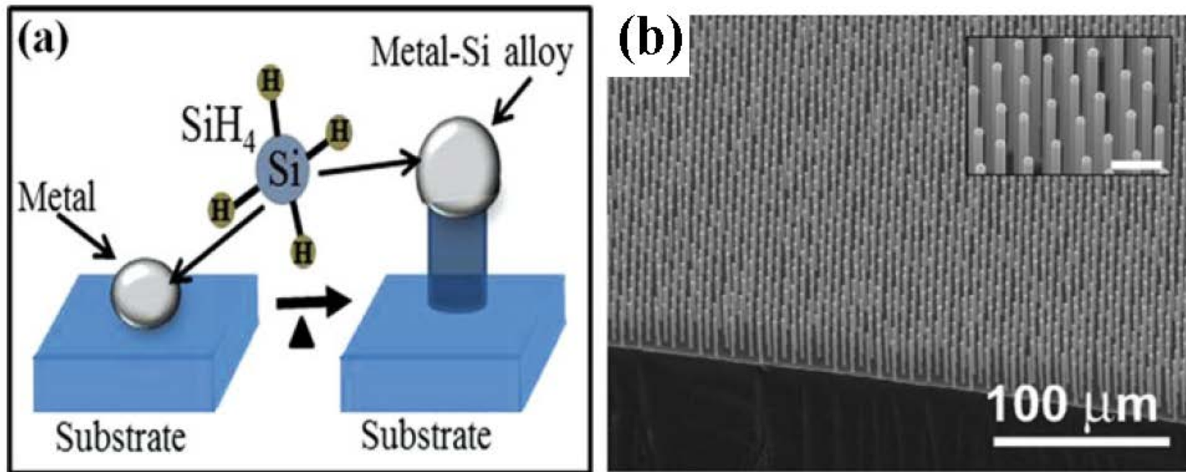

Figure 1.11: a) Schematic illustration of the VLS growth mechanism [9]. (b) Tilted SEM view of a Cu-catalyzed VLS-grown SiNWs array [10]. Adapted from [9].

Thus, the growth of nanowires occurs in 3 stages: (1) the formation of a Si-Au melt, (2) the formation of nuclei of a nanocrystal, (3) elongation of Si nanowires (due to the predominant deposition of Si vapors on the melt drop, and not on the lateral surface of the growing nanowire). The schematic illustration of VLS growth is shown in Fig. 1.11 (a).

For the implementation of the VLS method, it is important that the solvent and the synthesis temperature satisfy the following conditions: first, the solvent and nanowire materials should be able to form a melt, and it is desirable that the melt has a eutectic point; secondly, the synthesis temperature should be in the range between the eutectic point and the melting point of the nanowire material [76]. Si vapour, required during the growth of SiNWs, can be obtained both by physical (laser ablation, thermal evaporation) and chemical methods (chemical vapor deposition, etc.).

While most of the SiNWs grown by VLS process are made using Au as a catalyst, it was found that Au introduces the impurity energy levels within the Si bandgap, which act as deep level traps that decrease free charge carrier mobility [10, 77]. This disadvantage of the Au catalyst provoked the search for alternative metal catalysts, such as Al, Ag, Cu, Ni, Pt, etc. [9].

b) Morphology and crystalline structure of VLS-SiNWs

For the applications, the arrays of nanowires on the substrate rather than individual nanowires are needed, and it is important that all nanowires in the array are oriented in the same direction relative to the substrate. In the VLS method, nanowires grow epitaxially, that is, the crystallographic orientation of the growing atomic layers repeats the crystallographic orientation of the previous

Cette thèse est accessible à l'adresse : http://theses.insa-lyon.fr/publication/2019LYSEI129/these.pdf
© [S. Rodichkina], [2019], INSA de Lyon, tous droits réservés

ones. As a rule, nanowires have certain crystallographic growth directions, in the case of silicon nanowires it is $< 111 >$ direction. Using Si plates with the (111) crystallographic orientation as substrates for the synthesis of SiNWs, one can obtain arrays of the same (vertically) oriented nanowires [78]. When using (001) substrates, 3 sets of nanowires are formed, oriented along 3 directions equivalent to $< 111 >$ [76].

The VLS method also allows to control the arrangement of nanowires on the substrate, which is determined by the initial arrangement of particles or thin Au films. Using various lithographic techniques, one can create the templates of the thin films or nanoparticles of the solvent to produce ordered arrays of nanowires. To control the density of nanowires on the substrate, in addition to templates, thin Au films are also used. When heated, thin films congregate into Au droplets close to each other, and the diameters and density of the droplets on the substrate depend on the thickness of the initial film and the synthesis temperature. During the synthesis of nanowires using thin solvent films, the density of nanowires on the substrate is controlled by changing the thickness of the original Au film [76].

Fig. 1.11 shows a typical SEM image of SiNWs array grown by VLS technique. Highly ordered, vertically aligned and regular SiNWs can be seen. Fig. 1.9 shows a typical TEM image of individual SiNW. The epitaxial growth of SiNWs results in single crystalline structure, which was also proved by X-ray diffraction and SAED [79]. The one-phonon Raman spectra of VLS-SiNWs represent a single peak at about 520 cm^{-1}, the same as that of c-Si [80].

1.1.4 Hexagonal diamond silicon and other polymorphs

Thermoelectric properties of SiNWs can be improved by using various polymorphs of silicon. Fig. 1.12 shows the overview of the most common silicon polymorphs, including high pressure phases, low pressure phases that can potentially be stabilized at ambient conditions, as well as theoretically proposed but not yet observed phases. Among the known Si polymorphs, hexagonal diamond silicon (hex-Si) attracts increasing research interest due to the possible superior thermoelectric properties [43, 81]. Unlike other Si polymorphs, it is metastable at the room temperature [11] and can be rather easily synthesized in SiNWs by VLS-method among with the cubic diamond (cub-Si) phase and other Si polymorphs [12, 82, 83]. It is worth to note that the crystalline phase transition from cub-Si to hex-Si phase can occur in bulk Si under high pressures (>11 GPa) at $T = 300$ K with subsequent annealing above 470 K [11, 84]. The same phase transition was also observed upon indentation of bulk cub-Si [13].

Cette thèse est accessible à l'adresse : http://theses.insa-lyon.fr/publication/2019LYSEI129/these.pdf
© [S. Rodichkina], [2019], INSA de Lyon, tous droits réservés

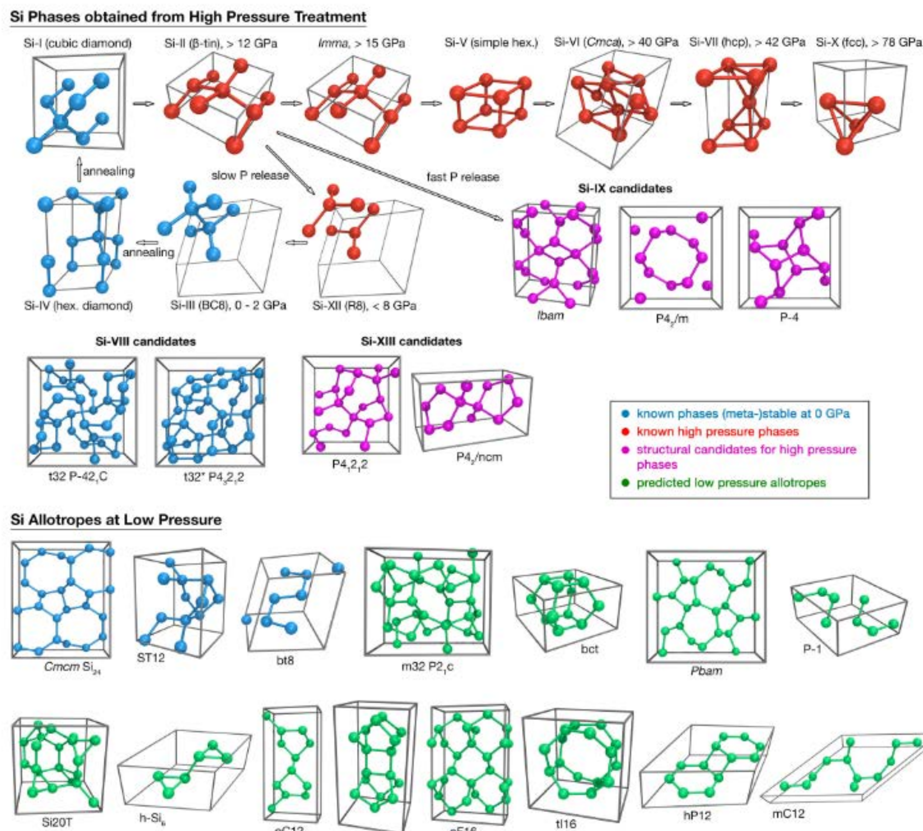

Figure 1.12: Schematic overview of silicon high pressure phases (red) and low pressure low energy allotropes that can potentially be stabilized at ambient conditions. Structures known to exist at ambient conditions are marked in blue. Theoretically proposed but not yet observed structures are shown in green. Violet denotes structures proposed for the still elusive Si-IX and Si-XIII phases [11].

Fig. 1.13 shows the hex-Si phase in SiNWs grown by VLS method. The shown SiNW has a diameter of about 5 nm at its base and a length of about 20 nm. A thin amorphous SiO_x can be seen at the surface SiNW, the core part has crystalline structure. It can be seen that SiNW exhibits a cub-Si phase near its base and a 2H hex-Si phase at its top. The electron diffraction pattern of SiNW also exhibits 2H diffraction spots that cannot be interpreted as originating from cubic stacking [12]. Note, that the difference between the types of stacking of close packed planes (which defines polytypism) is only directly visible in $[110]_{3C}/[1\bar{2}10]_{2H}$, shown in Fig. 1.13, while any other zone axis will give ambiguous results [12]. The 2H hex-Si phase in SiNWs was observed to be quite stable: it remained after 5 months in air, and after annealing at 700 ^{0}C. The switching from cub-Si to hex-Si phase indicates that the latter was energetically favourable at the certain stage of growth, under the precise growth conditions that were present. Size effects could play a predominant role in formation of hex-Si phase in SiNWs. Since the surface-to-volume ratio in SiNWs with such a diameter is high, the surface tension from the side-walls can become

Cette thèse est accessible à l'adresse : http://theses.insa-lyon.fr/publication/2019LYSEI129/these.pdf
© [S. Rodichkina], [2019], INSA de Lyon, tous droits réservés

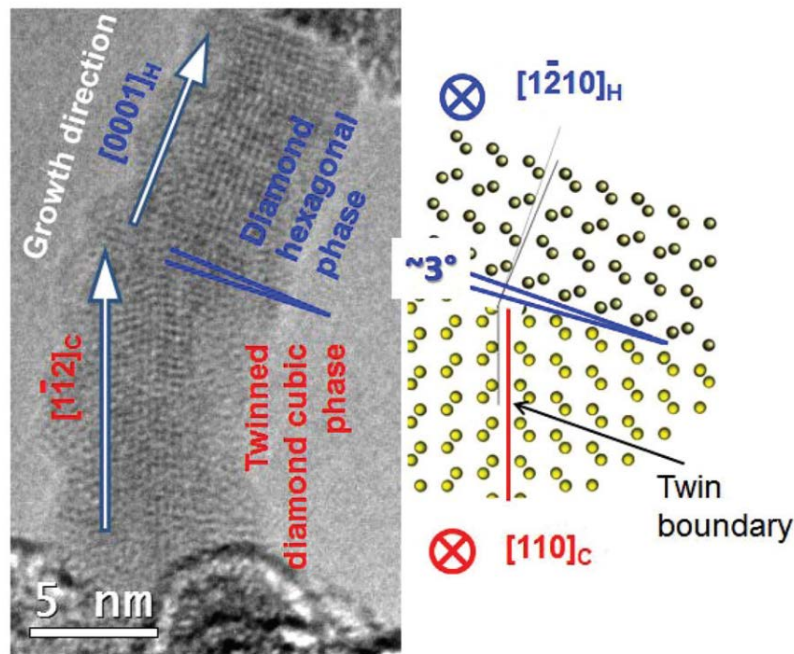

Figure 1.13: Switch from the twinned cubic phase to the 2H hexagonal phase in SiNWs, grown by VLS method, associated with a change in the growth direction. The schematic shows that the relationship between the two phases is close to epitaxial [12].

significant and cause a strong anisotropic stress on the nanowire structure, which can become an origin of hex-Si formation [12]. Also, the hexagonal phase would have atomic surface structures with lower energy, so that the global (surface + volume) free energy would be lower [12, 85].

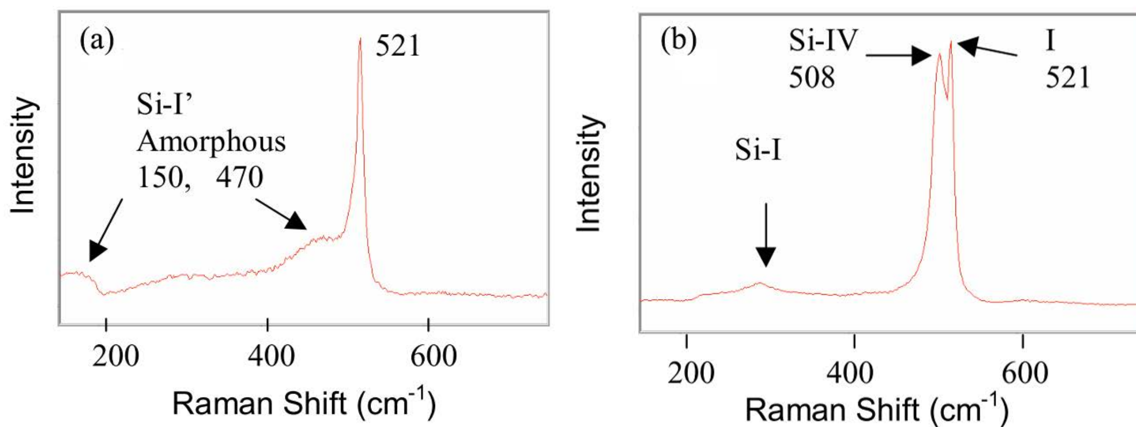

Figure 1.14: Typical Raman spectra for lapped silicon wafer surfaces. (a) cub-Si at 521 cm^{-1} and a-Si at $\sim$ 470 cm^{-1} and $\sim$ 150 cm^{-1}, (b) hex-Si at 508 cm^{-1}. Adapted from [13].

Along with TEM, the Raman spectroscopy was shown to be an efficient technique to identify presence of hex-Si at near-surface regions in bulk and nanoscale cub-Si due to different phonon frequencies of the polymorphs [13, 82, 86]. In particular, it was established that the one-phonon Raman spectrum of hex-Si crystalline phase at $T = 300$ K consists of a single peak centered

Cette thèse est accessible à l'adresse : http://theses.insa-lyon.fr/publication/2019LYSEI129/these.pdf
© [S. Rodichkina], [2019], INSA de Lyon, tous droits réservés

in the range of 495-510 cm^{-1} [13, 87], while the Raman peak for cub-Si phase is centered at 520.5 cm^{-1}. Note, that the amorphous silicon (a-Si) phase exhibits the Raman peak at about 480 cm^{-1} [88]. However, the width of the Raman peak for a-Si at $T = 300$ K is usually about 70 cm^{-1} [88], while the one for hex-Si and cub-Si is of about 10 and 4 cm^{-1}, relatively [13]. MACE-SiNWs usually exhibit the single one-phonon Raman peak at 520.5 cm^{-1}, similar to bulk cub-Si (see Sec. 1.1.2). At that, the additional Raman peak at about 500 cm^{-1} was also reported for MACE-SiNWs [89, 90]. In Ref. [90] the origin of this additional peak was explained by the formation of hex-Si phase in SiNWs during MACE. In Ref. [91] a specific role of photoexcitation level in the hex-Si phase formation was emphasized for Si nanoparticles.

1.2 Impact of doping on structural properties of SiNWs

Uniform dopant incorporation into SiNWs is an important problem for their nano-electronic, sensor, photovoltaic and thermoelectric applications. The realization of the uniform doping has proven to be challenging. This section describes, how the most common fabrication techniques, such as VLS, RIE and MACE, can be adapted to obtain highly-doped SiNWs. The alternative doping strategies, which consist in the introducing of the dopant impurities into SiNWs after their fabrication, are reported and their influence on the structural properties of SiNWs is described.

1.2.1 In-situ doping during VLS growth

Among all the possible dopants for Si, P (phosphorus) and B (boron) represent the most common choice for n-type and p-type doping, respectively. Substitutional P and B atoms introduce very shallow energy levels in the band gap of crystalline silicon, resulting in small ionization efficiency of the impurities at room temperature and, consequently, in the presence of free charge carriers in the conduction and valence bands of Si [92]. The free charge carrier concentration of the order of 10^{20} and 10^{21} cm^{-3} can be achieved for B- and P-doping respectively, which is one of the highest values among possible Si dopants [16, 17].

The traditional approach to obtain highly-doped SiNWs is the dopant incorporation into the SiNWs during the VLS growth [14, 93]. One of the mechanisms responsible for the doping of SiNWs during the VLS growth is that the dopant atoms diffuse through the liquid phase and are incorporated in the growing SiNWs at the liquid-nanowire interface [14]. Non-uniform radial and axial p-type doping profiles were observed in SiNWs grown using SiH_4 and doped with

Cette thèse est accessible à l'adresse : http://theses.insa-lyon.fr/publication/2019LYSEI129/these.pdf
© [S. Rodichkina], [2019], INSA de Lyon, tous droits réservés

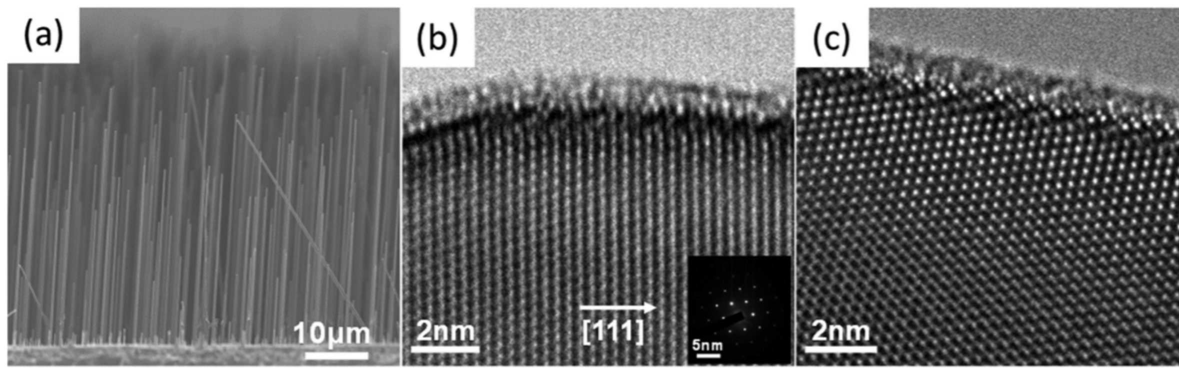

Figure 1.15: (a) Cross-section SEM micrograph of the VLS-grown p-doped SiNWs array. TEM micrographs of (b) tip and (c) base segment of an as-grown TMB-doped Si nanowire grown using $SiCl_4$. Both images reveal a single crystalline Si core surrounded by a 1 nm thick native oxide shell. Diffraction pattern (inset) confirms that the [111] orientation of as-grown nanowire [14].

boron from diborane (B_2H_6) [94] or trimethylboron (TMB) ([$(CH_3)_3B$]) [95] in a low pressure chemical vapor deposition. The recent approach to obtain more homogeneous doping is to use silicon tetrachloride ($SiCl_4$) as the Si source in an atmospheric pressure CVD process [14]. Fig. 1.16 shows the TEM images of p-type SiNWs synthesized by Au-catalyzed VLS epitaxial growth using $SiCl_4$ as the Si precursor and TMB as the dopant source in an atmospheric pressure CVD reactor at a temperature of 1050 ^{0}C. A single crystal core of SiNWs, surrounded by a 1 to 2 nm thick native silicon oxide shell, can be seen. No amorphous surface coating was observed along the entire length of the SiNW, suggesting that the SiNW growth occurs predominately in the axial direction [14]. The diffraction pattern confirms that SiNWs are single crystalline, as well as that the growth occurred along [111] direction. SiNWs with diameters up to 400 nm and lengths more than 7.5 μm were characterized by four-point resistivity measurements. Resistivity, corrected for surface charge, was determined to be 0.010 ± 0.002 Ω*cm along the entire length of SiNWs, which confirmed the uniform p-type doping of SiNWs using TMB and $SiCl_4$ as precursors [14].

1.2.2 Etching of highly-doped c-Si wafers

The simplest way to achieve the high doping of SiNWs, fabricated by MACE, is to use the highly-doped c-Si substrates. However, fabricated of SiNWs on c-Si wafers with the doping level more than 10^{18} cm^{-3} results in formation of porous SiNWs (see Fig. 1.8 and Ref. [72]). This fact is explained by the higher hole concentration at Ag/Si interface for highly-doped c-Si wafers, which leads to the strong etching of Si close to metal-covered areas. Thus, this effect can

Cette thèse est accessible à l'adresse : http://theses.insa-lyon.fr/publication/2019LYSEI129/these.pdf
© [S. Rodichkina], [2019], INSA de Lyon, tous droits réservés

hardly be reduced by varying the etching solution for MACE procedure.

The doping level of SiNWs, fabricated by RIE, is determined by the wafer used, and bulk core SiNWs are obtained both on low- and highly-doped c-Si substrates [44]. At that, it was reported that highly-doped n-type Si etches faster than undoped silicon, and highly-doped p-type Si etches slower than undoped silicon [96]. It was explained by the fact that the Coulomb attraction between uncompensated donors (As^{+}) and chemisorbed halogens (F) enhances etch rates in a highly-doped n-type Si, whereas the Coulomb repulsion between uncompensated acceptors (B) and chemisorbed halogens (F) inhibits etch rates in a highly-doped p-type Si [96].

1.2.3 Ex-situ doping of silicon nanowires

a) Ion implantation

The most common approach for ex-situ doping consists in the dopant incorporation into SiNWs by means of ion implantation. Phosphorus or boron ions are implanted at energies $\sim$ 10 keV with doses ranging from 10^{11} cm^{-2} to 10^{16} cm^{-2} [15, 37, 97, 98]. Implantation is commonly followed by thermal annealing at high temperature about 1000 ^{0}C in order to reduce the implantation defects and activate the dopants, i.e. restore the original crystalline structure [15, 20, 37, 97, 98].

Fig. 1.16 shows a typical high-resolution TEM images of SiNWs before and after the ion implantation. Ion implantation was performed as shown in Fig. 1.16 (e). Initial SiNWs are single crystalline with an amorphous SiO_x shell. After the ion implantation at a dose of $1*10^{16}$ B^{+}/cm^{2}, the crystalline core of SiNWs became amorphous, while the thermal annealing at 900 ^{0}C restored the crystallinity of SiNWs [15]. Accordingly to Fig. 1.16, ion implantation with $1*10^{16}$ B^{+}/cm^{2} results in polycrystalline core of SiNWs, while the one with $5*10^{15}$ B^{+}/cm^{2} results in single-crystalline SiNWs. Unlike in the case of B implantation, the crystalline structure of SiNWs was not fully restored after P implantation with $1*10^{16}$ P^{+}/cm^{2}, and the surface roughness significantly increased. The greater damage caused by P implantation was explained by the greater mass of P than that of B [15]. Fig. 1.16 (f) shows the B and P depth profiles for bulk Si, calculated using the simulations of transport of ions in matter (TRIM). The high doping levels $> 10^{19}$ cm^{-3} can be seen up to the depth of 200 nm with the maximum impurity concentration of 10^{21} cm^{-3}. The shown TEM images correspond to the most damaged SiNWs for each implantation dose [15]. Thus, the single-crystalline structure of SiNWs can be obtained using the high-temperature annealing after ion implantation, however the possible polycrystalline structure and increase of surface roughness after the ion implantation should be taken into

Cette thèse est accessible à l'adresse : http://theses.insa-lyon.fr/publication/2019LYSEI129/these.pdf
© [S. Rodichkina], [2019], INSA de Lyon, tous droits réservés

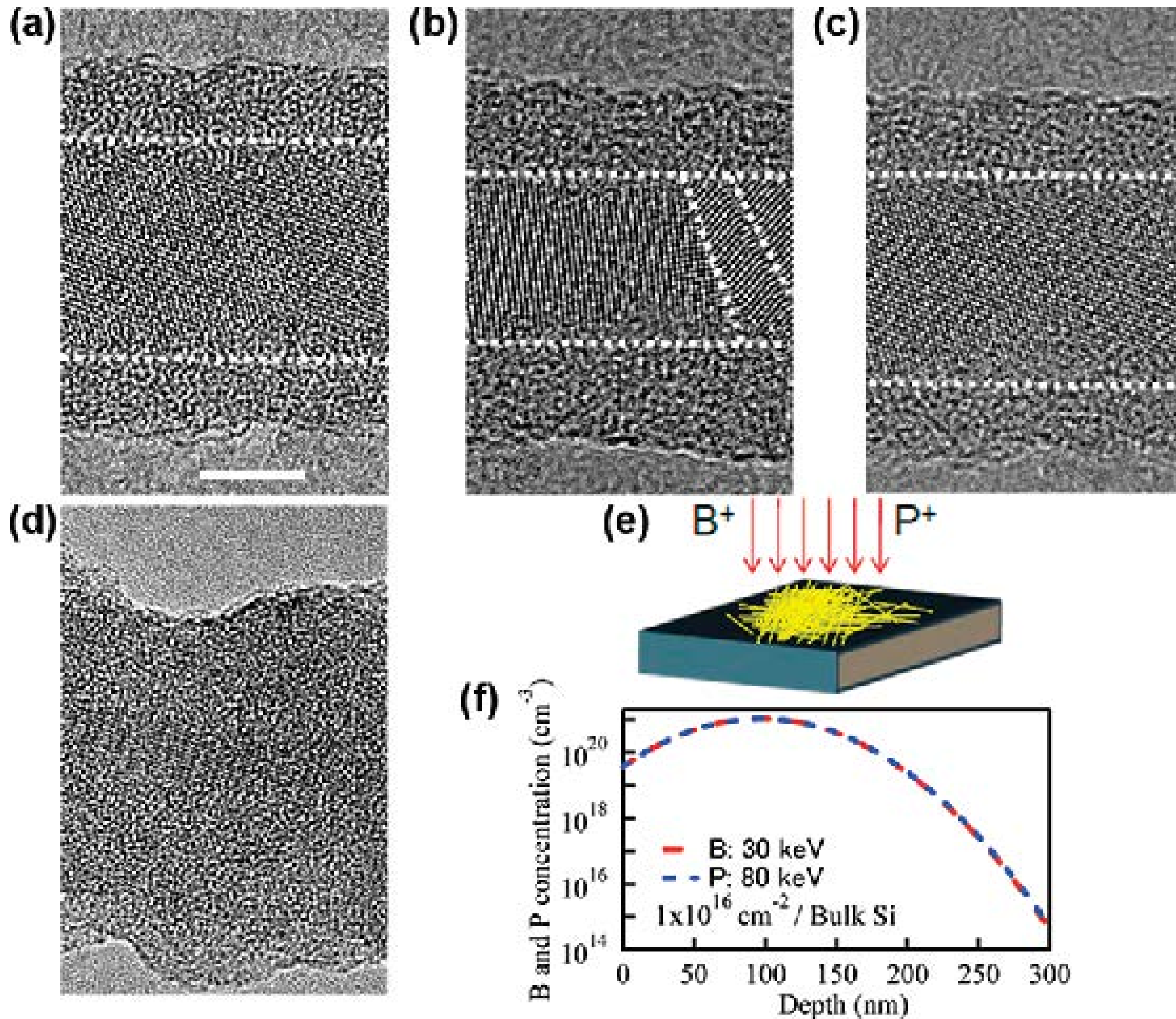

Figure 1.16: Typical TEM images of SiNWs (a) before ion implantation, and after ion implantation with a dose of (b) $1 * 10^{16}$ B^{+}/cm^{2}, (c) $5 * 10^{15}$ B^{+}/cm^{2}, (d) $1 * 10^{16}$ P^{+}/cm^{2}. The activation annealing of dopant atoms was performed at 900 ^{0}C after implantation. The scale bar is 5 nm. (e) Illustration of ion implantation for SiNWs. (f) Depth profiles of B and P as estimated by simulation of transport of ions in matter [15].

account.

Raman scattering measurements were performed to investigate the amortization and recrystallization of SiNWs, as well as activation of B and P impurities in SiNWs by annealing. The results are summarized in Fig. 1.17. One can see than after the ion implantation with both B and P atoms the Raman peak at 520 cm^{-1}, corresponding to c-Si is significantly decreased, and a broad peak related to amorphous Si (a-Si) appears at around 470 cm^{-1}. The relative intensity of the a-Si Raman peak is much greater for P than for B ion implantation, which indicates that damage by P implantation is much greater than for B implantation. The intensity of c-Si Raman peak increases with increasing annealing temperature, and crystallinity of SiNWs is almost completely recovered after annealing at 900 ^{0}C. In addition to the increase in c-Si Raman peak, the intensity

Cette thèse est accessible à l'adresse : http://theses.insa-lyon.fr/publication/2019LYSEI129/these.pdf
© [S. Rodichkina], [2019], INSA de Lyon, tous droits réservés

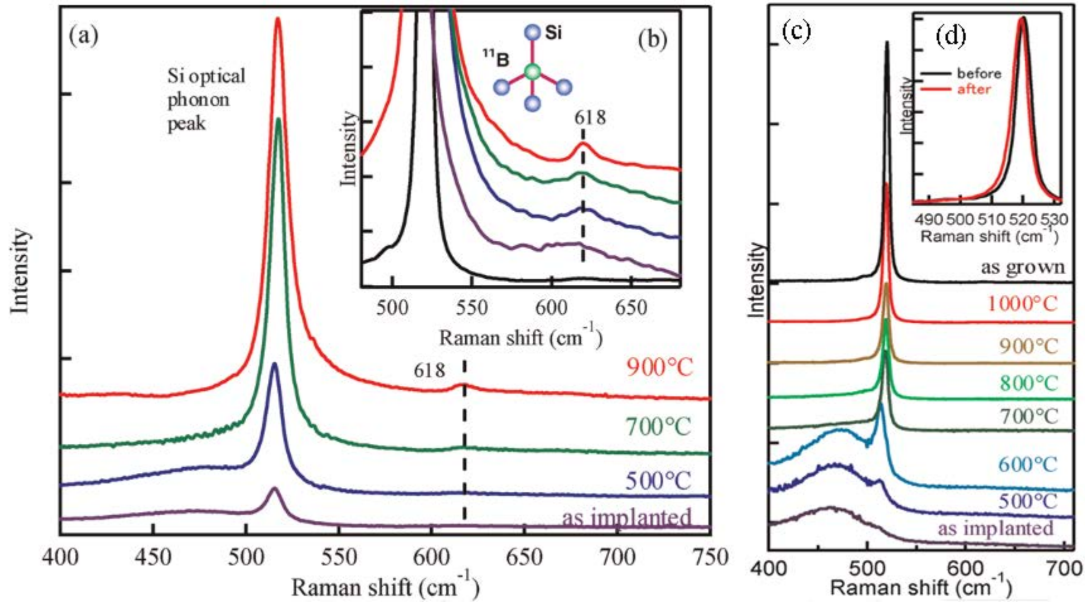

Figure 1.17: (a) Raman spectra of SiNWs, which show the Si optical phonon peak and B local vibrational peak, after B ion implantation with a dose of $1 * 10^{16}$ B^+/cm^2 and subsequent activation annealing. (b) Magnified image of (a). (c) Raman spectra of SiNWs after P ion implantation with a dose of $1 * 10^{16}$ P^+/cm^2 and subsequent activation annealing. (d) Raman spectrum of SiNWs before and after the ion implantation doping with P. Adapted from [15].

of B local vibrational peak at about 618 cm^{-1} increases with the annealing temperature (see Fig. 1.17 (b)), showing that the B atoms are doped in Si substitutional sites in the crystalline Si core of SiNWs during the recrystallization process [15]. The correlation between the peak intensity of the B local vibrational peak and the electrically active B concentration in B-implanted SiNWs was observed [15]. The c-Si Raman peak shows a broadening toward higher wavenumbers for B (p-type) doping and a broadening toward lower wavenumbers for P (n-type). This broadening was explained by the Fano effect [15], that indicated the high free charge carrier concentration in SiNWs and activation of B and P atoms. The activation efficiencies for B-implanted SiNWs were estimated to be about 10 %. The low activation ratio was explained by the compensation by residual defects, as well as by segregation of B atoms into the surface oxide layer during the activation annealing after ion implantation [15].

The high effectiveness of ion implantation doping procedure was experimentally shown for horizontal SiNWs on Si-on-insulator substrates with Si layer depth about 100 nm [37, 98]. Applied to 50 nm wide n- and p-type SiNWs, phosphorus and boron doping concentrations of $1 * 10^{20}$ cm^{-3} were achieved, as shown by secondary ion mass spectroscopy (SIMS), and the electrical resistivity of such SiNWs was of about 1 mΩ*cm, which implies the good electric transport in these SiNWs and bulk-like free charge carrier mobility [38]. However, the ion

Cette thèse est accessible à l'adresse : http://theses.insa-lyon.fr/publication/2019LYSEI129/these.pdf
© [S. Rodichkina], [2019], INSA de Lyon, tous droits réservés

implantation technique was shown to be inefficient for SiNWs arrays due to non-uniform doping across NW cross-section [55].

b) Spin-on doping

An alternative experimental approach is the thermal diffusion of dopant atoms from the spin-on dopant (SOD) solutions. This technique is commonly used to create shallow p^+-n junctions in Si wafers [99]. In this doping method spin-on dopant is usually deposited directly on a silicon substrate. A post-spin baking at a temperatures of about 200 ^{0}C is applied to remove excess solvent. Then the dopant atoms are incorporated into Si by thermal diffusion at about 1000 ^{0}C. During thermal annealing, dopant oxide evaporates from the spin-on dopant solution and is adsorbed onto Si surface. Boron diffusion is then accomplished by means of a surface oxidation-reduction reaction between the dopant oxide (B_2O_3) and the silicon wafer, given by

$$2B_2O_3 + 3Si \rightarrow 4B + 3SiO_2. \quad (1.1)$$

In this reaction doped SiO_2 is formed and becomes a dopant source for elemental boron, which diffuses into the silicon substrate [20].

One of the main factors determining the resulting doping concentration in Si wafer is the annealing temperature. Fig. 1.18 shows the solid solubility limit for different commonly used dopants in Si. As can be seen from the figure, the solubility limit for Boron and Phosphorus increases with the annealing temperature up to 1200 ^{0}C. At $T \approx 1000$ ^{0}C, frequently used for the annealing of Si, it is of about $4 * 10^{20}$ cm^{-3} for Boron and $1 * 10^{21}$ cm^{-3} for Phosphorus, which corresponds to electrical resistivities of about 0.4 and 0.13 mΩ*cm, correspondingly [16].

Fig. 1.19 shows the SIMS doping profiles in Si wafers obtained by SOD with RTA at 1060 ^{0}C for different time. As can be seen from the figure, the diffusion profiles exhibit the strong decrease in the dopant concentration with depth. The doping depth can be estimated of about 0.2-0.4 μm for the annealing temperature about 1000 ^{0}C [20, 100]. Therefore, for SiNWs with a diameter of about 100 nm the SOD method can allow to obtain almost homogeneous cross-sectional doping from surface to core.

After the annealing the residual SOD film on Si wafer can be removed in HF [101]. Films, obtained prior the diffusion, can be removed in water. One should take into account that in certain cases a carbon-rich residual film, insoluble in HF, was reported to be formed on the surface of the silicon [102]. Also, the excessive amounts of B_2O_3, formed during the thermal

Cette thèse est accessible à l'adresse : http://theses.insa-lyon.fr/publication/2019LYSEI129/these.pdf
© [S. Rodichkina], [2019], INSA de Lyon, tous droits réservés

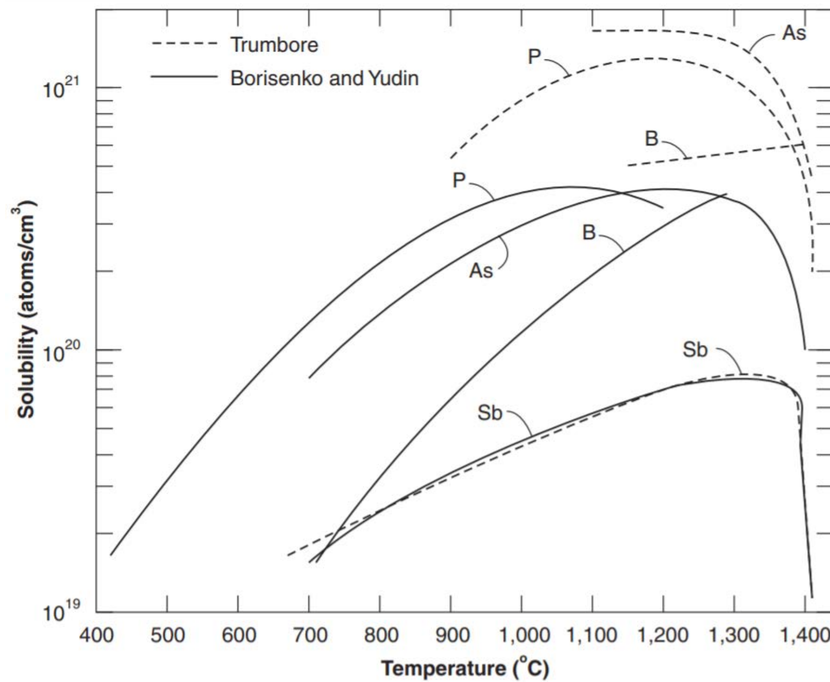

Figure 1.18: Solid solubility for common dopants in silicon [16] (summarized from [17, 18]).

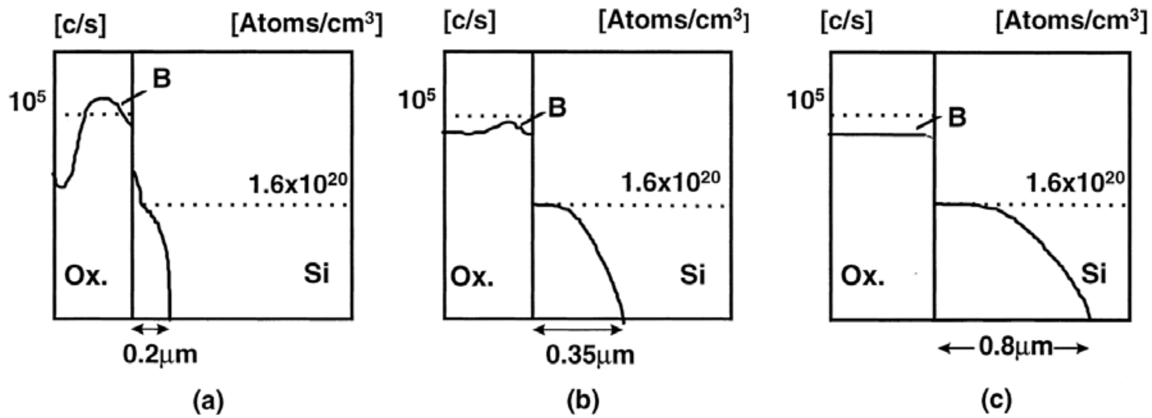

Figure 1.19: SIMS profiles of boron in doped oxide and in the silicon substrate after RTA at 1060 ^{0}C for: (a) 30 s, (b) 1 min, and (c) 3 min. The solid solubility of boron in silicon at the given temperature of $1.6 * 10^{20}$ cm^{-3} [19] is shown as the dotted horizontal lines [20].

annealing, can lead to the formation of silicides and other compounds of boron on the silicon surface [103]. It worth to note, that to avoid the above problems, the doping of Si wafer spatially separated (0.5 mm) from SOD layer was successfully used [20].

SOD doping procedure was successfully applied to SiNWs. SiNWs arrays with diameter of 120-180 nm and length of 4-6 μm were synthesized by Au-catalyzed VLS growth technique. The B-containing SOD was applied onto silicon nitride substrate, which was placed at approximately 400 μm from SiNWs, and then the annealing was performed at 800 or 950 ^{0}C to control the doping level of SiNWs, followed by the dopant drive-in at 975 ^{0}C [21]. Fig. 1.20 shows the

Cette thèse est accessible à l'adresse : http://theses.insa-lyon.fr/publication/2019LYSEI129/these.pdf
© [S. Rodichkina], [2019], INSA de Lyon, tous droits réservés

HRTEM images of SiNWs before and after the annealing at 950 ^{0}C. The crystalline structure of SiNWs maintained after the doping procedure, and no significant defects were observed in either doped or as-grown SiNWs. Moreover, no B segregation or clustering in SiNWs was observed [21]. The SiNWs diameter reduced after the doping procedure, and the surface oxide layer increased, which was explained by the fact that silicon from SiNWs surface is consumed during the doping due to the reaction with B_2O_3 (see Eq. 1.1) [21]. The high doping level in SiNWs of the order of 10^{18} and 10^{20} cm^{-3} for the annealing at 800 or 950 ^{0}C, respectively, was shown by the four-probe electrical measurements of the electrical resistivity of SiNWs, assuming the bulk free charge carrier mobility [21]. The doping level profiles along SiNWs were not studied.

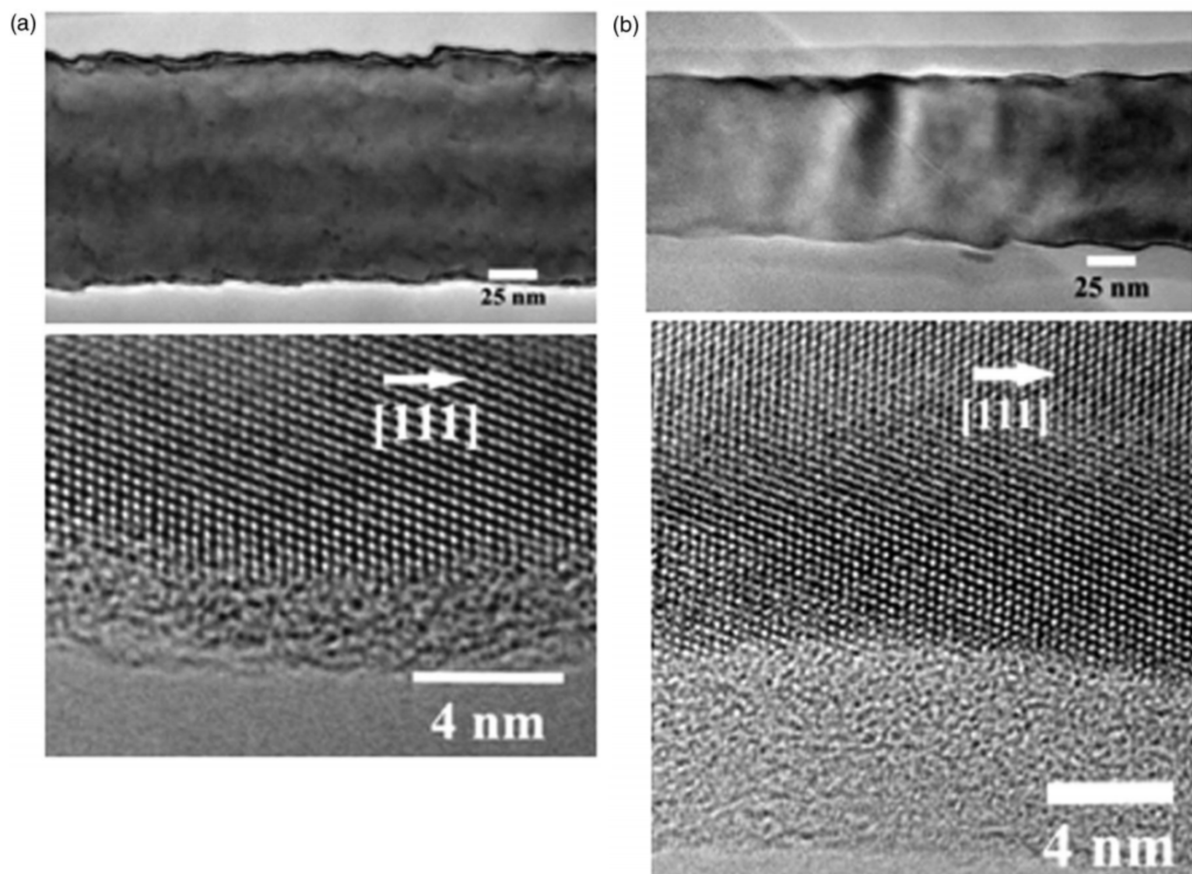

Figure 1.20: High-resolution TEM micrographs of (a) undoped SiNWs and (b) doped SiNWs using the annealing at 950 ^{0}C. The high magnification images show the nanowire section near the surface along with the surface oxide layer of 23 nm for the undoped SiNWs and somewhat thicker oxide layer of 5-6 nm after the doping. The $< 111 >$ axis lies along the growth direction [21].

SOD doping procedure was applied to SiNWs arrays, fabricated by MACE of low-doped c-Si wafers [55]. The high Boron concentrations at SiNWs tips $\sim 10^{19} \div 10^{20}$ cm^{-3} were obtained. The uniform cross-sectional profiles in a nanowire with diameter of about 100 nm were observed for the annealing at 950 ^{0}C over 15 min. Variation in concentration of doping atoms along the

Cette thèse est accessible à l'adresse : http://theses.insa-lyon.fr/publication/2019LYSEI129/these.pdf
© [S. Rodichkina], [2019], INSA de Lyon, tous droits réservés

length of the nanowires was characterized by SIMS, and the uniform doping was observed up to depth about 1 μm, limited by the nanowire length [55].

1.3 Thermal properties of SiNWs

This section describes the effect SiNWs size on their thermal conductivity. The temperature dependencies of thermal conductivity of SiNWs are reported and compared to those for c-Si. The influence of free charge carriers on thermal conductivity of SiNWs is described. The effect of surface roughness on thermal conductivity of SiNWs is emphasized and discussed in view of thermoelectric applications of SiNWs.

1.3.1 Thermal transport in bulk crystalline silicon (c-Si)

Thermal conductivity of a bulk crystal due to heat transport of phonons, considered within the Debye's model and the relaxation-time approximation, is given by the Klemens-Callaway's expression [22]

$$k_l = \left(\frac{k_B}{\hbar}\right)^3 \frac{k_B}{2\pi^2 \upsilon} T^3 \int_0^{\Theta_D/T} \tau_{ph} \frac{x^4 e^x}{(e^x - 1)^2} dx, \tag{1.2}$$

where k_B is the Boltzmann constant, $\hbar$ is the Planck constant, υ is the phonon group velocity, T is temperature, Θ_D is the Debye temperature, τ_{ph} is the combined phonon relaxation (scattering) time, and $x = \hbar\omega/k_B T$. Lattice thermal conductivity of a crystal, as follows from Eq. (1.2), depends on two parameters: phonon group velocity and phonon scattering time. For a bulk crystal considered within Debye's model the phonon group velocity does not depend on phonon frequency. The value of υ usually used for bulk Si in calculations represents the phonon group velocity for transversal acoustical phonons (6500 m/s) [29], which have the lowest frequency and contribute the most to phonon thermal conductivity.

Several approaches were used to describe the phonon scattering time in bulk Si [22, 29, 104]. As a first approximation, the phonon scattering rate τ_{ph}^{-1} can be considered as a sum of phonon scattering rates due to different scattering processes, which are responsible for thermal resistance of a material [22, 29]. These processes are: three-phonon Umklapp scattering, mass-difference (impurity) scattering, phonon-electron scattering and boundary scattering. The three-phonon normal scatting, which conserves the total momentum of phonons involved, does not contribute to the thermal resistance of a material, thus the effect of normal phonon scattering is neglected

Cette thèse est accessible à l'adresse : http://theses.insa-lyon.fr/publication/2019LYSEI129/these.pdf
© [S. Rodichkina], [2019], INSA de Lyon, tous droits réservés

in this approach. The thermal conductivity of bulk Si calculated using the above τ_{ph}^{-1} has good correlation with experimental data. However, for the more rigorous description of thermal transport the effect of redistribution of phonons between the branches due to normal processes should be considered [104].

Accordingly to Ref. [22], the resistive phonon scattering rate τ_{ph}^{-1} in bulk Si above room temperature can be calculated as follows. Total τ_{ph} represents the sum of the inverse relaxation times for different scattering processes:

$$\frac{1}{\tau_{ph}} = \frac{1}{\tau_U} + \frac{1}{\tau_M} + \frac{1}{\tau_{ph-e}} + \frac{1}{\tau_B}, \tag{1.3}$$

where $\tau_{U,M,ph-e,B}$ are the time of three-phonon Umklapp, mass-difference (impurity), phonon-electron and boundary scattering, correspondingly. The relaxation rate for Umklapp scattering is given by

$$\tau_U^{-1} = B_U \omega^2 T \tag{1.4}$$

where $B_U = 2\gamma^2 \frac{k_B}{\mu V_0 \omega_D}$ is considered as temperature independent constant, γ is the Gruneisen anharmonicity parameter, μ is the shear modulus, V_0 is the volume per atom, and ω_D is the Debye frequency. The shear modulus μ is treated as a velocity dependent effective value calculated for a given geometry.

The relaxation rate for the mass-difference scattering is given by:

$$\tau_M^{-1} = B_M \omega^4 \tag{1.5}$$

where $B_M = \frac{V_0 \Gamma}{4\pi \upsilon^3}$, $\Gamma = \sum_i f_i (1 - M_i/\overline{M})^2$, f_i is the fractional concentration of the impurity atoms of mass M_i and $\overline{M} = \sum_i f_i M_i$ is the average atomic mass.

At low doping levels, the relaxation time for acoustic phonons scattered by electrons can be expressed as

$$\frac{1}{\tau_{ph-e}} = \frac{n_e \varepsilon_1^2 \omega}{\rho \upsilon^2 k_B T} \sqrt{\frac{\pi m^* \upsilon^2}{2 k_B T}}\, exp\left(-\frac{m^* \upsilon^2}{2 k_B T}\right) \tag{1.6}$$

where n_e is the concentration of conduction electrons, ε_1 is the deformation potential, ρ is the mass density, and m^* is the electron effective mass.

The boundary scattering rate is

Cette thèse est accessible à l'adresse : http://theses.insa-lyon.fr/publication/2019LYSEI129/these.pdf
© [S. Rodichkina], [2019], INSA de Lyon, tous droits réservés

$$\tau_B^{-1} = \upsilon / D * (1 - p) \tag{1.7}$$

where D is the characteristic size of a studied crystal, p is the parameter describing the amount of phonons reflected specularly at crystal boundary. If $p = 1$ the boundary scattering is purely specular and the boundary scattering does not contribute to the thermal resistivity, if $p = 0$ the boundary scattering is purely diffuse and the thermal conductivity of a crystal reduces to the well-known Casimir limit [105]. At the room temperature and higher the boundary scattering can be neglected for a bulk crystal.

Fig. 1.21 (upper part) shows the scattering rates for bulk Si with the electron concentration of 10^{18} cm^{-3} as a function of phonon frequency at room temperature of 300 K. As one can see from the figure, the phonon scattering rates significantly increase with phonon frequency, thus the low-frequency phonons have the largest contribution to bulk Si thermal conductivity. Fig. 1.22

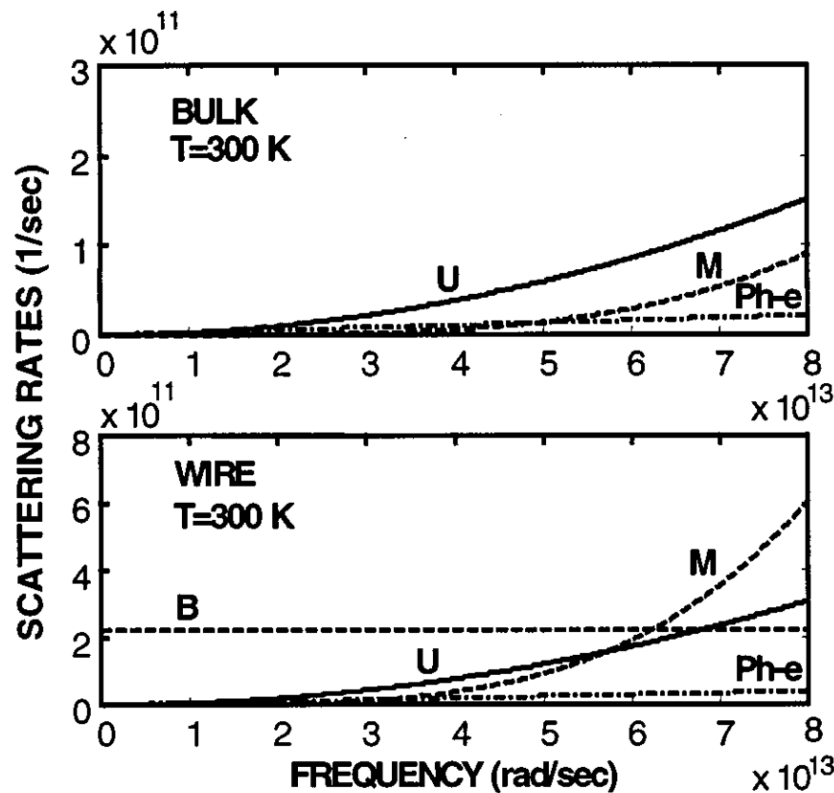

Figure 1.21: Phonon scattering rates in bulk Si and Si nanowire with diameter of 20 nm due to the different scattering mechanisms as functions of the phonon frequency. The results are shown for the three-phonon Umklapp, mass-difference, phonon-electron, and boundary scattering at $T = 300$ K [22].

shows the accumulated contribution of phonons with different frequency to the total k_l for bulk Si. One can see that at T = 300 K 90% of heat is transferred by phonons with frequency less than

Cette thèse est accessible à l'adresse : http://theses.insa-lyon.fr/publication/2019LYSEI129/these.pdf
© [S. Rodichkina], [2019], INSA de Lyon, tous droits réservés

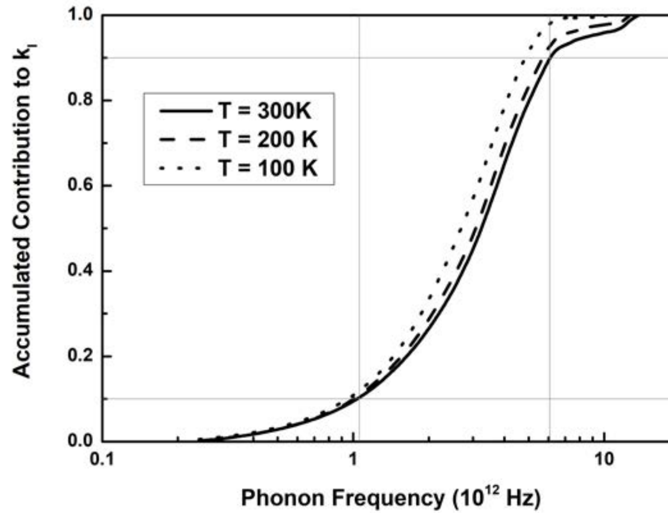

Figure 1.22: Accumulated contributions to the thermal conductivity of the phonon modes in bulk c-Si with respect to their frequency at $T = 300$ K (solid line), 200 K (dashed line) and 100 K (dotted line). The results are obtained for lightly doped n-type silicon. Adapted from [23].

$6 * 10^{12}$ Hz and about 100% with frequency less than 10^{13} Hz. Note, that temperature variation does not significantly affect the percentage contribution of phonons with different frequency to the thermal conductivity of bulk Si, the higher contribution of phonons with lower frequency at $T < 300$ K can be explained by lower occupation numbers for high frequency phonons.

The contribution of phonon-electron scattering in thermal conductivity for Si with $N = 10^{18}$ cm^{-3} is small compared to that of Umklapp and mass-difference scattering. For higher carrier concentrations, phonon-electron scattering can become important, reaching the level of other relaxation mechanisms [22].

Thus, to significantly reduce the thermal conductivity of Si one should increase the scattering rates of low-frequency phonons. The phonon frequency independent boundary scattering is responsible for thermal conductivity reduction in Si nanostructures, increasing as $1/D$, accordingly to Eq. (1.7). The effect of nanoscale boundaries on thermal conductivity of Si is studied in detail in the next chapter.

1.3.2 Effect of nanoscale boundaries

Introduction of nanoscale boundaries in a crystal modifies both the phonon group velocity and the phonon scattering time. In general, the phonon group velocity υ is a function of the size of the low-dimensional structure and depends on the particular type of boundaries. In was shown

Cette thèse est accessible à l'adresse : http://theses.insa-lyon.fr/publication/2019LYSEI129/these.pdf
© [S. Rodichkina], [2019], INSA de Lyon, tous droits réservés

that in 22 nm nanowire, in contrast to bulk Si, the average phonon group velocity depends on the phonon frequency and is lower than in bulk Si in the entire frequency range [22]. The phonon scattering rates for Umklapp, mass-difference and phonon-electron scattering, despite they do not depend directly on the crystal size, change in a nanocrystal through their dependence on υ. Fig. 1.21 (bottom part) shows the scattering rate for these processes in the 22 nm Si nanowire as a function of the phonon frequency. One can see, that the dependencies of these scattering rates on the phonon frequency follow the same trend as in bulk Si, although they are slightly higher in nanowires due to the lower phonon group velocity. Besides, the ratio between the scattering rates for different processes can be different in SiNWs and in bulk Si, e.g. the mass difference scattering rate in SiNW is higher than Umklapp scattering rate at high frequencies.

The effect of the phonon group velocity in SiNWs on their thermal conductivity is shown in Fig. 1.23. In the case of purely specular boundary scattering ($p = 1$), the boundary scattering does not affect the thermal conductivity, and the modification of k_l is due only to a change in the phonon group velocity. As one can see from the figure, the change in the phonon group velocity reduces the thermal conductivity of SiNW by 22% from 150 to 117 W/(m K).

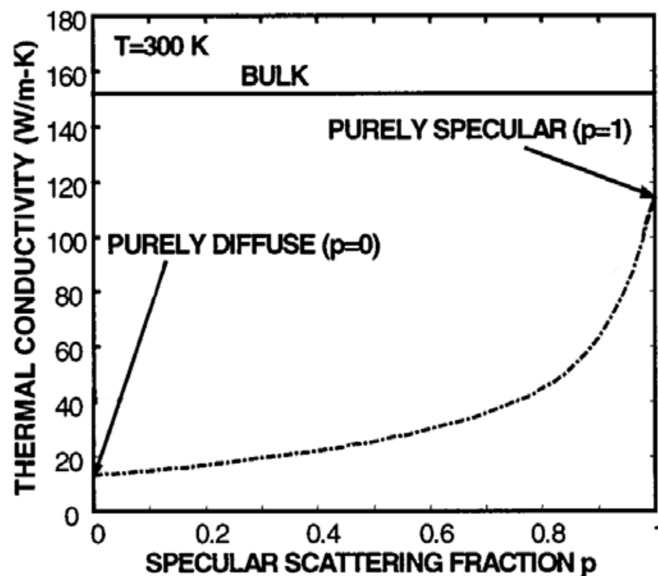

Figure 1.23: Lattice thermal conductivity of bulk Si and SiNW with $D = 20$ nm at room temperature as a function of specular phonon-boundary scattering fraction p. Adapted from [22].

If the boundary scattering is not specular ($p < 1$), it additionally affects the thermal conductivity of SiNWs. The relative ratio of the boundary scattering rate for 22 nm SiNW and other scattering processes is shown in Fig. 1.21 (bottom part). Since, unlike other scattering processes,

Cette thèse est accessible à l'adresse : http://theses.insa-lyon.fr/publication/2019LYSEI129/these.pdf
© [S. Rodichkina], [2019], INSA de Lyon, tous droits réservés

the boundary scattering rate does not depend on the phonon frequency, it can significantly decrease the scattering time for low-frequency phonons, which have the largest contribution to the thermal conductivity. As can be seen from Fig. 1.21, the boundary scattering rate for 22 nm SiNW has the same order as the scattering rates for high-frequency phonons in bulk Si. In general, the boundary scattering rate increases with reduction of SiNW diameter, accordingly to Eq. (1.7) it is proportional to $1/D$.

Fig. 1.23 shows that the increase of fraction phonons, diffusely scattered at the boundary of SiNW, significantly reduces the thermal conductivity of SiNWs. In the case of purely diffusive scattering ($p = 0$) a further decrease in k_l of SiNWs from 117 to 17 W/(m K) is observed, which is an order of magnitude lower than in bulk material.

The fraction of the phonons, which are scattered specularly or diffusely at the crystal boundary, is determined by the boundary surface roughness [106]. The surface roughness is usually characterized by a root-mean-square height (Δ). If the disordered boundary is considered as two reflecting planes at the distance of Δ, the maximum path length difference between the phonons reflected from these planes is 2Δ. Similarly to the reflection of electromagnetic waves, the reflection of the phonon from the disordered boundary can be considered specular if this path length difference is much shorter than the phonon wavelength, in such case the interference effects between the phonons reflected from the planes can be neglected. One can argue that the phonons for which $\Delta * \omega/\upsilon \leq 1$ are scattered specularly from the boundary, and the phonons with $\Delta * \omega/\upsilon > 1$are scattered diffusely. It was shown that at low temperatures, the unusual linear behavior of the thermal conductivity of thin silicon nanowires (D of about 20 nm) on the temperature can be explained by the effect of specularly scattered phonon modes with low frequency. However, for thick nanowires (D of about 100 nm) it is still appropriate to ignore the specularly scattered modes since the other modes with higher frequency contribute the most to the thermal conductance [24, 106].

The dependence of the thermal conductivity of SiNWs with smooth surface on their diameter at $T = 300$ K is shown in Fig. 1.24. The presented data show both the experimental and simulation data, where the boundary scattering is considered purely diffusive. Accordingly to Fig. 1.24 the thermal conductivity of SiNWs exhibits the square root dependence on their diameter. The presented dependence can be used to estimate the reduction of thermal conductivity in SiNWs due to the presence of nanoscale boundaries.

Cette thèse est accessible à l'adresse : http://theses.insa-lyon.fr/publication/2019LYSEI129/these.pdf
© [S. Rodichkina], [2019], INSA de Lyon, tous droits réservés

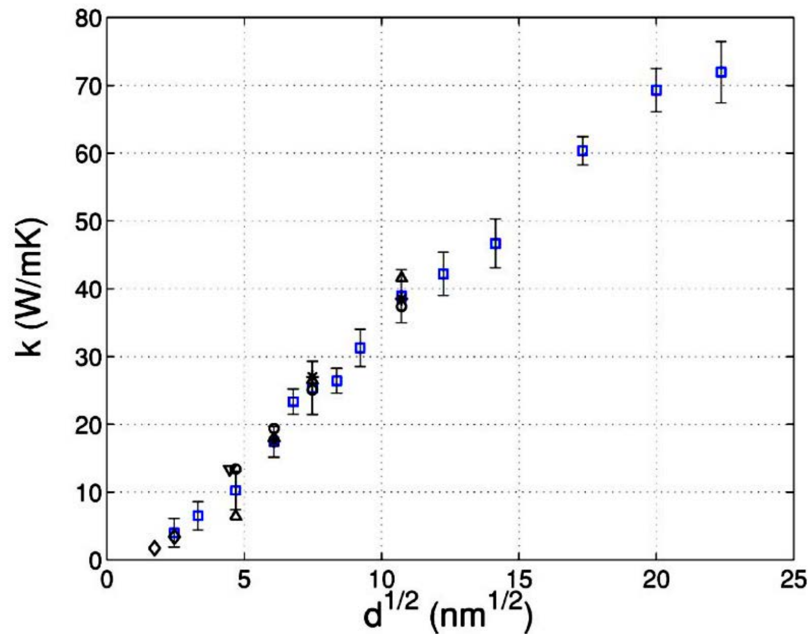

Figure 1.24: Nanowire thermal conductivity vs diameter 6 nm < d < 500 nm. The experimental results (up triangles) of Li et al. (Ref. [24]) are compared to Monte-Carlo simulation data (squares) of Lacroix et al. (Ref. [25]), kinetic theory results (circles) of Chantrenne et al. (Ref. [26]), molecular dynamic results (diamonds) of Volz and Lemonnier (Ref. [27]), kinetic theory+molecular dynamic results (stars) of Mingo (Ref. [28]), and kinetic theory with modified dispersion curves (down triangles) of Zou and Balandin (Ref. [22]) [25].

1.3.3 Dependence on temperature

Typical dependence of the thermal conductivity of bulk Si crystal on the temperature is shown in Fig. 1.25. As can be sen from the figure, the thermal conductivity of c-Si increases at low temperatures due to the increase of average number of phonons in crystal and decreases at high temperatures due to the increase of combined phonon scattering rate, the maximum of the thermal conductivity occurs around 30 K. Here the two temperature limits are of particular interest. In the low temperature limit, the boundary scattering of phonons is dominant, therefore the dependence of c-Si thermal conductivity on the temperature follows the trend of its heat capacity and is proportional to T^3. At high temperatures the Umklapp three-phonon scattering processes are dominant, which results in the thermal conductivity proportional to T^{-1}, accordingly to Eq. (1.2).

In Si nanowires, the phonon boundary scattering decreases their thermal conductivity as compared to c-Si in the entire studied temperature range of $T < 350$ K [7, 24]. Fig. 1.26 shows the temperature dependence of the thermal conductivity of SiNWs with different diameter in the low-temperature limit. Accordingly to Fig. 1.26, the low-temperature thermal conductivity for SiNWs can exhibit the T^n dependence on the temperature, where $n = 1...3$ depending on

Cette thèse est accessible à l'adresse : http://theses.insa-lyon.fr/publication/2019LYSEI129/these.pdf
© [S. Rodichkina], [2019], INSA de Lyon, tous droits réservés

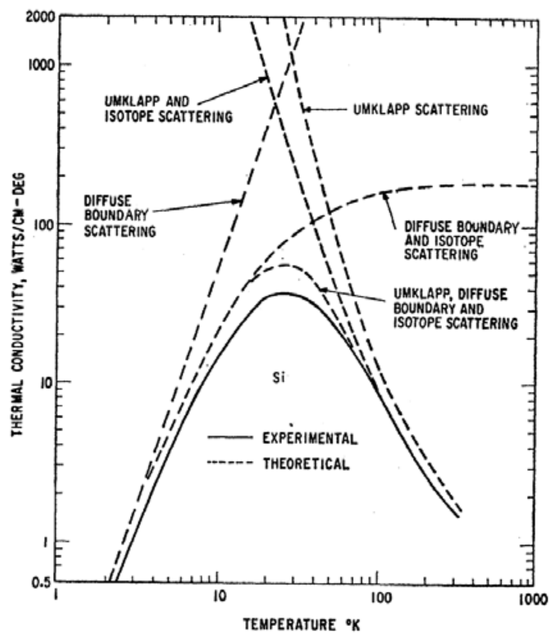

Figure 1.25: Experimental (solid line) and theoretical (dashed line) dependencies of the thermal conductivity coefficient on temperature for bulk c-Si. Varoius dashed line correspond to the thermal conductivity values, obtained theoretically considering particular scattering mechanisms [29].

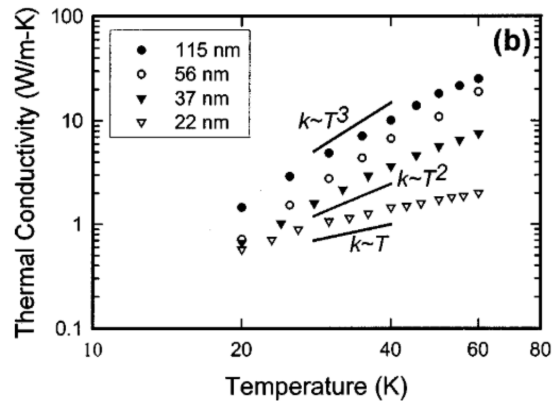

Figure 1.26: Low temperature experimental data on the thermal conductivity of SiNWs with different diameter, grown by VLS technique. The T^3, T^2, and T^1 curves are shown for comparison [24].

the diameter of SiNWs. For SiNWs with $D = 115$ nm the thermal conductivity $k_l \sim T^3$, similar to the bulk Si. The deviation of the thermal conductivity dependence from the Debye T^3 law for thinner SiNWs with diameter of less than 37 nm can be explained by the effect of specular phonon-boundary scattering for low-frequency modes [106]. This effect results in $k_l \sim T$ for SiNWs with $D = 22$ nm.

1.3.4 Effect of free charge carriers

Fig. 1.27 shows the thermal conductivity of p-type c-Si with different doping concentration as a function of temperature for $T > 300$ K. As can be seen from the figure, the samples with $N < 5 * 10^{18}$ cm^{-3} exhibit the close thermal conductivity coefficient in the studied temperature range. The highly doped sample with $N = 8 * 10^{19}$ cm^{-3} shows lower thermal conductivity in the temperature region of 300-500 K, which can be explained by the reinforced scattering of the phonons by the impurities [30] and free charge carriers [107] in the highly doped Si. In the high-temperature region the thermal conductivity difference among the samples with different charge carrier concentration is slight due to the dominant effect of the phonon-phonon scattering,

Cette thèse est accessible à l'adresse : http://theses.insa-lyon.fr/publication/2019LYSEI129/these.pdf
© [S. Rodichkina], [2019], INSA de Lyon, tous droits réservés

limiting the thermal transport in this temperature range. The phonon-phonon scattering is also responsible for the decrease of the thermal conductivity of c-Si with temperature in the high-temperature range. The analytical modeling of low doped Si thermal conductivity by Morelli et al. (Ref. [104]), based on the phonon scattering time approach, shows a good agreement with the experiment at high temperatures.

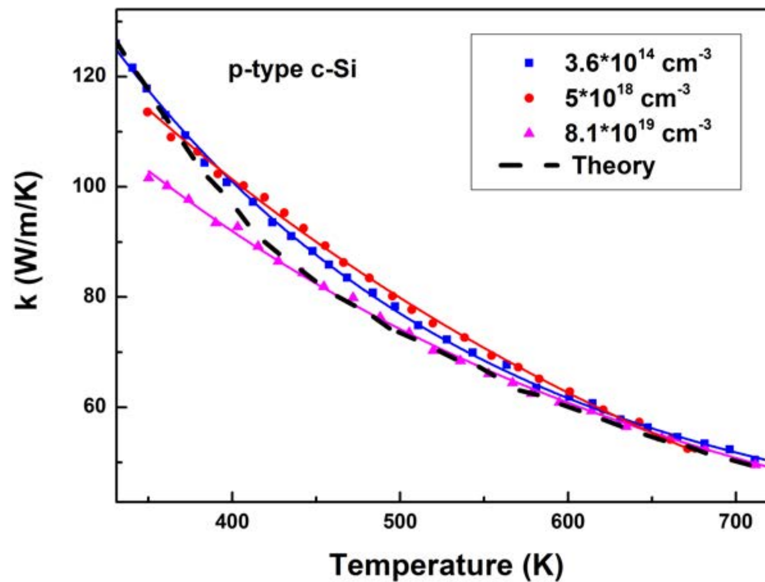

Figure 1.27: Thermal conductivities of p-type bulk c-Si samples with different doping concentrations as a function of temperature. Adapted from [30].

The effect of the doping on the thermal conductivity was thoroughly studied for Si thin films with different thickness [107]. It was shown, that similarly to c-Si, the thermal conductivity of 3 μm Si films with N below 10^{18} cm^{-3} shows no dependence on the concentration and type of dopants at $T = 300$ K. The thermal conductivity of Si films with thickness of 174 and 75 nm and $N \sim 10^{19}$ cm^{-3} at $T = 300$ K reduces in comparison with the undoped ones, and the decrease is stronger for films with lower thickness. The experimental data suggest that the boundary scattering in these thin films outweighs some effects of impurity and phonon-electron scattering, so that a doping level, which leas to a decrease in the thermal conductivity for c-Si, may not affect the film [107]. It was shown that the boron doping decreases the thermal conductivity stronger then the arsenic doping for all investigated Si film thicknesses, that can not be explained by the different impurity scattering times for different dopant atoms, since the impurity scattering rate for arsenic is 2.5 times stronger than for boron (see Eq. (1.5)) [107]. This fact implies that the phonon-electron scattering can significantly affect the thermal conductivity of Si thin films, along with the phonon-boundary and phonon-impurity scattering.

Cette thèse est accessible à l'adresse : http://theses.insa-lyon.fr/publication/2019LYSEI129/these.pdf
© [S. Rodichkina], [2019], INSA de Lyon, tous droits réservés

Fig. 1.28 (b) shows the thermal conductivity of individual MACE-SiNWs, having the bulk core/ rough surface morphology, before and after the post-fabrication doping. Highly-doped SiNWs (52 nm diameter, $N \sim 10^{19}$ cm^{-3}, shown by green squares) etched from a 10^{-1} Ω*cm wafer have a slightly lower *k* than the undoped SiNWs of the same diameter, etched from the 10 Ω*cm wafer. This small decrease in *k* was attributed to the higher rates of phonon-impurity scattering in highly-doped SiNWs, as well as to possibly higher surface roughness [7]. SiNWs etched from a 10^{-2} Ω*cm wafer have a much lower *k* than the other nanowires, which can be explained by higher porosity of these SiNWs.

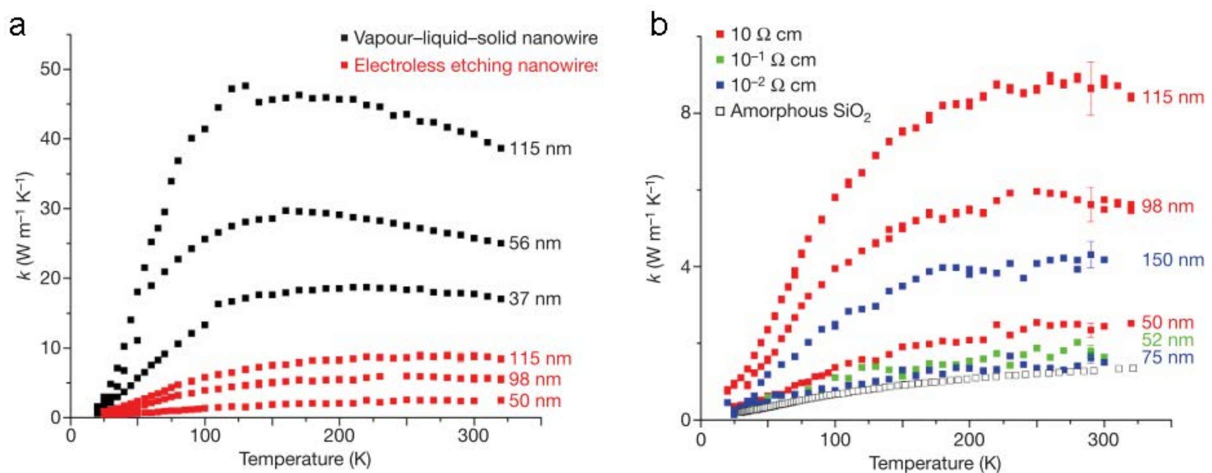

Figure 1.28: (a) The temperature-dependent thermal conductivity of VLS- (black squares; reproduced from Ref. [24]) and MACE-SiNWs (red squares). (b) Temperature-dependent thermal conductivity of MACE-SiNWs etched from wafers of different resistivities: 10 Ω*cm (red squares), 10^{-1} Ω*cm and doped post-synthesis to 10^{-3} Ω*cm (green squares), and 10^{-2} Ω*cm (blue squares). For the purpose of comparison, the *k* of bulk amorphous silica is plotted with open squares. The highly doped MACE-SiNWs have a *k* approaching that of insulating glass, suggesting an extremely short phonon mean free path [7].

1.3.5 Role of surface roughness

As it was stated in Sec. 1.3.2, a decrease in SiNWs diameter below 500 nm leads to a drastic reduction of their thermal conductivity. Fig. 1.24 shows, that the thermal conductivity of SiNWs, grown by VLS, is close to the Casimir limit, which corresponds to the purely diffuse scattering of phonons at nanowire's boundaries. The VLS-SiNWs possess the smooth surface (Δ of about 1-3 Å) and the Casimir limit seems to represent the lowest thermal conductivity of such Si nanocrystals. At the same time, MACE-SiNWs with diameter of 500-100 nm show the thermal conductivity as low as 1-9 W/(m K) at the room temperature (see Fig. 1.28), far below the

Cette thèse est accessible à l'adresse : http://theses.insa-lyon.fr/publication/2019LYSEI129/these.pdf
© [S. Rodichkina], [2019], INSA de Lyon, tous droits réservés

Casimir limit. The decrease of the thermal conductivity for MACE-SiNWs below the Casimir limit is usually ascribed to the effect of the surface roughness [7, 31, 108]. The surface of MACE-SiNWs is known to be much more rough (root-mean-square roughness height Δ of about 3 nm) than the surface of VLS-SiNWs, the structure of MACE-SiNWs can be considered to represent a crystalline core with a porous shell. It was established that such morphology is responsible for the small values of the thermal conductivity of MACE-SiNWs close to the amorphous limit for Si of about 1 W/(m K).

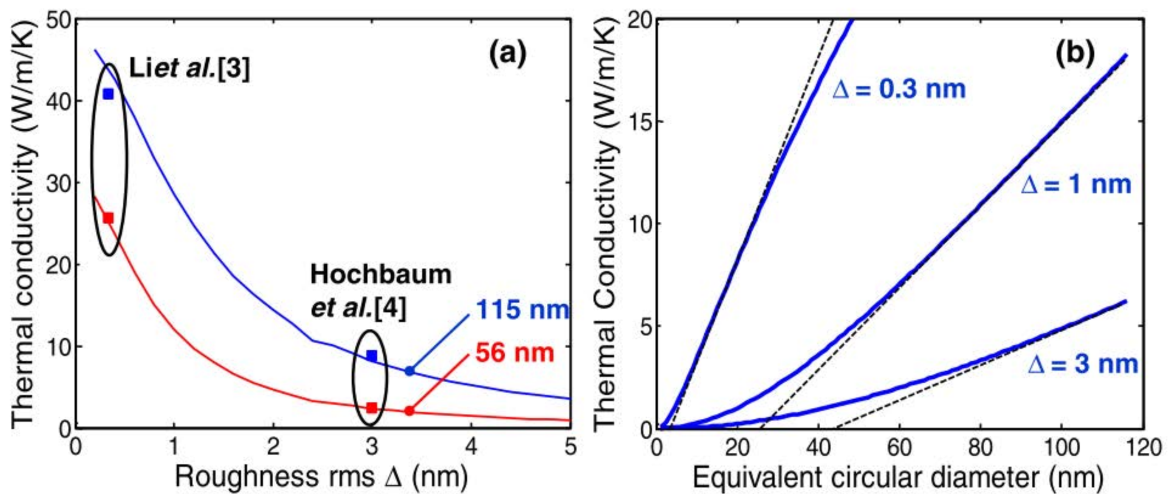

Figure 1.29: (a) Predicted effect of roughness rms on the thermal conductivity of 115 and 56 nm NW at $T = 300$ K, roughness autocorrelation length is of 6nm. (b) Effect of roughness rms on the dependence of NW thermal conductivity on equivalent circular diameter [31].

In a nanowire the effect of the surface roughness on the thermal transport can be treated as the variations of the confinement width for the phonons perpendicular to their propagation direction [31]. An additional frequency-dependent phonon scattering rate due to surface roughness scattering was computed from the perturbation theory and related to a description of the surface through the root-mean-square roughness height Δ and autocovariance length. The phonon scattering rates related to the surface roughness scattering, calculated for different Δ and autocorrelation length of 6 nm, increase with higher roughness rms values as Δ^2. The values of the thermal conductivity coefficient for SiNWs with diameter 115 and 56 nm, calculated as a function on roughness rms height from Eq. (1.2), considering the Umklapp, normal, impurity, boundary and surface roughness scattering mechanisms, are shown in Fig. 1.29 (a). As one can see from the figure, the additional roughness scattering explains the difference in the thermal conductivity coefficient between SiNWs, possessing the smooth and rough surface. The increase in Δ from 3 Å to 3 nm leads to the thermal conductivity drop from 39 to 9 W/(m K) for 115 nm SiNWs and

Cette thèse est accessible à l'adresse : http://theses.insa-lyon.fr/publication/2019LYSEI129/these.pdf
© [S. Rodichkina], [2019], INSA de Lyon, tous droits réservés

from 25 to 3 W/(m K) for 56 nm SiNWs, which is in excellent agreement with the experimental data. The decrease in the thermal conductivity due to the surface roughness is about 2 times greater for 56 nm SiNWs than for 115 nm SiNWs, which means that the effect of the roughness is stronger for thinner SiNWs. Fig. 1.29 (b) shows the calculated dependence of the thermal conductivity of SiNWs on the diameter for different surface roughness rms height. The deviation from the square root dependence for $\Delta = 1$ and 3 nm is observed, which is can be approximated as D^2 for low SiNWs diameters. For $D > 80$ nm the rough SiNWs exhibit the linear dependence of k_l on the diameter.

The strong effect of surface roughness on the thermal conductivity of SiNWs is crucial for their thermoelectric applications since in reduces the thermal conductivity coefficient of SiNWs close to the amorphous Si limit, while the surface-related effects can not significantly affect the electrical transport in SiNWs, which makes SiNWs with rough surface the perfect candidate for thermoelectrics accordingly to the concept "phonon-glass electron-crystal".

1.4 Electrical properties of SiNWs

This section describes the effect of nanowire size on electrical conductivity of SiNWs. The effect of SiNWs surface on both the free charge carrier concentration and mobility is described. The temperature dependencies of electrical conductivity for bulk c-Si and SiNWs are compared. The experimental data on electrical conductivity of SiNWs are reported.

1.4.1 Electrical transport in c-Si

The electrical properties of bulk c-Si at room temperature are determined by the concentration of dopant atoms. The electrical conductivity of bulk Si (which represents the inverse of electrical resistivity) is determined by the free carrier concentration and mobility, accordingly to the formula

$$\sigma = e\mu N \tag{1.8}$$

where σ is the electrical conductivity, e is the electron charge, μ is the electron (hole) mobility, N is the free charge carrier concentration. For c-Si at $T = 300$ K, the free charge carrier density is usually assumed to be equal to the total concentration of acceptor/donor dopant atoms [34]. Fig. 1.30 shows the correlation between the free charge carrier concentration and resistivity for n- and

Cette thèse est accessible à l'adresse : http://theses.insa-lyon.fr/publication/2019LYSEI129/these.pdf
© [S. Rodichkina], [2019], INSA de Lyon, tous droits réservés

p-type doped c-Si. As can be seen from the figure, the resistivity of intrinsic c-Si can be reduced by several orders of magnitude with an increase in the free charge carrier concentration. Despite the carrier mobility reduces with the dopant concentration due to the scattering of charge carriers on ionized dopant atoms [33], the increase in the carrier concentration leads to the decrease of resistivity. The resistivity of n-type c-Si is lower than of p-type Si with the same carrier concentration, which is explained by the lower mobility of holes than of electrons [34].

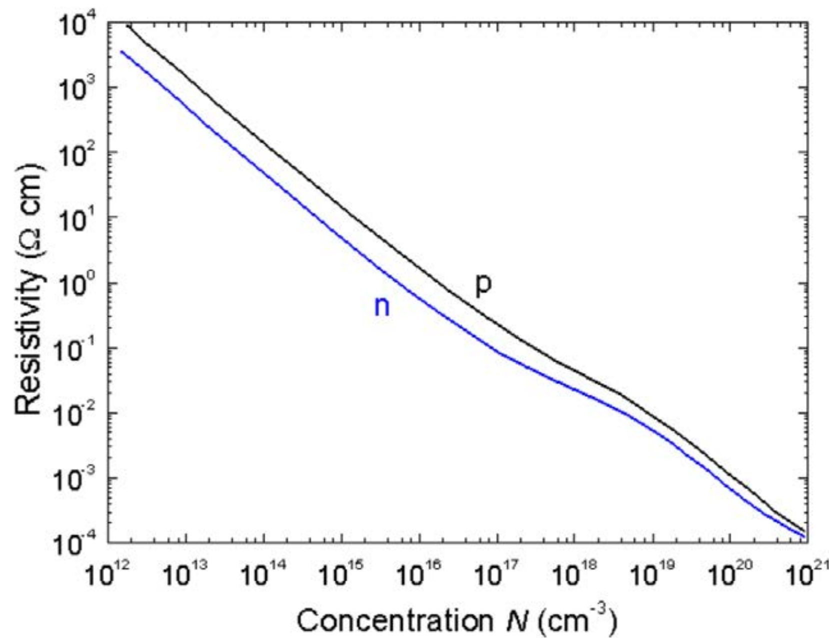

Figure 1.30: Resistivity as a function of the impurity concentration for bulk Si at 300 K. Ref. [32], adapted from [33].

Fig. 1.31 shows the dependence of the electrical resistivity of c-Si with low, moderate and high doping on the temperature. For the moderate- and high-doped samples the free carrier concentration above $T = 300$ K can be considered constant due to full ionization of the dopant atoms in this temperature range. The increase in the resitstivity with the temperature for these samples is related to the decrease of the mobility due to the enhanced scattering rate of charge carriers on phonons. It was shown that at high temperatures, the mobilities of electrons and holes in c-Si are independent of impurity concentration [109]. The mobility in this temperature range is determined by scattering by vibrations of the crystal lattice, and the contribution of impurity scattering is rather small. In this case, the temperature-dependent mobility for the medium- and high-doped bulk Si can be described by the formula $\mu_{e,h} = k_{e,h}T^{-3/2}$ [109]. The corresponding theoretical dependencies for resistivity are plotted by lines in Fig. 1.31 and show the excellent agreement with the experimental data. The different values of $k_{e,h}$ for electrons

Cette thèse est accessible à l'adresse : http://theses.insa-lyon.fr/publication/2019LYSEI129/these.pdf
© [S. Rodichkina], [2019], INSA de Lyon, tous droits réservés

and holes, correspondingly, are related to the difference in their effective masses. At lower temperatures, the scattering by both ionized and neutral impurity centers has a significant impact on the charge carrier mobility in c-Si, and the mobility is higher for the more pure samples. The contribution of the impurity scattering increases rapidly with decrease in temperature, and the temperature dependence of mobility passes through a maximum, which depends on impurity concentration.

For the low-doped samples, the formulas $\mu_e = k_1 T^{-2.6}$ and $\mu_h = k_2 T^{-2.3}$ (Ref. [110]) can be used to calculate the temperature-dependent carrier mobility. The calculated resistivity in the assumption of constant free carrier concentration is shown by the dash-dotted line in Fig. 1.31. The good agreement with experimental data is observed only up to 420 K for the p-doped sample and 550 K for the n-doped sample, for higher temperatures the transition from the impurity to intrinsic conduction takes place. For the intrinsic range at high temperatures, the electrical conductivity results from the electrons thermally excited from the valence band to the conduction band, and both the temperature dependencies of concentration and mobility of free carriers should be considered to describe the electrical resistivity.

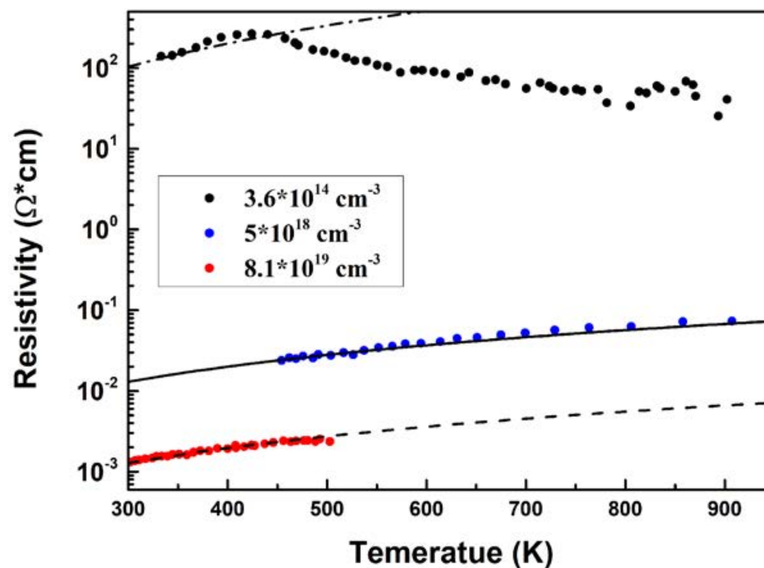

Figure 1.31: Electrical resistivities of p-type bulk Si samples with different doping concentrations as a function of temperature. Adapted from [30].

1.4.2 Free charge carrier concentration

The electrical properties of Si nanowires, in contrast to bulk Si, are not determined solely by the dopant concentration. Accordingly to Eq. (1.8), the difference in the electrical conductivity

Cette thèse est accessible à l'adresse : http://theses.insa-lyon.fr/publication/2019LYSEI129/these.pdf
© [S. Rodichkina], [2019], INSA de Lyon, tous droits réservés

between SiNWs and c-Si is related to difference in N and μ.

Firstly, unlike in c-Si, the free carrier concentration in SiNWs (N) can differ from the dopant concentration (N_D) at room temperature. When $N = N_D$ is considered for c-Si, the concentration of ionized donors N_D^+ is automatically assumed to be equal to N_D, as well as N is assumed to be equal to N_D^+. Both the assumptions can be not applicable for SiNWs at room temperature. The ionization efficiency of dopant atoms at a given temperature is determined by the impurity ionization potential. The electrostatic potential of the ionized impurity atom in bulk Si is shielded by the charge carriers in Si, which lowers the impurity ionization energy. When the volume of Si surrounding the dopant atom is reduced, the shielding of the electrostatic potential is also reduced, which in turn causes an increase of the ionization energy. For the same reason one should take into account the influence of the medium surrounding the nanowire. The difference between the dopant ionization energy in SiNWs and c-Si was found to be inversely proportional to the nanowire diameter and to depend on dielectric constants of nanowire and surrounding medium [34, 111]. This effect was shown to play an important role for thin SiNWs with diameter less than 30 nm [34].

Next, the Si surface can influence the free charge carrier concentration in SiNWs due to the surface states, which cause a depletion of Si in the vicinity of the surface by trapping charge carriers. The interface trap states, which can roughly be considered as Si dangling bonds, can either trap or release single electrons, depending on the position of the Fermi level. When the surface state traps or releases an electron in becomes negatively (positively) charged, the required electrons being taken from underlying Si. The Si surface to acquires a net charge, that causes a band bending and depletion of the Si in the vicinity of the surface, which lowers the average free carrier concentration in SiNWs.

Fig. 1.32 shows the calculated ratio of the average concentration of free electrons in SiNWs to the dopant concentration (N/N_D) as a function of the dopant concentration for different NW diameters, which takes into account both the effect of surface states and ionization energy change. Considering 80 nm SiNWs, one can see that $N/N_D \approx 0.7$ is maximal for $N \sim 10^{18}$ cm^{-3} and decreases to ≈ 0.1 for $N \sim 10^{20}$ cm^{-3}. For the dopant concentrations lower than the critical one ($5 * 10^{17}$ cm^{-3}) a sharp decrease in N/N_D down to 10^{-6} is observed, which takes place when the nanowire changes from being partially depleted to being fully depleted. SiNWs with $20 < D < 80$ nm exhibit the similar dependencies of N/N_D on N_D with the critical dopant concentration shifted towards higher dopant concentrations. SiNWs with $D = 14$ and 10 nm

Cette thèse est accessible à l'adresse : http://theses.insa-lyon.fr/publication/2019LYSEI129/these.pdf
© [S. Rodichkina], [2019], INSA de Lyon, tous droits réservés

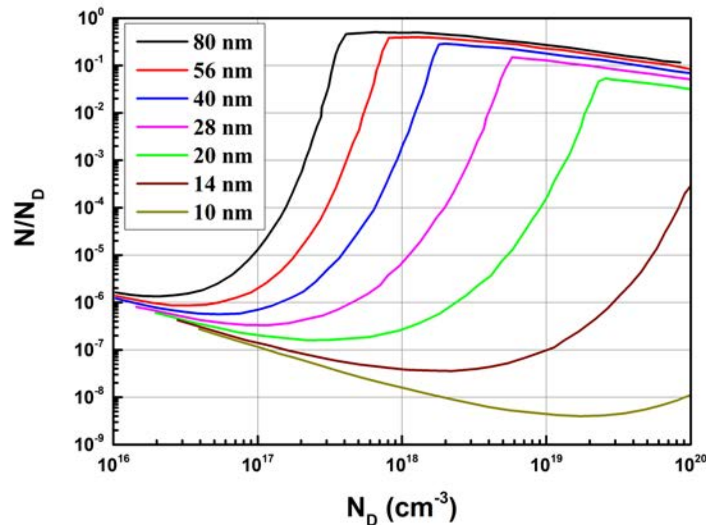

Figure 1.32: Ratio of the average electron concentration to the dopant concentration (N/N_D) as a function of the dopant concentration for various SiNWs diameters and the interface trap level density of 10^{12} $eV^{-1}cm^{-2}$. Dopant is P with a bulk ionization energy of 45 meV; $T = 300$ K. Adapted from [34].

are fully depleted in the whole dopant density range. At these small diameters, a proper surface passivation is essential. The effect of impurity ionization energy increase is also responsible for such low values of N/N_D ($< 10^{-4}$) for SiNWs with D =14 and 10 nm. In general, the decrease of N/N_D with NW diameter is observed in the whole dopant density range. Thus, to obtain the high free carrier concentration in SiNWs, the thick SiNWs are more preferable, as well as the high dopant concentration levels are required to avoid the effect of depletion of SiNWs. Note, the free charge carrier concentration in SiNWs was not studied experimentally, however the profiles of the dopant atom concentration in SiNWs arrays were investigated using SIMS technique [55].

1.4.3 Free charge carrier mobility

Secondly, the carrier mobility in SiNWs differs from c-Si change due to the different scattering time of charge carriers. One would expect a reduction of the charge carrier mobility in SiNWs compared to c-Si because of increased surface scattering of charge carriers, resulting from a high surface-to-volume ratio of SiNWs. The above assumption was confirmed by simulations, which showed that surface scattering determines the electron mobility for nanowires with diameter less than 5 nm [112]. In SiNWs with small diameters ($D <$ 5-10 nm) spatial confinement affects both the charge carriers and phonons. In general case, both the electron and acoustic phonon

Cette thèse est accessible à l'adresse : http://theses.insa-lyon.fr/publication/2019LYSEI129/these.pdf
© [S. Rodichkina], [2019], INSA de Lyon, tous droits réservés

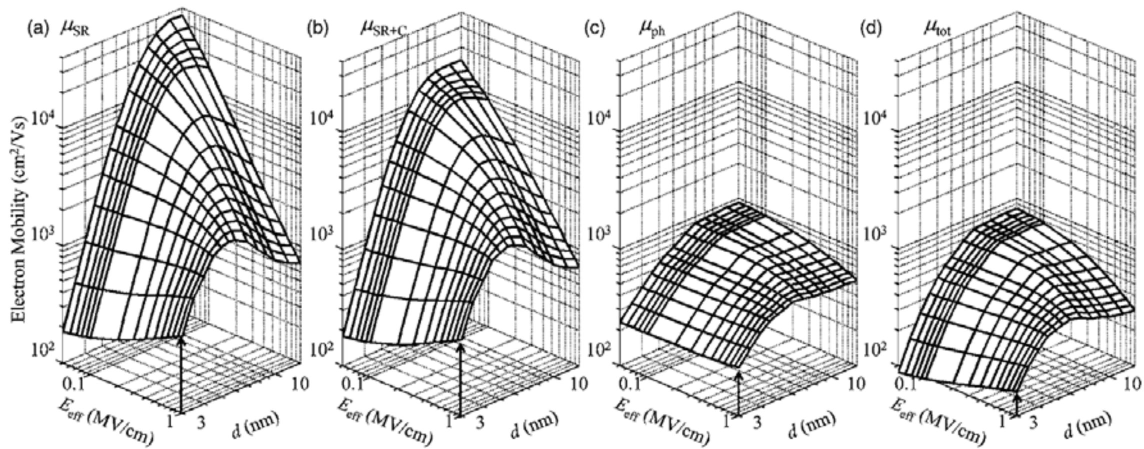

Figure 1.33: Calculated surface-roughness-limited (a), surface-roughness and Coulomb-limited (b), phonon-limited (c), and total (d) electron mobility as a function of the effective field ranging from 0.05 to 1 MV/cm and silicon body diameter ranging from 3 to 14 nm [35].

confinement in SiNWs should be taken into account. It was shown that for SiNWs, surrounded by SiO_2, which is an acoustically softer material, the decrease in acoustic phonon group velocity leads to the enhanced electron-acoustic phonon scattering rates, compared to c-Si [112]. For 8 nm SiNWs, the electron mobility, calculated accounting the modification of the acoustic phonon spectrum due to confinement, is about 10% lower than the mobility calculated with bulk acoustic phonons. This result clearly emphasizes the need to account for the acoustic phonon confinement when calculating the electrical properties of SiNWs.

Fig. 1.33 shows the calculated electron mobility in silicon nanowires as a function of their diameter ranging from 3 to 14 nm and the effective electric field ranging from 0.05 to 1 MV/cm, where the different electron scattering processes are taken into account, i.e. (a) surface-roughness scattering, (b) surface-roughness and Coulomb-limited scattering, (c) phonon scattering and (d) total scattering rate, including all the above scattering processes. The low-field electron mobility for each electron subband was obtained from the Kubo-Greenwood formula, modified for 1D transport, the effective electron mobility was calculated as the average of the electron mobility in every subband [35]. The electron momentum relaxation time was calculated accordingly to Matthiessen's rule using the scarring times for surface roughness scattering, Coulomb scattering by ionized impurities in the silicon body or fixed charges at the interface and in the surrounding insulator, intravalley and intervalley phonon scatterings. The calculations were performed for lightly p-type doped SiNWs with $N = 10^{16}$ cm^{-3} with the rough surface with rms of $\Delta = 0.48$ nm, covered by a silicon oxide layer with the thickness of 1 nm, the density of fixed interface charges was assumed of 10^{11} cm^{-2}. Since the doping level of SiNWs is low, for the calculation of the

Cette thèse est accessible à l'adresse : http://theses.insa-lyon.fr/publication/2019LYSEI129/these.pdf
© [S. Rodichkina], [2019], INSA de Lyon, tous droits réservés

Coulomb scattering rate only the surface charge carriers were taken into account. The other calculation details can be found in Ref. [35].

Accordingly to Fig. 1.33 (d) the total mobility decreases monotonically with shrinking SiNWs diameter for $E_{eff} = 0.05$ MV/cm and shows a maxi- mum around d = 5 nm for $E_{eff} = 1$ MV/cm. The surface effects limited electron mobility (see Fig. 1.33 (b)), which was calculated taking into account only the electron surface scattering and Coulomb scattering by surface charges, shows the similar characteristics. Comparing pure surface-roughness and surface-roughness+Coulomb scattering limited electron mobility, one can notice the minor contribution of the Coulomb scattering due to the fixed interface charges on the electron mobility, compared with other scattering mechanisms, for the given interface charge density. Also, the phonon-limited electron mobility decreases almost monotonically with shrinking diameter and increasing effective field (see Fig. 1.33 (c)). The contribution of the surface-related electron scattering is the strongest for SiNWs with diameter less than 10 nm. At $E_{eff} = 0.05$ MV/cm, for SiNWs with D from 10 to 14 nm, the values for phonon scattering-limited and total electron mobility in SiNWs almost coincide and do not depend on nanowire diameter. For SiNWs with $D = 14$ nm, the value of electron mobility of about 800 $cm^2V^{-1}s^{-1}$ correlates well with the bulk c-Si value for the same hole concentration of 430 $cm^2V^{-1}s^{-1}$, the higher values for SiNWs can be attributed for not taking into account the bulk impurity scattering. It is important to note that the Coulomb and surface roughness scattering rates decrease with increasing a dielectric constant of the insulator surrounding SiNWs [35].

The effect of SiNWs coating on the electron mobility was studied in Ref. [36]. The theoretical electron mobility was calculated in the relaxation time approximation, using the electron-phonon and electron-impurity scattering times for confined acoustical phonons and confined electrons, in which the influence of surface was taken into account using the appropriate boundary conditions [36]. Fig. 1.34 (a) shows the calculated electron mobility for SiNWs with impurity concentration of $5 * 10^{19}$ cm^{-3} and diameter of 4 nm using the confined acoustic phonon and electron spectra. The mobility values for SiNWs, coated with diamond, are between the limits corresponding to the free-standing and clamped (with fixed surface atoms) SiNWs for all considered temperatures. In the case of bulk-like acoustical phonons, the electron mobility also lies between the same limits. As the thickness of diamond barrier shell increases, the mobility approaches the limit of the clamped NW. The strong mobility enhancement in diamond-coated SiNWs in comparison with the free-standing SiNWs was explained by the decrease in the confined electron-confined

Cette thèse est accessible à l'adresse : http://theses.insa-lyon.fr/publication/2019LYSEI129/these.pdf
© [S. Rodichkina], [2019], INSA de Lyon, tous droits réservés

phonon scattering rates in diamond-coated SiNWs [36]. To understand the physics underlying this phenomenon, one should consider that, accordingly to the phonon dispersion curves, the number of phonons participating in the scattering for clamped SiNWs is less and the amplitude of the scattering is lower than that for the free-standing NW.

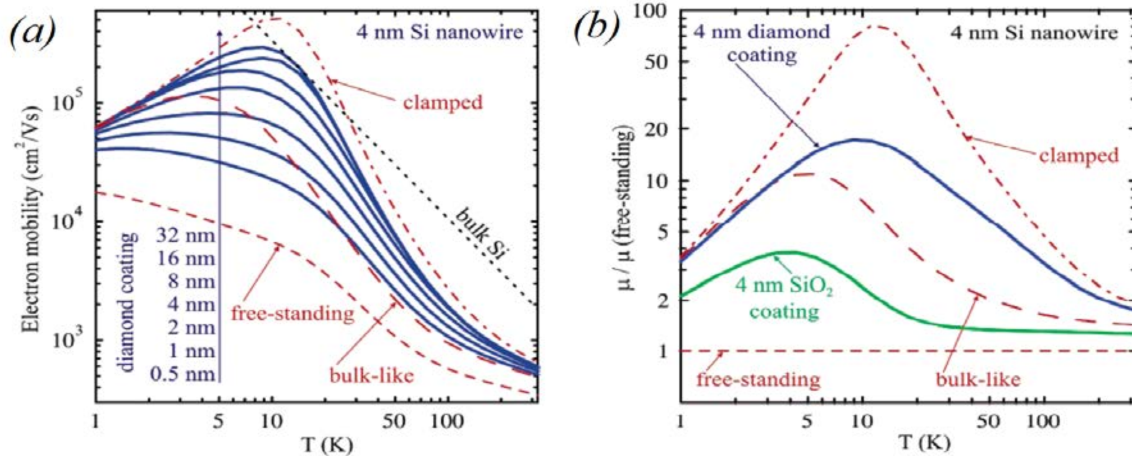

Figure 1.34: (a) Low-field electron mobility as a function of temperature for 4-nm silicon nanowires with and without diamond coating. Dotted line shows electron mobility for pure bulk silicon. (b) Enhancement of low-field electron mobility for coated 4-nm silicon nanowires in comparison with the free-standing nanowire[36].

One can also see from Fig. 1.34 (a) that at low temperatures the mobility is limited by impurities and proportional to $T^{1/2}$. At high temperatures the mobility is limited by phonons and proportional to $T^{-1/2}$. The change of the temperature dependence of mobility from the $T^{3/2}$ ($T^{-3/2}$) in bulk c-Si to the $T^{1/2}$ ($T^{-1/2}$) dependence in SiNWs was explained by the change in the electron density of states [36]. It is interesting to note that the electron-phonon scattering rate in the free-standing SiNWs is very strong, and it limits the electron mobility even at low temperatures. On the other hand, the electron-phonon scattering in diamond-coated SiNWs is weak, and the electron mobility becomes comparable with the mobility of bulk c-Si. Fig. 1.34 (b) shows that at room temperature, even 0.5-nm-thick diamond coating results in the electron mobility higher than that in the case of bulk-like phonons. If the barrier shell (coating) material is softer than Si, e.g. SiO_2, the electron mobility is always lower than in the case of bulk-like phonons. The electron mobility enhancement due to diamond coating is about a factor of 2 at room temperature.

The main mechanism that limits the low-field carrier mobility in SiNWs near room temperature is the charge carrier scattering on lattice vibrations, i.e., acoustic phonons. For SiNWs with diameter $\sim$ 10 nm and $T \sim 100$ K, phonon confinement effects can be safely neglected,

Cette thèse est accessible à l'adresse : http://theses.insa-lyon.fr/publication/2019LYSEI129/these.pdf
© [S. Rodichkina], [2019], INSA de Lyon, tous droits réservés

and for the calculations of the carrier scattering rate one can assume "bulk-like" phonons. The term bulk-like phonon implies that NW is embedded in a hypothetical medium, impenetrable for the charge carriers, with the elastic parameters equal to those of NW. However, if one considers NWs with diameter $\sim$ 1 nm, the phonon confinement effects are strong and have to be taken into account.

1.4.4 Electrical resistivity

Fig. 1.35 (A) shows the results of current–voltage (I–V) characterization of SiNWs with the length of 40 μm, thickness of 50 nm and width of 80, 130 and 300 nm. SiNWs were fabricated by a top-down method on silicon-on-insulator substrate, using the electron beam lithography for the nanopatterning of SiNWs dimensions and the reactive ion etching. SiNWs was moderately doped with boron (B) by ion implantation (concentration of $5*10^{18}$ cm^{-3}), followed by rapid thermal

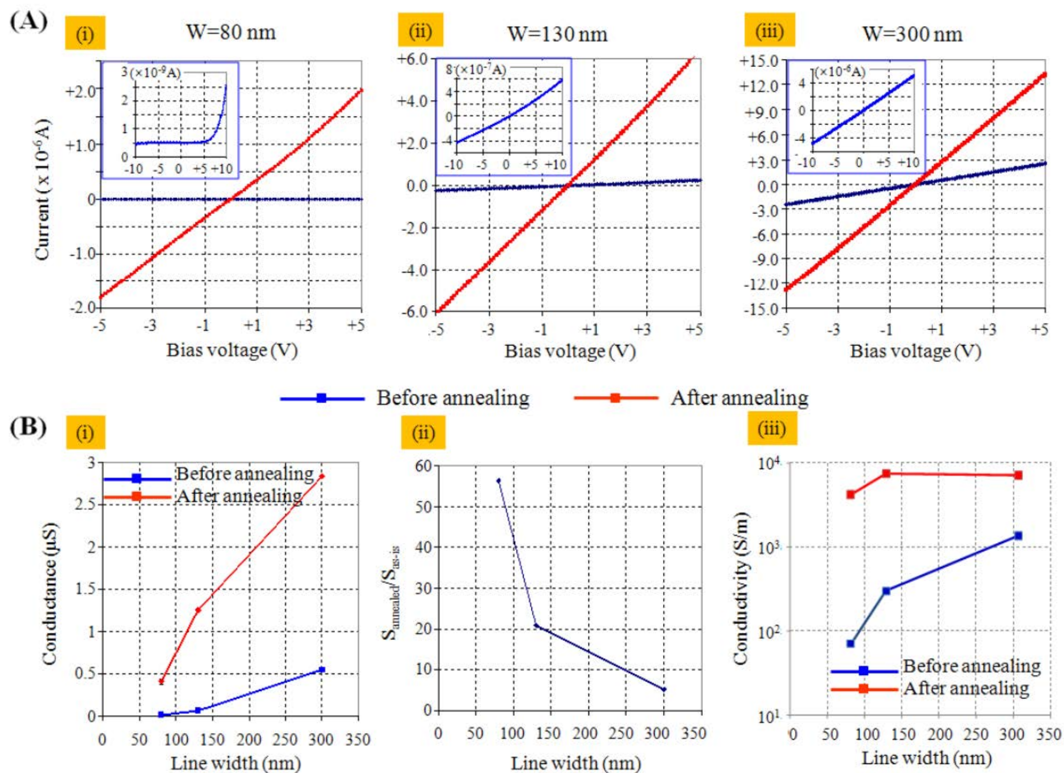

Figure 1.35: Electrical characterization of silicon nanowires: (A) I-V characterstics of silicon nanowires (length of 40 μm, thickness of 50 nm, width of 80, 130, 300 nm) before (blue lines) and after (red lines) thermal annealing, the insets show the magnification view of the I-V curves for SiNWs before annealing; (B) (i) electrical conductance and (iii) electrical conductivity of silicon nanowires before and after the thermal annealing as a function of their width, (ii) ratio between the electrical conductances of SiNWs before and after the thermal annealing as a function of their width [37].

Cette thèse est accessible à l'adresse : http://theses.insa-lyon.fr/publication/2019LYSEI129/these.pdf
© [S. Rodichkina], [2019], INSA de Lyon, tous droits réservés

annealing at 984 ^{0}C for 20 s in an argon environment [37]. As follows from the I-V curves, SiNWs behave like common ohmic resistors with a linear I–V relation after the thermal annealing, while a non-liner I-V curve is observed for 80 nm SiNWs before annealing. Fig. 1.35 (B-iii) shows the effect of the thermal annealing on the electrical conductivity of SiNWs, where the increase in the electrical conductivity of SiNWs after thermal annealing can be observed, stronger for SiNWs with lower diameter. Both the change in I-V curve behaviour and the increase in electrical conductivity of SiNWs after annealing are explained by the improvement of the Al-Si electrical contacts, but mainly by increase in the conduction of SiNWs itself [37]. The contact resistance at each Al-Si contact area was 2.64 kΩ before thermal annealing and 0.58 kΩ after annealing, both of which are much smaller than the total resistance of SiNWs after annealing, equal to 2.56 MΩ, 0.80 MΩ and 0.35 MΩ for nanowires with width of 80 nm, 130 nm and 300 nm, respectively. The enhancement of the electrical conductivity of SiNWs after the annealing was explained by the evaporation of the organic contaminants around the SiNWs, as well as by the reduction of the interface trapped charges or the oxide trapped charges, developed during the plasma etching, during the thermal annealing process.

Concerning the dependence of SiNWs electrical conductivity on their width, it was observed that σ for SiNWs with width of 80 nm is about 2 times smaller than that for 130 and 300 nm SiNWs. This difference is related to larger surface effects for smaller nanowires, i.e. surface damage, defects and trapped charges, which can be developed during the plasma etching process. Also, the ratio of line edge roughness to linewidth becomes larger for smaller nanowires. Therefore, electrical conductivity could be reduced by larger surface scattering of mobile charge carriers. The discrepancy between different sizes is reduced after the thermal annealing process, as shown in Fig. 1.35 (B-iii).

Fig. 1.36 shows the I-V characteristics of n- and p-type SiNWs with diameter of 50 nm, obtained by using the 4-point measurement technique. SiNWs have been fabricated by top-down process, Phosphorus (P) and Boron (B) doping concentrations in SiNWs, obtained after the ion implantation, are of $1.0 * 10^{20}$ cm^{-3} both for n- and p-type SiNWs. The I-V curves both for p- and n-type are linear, and the electrical resistivity values are about 1.1 and 1.2 mΩ*cm for n- and p-type SiNWs, correspondingly. The c-Si conductivity for the same impurity concentration is of 0.8 and 1.2 mΩ*cm for n- and p-type c-Si, correspondingly, which is close to the SiNWs values. This fact allows us to conclude no significant influence of SiWNs surface on free charge carrier mobility for investigated SiNWs. The close resistivity values for n- and p-type SiNWs

Cette thèse est accessible à l'adresse : http://theses.insa-lyon.fr/publication/2019LYSEI129/these.pdf
© [S. Rodichkina], [2019], INSA de Lyon, tous droits réservés

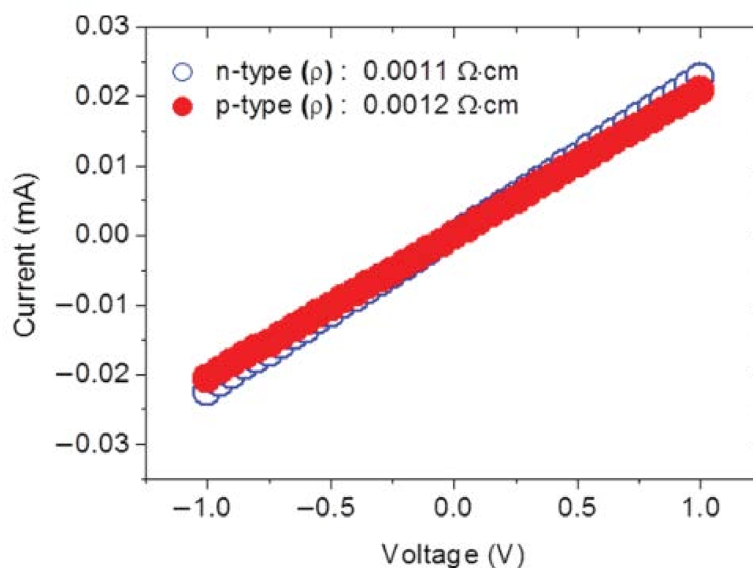

Figure 1.36: Ohmic current to voltage characteristic of n- and p-type silicon nanowire with diameter of 50 nm. The extracted resistivity is of 1.1 and 1.2 mΩ*cm for n- and p-type silicon nanowires, correspondingly [38].

are explained by the saturation of the free charge carrier mobility due to the strong impurity scattering of charge carriers, analogous to c-Si [113].

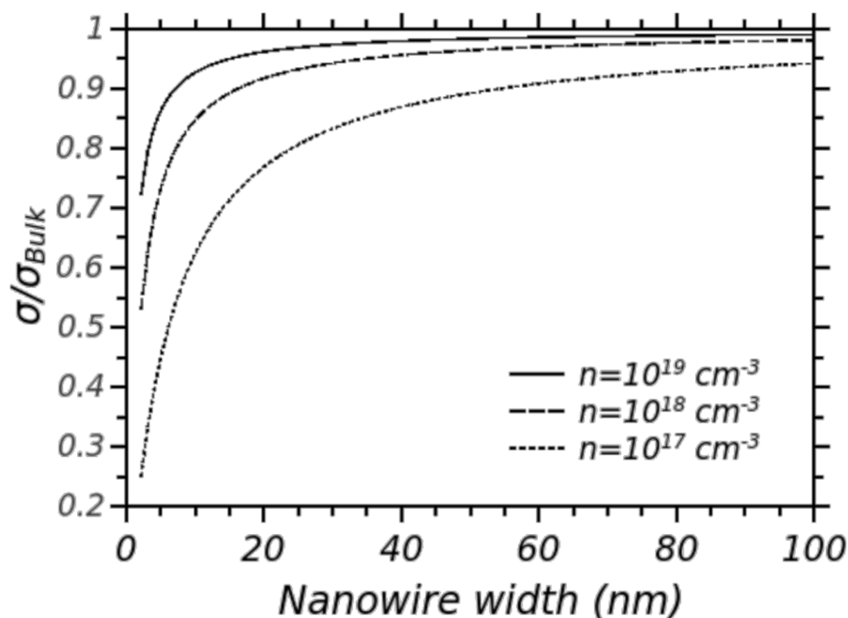

Figure 1.37: Theoretical electrical conductivity of n-type silicon nanowires as a function of the nanowire width (triangular cross section), normalized with respect to the bulk electrical conductivity [39].

Fig. 1.37 shows the theoretical electrical conductivity for n-doped silicon nanowires, normalized with respect to the value for bulk silicon with the same doping concentration. The theoretical

Cette thèse est accessible à l'adresse : http://theses.insa-lyon.fr/publication/2019LYSEI129/these.pdf
© [S. Rodichkina], [2019], INSA de Lyon, tous droits réservés

calucations were based on the Boltzmann transport equation, solved within the framework relaxation time approximation in assumption of parabolic law of electron dispersion. The calculation has been performed for nanowires with isosceles triangular cross section. The electron scattering processes in nanowires were considered independent, and the Matthiessen's rule was applied for the bulk scattering processes (i.e. impurity scattering, phonon scattering, and electron-electron scattering) and surface scattering processes, considering a completely diffusive scattering of electrons on the nanowire surfaces [114]. As one can see from the figure, the deviation of SiNWs electrical conductivity from its bulk value is significant (< 20 %) only for SiNWs with diameter less than 30 nm. The effect of SiNWs diameter is especially low for high doping concentrations, for which the electron mobility is limited by the impurity scattering, and the electron mean free path is small with respect to the nanowire diameter. Thus, the electron transport in SiNWs can be considered the same as in bulk c-Si for SiNWs with a diameter more than 50 nm and doping concentration more than 10^{18} cm^{-3}.

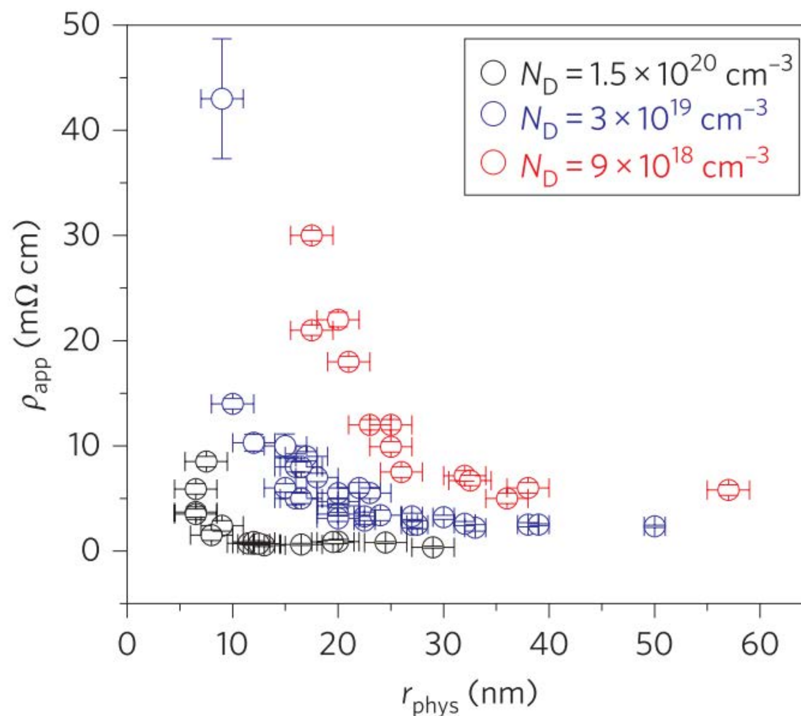

Figure 1.38: Experimental dependence of electrical resistivity of SiNWs on their radius for different donor densities [40].

Fig. 1.38 shows the experimental dependence of the electrical resistivity of n-type (Phosphorus) doped SiNWs on the diameter for different donor concentrations. SiNWs were grown by means of the vapour–liquid–solid mechanism, silane (SiH_4) was used as the precursor gas and phosphine (PH_3), 0.3% in He, as the n-type doping source [40]. The electrical resisitivity

Cette thèse est accessible à l'adresse : http://theses.insa-lyon.fr/publication/2019LYSEI129/these.pdf
© [S. Rodichkina], [2019], INSA de Lyon, tous droits réservés

of SiNWs increases with a decrease in nanowire diameter for all donor concentrations, which was explained by the deactivation of doping atoms caused by an increase in ionization energy of phosphorous donors due to a dielectric mismatch between the wire interior and the surrounding air [40]. Surface depletion of charge carriers due to interface states, trapped charges, and/or to a size-dependent incorporation of dopants during growth was shown to have only slight effect on SiNWs resistivity. Other factors, such as quantum confinement, surface segregation of dopants and size-dependent mobility were neglected because they are expected to take place for SiNWs diameter below 10 nm [35, 74]. The dependence of SiNWs resistivity, normalized to the resistivity of nanowire with the largest diameter, on the diameter was shown to be independent of SiNWs doping. For all SiNWs doping levels, it was well fitted using the formula $\rho = 1/eN\mu$, where the electron concentration N was calculated taking into account the change in the impurity ionization energy with diameter and the electron mobility μ was considered diameter-independent. The good agreement between theory and experiment allows us to conclude that the electron mobility in SiNWs is independent of diameter for the studied size range [40]. The values of electrical resistivity of SiNWs with the largest diameter (more than about 60-80 nm) are in a good agreement with the values for bulk Si with the same dopant concentration.

Fig. 1.39 shows the resistivity of SiNWs as a function of the silane to dopant precursor ratio data during CVD synthesis, considering different precursors such as phosphine (PH_3), diborane (B_2H_6), and trimethylborane ($B(CH_3)_3$). The figure shows that SiNWs resistivities as low as

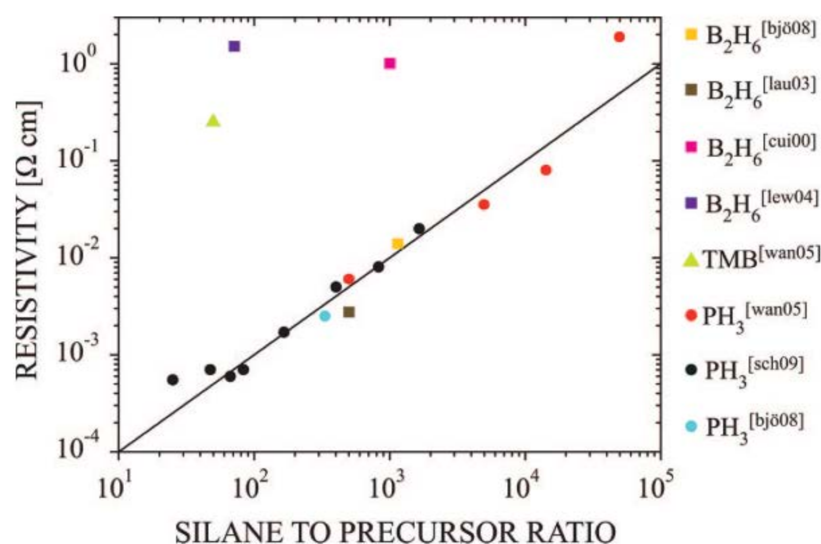

Figure 1.39: Si nanowire resistivity as a function of the silane to dopant precursor ratio during CVD synthesis [34].

Cette thèse est accessible à l'adresse : http://theses.insa-lyon.fr/publication/2019LYSEI129/these.pdf
© [S. Rodichkina], [2019], INSA de Lyon, tous droits réservés

0.8 mΩ*cm can be reached, depending on dopant precursor concentration, that allows to control SiNWs doping during the growth.

1.5 Thermoelectric performance of SiNWs

Thermoelectric (TE) generators are mainly used to generate electrical power in severe conditions, e.g. in space, due to their extreme reliability. Low efficiency and relatively high cost of current TE materials does not allow the widespread use of TE generators. This section describes the thermoelectric efficiency of solid thermoelectric materials and the "phonon-glass electron-crystal" strategy for its enhancement. The experimental data on the Seebeck coefficient and ZT for bulk c-Si and SiNWs are presented, and the potential of SiNWs as the thermoelectric materials is estimated.

a) Theory of thermoelectric materials

Thermoelectric generators convert thermal energy to electrical energy using the Seebeck effect, which consists in the appearance of the potential difference on a semiconductor when creating the temperature gradient along it, that is explained by the diffusion of charge carriers along the temperature gradient [115]. The capability of TE material to efficiently produce thermoelectric power is described by its TE figure of merit (Eq. (1)). The figure of merit of a TE material is related to the efficiency of TE generator. The optimal TE material should have thermal properties like that of a glass, and electrical properties like that of a single-crystal, which represents the concept of "phonon-glass electron-crystal" material [116]. Such a material possesses a low thermal conductivity and a good electrical conductivity, which enhances its TE performance, accordingly to Eq. (1).

In a bulk semiconductor the values of the Seebeck coefficient and the electrical conductivity are related to one another, since they are both functions of the free charge carrier concentration [117]. As shown in Fig. 1.40, the Seebeck coefficient of a material decreases with free charge carrier concentration, while the electrical conductivity increases. Also, the electron thermal conductivity increases with the free charge carrier concentration. Considering the above dependencies, the dependence of ZT on N has a maximum, and one can see that optimal thermoelectric materials are extrinsic semiconductors with free charge carrier concentration $\sim 10^{20}$ cm^{-3} [41].

Let us consider the thermoelectric figure of merit of a semiconductor in more detail. The total thermal conductivity of a semiconductor is a combination of of the lattice (phonon) thermal

Cette thèse est accessible à l'adresse : http://theses.insa-lyon.fr/publication/2019LYSEI129/these.pdf
© [S. Rodichkina], [2019], INSA de Lyon, tous droits réservés

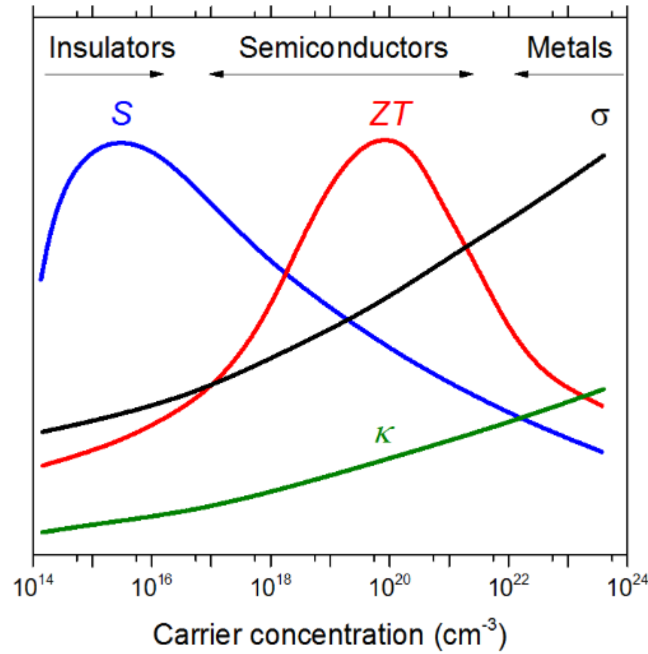

Figure 1.40: Illustrative plot of the dependence of Seebeck coefficient S, electrical conductivity σ, thermal conductivity k and thermoelectric figure of merit ZT on free charge carrier concentration in the materials [41].

conductivity k_{lat} and the electronic thermal conductivity k_{el}: $k = k_{lat} + k_{el}$. For the most heavily doped bulk semiconductors ($N \sim 10^{21}$ cm^{-3}), the total thermal conductivity is dominated by the lattice thermal conductivity contribution, while the latter is influenced by the phonon-impurity scattering (see Sec. 1.3). The electronic thermal conductivity can be determined according to the Wiedemann-Franz law [117]:

$$k_{el} = \frac{L_0 T}{\rho}, \tag{1.9}$$

where $L_0 = (\pi^2/3) \cdot (k_B/e)^2 = 2.44 * 10^{-8}$ WΩK^{-2} is the Lorentz number.

The Seebeck coefficient and electrical conductivity strongly depend on the Fermi level in semiconductor, which in turn depends on the carrier concentration, carrier effective mass, and temperature [117]. Therefore, it is convenient to express the Seebeck coefficient and electrical conductivity in terms of the Fermi energy. Since the thermal conductivity of a semiconductor is weakly dependent on the free charge carrier concentration (see Sec. 1.3), an increase in the figure of merit with N is mainly due to the increase in the power factor $S^2\rho$.

In the case of a single parabolic electron band, assuming that the charge carriers obey classical statistics, the Seebeck coefficient can be expressed as [117]:

Cette thèse est accessible à l'adresse : http://theses.insa-lyon.fr/publication/2019LYSEI129/these.pdf
© [S. Rodichkina], [2019], INSA de Lyon, tous droits réservés

$$S = \pm \frac{k_B}{e}(5/2 + s - \eta^*), \tag{1.10}$$

where the "+" or "-" sign is for the valence or conduction band, correspondingly (p- or n-type semiconductor), s is the scattering parameter and $\eta^* = \eta/k_BT = (F - E_c)/k_BT$ is the reduced Fermi level.

The electrical resistivity, given by Eq. (1.8) includes the free charge carrier concentration, which is related to the reduced Fermi energy as [117]:

$$N = 4\pi \left(\frac{2m^* k_B T}{h^2}\right)^{3/2} exp(\eta^*), \tag{1.11}$$

where m^* is the free charge carrier effective mass, h is the Planck's constant.

The use of classical statistics in describing the behavior of the carriers is justified only in the limit of low carrier concentration. Because the thermoelectric material has to be doped heavily, Fermi-Dirac statistics should be employed. The Seebeck coefficient and free charge carrier concentration in this case can be expressed as [117]:

$$S = \pm \frac{k_B}{e}\left(\frac{(2+s)F_{1+s}(\eta^*)}{(1+s)F_s(\eta^*)} - \eta^*\right), \tag{1.12}$$

$$N = 4\pi \left(\frac{2m^* k_B T}{h^2}\right)^{3/2} F_{1/2}(\eta^*), \tag{1.13}$$

where F_n is the Fermi integral of the order of x:

$$F_n = \int_0^\infty \frac{x^n}{1 + exp(x - \eta^*)} dx. \tag{1.14}$$

For the pure phonon or lattice vibration scattering of the charge carriers, $s = 0$. When the carriers are scattered primarily by charged impurities (ionized donors and acceptors), $s = 2$; the intermediate value $s = 1$ represents mixed scattering. The scattering of electrical carrier transport is represented mainly by two scattering mechanisms, namely, the acoustic phonon and ionized impurity scattering mechanisms. The scattering mechanism that affects electrical transport can be determined from the temperature dependence of carrier mobility. The acoustic phonon and ionized impurity scattering mechanisms result in $T^{-3/2}$ and $T^{3/2}$ dependence of free charge carrier mobility, respectively [117].

Finally, Table 1.2 shows the typical values of thermoelectric parameters for metals, semicon-

Cette thèse est accessible à l'adresse : http://theses.insa-lyon.fr/publication/2019LYSEI129/these.pdf
© [S. Rodichkina], [2019], INSA de Lyon, tous droits réservés

ductors and insulators.

Table 1.2: Comparison of thermoelectric properties of metals, semiconductors and insulators at $T = 300$ K. Adapted from [45].

Property	Metals	Semiconductors	Insulators
S	$\sim \pi^2 \frac{k_B}{e\eta^*} \sim 5\ \mu$V/K	$\pm\frac{k_B}{e}(2+\eta^*) \sim 200\ \mu$V/K	$\pm\frac{k_B}{e}(2+\eta^*) \sim 1$ mV/K
$\sigma = eN\mu$	$10^6\ \Omega^{-1}$cm^{-1}	$\sim 10^3\ \Omega^{-1}$cm^{-1}	$\sim 10^{-12}\ \Omega^{-1}$cm^{-1}
$k = k_{el} + k_{lat}$	$\sim k_{el}$	$\sim k_{lat}$	$\sim k_{lat}$
$k_{el} = L_0\sigma T$	~ 700 W/(m*K)	~ 0.7 W/(m*K)	$\sim 10^{-15}$ W/(m*K)
ZT	$\sim 10^{-3}$	~ 0.6	$\sim 10^{-14}$

b) Thermoelectric properties of c-Si

Fig. 1.41 shows the Seebeck coefficient and calculated ZT values for n- and p-type c-Si with different free hole concentration (thermal and electrical conductivity of these samples is shown in Figs. 1.27 and 1.31). It can be seen that the absolute value of S decreases with the free charge carrier concentration in c-Si, that is in accordance with Eq. (1.12). S for highly-doped c-Si is almost independent of temperature, and it is about -0.4 and 0.3 mV/K for n-type ($N = 1.4 * 10^{19}$ cm^{-3}) and p-type c-Si ($N = 8 * 10^{19}$ cm^{-3}), correspondingly, at $T = 350$ K [30]. The observed experimental values of S for c-Si are in the good agreement with the theoretical ones, obtained from first principles calculations for c-Si with $N = 1 * 10^{19}$ cm^{-3} [42] and shown as the dashed line in Fig. 1.41 (a).

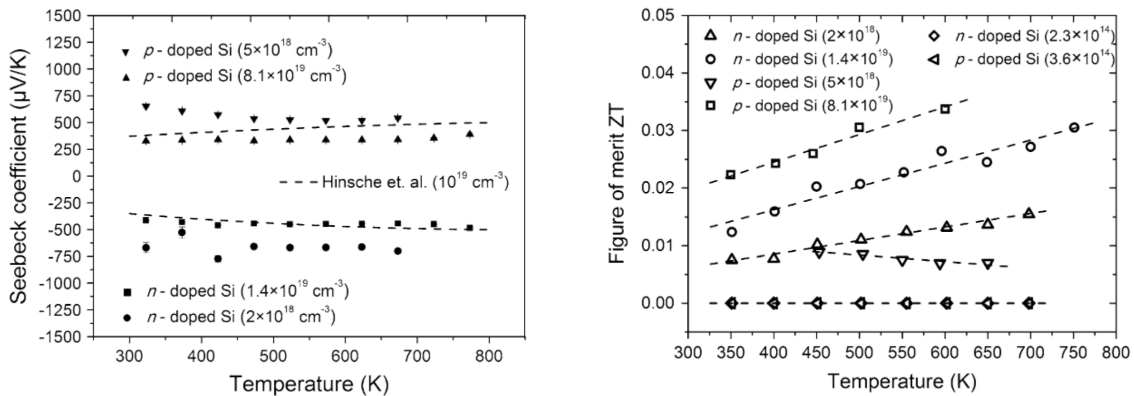

Figure 1.41: (a) Seebeck coefficient of medium- and highly-doped p- and n-type c-Si as a function of temperature. Dashed lines show the results of the Seebeck coefficient calculation for n- and p-type c-Si with $N = 1 * 10^{19}$ cm^{-3} from Ref. [42]. (b) Calculated ZT values of medium- and highly-doped p- and n-type c-Si as a function of temperature [30].

Fig. 1.42 shows the calculated values of the Seebeck coefficient and power factor for n-type

Cette thèse est accessible à l'adresse : http://theses.insa-lyon.fr/publication/2019LYSEI129/these.pdf
© [S. Rodichkina], [2019], INSA de Lyon, tous droits réservés

c-Si as a function of free electron concentration at $T = 500$ and 900 K. As can be seen from the figure, the Seebeck coefficient for c-Si reaches a maximum at $N \sim 10^{15}$ cm^{-3} at 500 K and $N \sim 10^{18}$ cm^{-3} at 900 K. The maximum of the more relevant power factor occurs at huge electron concentrations of about $1 * 10^{21}$ cm^{-3}. This is related to the strong increase in the electrical conductivity of c-Si with increasing free charge carrier concentration. Considering the linear dependence of the Seebeck coefficient on temperature for highly-doped c-Si [42], one can extrapolate the maximal power factor for c-Si at $T = 300$ K, and it is about 14 mW m^{-1} K^{-1} for the doping level of about $1 * 10^{21}$ cm^{-3}. The maximum of ZT can be shifted to lower electron concentrations due to the increase in electronic thermal conductivity with free charge carrier concentration.

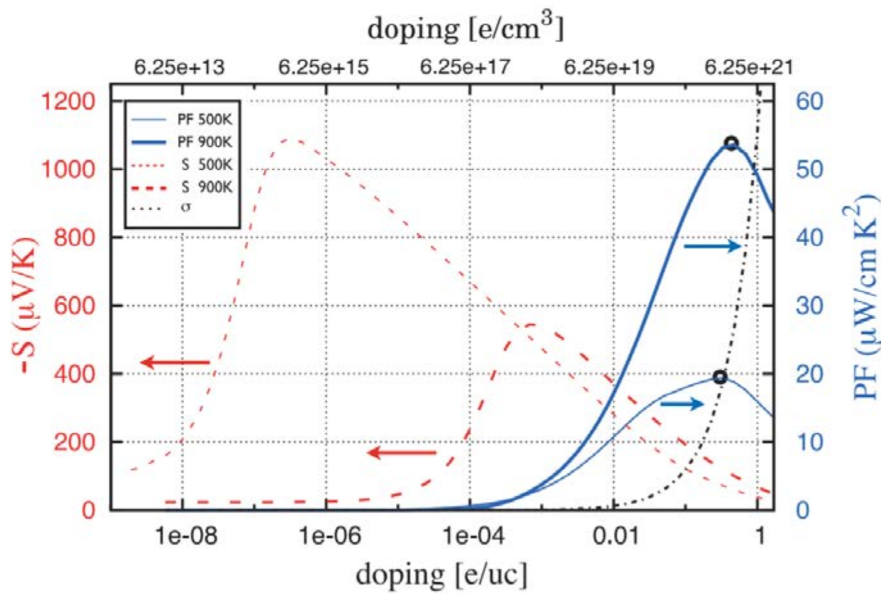

Figure 1.42: Seebeck coefficient (red dashed lines, refer to left scale, red units) and power factor (blue solid lines, refer to right scale, blue units) for electron-doped silicon in dependence on the doping level. The doping dependence of the electrical conductivity is given as a dashed–dotted line in arbitrary units. The maxima of the power factor are marked by black open circles [42].

Fig. 1.41 (b) shows the values of ZT for the same c-Si samples, as in Fig. 1.41 (a), ZT was calculated using Eq. (1). ZT of highly-doped c-Si samples exhibits an increase with temperature in the studied temperature range of 350-700 K. This fact can be attributed to the temperature decrease of thermal conductivity of c-Si due to the enhancement of the phonon scattering. At that, the electrical conductivity of highly-doped c-Si also decreases with temperature (see Sec. 1.4), which leads to a decrease in ZT. The Seebeck coefficient of highly-doped c-Si is almost independent of temperature. Higher doping concentrations in both p-type and n-type c-Si lead to higher values of ZT, the optimal doping concentration for c-Si is higher than the studied ones,

Cette thèse est accessible à l'adresse : http://theses.insa-lyon.fr/publication/2019LYSEI129/these.pdf
© [S. Rodichkina], [2019], INSA de Lyon, tous droits réservés

and it is expected to be of the order of 10^{20} cm^{-3} [41]. Low-doped c-Si samples ($N \sim 10^{14}$ cm^{-3}) exhibit ZT of the order of 10^{-6}, almost independent of temperature. Highly-doped c-Si samples ($N \sim 10^{19}$ cm^{-3}) exhibit ZT of 0.01-0.02 at room temperature. Considering the 2 order of magnitude drop of thermal conductivity for SiNWs [7] and bulk-like electrical properties, one can expect ZT = 1-2 at $T = 300$ K for highly-doped SiNWs, which is close or even higher than that for commonly used bismuth chalcogenides (ZT = 0.8-1.0) [118].

c) Thermoelectric properties of SiNWs

Fig. 1.43 shows the Seebeck voltage as a function of temperature difference for highly-doped n- and p-type SiNWs. The dopant concentration in both n- and p-type SiNWs is of $1.0 * 10^{20}$ cm^{-3}, the electrical resistivity is of 1.1 and 1.2 mΩ*cm for n- and p-type SiNWs, correspondingly [38]. The determined Seebeck coefficient is of -0.13 and 0.14 mV/K, and the corresponding power factor is of 1.46 and 1.66 mW·m^{-1}·K^{-2} for n- and p-type SiNWs, respectively. The size effects for electrical properties of investigated SiNWs can be neglected since their diameter is 50 nm (see Sec. 1.4). Lower values of the Seebeck coefficient for SiNWs than for c-Si, shown in Fig. 1.41 (a) can be attributed to higher doping levels of SiNWs.

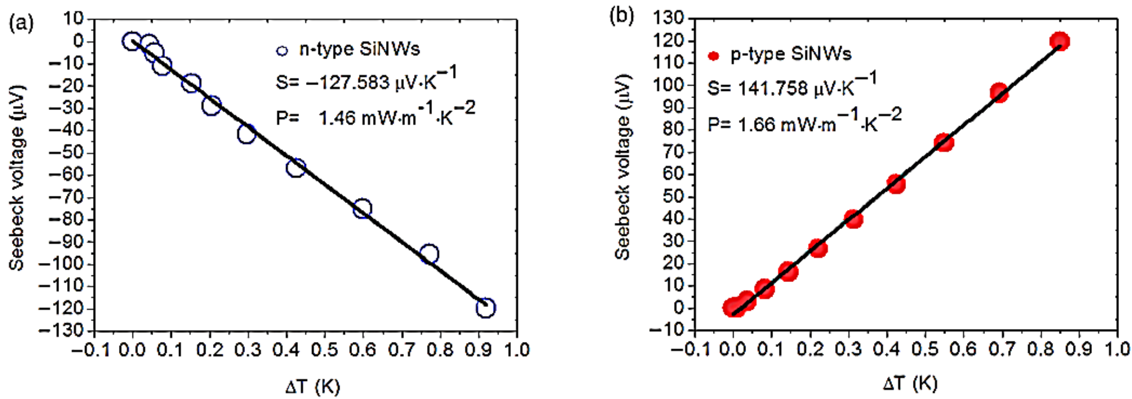

Figure 1.43: Seebeck voltage as a function of temperature difference. (a) Seebeck coefficient and power factor are of -0.13 mV/K and 1.46 mW·m^{-1}·K^{-2}, respectively for n-type SiNWs. (b) Seebeck coefficient and power factor are of 0.14 mV/K and 1.66 mW·m^{-1}·K^{-2}), respectively for p-type SiNWs [38].

Fig. 1.44 shows the power factor and ZT of individual SiNWs. SiNWs, which have p-type doping, diameter of 48 nm and electrical conductivity of 1.7 mΩ*cm, exhibit $S = 0.24$ mV/K and $S^2\sigma = 3.3$ mW·m^{-1}·K^{-2}. The thermal conductivity coefficient of similar 52 nm doped SiNWs is of 1.6 ± 0.13 W/(m*K) [7]. The electronic thermal conductivity of such SiNWs, calculated using the Wiedemann–Franz law (Eq. (1.9)), is 0.4 W/(m*K), so that the lattice thermal conductivity is 1.2 W/(m*K). Note, that doped SiNWs has a slightly lower thermal

Cette thèse est accessible à l'adresse : http://theses.insa-lyon.fr/publication/2019LYSEI129/these.pdf
© [S. Rodichkina], [2019], INSA de Lyon, tous droits réservés

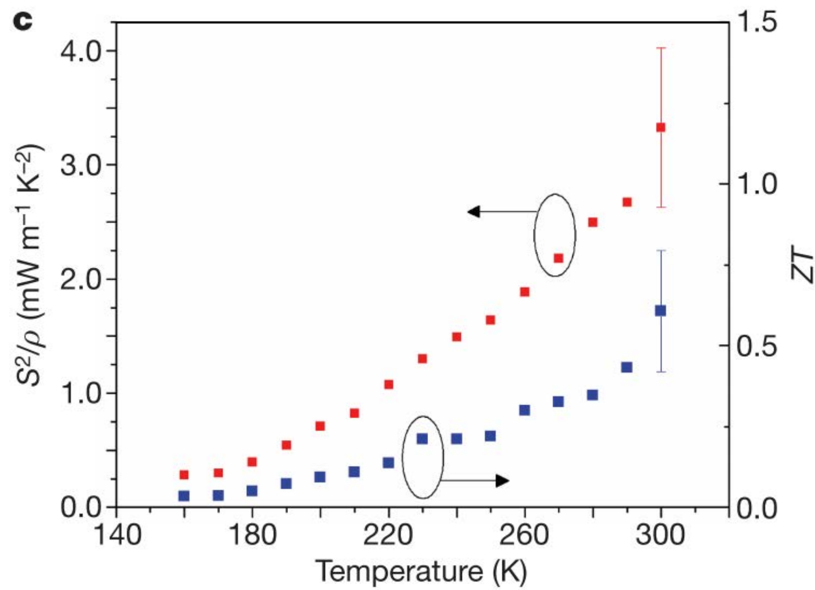

Figure 1.44: Single SiNWs power factor (red squares) of 48 nm nanowire and calculated ZT (blue squares) using the measured *k* of 52 nm nanowire [7].

conductivity coefficient than undoped ones, which was attributed to the higher rates of phonon-impurity scattering [7]. Thermoelectric figure of merit of such SiNWs is of about 0.7, which is essential for thermoelectric applications of SiNWs. It is possible that the values of ZT in SiNWs can be increased by increasing the doping level of SiNWs (see Fig. 1.42). Also, for practical applications, the fabrication techniques to produce the SiNWs arrays with high average ZT are required.

1.6 Thermal and electrical properties of hexagonal diamond silicon

This section presents the available data on thermal and electrical properties of bulk hex-Si and hex-SiNWs. The reported data for hex-Si are comapred to those for cub-Si, and the potential of hex-Si phase is estimated. However, the properties of hex-Si are poorly investigated due to the difficult fabrication of hex-Si phase (see Sec. 1.1).

Fig. 1.45 shows the calculated thermal conductivity of cub-Si and hex-Si crystalline phases of Si for bulk materials and SiNWs. For the calculations, the density-functional theory was used to determine the second and third order interatomic force constants, and full linearized Boltzmann transport equation within the relaxation time approximation was used to calculate the thermal conductivity coefficient. One can see that the thermal conductivity of hex-Si is about 2

Cette thèse est accessible à l'adresse : http://theses.insa-lyon.fr/publication/2019LYSEI129/these.pdf
© [S. Rodichkina], [2019], INSA de Lyon, tous droits réservés

times lower than that of cub-Si both in bulk and SiNWs. The ratio of the thermal conductivity between hex-Si and cub-Si is slightly dependent on NW diameter and temperature.

This strong suppression of thermal conductivity in hex-Si is at first sight surprising, since the only difference between cub-Si and hex-Si is the atom stacking along the [111] crystal axis [43]. It was suggested that the lower thermal conductivity of hex-Si phase compared to cub-Si phase is a general feature of cubic vs hexagonal polytypes, which can be attributed to the strong acoustic-acoustic-optical three-phonon scattering involving $8-11$ THz optical phonons, which are not present in cub-Si.

Considering the electrical properties of hex-Si phase of Si, from the first-principle calculations performed in the density-function theory framework, it was shown that the effective electron mass in hex-Si is about 5 times smaller than in cub-Si ans can be further reduced under uniaxial compression. The small effective electron mass in hex-Si would lead to higher electron mobility, compared to cub-Si phase, and consequently to higher electrical conductivity.

Thus, the theoretical study shows that hex-Si phase can have better thermoelectric properties than cub-Si phase, therefore the creation of hex-Si phase in SiNWs is interesting for thermoelectric applications of SiNWs.

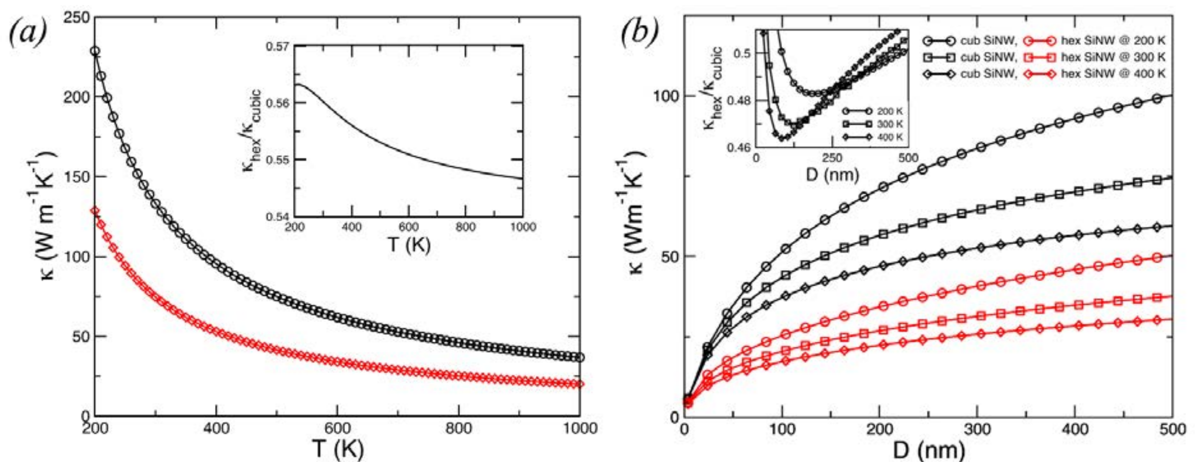

Figure 1.45: (a) Thermal conductivity of bulk cub-Si (circles) and hex-Si (diamonds) as a function of temperature. (b) Thermal conductivity of cun-Si (black lines) and hex-Si (red lines) SiNWs as a function of their diameter at $T = 200$, 300 and 400 K. Insets: ratio of the thermal conductivity between hexagonal and cubic NWs [43].

Cette thèse est accessible à l'adresse : http://theses.insa-lyon.fr/publication/2019LYSEI129/these.pdf
© [S. Rodichkina], [2019], INSA de Lyon, tous droits réservés

1.7 Conclusions to the state of the art

In view of the general motivation of this PhD project, which is the application of SiNWs arrays in thermoelectricity, we reviewed the fabrication, structural, thermal and electrical properties of SiNWs. The following conclusions regarding the fabrication and properties of SiNWs, as well as the insufficiently investigated problems, were made.

a) Fabrication of SiNWs arrays by MACE

The arrays of single crystalline SiNWs with diameter of about 100 nm and length $\sim 10\ \mu$m, required for thermoelectricity, were formed by the Ag-assisted chemical etching of c-Si substrates. It is a low-cost method, which allows large-area fabrication and versatile control of SiNWs morphology. SiNWs arrays fabricated by Ag-assisted MACE represent quasi-one-dimensional structures, since nanowires in the array are interconnected. At that, lateral thermal and electrical transport in such SiNWs arrays is strongly suppressed compared to that along SiNWs.

The diameter and length of SiNWs were controlled by the $AgNO_3$ concentration and etching time, respectively. The porosity of SiNWs for a given c-Si substrate was dependent on the H_2O_2 concentration in the etching solution. However, various parameters including the concentration of $AgNO_3$, HF and H_2O_2 were shown to affect the morphology of resulting SiNWs, that should be taken into account for SiNWs fabrication. SiNWs had a rough surface, which was explained by the Ag redeposition during the MACE, hole diffusion from the metal-covered areas and stain etching of SiNWs. The pore formation during MACE increased with the doping level of the c-Si substrate, and porous SiNWs are formed on c-Si wafers with $N \sim 10^{18}$ cm^{-3} or higher.

Thus, highly-doped non-porous SiNWs with rough surface, which are preferable for thermoelectricity, can not be formed by MACE of highly-doped c-Si. To overcome this limitation, the low-doped SiNWs can be formed and then additionally doped using ex-situ doping techniques.

b) Post-fabrication doping of SiNWs using spin-on dopants

The prospective method for the post-fabrication doping of SiNWs arrays is the thermal diffusion of dopant atoms from spin-on dopant solutions. This method was applied to MACE- and VLS-SiNWs arrays, and the boron concentrations in SiNWs up to $\sim 10^{19} \div 10^{20}$ cm^{-3} were achieved. The control of the doping level of SiNWs was performed by varying the annealing temperature from 800 to 1000 ^{0}C, which allowed to obtain the boron concentrations in SiNWs in the range

Cette thèse est accessible à l'adresse : http://theses.insa-lyon.fr/publication/2019LYSEI129/these.pdf
© [S. Rodichkina], [2019], INSA de Lyon, tous droits réservés

from 10^{18} to 10^{20} cm^{-3}. The uniform in-depth doping profiles were observed for SiNWs arrays up to the depths of about 1 μm, limited by the nanowire length.

It was shown that SOD doping procedure does not affect the crystallinity of SiNWs. The diameter of SiNWs was slightly reduced due to the formation of silicon oxide on the surface during the doping procedure. The maximum free charge carrier concentration in SiNWs is limited by the dopant solid solubility limit at the annealing temperature used. Boron and phosphorus solid solubility limit for the typical annealing temperature of 1000 ^{0}C is of about $4 * 10^{20}$ and $1 * 10^{21}$ cm^{-3}, correspondingly.

Despite the fact that SOD doping procedure was successfully applied for SiNWs arrays, the influence of the SiNWs morphology and annealing parameters on the doping level of SiNWs, as well as its homogeneity along SiNWs with length $\sim$10 μm was not investigated.

c) Fabrication of highly-doped SiNWs arrays by other techniques

Other common techniques for the fabrication of the arrays of highly-doped SiNWs are the VLS growth and RIE. In the VLS method, highly-doped SiNWs are obtained using the dopant-containing gas in the synthesis, so that dopant atoms are incorporated into SiNWs during the growth. In the RIE method, highly-doped SiNWs are obtained by RIE of highly-doped c-Si wafers. Arrays of single crystalline SiNWs with controlled diameter and length can be obtained by both VLS synthesis and RIE. VLS- and RIE-SiNWs have smooth surface, which is not preferable for thermoelectric applications due to higher thermal conductivity than in the case of SiNWs with rough surface. Both VLS and RIE techniques have a high cost, compared to MACE.

Another common ex-situ doping technique, which was applied to SiNWs, is the ion implantation. Ion implantation initially leads to the amorphization of SiNWs, and the crystalline structure of SiNWs was recovered using the high-temperature annealing at about 1000 ^{0}C. Despite the fact, that single-crystalline SiNWs with high concentration of 10^{20} cm^{-3} were obtained using the ion implantation doping method, the ion implantation at such a high doses can lead to the formation of polycrystalline SiNWs, that should be taken into account. Also, the ion implantation method was reported to be inefficient for SiNWs arrays due to inhomogeneous doping. The ion implantation technique has a high cost, compared to the SOD doping technique.

d) Hexagonal diamond SiNWs

One of the possible ways to increase the thermoelectric characteristics of SiNWs is to use Si polymorphs. Among them, the most promising is hexagonal diamond silicon. Theoretical

Cette thèse est accessible à l'adresse : http://theses.insa-lyon.fr/publication/2019LYSEI129/these.pdf
© [S. Rodichkina], [2019], INSA de Lyon, tous droits réservés

calculations predicted lower thermal conductivity and lower electron effective mass in hex-SiNWs compared to cub-SiNWs. VLS technique was adapted to synthesize hex-SiNWs, which were stable at the room temperature. Bulk cub-Si can undergo a phase transition into hex-Si under high pressures ($>$ 11 GPa) at $T = 300K$ with subsequent annealing above 470 K. The cubic-to-hexagonal crystalline lattice transformation was reported for Si nanoparticles under intense photoexcitation.

e) Thermal properties of SiNWs

Thermal conductivity of SiNWs was shown to be 1-2 orders of magnitude lower than that of c-Si. The square root dependence of the thermal conductivity for SiNWs with smooth surface on their diameter was observed at room temperature. The optimum diameter of SiNWs for thermoelectricity is of 50-100 nm, it represents the minimum nanowire diameter, for which the electrical proprieties of SiNWs are not affected by the surface. The measured thermal conductivity ($T = 300$ K) for SiNWs with the smooth surface and diameter of 50 and 100 nm was of 20 and 40 W/(m*K), correspondingly, that was associated with the additional diffuse scattering of phonons at SiNWs surface. For c-Si, the thermal conductivity is of 150 W/(m*K).

SiNWs with rough surface, fabricated by MACE, exhibit further decrease in thermal conductivity, compared to SiNWs with smooth surface, from $\sim$ 10 W/(m*K) to $\sim$ 1 W/(m*K). The thermal conductivity of SiNWs with rough surface (rms $\approx$ 3 nm) and diameter of 50 and 100 nm was of about 2 and 8 W/(m*K), respectively. An increase in the surface roughness rms was predicted to lead to a decrease in SiNWs thermal conductivity. The high doping (boron) level ($\approx 10^{19}$ cm^{-3}) was shown to reduce the thermal conductivity of SiNWs with diameter of 50 nm from 2 to 1.6 W/(m*K). Similarly to c-Si, this fact was explained by the effect of phonon-impurity scattering. The ratio between the thermal conductivity for SiNWs and c-Si with similar doping level was of 0.013. The electron contribution to the thermal conductivity for highly-doped SiNWs with $N \sim 10^{19}$ cm^{-3} was estimated of about 0.4 W/(m*K).

The low values of thermal conductivity for highly-doped bulk core/rough surface SiNWs, fabricated by MACE, are close to that of amorphous silicon, which is crucial for thermoelectric applications of SiNWs in accordance with the concept of "phonon-glass electron-crystal". While the thermal properties of individual low-doped VLS- and MACE-SiNWs have been studied in detail, the thermal conductivity of arrays and individual highly-doped SiNWs has not been sufficiently investigated.

Cette thèse est accessible à l'adresse : http://theses.insa-lyon.fr/publication/2019LYSEI129/these.pdf
© [S. Rodichkina], [2019], INSA de Lyon, tous droits réservés

f) Electrical properties of silicon nanowires

Highly-doped SiNWs ($N > 10^{19}$ cm^{-3}) with diameter of more than 50 nm exhibit the electrical conductivity close to that for c-Si with the same dopant concentration, that implies that free charge carrier transport in such SiNWs can be considered the same as in c-Si. For moderately-doped SiNWs ($N \sim 10^{18}$ cm^{-3}), the effect of nanowire diameter on the electrical conductivity is sufficient for SiNWs diameter less than about 70 nm. This fact was explained by the effect of the interface states and trapped charges, which cause a depletion zone at the nanowire surface. The thickness of the depletion zone decreases with the doping level in a nanowire.

The electrical conductivity of SiNWs with diameter less than 50 nm was observed to decrease with a decrease in nanowire diameter, which was explained by an increase in the impurity ionization energy in SiNWs due to dielectric mismatch, that reduces the free charge carrier concentration in SiNWs. At that, the effect of surface scattering on the charge carrier mobility was observed for SiNWs diameter less than 20 nm. The nanowire size has a stronger effect on the thermal conductivity of SiNWs than on electrical conductivity due to a shorter mean free path of electrons than that of phonons.

The low electrical receptivity of about 1-2 mΩ*cm were achieved for both VLS- and MACE-SiNWs. As in the case of thermal properties, the electrical resistivity was studied mainly for individual SiNWs, while SiNWs arrays are insufficiently investigated.

g) Thermoelectric performance of SiNWs

Highly n-type doped c-Si with $N = 1.4 * 10^{19}$ cm^{-3} and p-type doped c-Si with $N = 8.1 * 10^{19}$ cm^{-3} have ZT of about 0.01 and 0.02 at room temperature, respectively. The observed values of ZT can be increased by increasing the doping level of c-Si. It was calculated, that the maximum of the power factor ($S^2\rho$) for n-type doped c-Si was occurs at $N \approx 1 * 10^{21}$ cm^{-3} for $T = 500 - 900$ K. Considering the two order of magnitude drop of thermal conductivity for SiNWs and bulk-like electrical properties, one can expect ZT = 1-2 at $T = 300$ K for highly-doped SiNWs, which is close or even higher than that for commonly used bismuth chalcogenides (ZT = 0.8-1.0). Considering the estimated maximum power factor for c-Si at $T = 300$ K of 14 mW m^{-1} K^{-2} and SiNWs thermal conductivity of 1.6 W/(m*K), the maximum ZT for SiNWs can be estimated of about 3.

The Seebeck coefficient for individual SiNWs at $T = 300$ K was reported to be close to that for c-Si with the same doping level. The calculated thermoelectric figure of merit for

Cette thèse est accessible à l'adresse : http://theses.insa-lyon.fr/publication/2019LYSEI129/these.pdf
© [S. Rodichkina], [2019], INSA de Lyon, tous droits réservés

individual SiNWs with electrical conductivity of 1.7 mΩ*cm was of about 0.6, which can be further increased by increasing the doping level in SiNWs. For the practical applications, the SiNWs arrays with high average ZT should be fabricated.

h) Characterization of SiNWs

Characterization of the morphology and structural properties of SiNWs is traditionally performed using the SEM and TEM (HRTEM) microscopy. The non-destructive characterization of the crystalline lattice for c-Si and SiNWs arrays using the Raman spectroscopy was shown, that allowed us to distinguish between the amorphous phase, cubic diamond and hexagonal diamond crystalline phases of silicon.

Characterization of thermal and electrical properties of SiNWs was performed mainly by direct methods, similar to those for bulk Si. The contacts were nanofabricated to the individual SiNWs, and the thermal and electrical conductivity was measured. The dopant concentration in SiNWs arrays was studied by the SIMS method, however in SiNWs the dopant concentration can be not equal to the free charge carrier concentration due to donor deactivation. Thus the contactless methods for characterization of SiNWs arrays are of high importance for the development and application of SiNWs-based thermoelectric devices.

1.8 Statement of the research tasks for PhD thesis

Considering the state of the art for fabrication techniques and electrical and thermal properties of SiNWs, the following problems for the PhD thesis were set:

1. Fabricate the arrays of SiNWs with nanowire diameter of about 100 nm, length $\sim 10\ \mu$m and bulk core/rough surface morphology of nanowires, using the metal-assisted chemical etching.
2. Investigate the crystalline structure of SiNWs by means of Raman spectroscopy and examine the photoinduced lattice transformation in SiNWs from cubic diamond to hexagonal diamond Si.
3. Develop the optical techniques, i.e. infrared and Raman spectroscopy, to monitor the free charge carriers in SiNWs.
4. Optimize the spin-on dopant post-fabrication doping technique for SiNWs arrays to obtain a homogeneous in-depth doping profile in SiNWs with $N \sim 10^{20}$ cm^{-3}.

Cette thèse est accessible à l'adresse : http://theses.insa-lyon.fr/publication/2019LYSEI129/these.pdf
© [S. Rodichkina], [2019], INSA de Lyon, tous droits réservés

5. Determine the electrical conductivity of highly-doped SiNWs by means of the optical and electrical measurements.
6. Determine the thermal conductivity of low- and highly-doped SiNWs by using the Raman scattering spectroscopy.
7. Evaluate the potential of highly-doped SiNWs arrays, fabricated by metal-assisted chemical etching, as a thermoelectric material.

Cette thèse est accessible à l'adresse : http://theses.insa-lyon.fr/publication/2019LYSEI129/these.pdf
© [S. Rodichkina], [2019], INSA de Lyon, tous droits réservés

Chapter 2
Materials and methods

2.1 Fabrication of silicon nanowires

2.1.1 Metal-assisted chemical etching

High aspect-ratio SiNWs were obtained by MACE of low and moderately boron (p-type) doped (100)-oriented c-Si wafers with the specific resistivity ranged from 50 to 0.1 Ω*cm. Macroporous Si samples were obtained by MACE of low phosphorus (n-type) doped (100)-oriented c-Si wafers with the specific resistivity of 1-10 Ω*cm. MACE procedure was implemented in two steps. At the first step, the c-Si substrates were immersed in an aqueous solution containing 5 – 10 mM of $AgNO_3$ and 2.4 – 4.8M HF for 25 sec. At the second step, the c-Si wafers with Ag nanoparticles were etched in an aqueous solution containing 4.8 – 9.6M HF and 0.3 – 0.9M H_2O_2 for 5 – 60 min. To remove residual Ag particles, the samples were dipped in concentrated nitric acid, i.e. 65% HNO_3, for 15 min and then they were rinsed in de-ionized water and dried in air.

The diameter of SiNWs was controlled using the different concentration of $AgNO_3$, and it was in the range from 50 to 300 nm. The length of SiNWs was varied from 4 to 27 μm by increasing the etching time from 5 to 60 min. To vary the surface roughness of SiNWs, the different concentrations of H_2O_2 in the etching solution were used. The doping level in SiNWs was varied by post-fabrication doping.

Table 2.1: The parameters of MACE procedure used to obtain high aspect ratio SiNWs.

MACE	**[$AgNO_3$]** (mM)	**[HF]** (M)	**[H_2O_2]** (M)
I	10	4.8	0.9
II	5	9.6	0.3

Table 2.1 shows the parameters of MACE procedures used for fabrication of SiNWs arrays. MACE-I is a common procedure used for SiNWs fabrication [119, 120], MACE-II was optimized

Cette thèse est accessible à l'adresse : http://theses.insa-lyon.fr/publication/2019LYSEI129/these.pdf
© [S. Rodichkina], [2019], INSA de Lyon, tous droits réservés

to obtain high aspect ratio SiNWs [4]. To remove the surface silicon oxide from SiNWs walls after the MACE, samples were placed in an aqueous solution of [HF (48%) : C_2H_5OH] = 9:1 for 10 min.

2.1.2 Post-fabrication doping

Post-fabrication doping of SiNWs was performed by the thermally activated diffusion of dopant atoms into SiNWs from the spin-on dopant (SOD) solutions. The applied SOD doping procedure consisted of the following steps:

(a) Deposition of the spin-on dopant solution. A drop of about 0.1 ml of the SOD solution (Borofilm (p-type) or Phosphorofilm (n-type), Emulsitone Chemicals, LLC) was applied to the surface of SiNWs samples. Then the spin-coating of SOD at 3000 rpm for 30 s was performed to obtain the thin SOD layer on the surface of SiNWs samples. To obtain the thick SOD layer, the spin-coating step was avoided.

(b) Post-spin baking at the temperatures of about 200 ^{0}C for 10 min to remove excess solvent. At this step, the spin-coating and post-spin baking procedures could be applied for several times to increase the thickness of the deposited SOD layer.

(c) High-temperature annealing. The high-temperature annealing activates the diffusion of dopant atoms from SOD film into SiNWs. The annealing was performed using the rapid thermal annealing (RTA) device or the oven. The annealing temperatures were varied in the range from 900 to 1000 ^{0}C, the annealing time was varied from 5 s to 5 min. The annealing was performed in the nitrogen (N_2) atmosphere.

After the annealing the rest SOD film, as well as surface silicon oxide, were removed in an aqueous solution of [HF (48%) : C_2H_5OH] = 9:1 for 10 min.

The standard SOD doping procedure consisted in the spin-coating and post-spin baking of the SOD solution with the following annealing in RTA furnance for 15 s (maximum temperature of 950 ^{0}C).

2.1.3 Investigated samples

Investigated samples represented undoped and doped por-Si layers and SiNWs arrays with the length of 4-27 μm and diameter of 50-300 nm. SiNWs possesed bulk core/rough surface nanostructure and had nearly uniform diameter. Porosity of SiNWs arrays was of about 75 %.

Cette thèse est accessible à l'adresse : http://theses.insa-lyon.fr/publication/2019LYSEI129/these.pdf
© [S. Rodichkina], [2019], INSA de Lyon, tous droits réservés

Initial SiNWs were p-type (boron) doped, and highly-doped SiNWs were additionally doped with boron (p-type) or phosphorus (n-type). The doping level for low-doped SiNWs was of the order of $10^{14} - 10^{15}$ cm^{-3}, for highly-doped SiNWs it was varied in the range from $5 * 10^{18}$ to $3 * 10^{20}$ cm^{-3} both for p- and n-type impurities.

The summary for the investigated samples is given in Table 2.2.

Table 2.2: Investigated samples, their morphology and doping parameters. *D* is the diameter and *L* is the length of nanowires in SiNWs array, *N* is the free charge carrier concentration. MACE column refers to the MACE procedure from Table 2.1, used for SiNWs fabrication.

Sample	**Substrate** (100) c-Si, ρ (Ω*cm)	**MACE**	*D* (nm)	*L* (μm)	**Dopants** (initial/ doping)	*N* (10^{19} cm^{-3}) after doping
SiNWs-A	1-10	I	100-300	4; 8; 15; 22	B/ B	4.2-10.6
SiNWs-B	1-10	I	100-300	4; 8; 15	B/ P	0.2-5
SiNWs-C	40-50	II	50-100	10; 21; 25; 27	B/ B	1-30
por-Si-A	1-10	I	100-1000	5; 15; 20	P/ P	1.3-3.4

2.2 Characterization of silicon nanowires

Structural properties of SiNWs were investigated by scanning and transmittance electron microscopy and by Raman spectroscopy. Electrical properties of SiNWs were investigated by infrared and Raman spectroscopy and by two-probe electrical measurements. Thermal properties of SiNWs were investigated by Raman spectroscopy.

2.2.1 Scanning electron microscopy

Scanning electron microscopy (SEM) is used to obtain images of SiNWs using a focused electron beam. The resolving power of the microscope is fundamentally limited by the wavelength of electrons or light used for illumination. While the visible light has wavelengths from 400 to 700 nm, electrons have much shorter wavelengths (e.g. $\sim 10^{-12}$ m at 30 keV), enabling better resolution. Practically, the resolution of SEM is limited to about 20 nm due to the objective lens system in electron microscopes [121].

The main components of SEM microscope include source of electrons, column down which electrons travel with electromagnetic lenses, electron detector, sample chamber and computer to view the images. Electrons are produced at the top of the column, accelerated down and focused

Cette thèse est accessible à l'adresse : http://theses.insa-lyon.fr/publication/2019LYSEI129/these.pdf
© [S. Rodichkina], [2019], INSA de Lyon, tous droits réservés

on the sample surface by a combination of lenses and apertures. The sample chamber and the column are usually evacuated. The position of the electron beam on the sample is controlled by scan coils situated above the objective lens, which enables the electron beam to scan the surface of the sample and produce an image of a defined area of the sample [122].

SEM produces images by scanning the sample with a high-energy beam of electrons. As the electrons interact with the sample, a number of signals are produced. These signals include secondary electrons, backscattered electrons, and characteristic X-rays. The topography of the sample is obtained using the secondary electrons. Secondary electrons occur due to inelastic interactions between the primary electron beam and the sample and have energies lower than that of primary electrons. The mean free path length of secondary electrons in many materials is about 10 Å. Thus, although the secondary electrons are generated throughout the region excited by the incident beam, only those electrons that originate less than 10 Ådeep in the sample are detected. This volume of production is very small compared with backscattered electrons and X-rays. Therefore, the resolution using secondary electrons is better than either of these and is effectively the same as the electron beam size. The secondary electron yield depends on many factors, and is generally higher for high atomic number targets, and at higher angles of incidence. [123]

Backscattered electrons occur due to elastic collisions of electrons with atoms, which causes a change in the electrons trajectory. They originate from a wide region within the interaction volume. The number of the backscattered electrons reaching the detector increases with the atomic number of atoms of the sample under the beam. The dependence of the number of backscattered electrons on the atomic number is used to obtain information on the sample composition [124].

2.2.2 Transmission electron microscopy

Transmission electron microscopy (TEM) is a major technique for characterization of the nanostructure morphology. By forming a nanometer-size electron probe, TEM is unique in identifying and quantifying the chemical and electronic structures of individual nanocrystals [125]. TEM is a microscopy technique in which a focused beam of energetic electrons is transmitted through the sample in the very high vacuum chamber, and the interaction of electrons with the sample forms an image [125, 126]. The image is then magnified and focused onto an imaging device, such as a charge coupled device. TEM image contrast is due to differential

Cette thèse est accessible à l'adresse : http://theses.insa-lyon.fr/publication/2019LYSEI129/these.pdf
© [S. Rodichkina], [2019], INSA de Lyon, tous droits réservés

absorption of electrons by the material due to differences in its composition or thickness. An improvement to TEM is high-resolution transmission electron microscopy (HRTEM). This provides imaging of the crystallographic structure of a sample.

2.2.3 Infrared spectroscopy

Infrared (IR) spectroscopy is the vibrational technique for nanostructure characterization which consists in measuring the transmittance/reflectance spectra of samples in the IR range. IR absorption/reflection spectrum depends on the vibrational levels of the sample, IR light being absorbed due to excitation of these vibrations by electromagneitc wave. Conventional dispersive infrared spectrometers have been replaced by Fourier-transform infrared equipment, which incorporates a Michelson interferometer and presents a series of advantages over dispersive systems, such as an improvement of energy and the simultaneous measurement of the wide spectral range [127].

There exist different techniques for IR spectroscopy [128]. The classical one is the transmittance spectroscopy, in which the sample is placed in the beam path of the infrared spectrometer, and the transmitted light is analyzed in relation to the incident radiation. The spectra of the absorption coefficient of the sample are calculated from the transmittance spectra according to the Beer-Lambert law: $\alpha = -ln(I/I_0)/d$, where α is the absorption coefficient of the sample, I_0 and I are the intensities of the incident and transmitted light, correspondingly, d is the thickness of the sample. Another technique is the specular reflectance IR spectroscopy, which uses the light falling at the sample at small angles of incidence to measure the reflectance spectra of a sample. This technique is especially important for opaque samples, where the classical transmittance technique can not be applied. Attenuated total reflectance (ATR) technique can be used as an alternative for the transmittance technique for opaque samples. In ATR mode, the IR beam is directed through and internal reflection element (e.g. Ge crystal) with a high index of refraction. The IR light is totally reflected internally of the back surface of Ge crystal, which is in contact with the sample. To observe the total reflectance, the sample refraction coefficient should fulfill the condition $n < n_{Ge} sin\theta$, where n is the refraction coefficient of the sample, n_{Ge} is the refraction coefficient of Ge prism, θ is the angle of light incidence. At total reflection, the transmitted wave inside the sample represents an evanescent wave, which travels along the Ge crystal/sample interface with an amplitude that decreases exponentially with the distance from the sample surface [129]. If the sample is transparent ($\alpha = 0$) and the condition of total

Cette thèse est accessible à l'adresse : http://theses.insa-lyon.fr/publication/2019LYSEI129/these.pdf
© [S. Rodichkina], [2019], INSA de Lyon, tous droits réservés

reflectance is fulfilled, the ATR signal close to 1 will be observed. If at the given wavelength the light is absorbed at vibrational level of the sample ($\alpha > 0$), the evanescent transmitted light is absorbed inside the sample, and the absorption peaks in ATR spectra are observed ($R < 1$), that resemble those observed for transmittance spectra.

IR spectra were measured using a Bruker Vertex 70/80 Fourier-transform infrared spectrometer in the reflectance and ATR mode using a single-reflection germanium (Ge) prism (45^0). For the ATR measurements, the mechanical contact between SiNWs sample and ATR (Ge) crystal was applied until the following enhancement did not produce any change in measured spectra.

2.2.4 Raman spectroscopy

Raman spectroscopy is a spectroscopic technique based on inelastic scattering of monochromatic light. When the sample is irradiated with monochromatic light (laser), the spectrum of scattered light contains a line at initial laser frequency (elastic Rayleigh scattering) and at other frequencies (inelastic scattering), which occur due to interaction of light with matter. This phenomenon is called the Raman effect.

Since the scattered light is due to interaction with matter the Raman spectrum provides the information about the matter. In crystalline nanostructures, the interaction of light with optical phonons is studied. Raman spectra in applications to silicon nanostructures can provide a non-destructive probe of chemical structure, crystallinity, size, temperature, impurity atoms free charge carriers electron properties, thermal and electrical transport, surface, intrinsic stress/strain. In combination with mapping Raman spectroscopy can provide a spatial distribution of the above parameters. Raman spectroscopy can be used for microscopic analysis, with a spatial resolution in the order of 0.5-1 μm. Such analysis is possible using a Raman microscope [130].

The Raman scattering in silicon and other crystals can be considered as an interaction of light with optical phonons of a crystal. The incident phonon is "absorbed" and takes system to a virtual level then the light is re-emitted at other frequency. If the energy of scattered photon energy is less that of incident one (due to creation of phonon), the scattering process is designated as 'Stokes', if the photon energy increases (due to absorption of phonon), the scattering process is designated as 'anti-Stokes'.

The systems to used to investigate the inelastically scattered light consist of one or more monochromatic light sources (lasers), microscope lenses (to focus the light onto the sample and to collect the scattered light), filters (to exclude the reflected and elastically scattered light),

Cette thèse est accessible à l'adresse : http://theses.insa-lyon.fr/publication/2019LYSEI129/these.pdf
© [S. Rodichkina], [2019], INSA de Lyon, tous droits réservés

diffraction grating to resolve the spectrum, very sensitive detector (to detect the weak light), computer to control the whole system and display the spectrum. Laser wavelengths used range from ultra-violet through visible to near infra-red. The choice of the laser wavelength has an important impact on experimental capabilities, such as sensitivity, spatial and spectral resolution, excitation depth and sample photoluminescence. In certain cases, sample photoluminescence carries useful information that can facilitate sample analysis and augment the Raman data, thus Raman microscopes can be used to analyze both Raman scattering and photoluminescence spectra of the samples.

Raman spectra were measured using a Horiba HR 800 spectrometer with excitation at 632.8 nm, a DFS-500 (LOMO, Russia) spectrometer with excitation at 514.5 nm and a LabRAM Aramis micro-Raman spectrometer under 473 nm excitation. The maximal laser intensity was of 15 kW/cm^2, the laser spot diameter was of 2-10 μm.

2.2.5 Photoluminescence spectroscopy

Photoluminescence (PL) spectroscopy is a characterization technique, which uses the light, or photons, to stimulate the emission of the photons from the material. It is a non-contact, nondestructive method for probing materials. In an emission process an electron (or possibly a quasi-particle) occupying an higher energy state makes a quantized (i.e. discrete) transition to an empty lower-energy state. For a radiative transition the energy difference between these two states is emitted as electromagnetic radiation, i.e. photons, whereas for non-radiative transitions, this energy difference is emitted in the form of heat, i.e. phonons [131].

Photoluminescence from semiconductors is most commonly characterized via spectroscopic techniques. These techniques involve measuring the energy distribution of emitted photons after optical excitation. To measure the PL spectra of Si materials, the sample is irradiated with a focused ultraviolet or visible laser, the PL light is collected by the lens system and analyzed using a monochromator and CCD camera. To measure the PL lifetime, the time-resolved measurements using a high speed detectors and ultra-low dead time electronics are performed [132]. Analysis of the PL spectra allows us to determine the material crystallinity, bandgap, defect types and concentrations, recombination mechanisms [131, 132]. For exapmple, the material bandgap can be determined from the spectral peak of the PL emission [133]. By combining Raman analysis with PL detection, it is possible to characterize both the vibrational and electronic properties of materials. A wide range of excitation wavelengths is possible, allowing control of the penetration

Cette thèse est accessible à l'adresse : http://theses.insa-lyon.fr/publication/2019LYSEI129/these.pdf
© [S. Rodichkina], [2019], INSA de Lyon, tous droits réservés

depth into the material, and thus, control of the volume sampled [132].

PL spectroscopy is usually used to measure the direct transitions, including band-to-band and free-to-bound recombination [131]. Indirect recombination processes, which involve the simultaneous emission of phonon(s) and a photon, are much less probable than the direct ones. Thus, since c-Si has indirect bandgap, the PL technique is not often used for its characterization due to weak photoluminescence [133]. PL spectroscopy is usually applied to study Si nanocrystals, which exhibit strong PL compared to c-Si, induced by quantum confinement [134]. The blue-shift of the PL emission with decreasing the size of nanocrystals is used to characterize the nanocrystal diameter distribution in the system [134]. The PL emission peak for c-Si represents a peak at about 1.1 eV, while the PL peak for Si nanocrystals is centered in the range from 1.2 to 2.0 eV when nanocrystal diameter ranges from 6 to 2 nm, correspondingly [134]. In highly-doped c-Si and Si nanocrystals the non-radiative Auger recombination should be additionally taken into account [131].

PL spectra were measured using a LabRAM Aramis micro-Raman spectrometer with 473 nm excitation and Mightex HRS spectrometer with 488 nm excitation.

2.2.6 Electrical resistance measurements

Four-point probe (4-wire sensing, or 4-terminal sensing) and two-point probe methods are the electrical impedance measuring techniques that uses separate pairs or combined current-carrying and voltage-sensing electrodes. The four-point probe method is more accurate than the simpler two-point probe sensing.

In 4-point method the electrical current is created by two extreme electrodes, and the potential drop is measured across two probes in the middle. The electrical resistivity is calculated as $\rho = VS/Id$, where V is the measured voltage, I is the electric current though the sample, S is the cross-section area of the sample, d is the distance between the middle electrodes. When the probes are not point contacts, the most accurate estimation of d is the distance between the centers of electrodes rather than the closest distance between them. 4-point method can eliminate the effects of contact resistance between the sample and electrical contacts and therefore is more accurate than 2-probe method [135].

Cette thèse est accessible à l'adresse : http://theses.insa-lyon.fr/publication/2019LYSEI129/these.pdf
© [S. Rodichkina], [2019], INSA de Lyon, tous droits réservés

Chapter 3
Structural properties of silicon nanowires

This section describes the fabrication of the arrays of high aspect ratio SiNWs with the diameter of about 100 nm and length $\sim 10\ \mu$m by Ag-assisted MACE. The morphology and crystallinity of SiNWs fabricated on c-Si substrates with different doping type and level is studied. The effect of the Ag redeposition during MACE on SiNWs morphology is emphasized. The morphology and crystallinity of SiNWs after the thermal annealing at about 1000 ^{0}C during the post-fabrication doping is investigated.

Further, the reversible photo-induced formation of hex-Si phase in initially cubic diamond MACE-fabricated SiNWs is reported. This effect was observed by means of micro-Raman spectroscopy. In particular, a key role of mechanical stresses in SiNWs emerging under a focused laser beam is emphasized to be responsible for the hex-Si phase formation. Finally, a huge enhancement of photoluminescence level for the SiNWs with hexagonal polytype regions is demonstrated.

3.1 Fabrication of SiNWs arrays by metal-assisted chemical etching

3.1.1 Morphology and crystalline structure of initial SiNWs

Fig. 3.1 shows SEM images of SiNWs, fabricated on low- and moderately-doped c-Si wafers by MACE-II procedure, optimized for high aspect ratio SiNWs. Boron (p-type) doped, (100)-oriented c-Si wafers with the specific resistivity of 40-50, 1-20 and 0.1-0.2 Ω*cm were used, and they will be denoted as p^{-}, p and p^{+} wafers.

Accordingly to SEM images, the fabricated samples represent the arrays of vertically aligned nanowires with diameter of 50-100 nm, nearly uniform along nanowires, on c-Si substrate. The etching time was 30 min for all wafers, and the length of p^{-}-, p- and p^{+}- SiNWs is of 27, 25 and 21 μm, correspondingly. The decrease in the etching rate with increasing doping level of

Cette thèse est accessible à l'adresse : http://theses.insa-lyon.fr/publication/2019LYSEI129/these.pdf
© [S. Rodichkina], [2019], INSA de Lyon, tous droits réservés

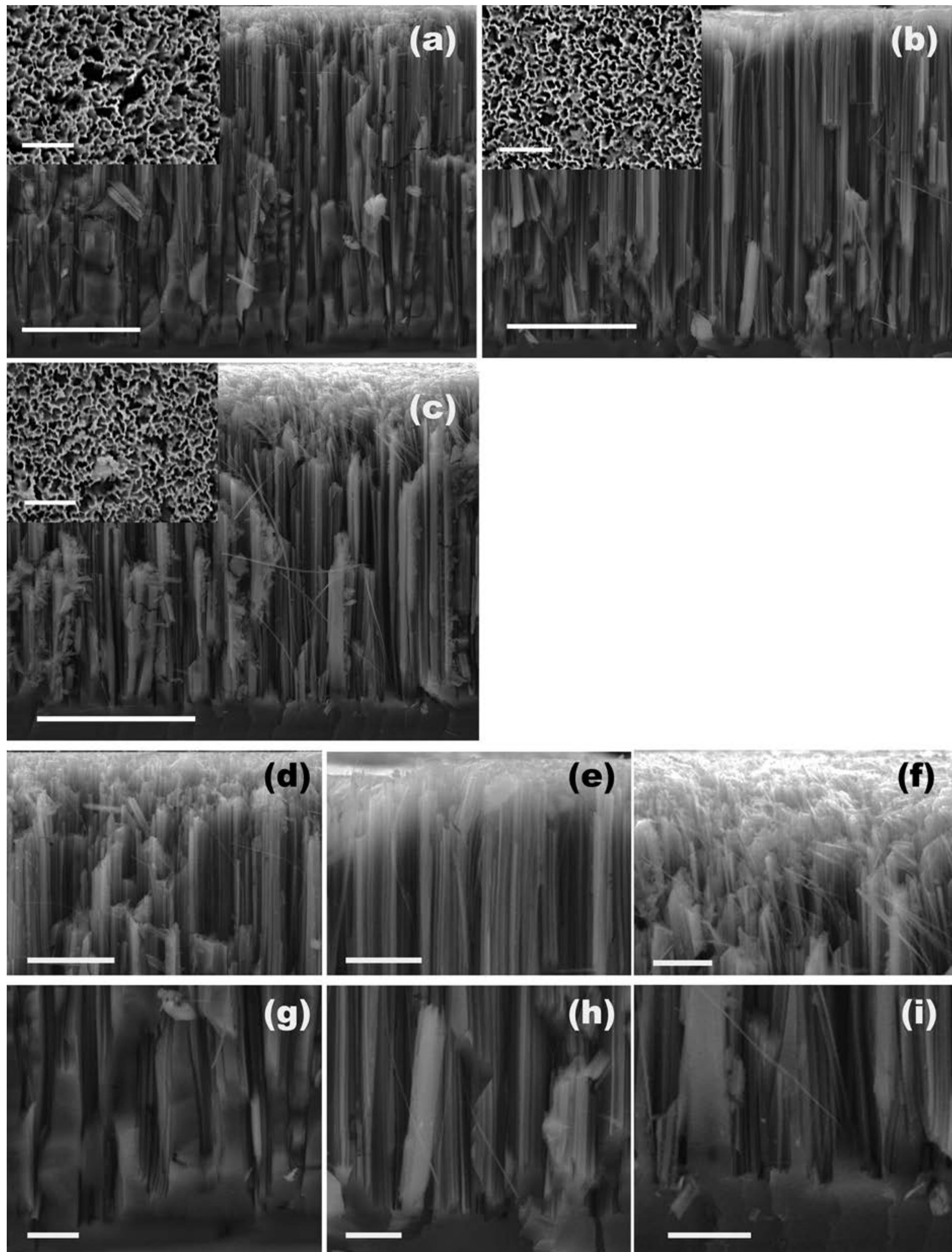

Figure 3.1: Cross-sectional and top-view (insets) images of SiNWs (series B), fabricated on c-Si wafers with the specific resistivity of (a) 40-50 Ω*cm, (b) 1-20 Ω*cm and (c) 0.1-0.2 Ω*cm. Images (d,g) show the magnified view of (a); (e,h) show the magnified view of (b); (f,i) show the magnified view of (c). The scale bars for (a-c) are 10 μm, for the instes in (a-c) are 500 nm, for (d-i) are 2 μm.

Cette thèse est accessible à l'adresse : http://theses.insa-lyon.fr/publication/2019LYSEI129/these.pdf
© [S. Rodichkina], [2019], INSA de Lyon, tous droits réservés

c-Si wafer can be associated with the decrease in the rate of Ag^+ reduction at Ag/Si interface. Considering that the Ag/Si interface behaves close to ideal Schottky barrier [64], one can obtain that the free electron concentration at the interface decreases with increasing p-type doping level [136], that slows down the reduction Ag^+ ions by the electrons form Si.

The pore diameters for p^--SiNWs reduce towards SiNWs/c-Si interface, that is not observed for *p*- and p^+-SiNWs (see Fig. 3.1 (g)–(i)). This fact is explained by the dissolution of Ag nanoparticles due to Ag redeposition during the etching, which is stronger in the case of p^--SiNWs, than for *p*- and p^+-SiNWs. The latter can not be associated with the doping level of the c-Si wafer, because the rate of Ag^+ ion reduction is higher for p^--SiNWs, than for *p*- and p^+-SiNWs. The possible explanation is the different morphology of the deposited Ag layer for the c-Si wafers with different doping level, that can influence the Ag redeposition rate. The Ag redeposition during MACE results also in partial dissolution of SiNWs tips, which can be seen in Fig. 3.1 (d). Comparing Fig. 3.1 (d) and (e), one can see, that SiNWs diameter at the top of the array is less uniform for p^--SiNWs, than for *p*-SiNWs.

p^+-SiNWs are more rough than *p*-SiNWs, and the formation of por-Si layer at the top of SiNWs can be seen (see Fig. 3.1 (f)). Higher surface roughness for p^+-SiNWs can be understood considering both the Fermi level in c-Si and zone bending at Ag/Si interface, which lead to higher free hole concentration at Ag/Si interface for p-type c-Si with higher doping level. The free holes diffuse away from metal-covered zones and facilitate Si dissolution around Ag nanoparticle. The formation of por-Si layer can be explained by both the redeposition of small Ag particles and the increase in free hole concentration at Ag/Si interface with p-type doping level. Note, that strong Ag redeposition creates a general bulk etch effect in the case of p^+-SiNWs, however its effect is less pronounced. The formation of surface roughness for SiNWs occurs also due to the stain etching of silicon, which takes place simultaneously with MACE, but this process is much slower than MACE and was not taken into account.

Accordingly to the top-view SEM images, the SiNWs diameter is of 50-100 nm for all the wafers, while the pore size for *p* and p^+ wafer is smaller than for p^- wafer, which is related to the different morphology of Ag layers deposited onto the wafers. The porosity of SiNWs arrays was determined from the top-view SEM images as a ratio of the number of dark pixels (brightness less than 50 %) to the total ones, and it is of 75 ± 5 % for all samples. SiNWs samples in this series are marked as SiNWs-C.

Fig. 3.2 (a) shows the SEM image of SiNWs fabricated by MACE-I on low boron (p-type)

Cette thèse est accessible à l'adresse : http://theses.insa-lyon.fr/publication/2019LYSEI129/these.pdf
© [S. Rodichkina], [2019], INSA de Lyon, tous droits réservés

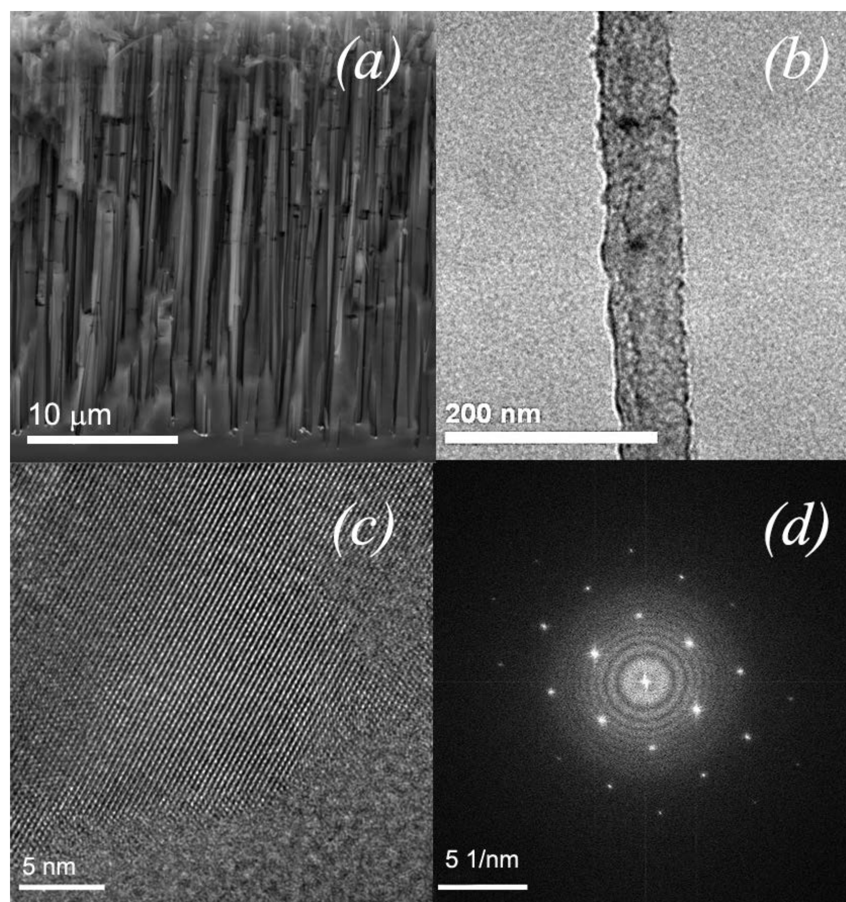

Figure 3.2: (a) Cross-section SEM image of SiNWs (series A) with the length of 22 μm, (b) TEM image of an individual nanowire, (c) HRTEM image of a SiNW, (d) Fourier transform of the HRTEM image, shown in (c).

doped, (100)-oriented c-Si wafers with the specific resistivity of 1-20 Ω*cm. As can be seen from the figure, the arrays of SiNWs fabricated by MACE-I procedure are similar to those, fabricated by MACE-II procedure (see Fig. 3.1). The absence of the effect of an increase in the oxidant concentration on the morphology of SiNWs can be associated with the relatively high etching rate of SiNWs. Fig. 3.2 (b) shows the TEM image of individual SiNW from the array. The non-porous structure and rough surface of the nanowire can be seen. The analysis of the crystalline structure of SiNWs was performed by means of Fourier-transform analysis of HRTEM image of SiNWs, shown in Fig. 3.2 (c,d). The position of white spots in the Fourier transform of the HRTEM image, analogous to the diffraction pattern, indicates the cubic diamond crystalline lattice of SiNWs, which is inherited from the initial c-Si wafer. Accordingly to the SEM observations (see Fig. 3.3), the mean diameter of SiNWs is in the range from 100 to 300 nm. The length of SiNWs, controlled by the MACE duration, was varied from 4 to 22 μm. The mean diameter of SiNWs was found to slightly increase with the length of SiNWs, which is explained

Cette thèse est accessible à l'adresse : http://theses.insa-lyon.fr/publication/2019LYSEI129/these.pdf
© [S. Rodichkina], [2019], INSA de Lyon, tous droits réservés

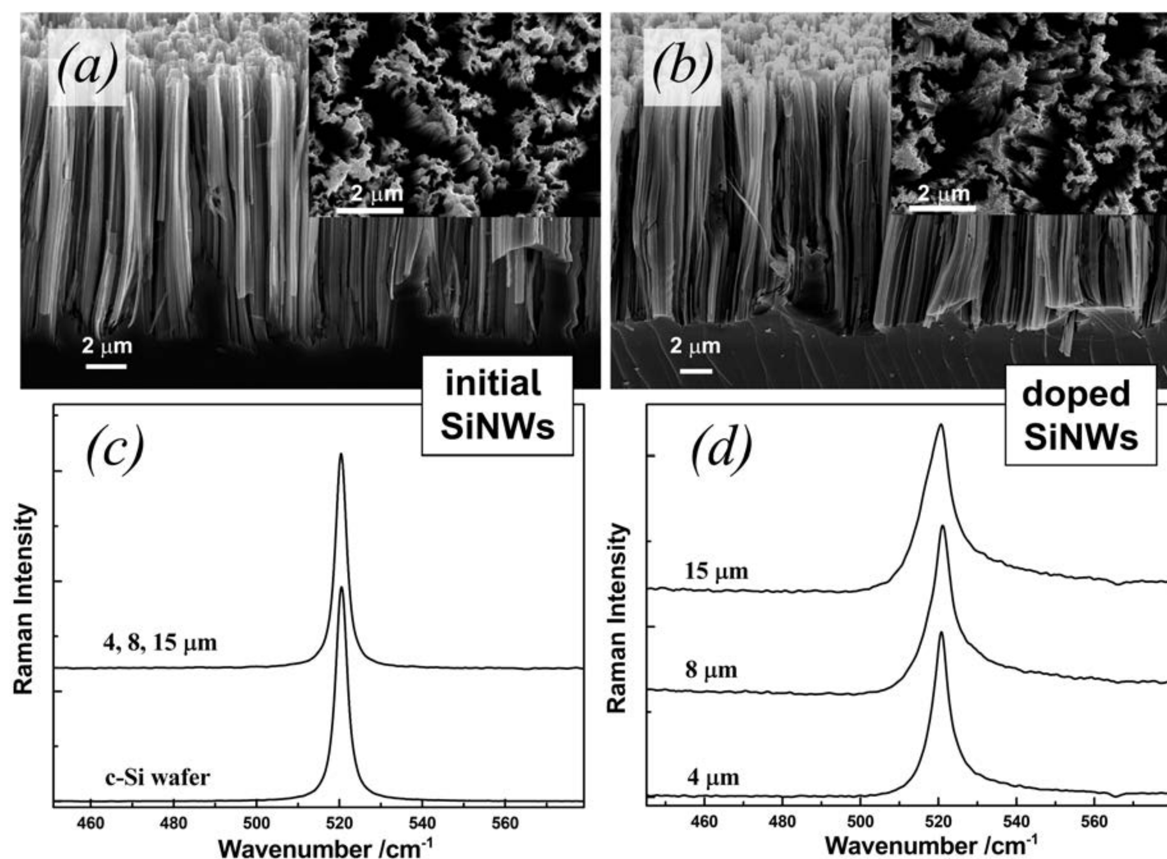

Figure 3.3: (a) Cross-sectional SEM image of initial SiNWs (SiNWs-A series) with the length of 15 μm (b) Cross-sectional SEM image of the same SiNWs after the additional doping with boron. The insets show the top-view images of the corresponding samples. (c) Normalized Raman spectra of SiNWs with different length and c-Si substrate. (d) Normalized Raman spectra of additionally boron-doped SiNWs with different length. The laser wavelength used for the Raman measurements was 632.8 nm.

by a redeposition of Ag nanoparticles during the etching, which leads to partial porosification and dissolution of SiNWs tips. The porosity of SiNWs arrays is of $75 \pm 5\%$. SiNWs samples in this series are marked as SiNWs-A and SiNWs-B, depending on post-fabrication doping type.

Despite the MACE-II procedure is frequently used to fabricate SiNWs arrays [119, 120], the low reproducibility of this procedure was observed, and the formation of por-Si layer instead of SiNWs occured in certain cases. This fact can be related to rather high concentration of oxidant H_2O_2 and low concentration of HF in the etching solution, which results both in (i) high rate of stain etching of SiNWs and Ag redeposition and (ii) low rates of anisotropic etching of c-Si wafers, that leads to attenuation of the etching anisotropy. On the contrary, the MACE-I procedure was observed to be reproducible. The different SiNWs diameter, obtained using MACE-I and MACE-II procedures for identical c-Si wafers (see Figs. 3.1 and 3.3) is explained by the different concentration of $AgNO_3$ at the first step of MACE.

Cette thèse est accessible à l'adresse : http://theses.insa-lyon.fr/publication/2019LYSEI129/these.pdf
© [S. Rodichkina], [2019], INSA de Lyon, tous droits réservés

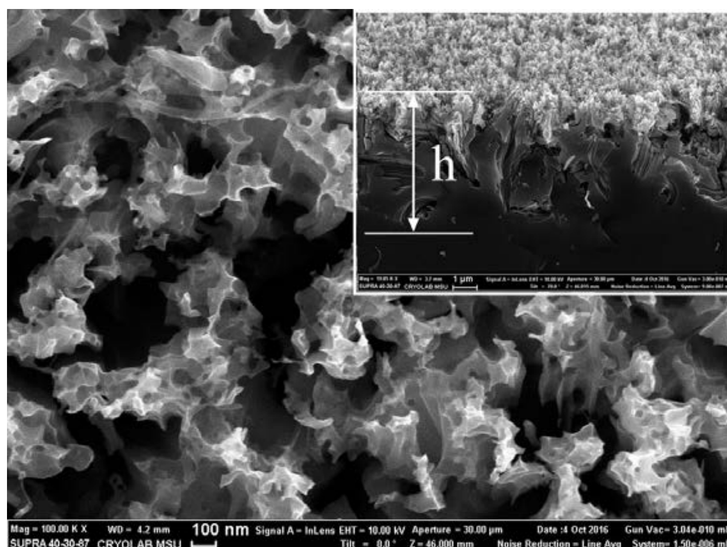

Figure 3.4: Top-view SEM image of a por-Si (series A) sample prepared for the etching time of 5 min, the inset shows a cross-sectional view of this sample.

Fig.3.4 shows SEM images of por-Si sample, fabricated by MACE-I of low phosphorus (n-type) doped, (100)-oriented c-Si wafers (specific resistivity of 1-10 Ω*cm, free electron concentration $\sim 10^{15}$ cm^{-3}). The formation of por-Si structure, instead of SiNWs under the described fabrication process can be explained by slower etching rate for n-type c-Si wafer than for p-type one and by Ag redeposition during the MACE process. One can see that the fabricated por-Si layer consists of Si nanostructures of varying porosity, which is maximal at the top of the sample and tends to zero at the depth ~ 10 μm. The effective thickness of the samples (h) is varied from 5 to 20 μm when the etching time increases from 5 to 60 min. The characteristic size of residual Si regions (nanocrystallites) is of about 100 nm and larger, while the typical pore size is in the range 50-200 nm. Porosity of por-Si at the top of the samples was determined from the top-view SEM images, for all samples the estimated porosity is of 70 ± 10 %. Por-Si samples in this series are marked as por-Si-A.

3.1.2 Structural properties of additionally doped SiNWs

Fig. 3.3 (a,b) shows typical SEM images of SiNWs samples before and after the additional doping, respectively. The standard spin-on doping technique was used, which included annealing of SiNWs at a temperature of about 950 ^{0}C (for details, see Sec. 2.1.2). Comparison of SEM images before and after the additional doping shows no significant changes in the SiNWs morphology after the doping procedure. Fig. 3.3 (c,d) shows the one-phonon Raman spectra of SiNWs samples before and after the additional doping. The spectral shape for both samples

Cette thèse est accessible à l'adresse : http://theses.insa-lyon.fr/publication/2019LYSEI129/these.pdf
© [S. Rodichkina], [2019], INSA de Lyon, tous droits réservés

corresponds to crystalline Si, and the absence of amorphous Si peak at about 480 cm^{-1} indicates no amorphization or melting of SiNWs during the high-temperature annealing. The change in the Raman line shape of SiNWs after the annealing is associated with increased free hole concentration in SiNWs after the doping procedure and is explained by the Fano effect between one-phonon and electron Raman scattering [137].

3.2 Photo-induced formation of hexagonal diamond phase in SiNWs

3.2.1 Evolution of Raman spectra of SiNWs with laser power

Fig.3.5 shows the one-phonon Raman spectra of low doped SiNWs (SiNWs-A with $L = 22$ μm) under different photoexcitation power densities. The Raman spectrum of SiNWs excited with relatively low laser intensity (15 W/cm^2) displays a single peak at 520 cm^{-1}, which corresponds to the well-known Raman peak of cubic bulk Si at room temperature. The Raman spectra of SiNWs at higher excitation levels ($>$ 4 kW/cm^2) exhibit several peaks. The Raman peaks

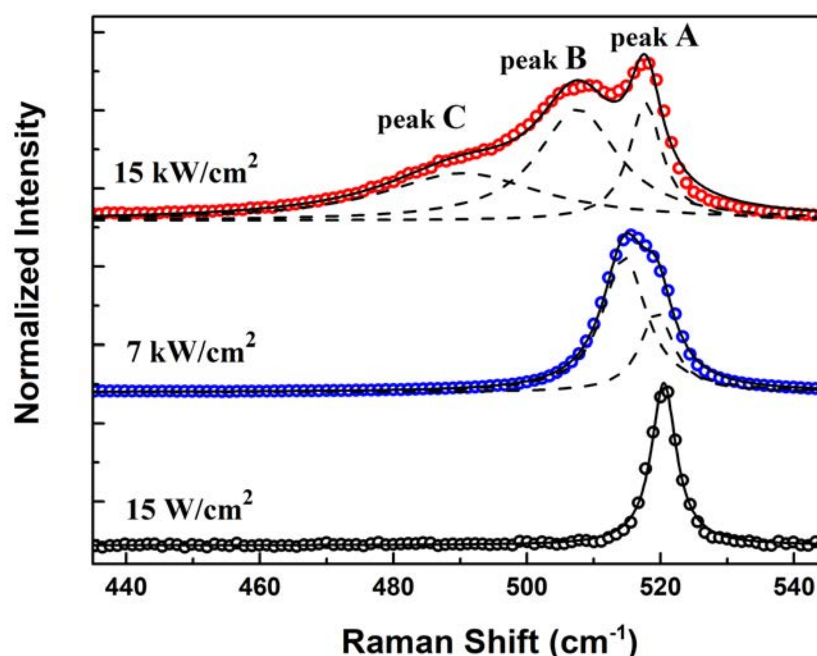

Figure 3.5: Normalized Raman spectra of low doped SiNWs (circles), obtained at excitation laser intensity of 0.015 (black), 7 (blue) and 15 kW/cm^2 (red). No observable laser-induced heating occurs at the laser intensity of 0.015 kW/cm^2. Additional Raman peaks (B and C) appear at laser excitation intensities $>$ 4 kW/cm^2. The dashed lines visualize the peaks A, B, C after the deconvolution of the Raman spectra by Lorentzians. The solid lines correspond to the sum of the Lorentzian peaks and fit well the experimental data.

Cette thèse est accessible à l'adresse : http://theses.insa-lyon.fr/publication/2019LYSEI129/these.pdf
© [S. Rodichkina], [2019], INSA de Lyon, tous droits réservés

centered near 517 cm^{-1} (peak A) and 510 cm^{-1} (peak B) can correspond to singlet (LO) and doublet (TO) phonon modes of cub-Si under heating and mechanical stresses [138, 139] caused by a temperature gradient along SiNWs. Despite the fact that the doublet phonon Raman scattering is normally forbidden in backscattering geometry for (001)-oriented cub-Si surface [140], multiple light scattering in SiNWs array leads to a breakdown of this selection rule with subsequent simultaneous observation of both phonon modes (LO and TO) in the heated and stressed SiNWs. Concerning the Raman peak (C) centered near 490 cm^{-1}, it corresponds to hex-Si (2H) phase [13, 84]. The photo-induced formation of the hex-Si phase is provoked by strong mechanical stresses in inhomogeneously heated (over 400 K) SiNWs [84, 141].

To exclude the existence of amorphous silicon (a-Si) phase in photo-excited SiNWs, which exhibit the Raman peak at about 480 cm^{-1}, one can refer to Fig. 3.7. Indeed, the observed disappearance of the peak C under external heating of silicon substrate, leading to decrease of the temperature gradient along SiNWs, could not happen if it would correspond to any amorphous phase. Moreover, the FWHM for the Raman peak of a-Si at T = 300 K is usually about 70 cm^{-1} (Ref. [88]), which is much larger than the FWHM for the peak C of about 15-30 cm^{-1}. It is worth to remark reversible nature of the photo-induced cub-Si $\leftrightarrow$ hex-Si transition. A decrease in the laser intensity leads to disappearance of the Raman peaks corresponding to hex-Si phase, as well as to the split phonon modes of cub-Si. At the same time, the phase transition in SiNWs can be only observed under photo-induced heating of the SiNWs tips, while the homogeneous heating of SiNWs even up to 1200 K does not lead to emergence of the Raman peaks B and C [142].

3.2.2 Temperature gradient induced mechanical stresses

To emphasize the role of the inhomogeneous heating-induced mechanical stresses in SiNWs, one can estimate temperature gradients ensured by photoexcitation. Fig. 3.6 shows the simulated profile of ΔT along SiNWs under photoexcitation. The profiles were obtained by the finite element method, considering SiNWs as a homogeneous medium, heated at the top side by a heat flux with an area and intensity equal to that of the laser radiation, the SiNWs/c-Si interface was maintained at room temperature. The steady-state heat equation was solved in the three-dimensional case, z-axis was directed along SiNWs with $z = 0$ at SiNWs/c-Si interface and $z = 22$ μm at SiNWs tips, which were heated by the heat flux. From the figure one can see the linear dependence of ΔT on z for $z < 10$ μm, while the strong temperature gradient is observed

Cette thèse est accessible à l'adresse : http://theses.insa-lyon.fr/publication/2019LYSEI129/these.pdf
© [S. Rodichkina], [2019], INSA de Lyon, tous droits réservés

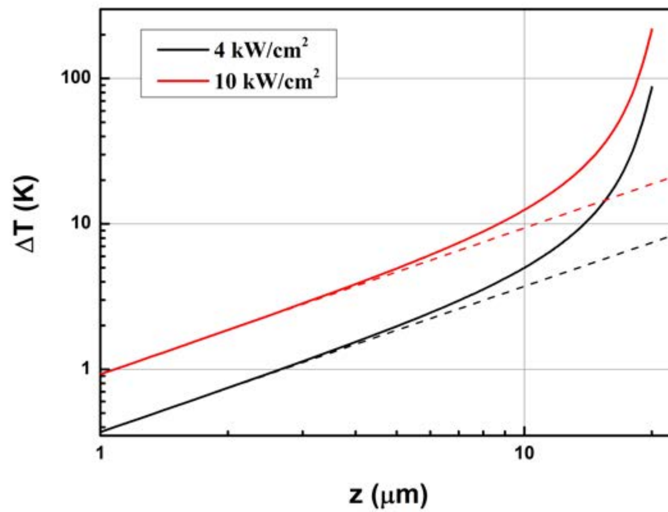

Figure 3.6: Calculated heating profile along SiNWs for the laser excitation intensities of 4 and 10 kW/cm^2, required for the LO-TO phonon splitting and hex-Si phase formation, respectively. The dashed lines show the linear $\Delta T \sim z$ dependence.

in the upper part of SiNWs with $z > 10$ μm, which is responsible for the hex-Si phase formation in SiNWs. The values of the temperature gradient at SiNWs tips are equal to 50 and 100 K/μm for the laser intensities of 4 and 10 kW/cm^2, respectively. The thermal conductivity coefficient of SiNWs, estimated at laser intensities < 4 kW/cm^2, is about 0.8 W/(m K).

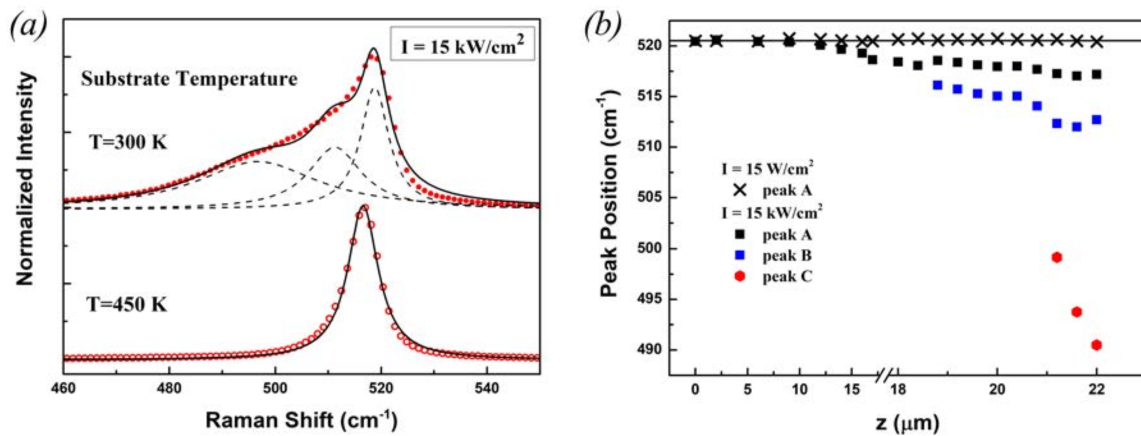

Figure 3.7: (a) Raman spectra at the high laser intensity of 15 kW/cm^2 for SiNWs samples with the c-Si substrate at room temperature (upper spectrum) and heated to 450 K (bottom spectrum). (b) Dependence of the spectral position of the Raman peaks of SiNWs as a function of a distance between the c-Si substrate and the heated part of SiNWs. The dependence was measured both at low (15 W/cm^2, black crosses) and high (15 kW/cm^2) laser intensity.

The breakdown or decrease of the temperature gradient in SiNWs leads to disappearance of hex-Si phase in SiNWs. Fig. 3.7 shows that the destruction of the temperature gradient in SiNWs by thermal heating of the underneath Si substrate or the decrease of the distance

Cette thèse est accessible à l'adresse : http://theses.insa-lyon.fr/publication/2019LYSEI129/these.pdf
© [S. Rodichkina], [2019], INSA de Lyon, tous droits réservés

between the heated part and the substrate (by scanning the laser beam along nanowires) leads to a disappearance of the Raman peak C, corresponding to the hex-Si phase, as well as to a disappearance of the LO-TO phonon spectral splitting.

3.2.3 Cubic-to-hexagonal polytype transformation

In order to study progressive formation of the hex-Si phase in SiNWs, evolution of spectral position of the Raman peaks was studied as the function of excitation laser intensity (see Fig. 3.8). At relatively low excitation levels (< 4 kW/cm^2, Zone I) a spectral shift of the single peak, corresponding to the cub-Si phase, towards lower frequencies is observed. It is related to the heating of SiNWs under laser radiation, as well as to the heating-induced mechanical stresses due to a temperature gradient in photoexcited SiNWs. To illustrate simultaneous co-existence of the thermal and stress effects in the photoexcited SiNWs, dependence of width of peak A (Γ) on its spectral position (Ω) is shown in Fig.3.9. As one can see from this figure, the slope of the $\Gamma(\Omega)$ dependence for Raman peak A obtained for SiNWs under photoexcitation is about 3 times higher than that obtained under homogeneous thermal heating. Moreover, the dependencies of $\Gamma(\Omega)$ for SiNWs and bulk cub-Si under homogeneous heating coincide. These facts can be understood if one considers presence of an average compressive mechanical stress in the photoexcited SiNWs,

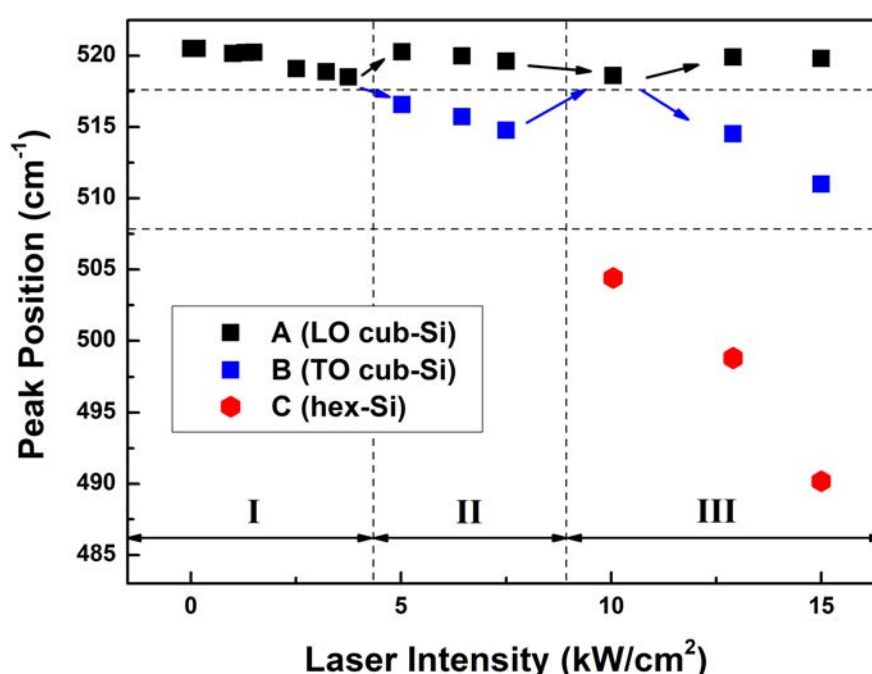

Figure 3.8: Spectral positions of the Raman peaks of SiNWs as function of laser intensity. Black and blue squares correspond to the Raman peaks A and B (stressed and heated cub-Si phase of SiNWs). Hexagons correspond to peak C (hex-Si phase of SiNWs).

Cette thèse est accessible à l'adresse : http://theses.insa-lyon.fr/publication/2019LYSEI129/these.pdf
© [S. Rodichkina], [2019], INSA de Lyon, tous droits réservés

which leads to upshift of the phonon frequency for a given peak width [138, 143]. Taking into account temperature and stress dependencies of the peak position and width for bulk cub-Si [138, 144] one can estimate the mechanical stress and temperature rise to be respectively about 3 GPa and 85 K for the laser intensity of 4 kW/cm^2.

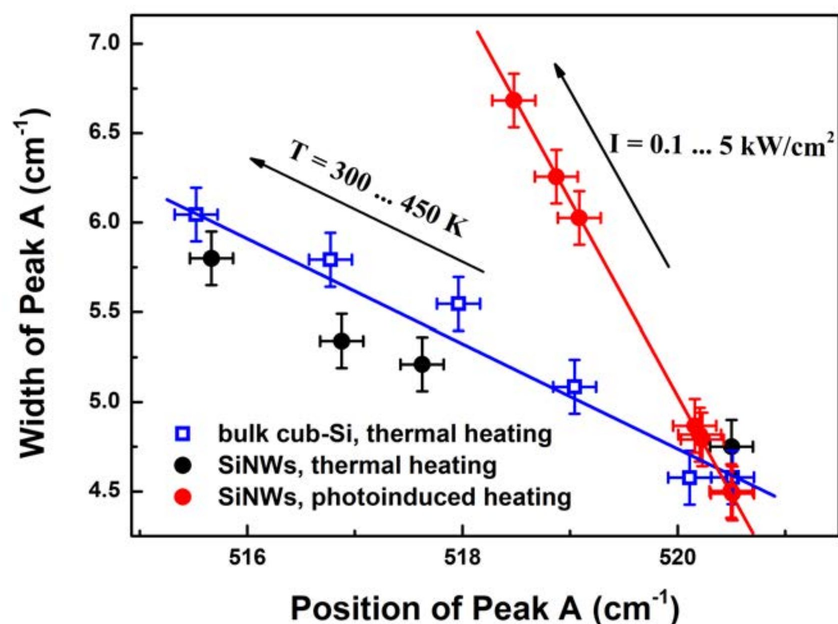

Figure 3.9: Relation between spectral position (Ω) and width (Γ) of the Raman peak A of cub-Si and SiNWs for the case of homogeneous thermal heating (blue squares and black circles, correspondingly) and of SiNWs under photoexcitation (red circles).

Further increase in the laser intensity (Zone II) leads to the rise of a temperature gradient along the length of SiNWs and, consequently, to the increase of thermally induced mechanical stresses. The strong stresses provoke easily observable singlet-doublet phonon splitting of the Raman peaks [138]. Considering backscattering geometry of the exciting laser beam propagating in <001> direction and the average compression occurring along SiNWs, the singlet and doublet components are concluded to correspond to LO and TO phonons. In this case, LO and TO phonons would be polarized parallel and perpendicular to the stress direction, respectively, and thus have different energy. Despite the doublet Raman band is forbidden for (001)-oriented cub-Si surface in backscattering geometry [140], both the enhanced multiple light scattering on the top overheated parts of a SiNWs array and their heating-induced crystalline disorder allow observation of the TO phonons. The splitting degree obviously increases with the laser intensity. According to the data for bulk cub-Si at 110 K [138], the stress magnitude estimated from the splitting value obtained for SiNWs is found to be, respectively, around 3.2 and 4.1 GPa at the beginning and the end of Zone II.

Cette thèse est accessible à l'adresse : http://theses.insa-lyon.fr/publication/2019LYSEI129/these.pdf
© [S. Rodichkina], [2019], INSA de Lyon, tous droits réservés

At a threshold laser intensity (beginning of Zone III), leading to a maximal thermally induced stresses, a structural relaxation in the overheated part of SiNWs occurs with a formation of the new hex-Si phase. The formed hex-Si phase is then maintained by a constant energy input due to a relatively high photoexcitation level. The formation of hex-Si phase is accompanied by a reduction of the overall mechanical stresses and, consequently, by a partial quenching of the splitting between LO and TO phonon modes. Further heating of SiNWs at laser intensities > 10 kW/cm^2 leads to a new round of the thermally induced mechanical stress enhancement in the cub-Si phase and subsequent splitting of the phonon modes, while the Raman peak of hex-Si phase shifts towards lower wavenumbers (end of Zone III). It is interesting to note that when the laser intensity decreases, the reverse transformation to the cub-Si phase is observed.

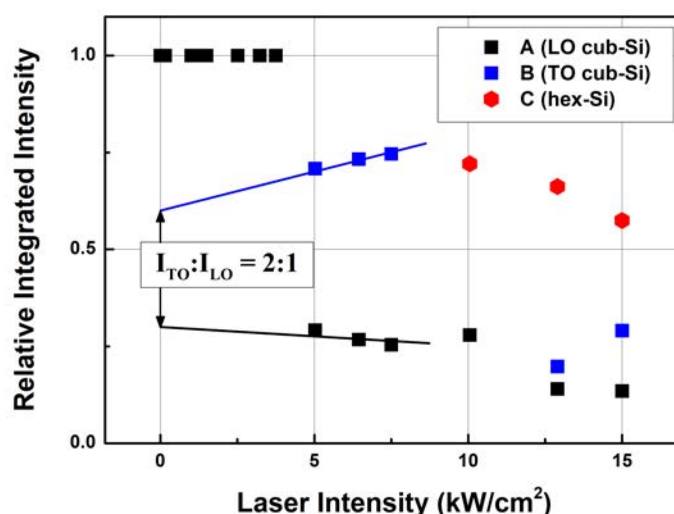

Figure 3.10: Relative integrated intensity of the Raman peaks of SiNWs as a function of the laser intensity.

Fig. 3.10 shows the relative integrated intensity of the Raman peaks of SiNWs as a function of the laser intensity. The change in the relative intensity between LO and TO Raman peaks of c-Si with the laser intensity for $I < 10$ kW/cm^2 can be related to the increase in spectral distance between the peaks which leads to a change in the ratio of the number of phonons for LO and TO modes. The linear extrapolation exhibits the 2:1 ratio between LO and TO phonon intensities at $I = 0$, where no phonon splitting occurs, that corresponds to the two-fold degenerate TO mode in Si. The decrease in the relative contribution of peak C at $I > 10$ kW/cm^2 can be related to the redistribution of the light in SiNWs array due to the thermal heating of SiNWs under high photoexcitation.

Cette thèse est accessible à l'adresse : http://theses.insa-lyon.fr/publication/2019LYSEI129/these.pdf
© [S. Rodichkina], [2019], INSA de Lyon, tous droits réservés

The temperature of SiNWs, at which the formation of hex-Si occurs, is estimated from the cub-Si Raman peak position to be more than 400 K. The latter value correlates well with the temperature of 470 K, required for formation of hex-Si in relaxed bulk Si [84]. The maximal observed mechanical stress in SiNWs of about 7.5 GPa, estimated from the singlet-doublet phonon splitting, corresponds to the value of about 10 GPa, required for the cub-Si $\rightarrow \beta$-tin phase transition in bulk Si [11, 145].

Mechanism of photoinduced crystalline lattice transformation

Thus, the following mechanism of hex-Si phase formation in SiNWs under photoexcitation can be suggested. The strong photo-induced temperature gradient appearing along SiNWs leads to significant mechanical stresses, which are observed as singlet-doublet phonon splitting of Raman peaks of SiNWs. When the stress magnitude in the overheated SiNWs ($T > 400$ K) reaches the value of more than 4 GPa, a partial phase transition cub-Si $\rightarrow \beta$-tin Si $\rightarrow$ hex-Si takes place, analogously to the case of bulk cub-Si [11, 145]. As a result, cub-Si and hex-Si phases coexist in SiNWs, as observed by Raman spectroscopy. The formation of the hex-Si phase is clearly illustrated by an appearance of the photoluminescence band in the spectral range of 1.3 - 1.6 eV at high photoexcitation.

Photoluminescence measurements

Fig. 3.11 (a) shows photoluminescence (PL) spectra of SiNWs obtained at different photoexcitation levels. As one can see from the inset, a huge enhancement of the PL signal at excitation intensities > 10 kW/cm^2 is observed. The strong PL signal of the highly excited SiNWs correlates well with a formation of the hex-Si phase, related to the Raman peak C, as can be seen in Fig. 3.11 (b). On the contrary, when SiNWs are constituted only by cub-Si phase and exhibit only Raman peaks A and B (see Fig. 3.11 (b) at $I < 10$ kW/cm^2), no PL signal is detected. Therefore, the emergence of strong PL in SiNWs can not be related to the quantum confinement effects and can be explained by the direct electron transitions in the stressed hex-Si phase. At increase of the photoexcitation level from 12 to 15 kW/cm^2, (i) the increase of PL intensities and (ii) the red-shift of PL maximum (60 meV) is observed. These facts can be explained by an increase in: (a) hex-Si volume, (b) temperature gradient induced mechanical stresses and (c) high concentration of photoexcited charge carriers. Indeed, all these reasons can lead to an enhanced probability of the direct electron transitions, as well as to reduction of the direct energy gap in hex-Si [81, 89]. Moreover, the spectral position of the PL maximum (Fig. 3.11)

Cette thèse est accessible à l'adresse : http://theses.insa-lyon.fr/publication/2019LYSEI129/these.pdf
© [S. Rodichkina], [2019], INSA de Lyon, tous droits réservés

at 1.44-1.50 eV can correspond to the energy of direct electron transitions of the mechanically compressed hex-Si [81, 89]. The similar transformation towards a direct bandgap semiconductor was observed in Ge under tensile strain combined with high n-type doping [146].

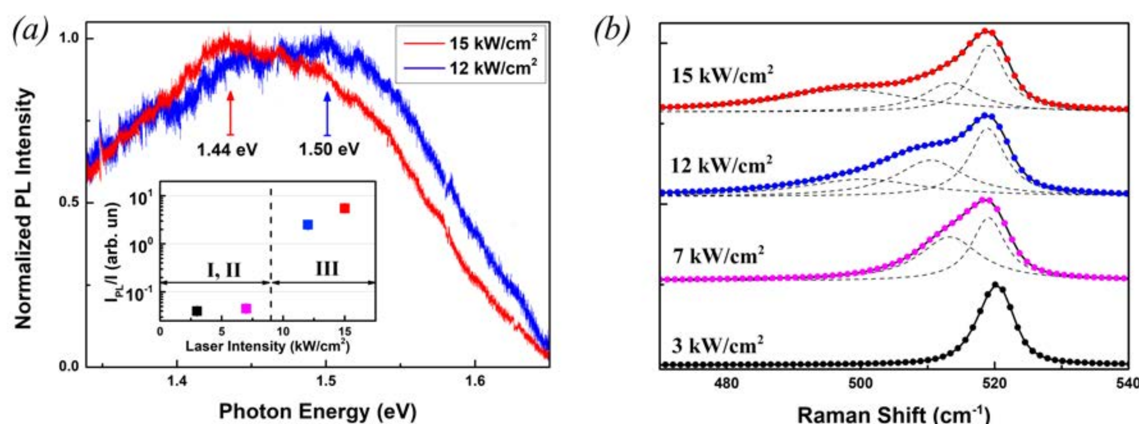

Figure 3.11: (a) Normalized PL spectra of SiNWs, obtained at the high laser excitation intensity ($>$ 10 kW/cm^2). Arrows indicate the spectral position of PL maximum. The inset shows the dependence of the PL maximum intensity, divided to the laser intensity, on the laser intensity. Dashed line illustrates the threshold of hex-Si phase formation in SiNWs. (b) Normalized Raman spectra Raman of SiNWs obtained at the same point for different excitation laser intensities. Dashed lines show the Raman peaks A,B and C after deconvolution of the spectra by Lorentzians, solid lines correspond to the sum of the Lorentzian peaks. The correlation between the observed PL and peak C can be observed.

Note, that the photoinduced cub-Si $\rightarrow$ hex-Si crystalline lattice transformation takes place also in highly-doped SiNWs. The transformation of the Raman peak with the laser intensity is analogous to those observed for undoped SiNWs. At low laser intensity, the Raman peak for p-type highly-doped SiNWs represents an asymmetric Fano peak, and at high laser intensity all the Raman peak can be fitted by symmetric Lorentzian peak. This fact is explained by the trapping of free charge carriers on the defects formed at cub-Si/ hex-Si interfaces.

3.3 Conclusions to Chapter 3

a) Fabrication of SiNWs arrays by metal-assisted chemical etching

Arrays of crystalline SiNWs with porosity of 75%, typical nanowire diameter of 100 nm and length of 4-27 μm, initial concentration of boron impurities $\sim 10^{15}$ cm^{-3} were fabricated by metal-assisted chemical etching of low p-type doped c-Si substrates with the electrical resistivity $\sim$ 10 Ω*cm. SiNWs have bulk core/rough surface morphology, which is important for thermoelectric applications of SiNWs. For c-Si substrates with the electrical resistivity of

Cette thèse est accessible à l'adresse : http://theses.insa-lyon.fr/publication/2019LYSEI129/these.pdf
© [S. Rodichkina], [2019], INSA de Lyon, tous droits réservés

$\sim 0.1\ \Omega$*cm, the formation of por-Si layer at the top of SiNWs occurs, explained by both the Ag redeposition during the etching and high free hole concentration at Ag/Si interface. Post-fabrication doping procedure, which includes the high-temperature annealing at about 1000 ^{0}C, does not influence the morphology and crystallinity of SiNWs.

b) Photo-induced formation of hexagonal diamond phase in SiNWs

The crystalline phase transition from cub-Si to hex-Si was observed in SiNWs, fabricated by MACE of low doped bulk cub-Si wafers, under laser excitation with an intensity of more than 10 kW/cm^2 and wavelength of 473 nm. Initially, SiNWs were shown to consist of only cub-Si phase and exhibit a single one-phonon Raman peak at 520.5 cm^{-1} at low photoexcitation. At high photoexcitation ($>$ 10 kW/cm^2), the Raman peaks of SiNWs at about 517 and 510 cm^{-1} were attributed to singlet-doublet phonon splitting in the cub-Si phase under mechanical stresses, and the Raman peak at about 505 cm^{-1} was associated with the hex-Si phase. The crucial role of mechanical stresses, arising in SiNWs due to inhomogeneous photo-induced heating, was emphasized as the main reason provoking formation of hex-Si phase. The photo-induced formation of the hex-Si phase was additionally illustrated by the enhanced photoluminescence of SiNWs in the spectral range of 1.3 - 1.6 eV at laser intensities above 10 kW/cm^2, correlated with the appearance of Raman peak at about 505 cm^{-1}.

Cette thèse est accessible à l'adresse : http://theses.insa-lyon.fr/publication/2019LYSEI129/these.pdf
© [S. Rodichkina], [2019], INSA de Lyon, tous droits réservés

Chapter 4
Contactless diagnostics of free charge carriers

This chapter is devoted to studiyng the effectiveness of the post-fabrication doping of SiNWs using the the thermally activated diffusion of dopant atoms from the spin-on dopant solutions. The contactless methods based on infrared spectroscopy and Raman scattering spectroscopy are developed to monitor the free charge carrier concentration in highly-doped SiWNs arrays.

4.1 Infrared spectroscopy

Infrared spectroscopy is a classical optical method to study the free charge carriers in c-Si [147–150]. It was also applied to mesoporous Si with nanocrystal sizes below 50 nm [147]. The IR reflectance spectra for c-Si and mesoporous Si were described using the isotropic effective medium approximation and Drude model for free charge carriers, that was used to determine the free charge carrier concentration in the samples [147]. Por-Si and SiNWs with a typical nanocrystal diameter of 100 nm have not been investigated by the IR spectroscopy. This section describes an application of IR spectroscopy to study free charge carriers in por-Si and SiNWs. The effect of the light scattering on the IR spectra of nanostructures with diameter about 100 nm is investigated. The modeling of the IR spectra for SiNWs based on the anisotropic effective medium approximation is presented.

4.1.1 Modeling of infrared spectra for nanostructured media

a) Isotropic medium

Let us consider isotropic nanostructured layers (por-Si). In the general case of an opaque homogeneous material the reflectance of attenuated total reflectance spectrum (R_{ATR}) can be calculated from the Fresnel equations, which give the following expression for the s-polarized light [129]:

Cette thèse est accessible à l'adresse : http://theses.insa-lyon.fr/publication/2019LYSEI129/these.pdf
© [S. Rodichkina], [2019], INSA de Lyon, tous droits réservés

$$R_s = \left| \frac{\sqrt{\varepsilon_{Ge}} cos\theta - \sqrt{\varepsilon_{PS} - \varepsilon_{Ge} sin^2\theta}}{\sqrt{\varepsilon_{Ge}} cos\theta + \sqrt{\varepsilon_{PS} - \varepsilon_{Ge} sin^2\theta}} \right|^2 , \qquad (4.1)$$

where ε_{Ge} and ε_{PS} are the dielectric constants of Ge prism and por-Si layer, θ is the light incident angle. For non-polarized light and incident angle $\theta = 0$ the Fresnel equations give the following value of $R_{ATR} = R_s$; if $\theta = 45^0$ the Fresnel equations lead to $R_{ATR} = (R_s + R_s^2)/2$ (see for example Ref. [129]).

The dielectric function of por-Si described as an isotropic effective medium, consisting of air and doped spherical Si nanocrystals, can be found accordingly to the Bruggeman formula (effective medium approximation) [147]:

$$f_A \frac{\varepsilon_A - \varepsilon_{PS}}{\varepsilon_A + 2\varepsilon_{PS}} + f_{nc} \frac{\varepsilon_{nc} - \varepsilon_{PS}}{\varepsilon_{nc} + 2\varepsilon_{PS}} = 0, \qquad (4.2)$$

where $f_A = p, f_{nc} = (1-p)$ are the volume fraction of air and Si nanocrystals in por-Si, correspondingly, p is the porosity of por-Si, $\varepsilon_A, \varepsilon_{Si}$ are the dielectric constants of air and Si nanocrystals, correspondingly.

The dielectric function of doped Si nanocrystals ε_{nc} can be found as $\varepsilon_{nc} = \varepsilon_\infty + \chi_{FC}$, where ε_∞ is the dielectric constant of pure undoped c-Si, χ_{FC} is the permittivity of free charge carriers. In the studied IR range from 600 to 5000 cm^{-1} undoped c-Si represents an optically transparent medium with $\varepsilon_\infty = 11.7$ [151]. Permittivity of free charge carriers can be described by the Drude model [147–150]

$$\chi_{FC} = -\frac{\omega_p^2}{\omega^2 + i\omega g}, \qquad (4.3)$$

where ω_p is the plasma frequency, g is the damping rate ($g = \tau^{-1}, \tau$ is the electron quasimomentum scattering time). The plasma frequency is given by the following formula:

$$\omega_p = \sqrt{N \frac{e^2}{m\varepsilon_0}}, \qquad (4.4)$$

where N is the concentration of charge carriers in the nanocrystal, e is the electron charge, m is the effective mass of charge carriers, ε_0 is the permittivity of free space. The effective mass of electrons and holes in c-Si is equal to $m = 0.26\ m_0$ and $m = 0.37\ m_0$, correspondingly, where m_0 is the free-electron mass [149].

In a Si nanocrystal the scattering time of charge carriers τ can be shorter than that in the bulk material due to the interaction of charge carriers with the nanocrystal surface [152]. This can be

Cette thèse est accessible à l'adresse : http://theses.insa-lyon.fr/publication/2019LYSEI129/these.pdf
© [S. Rodichkina], [2019], INSA de Lyon, tous droits réservés

considered as an additional term in the damping rate g, which is proportional to the number of interactions N_i of an electron with the nanocrystal surface during the period of electromagnetic wave, N_i can be estimated as vT/L, where v is the thermal velocity of charge carriers, $T = 2\pi/\omega$ is the wave period and L is the size of nanocrystal [147]. Hence, the damping rate g for the charge carriers can be expressed in the following way [147]:

$$g = g_0 \left(1 + \frac{g_1}{\omega}\right), \tag{4.5}$$

where g_0 is the volume damping rate of free charge carriers (in the bulk material), g_1 is the model parameter, which describes the surface damping rate of free charge carriers. For the bulk phosphorous-doped n-type Si at the room temperature an empirical dependence between the plasma frequency and the volume damping rate was found: $g_0 = 194 + 0.051\omega_p$ [148], where both g_0 and ω_p are given in cm^{-1}. Note, that spectroscopic units [cm^{-1}] for damping rate and frequency can be converted to [s^{-1}] by multiplying on $2\pi c$, where c is the speed of light in vacuum.

Overall, the model (4.1)-(4.5) describes the reflectance spectra for por-Si using the following parameters: porosity (p), concentration of free carriers in nanocrystals N (or the plasma frequency ω_p), bulk damping rate (g_0) and surface damping rate parameter (g_1). The range of applicability of this model is mainly determined by the applicability of effective medium approximation in the specific experimental conditions, and it will be discussed in the next parts of this section, devoted to the experimental study of the free charge carriers in por-Si and SiNWs.

b) Anisotropic medium

Let us consider a plane monochromatic electromagnetic wave falling on an uniaxial anisotropic crystal with an optical axis perpendicular to a surface of crystal, as it is shown in Fig. 4.1. The coordinate system is chosen in such a way that the z-axis is perpendicular to the sample surface (and parallel to the optical axis) and directed inside the sample, and the xz-plane represents the plane of incidence of light. The light falls from the transparent medium, which represents an ATR (Ge) crystal and is characterized by a refractive index n_{Ge}.

ATR signal measured for non-polarized light is given by the following expression:

$$R_{ATR} = (R_s + R_p)/2, \tag{4.6}$$

Cette thèse est accessible à l'adresse : http://theses.insa-lyon.fr/publication/2019LYSEI129/these.pdf
© [S. Rodichkina], [2019], INSA de Lyon, tous droits réservés

where $R_{s,p}$ is the reflectance for s- and p-polarized light, correspondingly [153].

In our case $R_{s,p}$ can be expressed in the following way:

$$R_s = \left| \frac{\frac{\omega}{c} n_{Ge} cos\theta - k_{zo}}{\frac{\omega}{c} n_{Ge} cos\theta + k_{zo}} \right|^2, \tag{4.7}$$

$$R_p = \left| \frac{\frac{\omega}{c} \varepsilon_{\perp} cos\theta - n_{Ge} k_{ze}}{\frac{\omega}{c} \varepsilon_{\perp} cos\theta + n_{Ge} k_{ze}} \right|^2, \tag{4.8}$$

where ω is the frequency of the incident light, c is the speed of light, θ is the angle of light incidence, $k_{zo,e}$ are the z-components of the light wave vector inside the sample for the ordinary and extraordinary rays, correspondingly, which are given by

$$k_{zo} = \frac{\omega}{c} \sqrt{\varepsilon_{\perp} - n_{Ge}^2 sin^2\theta}, \tag{4.9}$$

and

$$k_{ze} = \frac{\omega}{c} \sqrt{\varepsilon_{\perp} - \frac{\varepsilon_{\perp}}{\varepsilon_{\parallel}} n_{Ge}^2 sin^2\theta}, \tag{4.10}$$

where $\varepsilon_{\perp,\parallel}$ are the dielectric constants of an uniaxial anisotropic medium (see Appendix A).

In order to describe the dielectric function of SiNWs array, the latter can be considered within the effective medium approximation. SiNWs array consists of doped Si nanocrystals and air, and in the effective medium approximation it represents an anisotropic uniaxial medium with

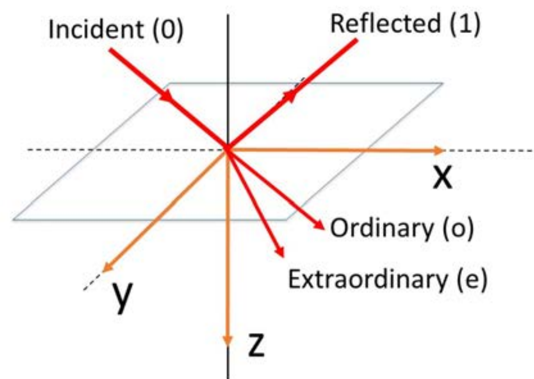

Figure 4.1: Illustration to the problem of calculating the reflectance from an anisotropic medium. Orange arrows show the chosen coordinate system. Light falls from the transparent medium (upper half-space, $z < 0$), while the sample is placed in the lower half-space ($z > 0$). z-axis coincides with the optical axis of the sample and is perpendicular to the sample surface. Red arrows illustrate the incident (0), reflected (1) and transmitted ordinary (o) and extraordinary (e) light waves.

Cette thèse est accessible à l'adresse : http://theses.insa-lyon.fr/publication/2019LYSEI129/these.pdf
© [S. Rodichkina], [2019], INSA de Lyon, tous droits réservés

dielectric constants given by the generalized Bruggeman formula, as follows:

$$f_A \frac{\varepsilon_{\perp,\parallel} - \varepsilon_A}{\varepsilon_{\perp,\parallel} + L_{\perp,\parallel}(\varepsilon_A - \varepsilon_{\perp,\parallel})} + f_{nc} \frac{\varepsilon_{\perp,\parallel} - \varepsilon_{nc}}{\varepsilon_{\perp,\parallel} + L_{\perp,\parallel}(\varepsilon_{nc} - \varepsilon_{\perp,\parallel})} = 0, \qquad (4.11)$$

where $f_A = p, f_{nc} = (1-p)$ are the volume fraction of air and Si nanocrystals in SiNWs array, correspondingly, p is the porosity of SiNWs array, $\varepsilon_A, \varepsilon_{Si}$ are the dielectric constants of air and Si nanocrystals, correspondingly [154]. In Eq. (4.11) for anisotropic uniaxial medium, one should consider $L_\perp = 1/2$; $L_\parallel = 0$. The generalized Bruggeman formula, given by Eq. (4.11), is also valid for an isotropic medium, such as por-Si, in this case $L_\perp = L_\parallel = 1/3$. The dielectric constant of Si nanocrystals can be described by the Drude model Eqs. (4.3)-(4.5).

Overall, the model Eqs. (4.6)-(4.11), (4.3)-(4.5) describes the ATR spectra for SiNWs using the following parameters: porosity (p), plasma frequency (ω_p), bulk damping rate (g_0) and surface damping rate parameter (g_1). It is worth to note, that Eqs. (4.7)-(4.8) are valid both for anisotropic (SiNWs) and isotropic medium (por-Si), and the corresponding dielectric constants in both cases can be found using Eq. (4.11).

The parameters ω_p, g_0, g_1 can be determined from the fit of the ATR spectra for Si nanostructure samples, while the porosity of Si nanostructures is usually known from other techniques (e.g. SEM or gravimetric analysis). The free charge carrier concentration in Si nanocrystals can be calculated from ω_p accordingly to Eq. (4.4).

c) Comparison of anisotropic and isotropic models

Fig. 4.2 (a) (solid lines) shows the calculated spectra of $-ln(R_{ATR})$ for highly p-type doped SiNWs and por-Si, obtained within anisotropic and isotropic models, correspondingly, by using Eqs. (4.6)-(4.11), (4.3)-(4.5). As can be seen from the figure, for the same parameters of Si nanocrystals, the ATR values for SiNWs are higher than for por-Si. This fact is related to the different dielectric constants of SiNWs and por-Si with the same parameters of Si nanocrystals, as it follows from Eq. (4.11). The ATR values for SiNWs for s-polarized incident light are about one order higher than for p-polarized one, and in the studied ATR geometry, are related to the ordinary and extraordinary ray in SiNWs, respectively (see Eqs. (4.7)-(4.8)). The big difference in R_s and R_p values in SiNWs is related to different absorption coefficient for ordinary and extraordinary rays in anisotropic medium and should be considered in ATR or specular reflectance measurements with polarized light.

One can represent the spectra for $-ln(R_{ATR})$ in the following form, similar to Beer–Lambert

Cette thèse est accessible à l'adresse : http://theses.insa-lyon.fr/publication/2019LYSEI129/these.pdf
© [S. Rodichkina], [2019], INSA de Lyon, tous droits réservés

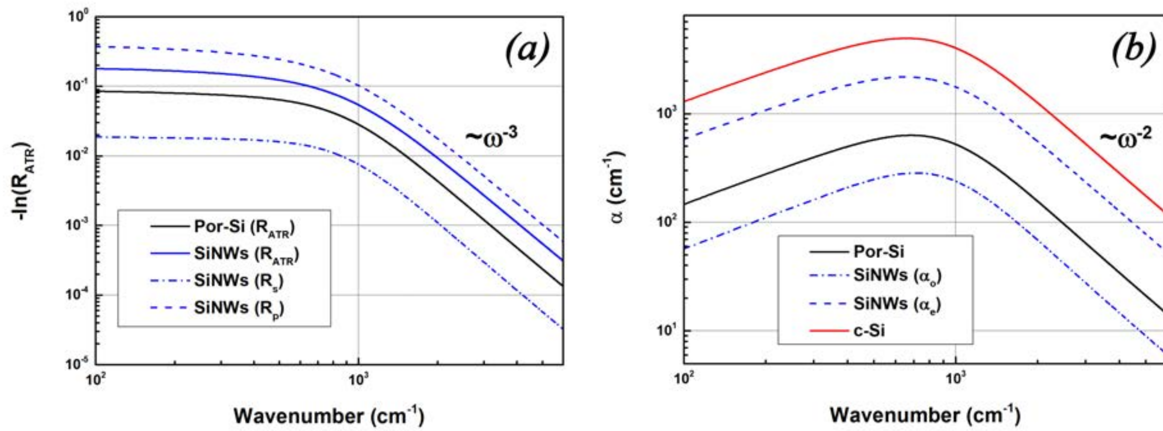

Figure 4.2: (a) Calculated ATR spectra for s-polarized (dash-dotted line), p-polarized (dashed line) and non-polarized (blue solid line) incident light for the anisotropic medium (SiNWs), as well as for non-polarized light for the isotropic medium (por-Si, black solid line) (b) calculated spectra of the absorption coefficient for ordinary (dash-dotted line) and extraordinary (dashed line) ray for the anisotropic medium, as well as the absorption coefficient for the porous (por-Si, black solid line) and non-porous (c-Si, red solid line) isotropic medium. The sample parameters, used for calculations, are the same for SiNWs and por-Si: $p = 0.75$, $\omega_p = 2000$ cm^{-1}, $g_0 = 500$ cm^{-1}, $g_1 = 1000$ cm^{-1}, $N = 1.6 * 10^{19}$ cm^{-3}.

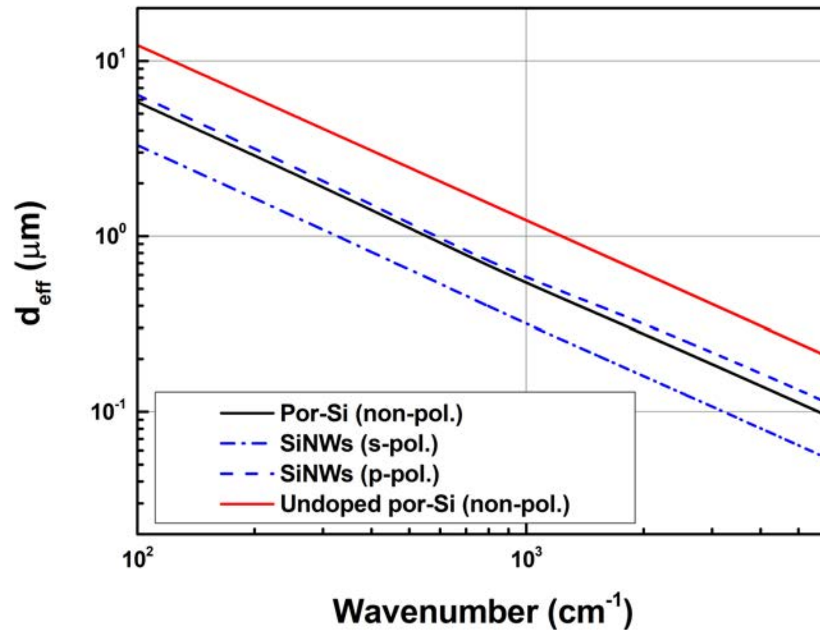

Figure 4.3: Calculated effective light penetration depth for s-polarized (dash-dotted line), p-polarized (dashed line) incident light for SiNWs and for natural incident light for doped (black solid line) and undoped (red solid line) por-Si.

law: $-ln(R_{ATR}) = \alpha_{\text{eff}} d_{\text{eff}}$, where α_{eff} is the effective absorption coefficient of the studied medium and d_{eff} is the effective light penetration depth. Fig. 4.2 (b) shows the theoretical absorption coefficient α_{eff} for the above samples, calculated as $\alpha_{\text{eff}} = 2\omega/c * Im\sqrt{\varepsilon}$, and for bulk c-Si ($p = 0$, while the other parameters are the same as for por-Si and SiNWs). The similarity

Cette thèse est accessible à l'adresse : http://theses.insa-lyon.fr/publication/2019LYSEI129/these.pdf
© [S. Rodichkina], [2019], INSA de Lyon, tous droits réservés

between the spectra of $-ln(R_{ATR})$ and α_{eff} can be clearly seen, with higher values of $-ln(R_{ATR})$ corresponding to higher values of α_{eff}. As expected, both α_{eff} and $-ln(R_{ATR})$ increase with the free charge carrier concentration in Si nanocrystals for SiNWs and por-Si. Therefore, for por-Si, the same values of $-ln(R_{ATR})$ are associated with higher values of N than for SiNWs.

Fig. 4.3 shows calculated values of the effective light penetration depth d_{eff}, which is defined as $-ln(R_{ATR})/\alpha_{\text{eff}}$, for highly doped SiNWs and por-Si, as well as for undoped por-Si, for comparison. The latter value is calculated for s-polarized light, according to the following equation:

$$d_{\text{eff}\perp} = \frac{2cn_{rel}cos\theta}{(1-n_{rel}^2)(sin^2\theta - n_{rel}^2)^{1/2}}\frac{1}{\omega}, \tag{4.12}$$

where n_{rel} is the relative refraction coefficient between the sample and Ge prism [155, 156]. Note, that Eq. (4.12) is valid only for transparent samples. As can be seen from the figure, for all the samples, d_{eff} decreases with light frequency, the magnitude of d_{eff} ranges from ~ 1 μm at 500 cm^{-1} to ~ 0.1 μm at 2000 cm^{-1}. The lower values of d_{eff} for highly-doped samples compared with low-doped ones are related to the additional light absorbance in highly-doped samples by free charge carriers. It is important that both for highly-doped SiNWs and por-Si, the spectra of d_{eff} can be approximated by $\sim \omega^{-1}$ in the whole wavenumber range, for undoped por-Si this fact follows directly from Eq. (4.12).

Considering the asymptotics for ATR spectra and absorption coefficient, it can be seen from Fig. 4.2 (b), that the spectra of α_{eff} exhibit the ω^{-2} asymptotics at high wavenumbers. In the case of c-Si, this fact follows directly from the Drude model (see Eq. (4.3)). For SiNWs and por-Si, the same asymptotics is related to the fact that the light absorption of the effective medium is due to the free charge carriers in Si nanocrystals, which are described by Drude model. The spectra of $-ln(R_{ATR})$ exhibit the ω^{-3} asymptotics at high wavenumbers that is shown in Fig. 4.2 (a). This asymptotics can be explained taking into account both the Drude model for Si nanocrystals and asymptotics of $d_{\text{eff}} \sim \omega^{-1}$.

4.1.2 Infrared diagnostics of isotropic nanostructured layers

a) Reflectance spectroscopy

In order to determine the free charge carrier concentration in c-Si, its IR reflactance spectra are usually fitted accordingly to the model Eqs. (4.1)-(4.5) with constant damping rate g ($g_1 = 0$), and N is determined from the plasma frequency using Eq. (4.4). Fig. 4.4 shows the application

Cette thèse est accessible à l'adresse : http://theses.insa-lyon.fr/publication/2019LYSEI129/these.pdf
© [S. Rodichkina], [2019], INSA de Lyon, tous droits réservés

of this method to n- and p-type c-Si wafers. The good fits of the experimental spectra can be seen both for n- and p-type c-Si. The plasma frequency, determined from the fitting, is of 2500 and 4700 cm^{-1} for n- and p-type c-Si, relatively. The obtained free charge carrier concentration in c-Si wafers is of $1.8 \cdot 10^{19}$ and $9.0 \cdot 10^{19}$ cm^{-3} for n- and p-type c-Si, relatively, which corresponds well to the values of *N* determined from the electrical resistivity of c-Si wafers [33].

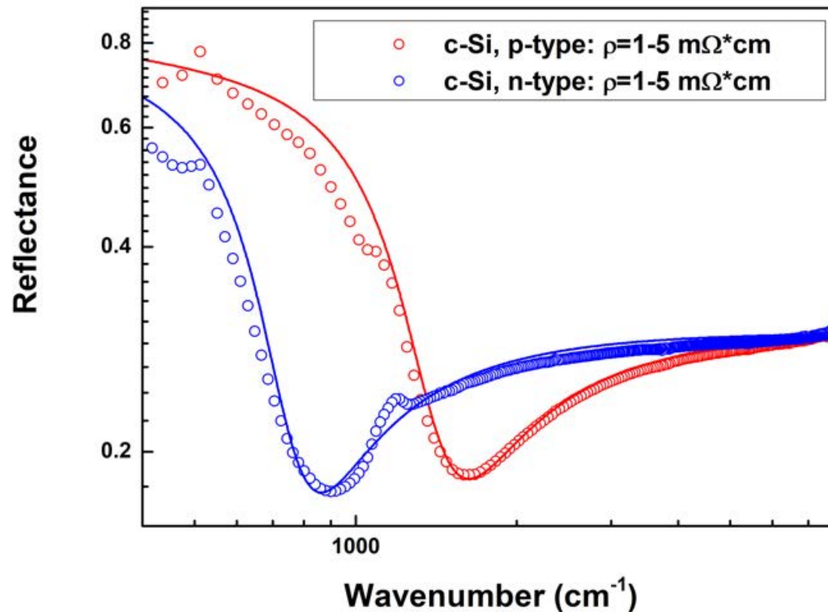

Figure 4.4: Spectra of specular reflectance for n-type (blue circles) and p-type (red circles) c-Si wafers. Lines show their fit using the Drude model (see Eqs. (4.1)-(4.5)).

Fig. 4.5 shows the application of the IR reflectance method to macroporous Si (por-Si-A series). It shows the specular reflectance spectra for low and highly doped por-Si samples, as well as for low and highly doped c-Si substrate. The reflectance spectra both for low and highly doped por-Si are not similar to those for c-Si, and the reflectance values for por-Si exhibit a strong decrease with light frequency. This fact can be explained by light scattering in the por-Si layers, with sizes of the scattering objects considerably smaller than the light wavelength. The difference between the reflectance spectra for the initial and doped samples can be due to a high density of free charge carriers (electrons) in Si nanostructures of the latter sample. The higher reflection for the doped sample in the spectral region below 1000 cm^{-1} seems to be directly related to free charge carriers, since in this region the effect of the light scattering is the smallest.

Note, that the IR reflectance spectra of mesoporous Si (nanocrystal sizes below 50 nm) can be well described within the effective medium model because the light scattering is negligible [147]. However, this approach is hardly applied to Si nanosctructures with size above 50 nm because the light scattering is strong, and spectral dependence of optical losses due to light

Cette thèse est accessible à l'adresse : http://theses.insa-lyon.fr/publication/2019LYSEI129/these.pdf
© [S. Rodichkina], [2019], INSA de Lyon, tous droits réservés

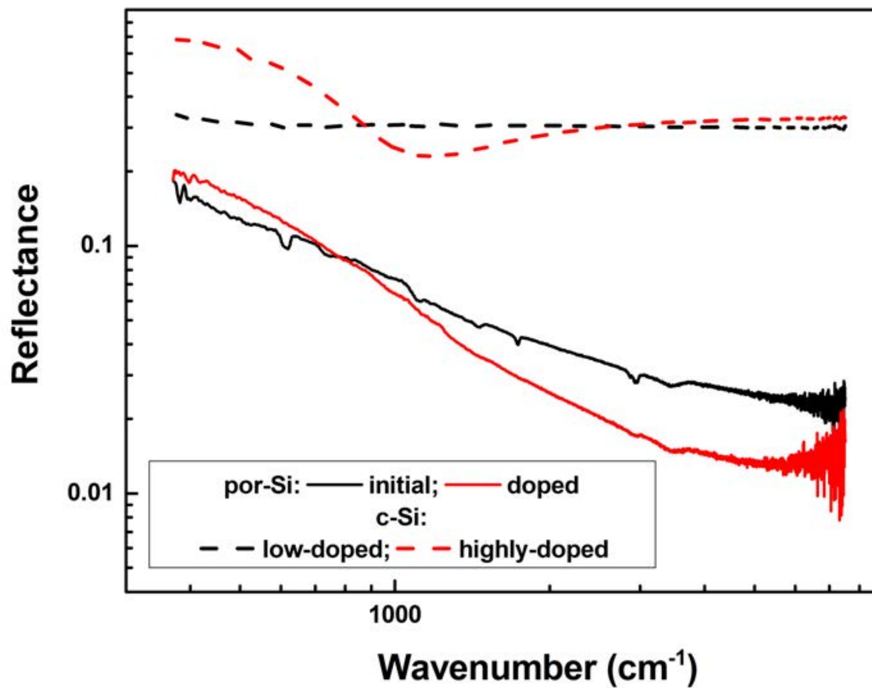

Figure 4.5: Spectra of specular reflectance for low- and highly-doped c-Si wafers (black and red dotted lines, respectively), initial (black line) and doped (red line) macroporous Si samples, prepared for the etching time of 5 min.

scattering is unknown.

b) Attenuated total reflectance spectrosopy

Since the standard reflectance spectroscopy in unsuitable for macroporous Si, the free charge carriers in the por-Si were studied by infrared attenuated total reflectance spectroscopy. Fig. 4.6 shows ATR spectra for initial and additionally doped por-Si layers. The ATR signal for initial por-Si is close to unity in all spectral range that indicates the case of total reflection and implies that the influence of light scattering is negligible. Thus, a decrease of the ATR signal at low frequencies for additionally doped samples can be explained purely by the light absorption related to the free electrons in Si nanocrystals. The absence of the light scattering in the ATR mode implies that optical properties of por-Si in this mode can be described on the basis of the effective medium approximation.

Fig. 4.7 (a) shows the relative ATR spectra for doped por-Si and their fit accordingly to the model (4.1) - (4.5). As previously stated, theoretical values of attenuated total reflectance depend on three parameters: porosity of por-Si p, concentration of free carriers in nanocrystals N (or the plasma frequency ω_p) and parameter g_1, describing the surface damping rate of free carriers. Porosity $p = 70\%$, accordingly to our measurements. The other two parameters, ω_p

Cette thèse est accessible à l'adresse : http://theses.insa-lyon.fr/publication/2019LYSEI129/these.pdf
© [S. Rodichkina], [2019], INSA de Lyon, tous droits réservés

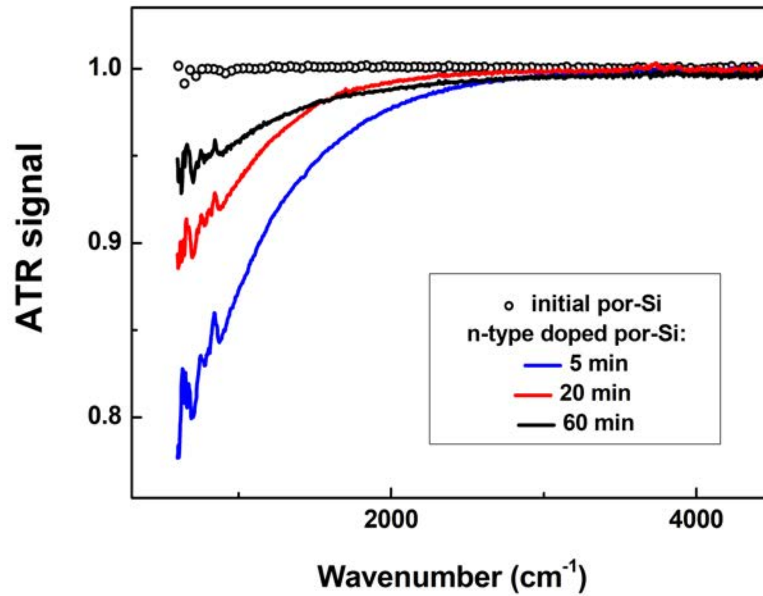

Figure 4.6: ATR spectra for the initial (circles) and doped (lines) por-Si layers prepared for the etching time of 5 (blue), 20 (red) and 60 min (black).

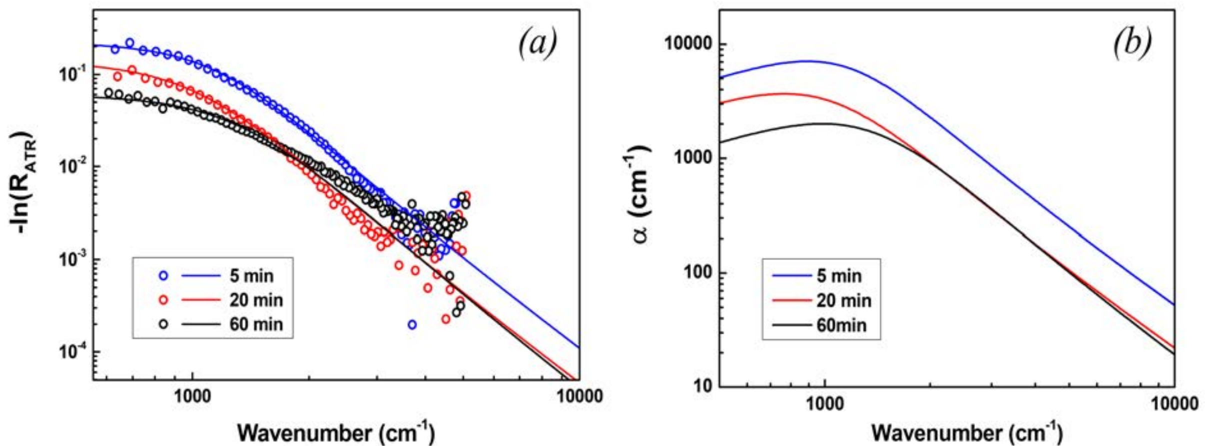

Figure 4.7: (a) Experimental (points) and theoretical (lines) spectra of $-ln(R_{ATR})$, where R_{ATR} are the relative ATR values for additionally doped por-Si layers etched for different time. (b) Calculated spectra of the absorption coefficient (α) for the same por-Si layers.

and g_1, were used as fit parameters. Good theoretical fits, as seen from the Fig. 4.7 (a), give us an experimental evidence that the free charge carrier concentration in por-Si layers can be determined using the IR ATR spectroscopy. Note, that the use of the common Drude model, given by Eq. (4.3) with the constant damping rate g, which gives good results for c-Si, does not describe ATR spectra for por-Si in the high frequency range. This fact implies the strong interaction of the charge carriers in por-Si with the surface of nanocrystals.

Table 4.1 shows an overview of the results of ATR spectra analysis for the studied por-Si layers. As seen from the table, for all samples the electron concentrations in the bulk of Si

Cette thèse est accessible à l'adresse : http://theses.insa-lyon.fr/publication/2019LYSEI129/these.pdf
© [S. Rodichkina], [2019], INSA de Lyon, tous droits réservés

Table 4.1: Sample parameters obtained from the experimental data and from the modeling of IR-ATR spectra for por-Si.

Etching time (min)	**Thickness** (μm)	ω_p (cm^{-1})	g_0 (cm^{-1})	g_1 (cm^{-1})	N (10^{19} cm^{-3})
5	5	3400	368	2400	3.4
20	15	2400	312	2400	1.5
60	20	2100	301	4700	1.3

nanocrystals N is of order of 10^{19} cm^{-3}, which is 4 orders higher than that of the initial c-Si wafers. The electron concentration increases for the por-Si layers with smaller thickness, which can be explained by the smaller effective volume of the layer filled by the same amount of dopant. The values of g_1 are rather high, compared to the values of the bulk scattering rate g_0, and of order of the values of g_1 for mesoporous Si [147], which can be attributed to the additional surface scattering of free carriers on the rough surface of Si nanocrystallites in por-Si. In consistence with this explanation, the largest value of surface scattering parameter was observed for the sample with largest etching time due to continuous formation of smaller nanocrystals (nanoroughness) on the surface of larger nanostructures during the etching [157].

Fig. 4.7 (b) shows the theoretical values of the absorption coefficient (α) in the IR range, calculated as $\alpha = \frac{2\omega}{c} Im(\sqrt{\varepsilon_{PS}})$ by using the parameters from Table 1. The similarity of the line shapes between the spectra of ATR signal and absorption coefficient, shown in Fig. 4.7 (a) and Fig. 4.7 (b), correspondingly, implies that in our case d_{eff} is almost independent of ω, and it can be estimated of the order of 0.1 μm. The frequency-dependent damping described by Eq. (4.5) is obviously responsible for the absorption decrease in the spectral range below 1000 cm^{-1}, which is significantly stronger than it was reported for mesoporous Si with hole concentration about 10^{18} cm^{-3} (see Ref. [152]).

The error bars for determination of N using the ATR technique arise from the error bars of porosity determination and modeling. Fig. 4.8 shows the $-ln(R_{ATR})$ spectrum of por-Si layer (5 min growth) and its modeling with different ω_p. The discrepancy between experimental and theoretical spectra is less than 10%, and the error bars for the electron concentration can be estimated of about 20%. For the ATR technique, one should take into account the mechanical contact quality between a sample and ATR crystal. To exlude this factor, the mechanical contact between porous Si and ATR crystal was applied until the following enhancement did not produce any change in measured spectra.

ATR measurements with powders, which were prepared from detached por-Si layers by

Cette thèse est accessible à l'adresse : http://theses.insa-lyon.fr/publication/2019LYSEI129/these.pdf
© [S. Rodichkina], [2019], INSA de Lyon, tous droits réservés

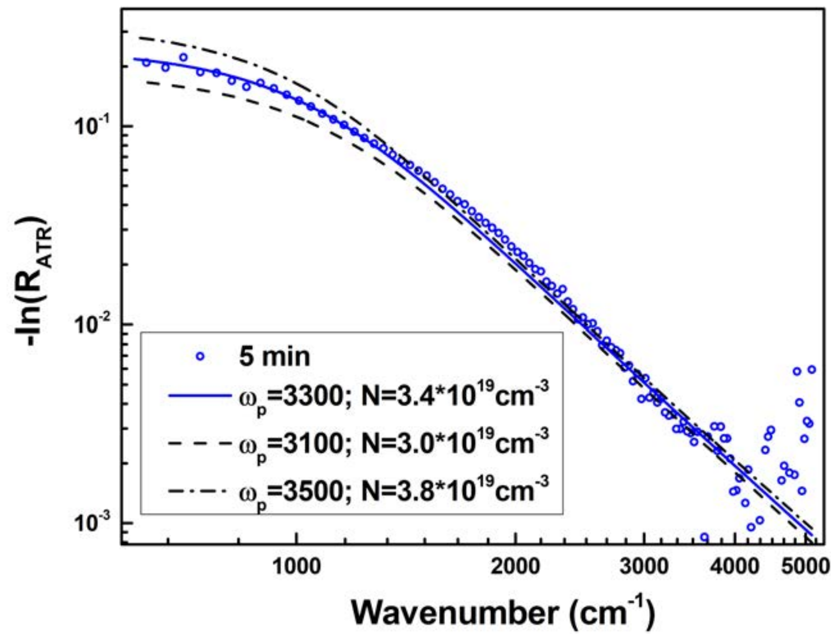

Figure 4.8: Absorption spectrum of por-Si layer (5 min etching) obtained from the ATR data (circles) and modeling results, where the fitting parameter ω_p is varied (lines).

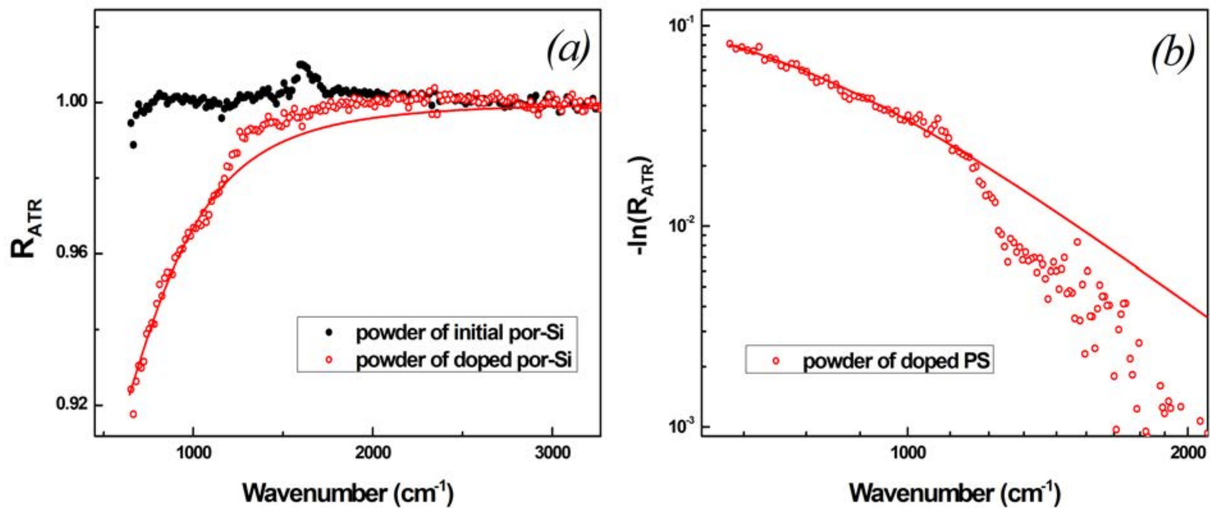

Figure 4.9: (a) ATR spectra for powder of initial (close circles) and doped (open circles) por-Si. (b) Spectra of $-ln(R_{ATR})$ for powder of doped por-Si. Line corresponds to the fit of experimental spectra with the theoretical model assuming $p = 0.9$ and electron concentration of about $2 * 10^{19}$ cm^{-3}.

mechanical grinding, also showed a high level of electron concentration in additionally doped por-Si. Fig. 4.9 shows that, similarly to the doped por-Si on c-Si substrate, the powders of por-Si exhibit a decrease of ATR signal at low wavenumbers. Assuming the high porosity of the investigated powder the free electron concentration in doped por-Si nanocrystals can be estimated as high as 10^{19} cm^{-3}. This fact confirms the high concentration of free charge carriers in Si nanocrystals in the investigated por-Si layers. Discrepancy between experimental data and

Cette thèse est accessible à l'adresse : http://theses.insa-lyon.fr/publication/2019LYSEI129/these.pdf
© [S. Rodichkina], [2019], INSA de Lyon, tous droits réservés

theoretical curve at large wavenumbers can be explained by partial breaking of the effective medium approximation due to stronger light scattering in por-Si powder.

Note, that he obtained high concentration of electrons in Si nanostructures is accompanied with relatively low damping rate and the corresponding Q-factor (the ratio between plasma frequency and damping rate) is about 7, which is only 3 times smaller than for local plasmons in gold [77].

4.1.3 IR-ATR diagnostics of anisotropic SiNWs arrays

It was shown in Sec. 4.1.2 that the IR spectroscopy in specular reflectance geometry is well suited to probe free charge carriers in c-Si, while for Si nanostructures it can be unsuitable because of the strong light scattering. The low light penetration depth in ATR geometry, which uses an evanescent mode of penetrated light, allows to reduce the effect of light scattering in Si nanostructured layers on the IR-ATR spectra. Indeed, Fig. 4.10 (inset) shows that the ATR spectra for undoped SiNWs exhibit the total reflectance ($R_{ATR} \approx 1$) in the studied mid-IR range, and no influence of the light scattering is observed. The decrease in ATR signal for highly-doped SiNWs at low wavenumbers can be, consequently, associated with the light absorption by free charge carriers in SiNWs. Note, a strong decrease in the specular reflectance with the wavenumber in mid-IR range was observed for macroporous silicon with the nanocrystal size $\sim$ 100 nm, which was explained by the light scattering by rather large nanocrystals, but no effect of the light scattering was observed for the ATR spectra for the same samples (see Sec. 4.1.2).

Fig. 4.10 (black line) shows the measured spectrum of $-ln(R_{ATR})$ for highly-doped SiNWs (SiNWs-A series) and its fittings according to the effective medium model with various parameters, given by Eqs. (4.6)-(4.11), (4.3)-(4.5). It can be seen from the figure, that $\sim \omega^{-3}$ dependence, which is typical for our model at high wavenumbers (see Fig. 4.2), can not approximate the experimental spectrum in this spectral range. This fact can be associated with the slight influence of the light scattering at high wavenumbers. Lower experimental values of $-ln(R_{ATR})$ for SiNWs than those given by $\sim \omega^{-3}$ approximation can be explained by lower effective light absorption in the scattering medium due to back-scattering of light, as well as by a change in the spectral dependence of d_{eff} due to the light scattering. Since the absolute divergence between the experimental values of $-ln(R_{ATR})$ and $\sim \omega^{-3}$ approximation is small, the effect of light scattering on ATR reflectance in SiNWs is not observed in the R_{ATR} spectra of SiNWs (see inset in Fig. 4.10). At low wavenumbers, the effect of light scattering is smaller due to the decrease in

Cette thèse est accessible à l'adresse : http://theses.insa-lyon.fr/publication/2019LYSEI129/these.pdf
© [S. Rodichkina], [2019], INSA de Lyon, tous droits réservés

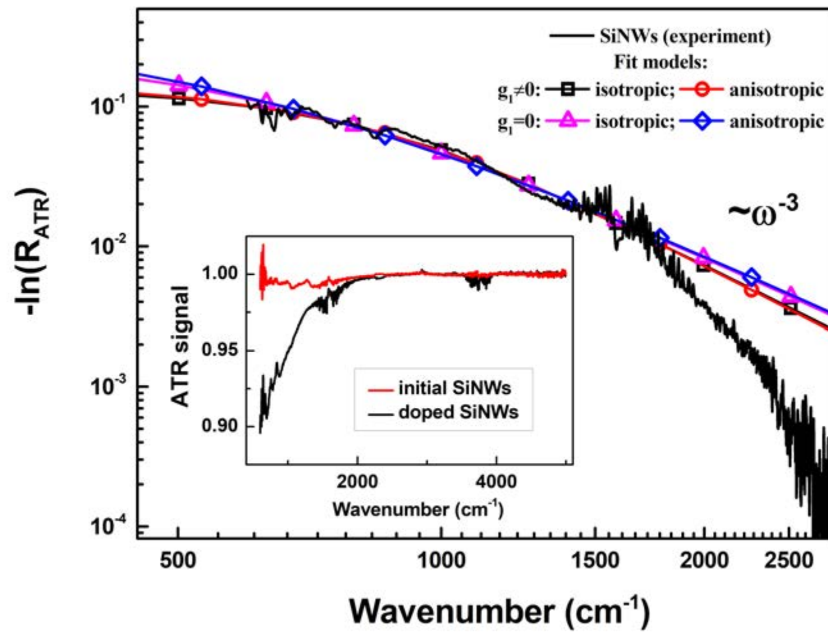

Figure 4.10: Spectrum of $-ln(R_{ATR})$ for highly-doped SiNWs with the length of 4 μm (black line) and its fitting using the anisotropic model with (magenta line) and without (black line) surface scattering of charge carriers, and isotropc model with (red line) and without (blue line) surface scattering of charge carriers. The inset shows the ATR spectra for this SiNWs sample before (red line) and after (black line) the additional doping.

the light scattering cross-section with decreasing light frequency.

Solid lines in Fig. 4.10 show the fits of the ATR spectrum for SiNWs using the anisotropic and isotropic models given by Eqs. (4.6)-(4.11), (4.3)-(4.5) with ($g_1 \neq 0$) and without ($g_1 = 0$) surface scattering of charge carriers in Si nanocrystals. As it can be seen from the figure, the models give almost the same approximation to the experimental spectrum in low wavenumber range. The good fit of the ATR spectrum using the effective medium approximation indicates the negligible light scattering in SiNWs at low wavenumbers. Indeed, in this spectral range the light wavelength is more than 6 μm, which is much larger than the SiNWs diameter of about 100-300 nm. The theoretical models with $g_1 \neq 0$ give better approximation to the experimental spectrum of SiNWs at high wavenumbers than that with $g_1 = 0$, which can indicate considerable surface-related effects in SiNWs. However, the influence of the light scattering on ATR spectra of SiNWs is more pronounced. At that, the use of anisotropic or isotropic model does not influence the resulting fitting curve. Note, that for macroporous Si the isotropic model gives a good approximation in whole mid-IR range in the case of $g_1 \neq 0$ (see Sec. 4.1.2), that can be related to the weaker light scattering in such a system, while the model with $g_1 = 0$ gives insufficient approximation.

Fit parameters of the ATR spectrum for SiNWs with different theoretical models are sum-

Cette thèse est accessible à l'adresse : http://theses.insa-lyon.fr/publication/2019LYSEI129/these.pdf
© [S. Rodichkina], [2019], INSA de Lyon, tous droits réservés

Table 4.2: Sample parameters obtained from the experimental data and from modeling of IR-ATR spectra for SiNWs using the isotropic and anisotropic effective medium approximation.

Fit model	**p**	$\omega_\mathbf{p}$ (10^3 cm^{-1})	$\mathbf{g_0}$ (10^3 cm^{-1})	$\mathbf{g_1}$ (10^3 cm^{-1})	N (10^{19} cm^{-3})
isotropic	0.75	2.5	0.6	0.6	2.6
anisotropic		1.9	0.4	1.5	1.5
isotropic ($g_1 = 0$)		2.5	1.0	0	2.5
anisotropic ($g_1 = 0$)		1.9	0.8	0	1.4

marized in Table 4.2. In this table, the values of the plasma frequency (ω_p) and the free carrier concentration (N), determined by ω_p, are of particular importance. One can see that the values of N obtained using the anisotropic model with $g_1 \neq 0$ and $g_1 = 0$ coincide within the experimental error. Thus, a more simple model with $g_1 = 0$ can be used to determine the free charge carrier concentration in SiNWs. The values of g_0 are higher in the case when $g_1 = 0$, which is consistent with Eq. (4.5). Similar results are observed for the isotropic model.

One should emphasize the difference in the values of N obtained using anisotropic and isotropic models. The determined free charge carrier concentration is about 1.5 times larger for the isotropic model than for the anisotropic one. This difference was already pointed out in the previous section, and it is related to the different dielectric constants for isotropic and anisotropic effective media with the same parameters of Si nanocrystals (see Fig. 4.2). For SiNWs arrays, the anisotropic model is more appropriate. However, both models give the same order of N, and a more simple isotropic model can be used to estimate the free charge carrier concentration in SiNWs samples.

Considering the error bars of N for the IR-ATR method, the main parameter affecting the obtained values of the free charge carrier concentration is the porosity of the samples. Considering both the error bars for porosity of 5% and the inaccuracy of fitting, the total error bars for N in the IR-ATR method are about 20%.

Fig. 4.11 shows the experimental ATR spectra and their fit for p-type highly-doped SiNWs of different length. The spectra were fitted using the anisotropic model with $g_1 \neq 0$. For all SiNWs lengths, the good fit is observed at low wavenumbers, while at high wavenumbers the discrepancy between experiment and modeling is seen, explained by the influence of light scattering. Considering $p = 0.75$, as determined by SEM measurements, the values of free hole concentration in SiNWs are $\sim 10^{19}$ cm^{-3}. The values of the free hole concentration in SiNWs, measured using the IR-ATR technique, will be compared with the ones, measured using the

Cette thèse est accessible à l'adresse : http://theses.insa-lyon.fr/publication/2019LYSEI129/these.pdf
© [S. Rodichkina], [2019], INSA de Lyon, tous droits réservés

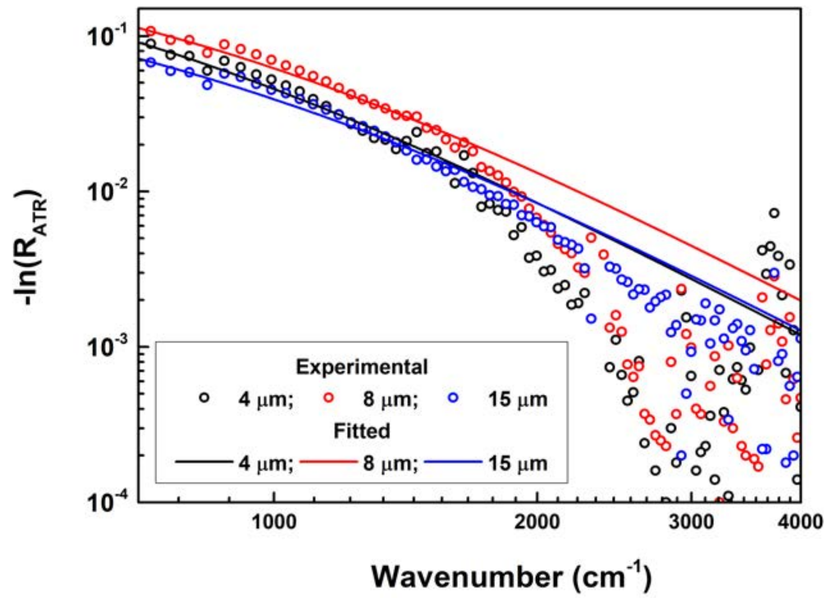

Figure 4.11: Experimental spectra (points) and fitting (lines) of the ATR signal ($-ln(R_{ATR})$) for p-type SiNWs with different length. The fitting was done using Eqs. (4.6)-(4.11), (4.3)-(4.5) considering $g_1 \neq 0$.

Raman spectroscopy, that will be discussed in detail in Sec. 4.3.

4.2 Raman scattering spectroscopy

The one-phonon Raman peak of highly-doped c-Si is modified in comparison with that of low-doped c-Si due to the Fano effect [137], related to the electron-phonon interaction [137, 158]. The Fano effect is much more pronounced in the case of p-type Si than for n-type Si [159]. This effect was used to determine the free hole concentration in p-type c-Si with $N > 10^{20}$ cm^{-3} [160, 161]. Similar modification of the Raman peak was observed in p- and n-type highly-doped SiNWs (see Sec. 1.2.3). The Fano effect together with the phonon confinement was observed in p- and n-type porous SiNWs [162]. This section describes an application of the Raman scattering spectroscopy to determine the free hole concentration in p-type SiNWs in the range of $N = 10^{19} \div 10^{20}$ cm^{-3} and in-depth doping level profiles in SiNWs arrays, using the half-width of the Raman peak for SiNWs.

4.2.1 Raman spectra of highly p-type doped SiNWs

Fig. 4.12 shows the one-phonon Raman spectra of low- and highly-doped SiNWs (SiNWs-A series), as well as of low-doped c-Si substrate. As one can see from the figure, the doped SiNWs

Cette thèse est accessible à l'adresse : http://theses.insa-lyon.fr/publication/2019LYSEI129/these.pdf
© [S. Rodichkina], [2019], INSA de Lyon, tous droits réservés

exhibit an asymmetrical line shape, which is typical for the Fano effect in p-type highly-doped c-Si [137]. The Fano-type Raman line shape indicates the high doping level of SiNWs, and it is explained by a discrete-continuum interaction between the optical phonons and the Raman-active inter-valence band electron excitations [137, 163]. Solid lines in Fig. 4.12 show that the Raman spectra of highly doped SiNWs can be well described by the Fano resonance function [137, 163]:

$$I(\omega) = C\frac{(q+\varepsilon)^2}{1+\varepsilon^2} \tag{4.13}$$

where $\varepsilon = (\omega - \overline{\Omega})/\Gamma$, ω is the Raman shift, q is the asymmetry parameter, Γ is the line width, $\overline{\Omega}$ is the phonon wavenumber (or the phonon frequency) and C is an intensity coefficient. Note, that Lorentzian peak, observed for low doped c-Si and SiNWs, can also be described by Eq. (4.13) with $q = \infty$. The fitting parameters for c-Si substrate, initial and doped SiNWs are listed in Table 4.3.

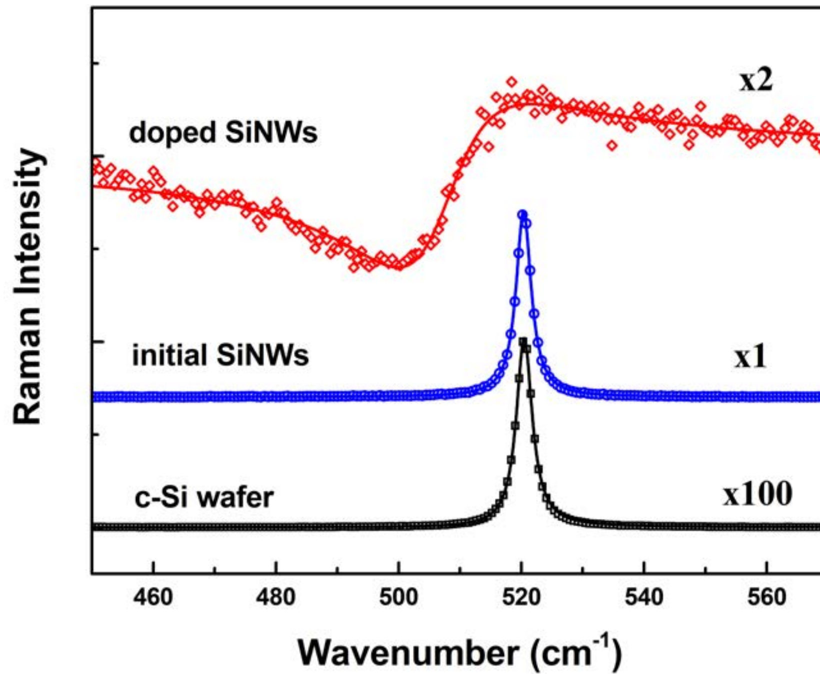

Figure 4.12: Raman spectra of initial and additionally doped SiNWs (length of 8 μm) and corresponding c-Si wafer under excitation with laser wavelength of 632.8 nm. Solid lines are fits of the spectra according to Eq.(4.13).

The data in Table 4.3 show a significant change in all parameters of the Raman peak of SiNWs after doping. The increase in the Raman peak half-width (Γ), usually interpreted as the phonon damping constant [164], is related to the enhanced phonon damping in highly doped SiNWs due to the electron-phonon interaction. One can expect an increase in Γ with the free carrier concentration because of the reinforced electron-phonon interaction. The electron-phonon

Cette thèse est accessible à l'adresse : http://theses.insa-lyon.fr/publication/2019LYSEI129/these.pdf
© [S. Rodichkina], [2019], INSA de Lyon, tous droits réservés

Table 4.3: Raman line shape parameters for c-Si wafers, initial and doped SiNWs (length of 8 μm) for different laser wavelengths, obtained by fitting the Raman spectra with Eq.(4.13)

λ (nm)	Γ (cm^{-1})			q		$\overline{\Omega}$ (cm^{-1})		Ω_{max} (cm^{-1})
	c-Si	initial SiNWs	doped SiNWs	c-Si, initial SiNWs	doped SiNWs	c-Si, initial SiNWs	doped SiNWs	doped SiNWs
632.8	1.6	1.5	10.2	∞	0.7	520.5	511.5	521.5
514.5	1.8	1.9	9.6		2.0		512.8	516.1
473.0	2.0	2.3	9.9		4.6		510.9	513.0

interaction is also responsible for a decrease in the phonon wavenumber $\overline{\Omega}$ for highly doped SiNWs. The Raman peak asymmetry parameter $(1/q)$ is proportional to a ratio of Raman matrix elements for pure-electron and one-phonon scattering [137, 159]. Thus, a decrease in q with increasing doping of SiNWs is related to an increase in the electron Raman scattering cross-section. The antiresonance on the low-wavenumber side of Raman line for doped SiNWs, corresponding to $q > 0$, is consistent with p-type Boron doping of SiNWs [137, 159]. Note that n-type doping of c-Si is known to lead to $q < 0$ [159].

It can be also seen from Fig. 4.12 that the intensity of Raman scattering exhibits a strong increase in the case of low doped SiNWs arrays, in comparison with c-Si wafers, which is related to the strong light scattering in SiNWs arrays [165, 166]. The Raman intensity for the highly doped SiNWs is about two times lower than for the initial ones, which is caused both by the Fano effect [163] and absorption of the excitation light by free charge carriers [167].

The identical Raman peaks for low doped SiNWs and c-Si wafers (see Fig.4.12 and Table 4.3) indicate that SiNWs maintain the c-Si crystalline structure. Size effects, i.e. phonon confinement, which are known to lead to a modification of Raman spectra for SiNWs [168, 169], are nearly absent because the cross-sectional sizes of SiNWs are more than 100 nm. One should take into account that only longitudinal optical phonons can be observed in the Raman measurements from (100) c-Si surface in backscattering geometry [140]. The strong light scattering in SiNWs breakes up this selection rule, and both the longitudinal and transverse optical phonon scattering can be observed. The latter effect does not affect the Raman line half-width for SiNWs, that is confirmed by the same spectral half-width for c-Si substrate and initial SiNWs (see Table 4.3).

Fig. 4.13 shows the Raman spectra for doped SiNWs measured at different excitation wavelengths and their fit with Eq. (4.13). The fitting parameters for Raman spectra of c-Si wafers, initial and doped SiNWs at different laser wavelength are presented in Table 4.3. Fig. 4.13 and Table 4.3 reveal the strong dependence of the Raman line shape for doped SiNWs

Cette thèse est accessible à l'adresse : http://theses.insa-lyon.fr/publication/2019LYSEI129/these.pdf
© [S. Rodichkina], [2019], INSA de Lyon, tous droits réservés

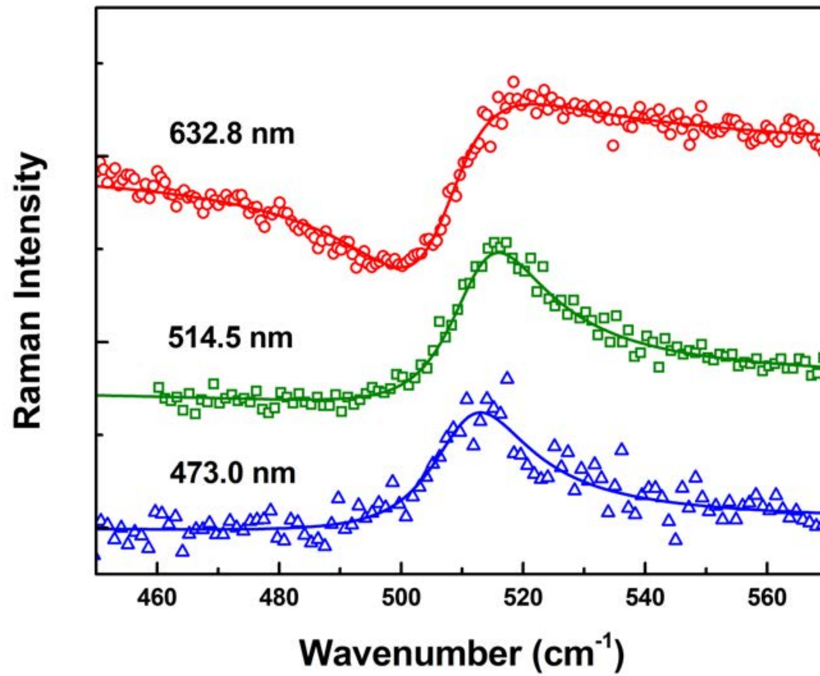

Figure 4.13: Raman spectra of highly doped SiNWs with the length of 8 μm for different laser wavelengths of 473, 514.5 and 632.8 nm. Solid lines are fits of the spectra according to Eq. (4.13).

on excitation laser wavelength that is typical for the Fano effect [170]. However, the values of Γ and $\overline{\Omega}$ for doped SiNWs, as well as for initial SiNWs and c-Si wafers, are independent of excitation wavelength, because Γ and $\overline{\Omega}$ are related to the real and imaginary parts of the phonon self-energy in crystal, respectively, which represents an intrinsic property of the studied material [137, 164].

The change of the Raman line shape for SiNWs with increasing laser wavelength can be described by $1/q$ parameter. Note, the value of q^2 is proportional to the ratio of transition probabilities for pure-electron and pure-phonon Raman scattering [137, 171]. Given the expressions for the Raman tensors $R_{p,e}$ for the pure-phonon and pure-electron scattering [171] and considering $q^2 \propto |R_p/R_e|^2$, one can see that R_p increases more rapidly than R_e while the laser frequency approaches the resonance near the direct gap of Si (3.4 eV). This fact explains the increase in q with increasing laser frequency (see Table 4.3). For low doped c-Si wafers and initial SiNWs the pure-electron Raman tensor is close to zero and $1/q = 0$ at all laser wavelengths. Since the asymmetry parameter q is dependent on the laser wavelength, and the maximum of the Fano function, obtained from Eq. (4.13), is equal to $\Omega_{max} = \overline{\Omega} + \Gamma/q$ [137], the spectral position of Fano peak maximum for SiNWs increases with laser wavelength (see Fig. 4.13). As can be seen from Table 4.3, the observed values of Ω_{max} are in good agreement with the above formula

Cette thèse est accessible à l'adresse : http://theses.insa-lyon.fr/publication/2019LYSEI129/these.pdf
© [S. Rodichkina], [2019], INSA de Lyon, tous droits réservés

within the experimental error.

a) Role of c-Si substrate and SiNWs length

The depth of probed SiNWs layer is determined by the light penetration depth in SiNWs array. Fig. 4.14 shows the Raman spectrum for the intermediately doped array of SiNWs with a length of 15 μm on a c-Si substrate, as well as for detached powder of the same SiNWs. It can be seen from the figure (upper spectrum, solid line), that a single Fano peak (Eq. (4.13)) can not fit the Raman spectrum for SiNWs array, which can be explained by the influence of the c-Si substrate. At the same time, the Raman spectrum for detached SiNWs is well fitted by a single Fano peak. Consequently, the Raman signal from doped nanowires represents a Fano resonance peak, while the Raman signal from c-Si substrate can be described by a Lorentzian peak. Fig. 4.14 (upper spectrum, dashed line) shows, that such two peaks approximate well the Raman spectrum for SiNWs/c-Si structure. The stronger Fano resonance for SiNWs arrays than for powders of detached SiNWs indicates the non-uniform doping profile along SiNWs with higher free hole concentration in upper layer of SiNWs array, that will be discussed in next sections. The absence of c-Si substrate peak in Raman spectra for SiNWs arrays with a distinct Fano resonance (see Fig. 4.13) is related to a high free hole concentration in these SiNWs, which results in low light penetration depth due to the strong free carrier absorption.

One can use the relative intensity of a c-Si substrate peak to estimate the effective light penetration depth for SiNWs arrays (d_{eff}). In general, d_{eff} is determined by the light scattering and the light absorption in SiNWs array. Considering the negligible influence of free charge carriers on the light penetration depth in SiNWs samples with a relatively strong c-Si substrate contribution, the light penetration depth in SiNWs arrays can be estimated from the formula

$$I_{c-Si}/I_{total} \sim exp(-L/d_{\mathrm{eff}}), \tag{4.14}$$

where I_{c-Si}/I_{total} is the relative integrated intensity of a c-Si peak in the total Raman peak of SiNWs samples, L is the length of SiNWs. An inset in Fig. 4.14 shows the dependence of I_{c-Si}/I_{total} on SiNWs length for a series of SiNWs samples and its fit with Eq. (4.14). The estimated light penetration depth in low and intermediately doped SiNWs arrays is of about 11 μm for the light wavelength of 632.8 nm. One can compare the obtained value with the light penetration depth of 5 μm for low doped c-Si [172], as well as with the theoretical value $d_{\mathrm{eff}} = 8$ μm for low doped SiNWs, considered within the effective medium approximation [173].

Cette thèse est accessible à l'adresse : http://theses.insa-lyon.fr/publication/2019LYSEI129/these.pdf
© [S. Rodichkina], [2019], INSA de Lyon, tous droits réservés

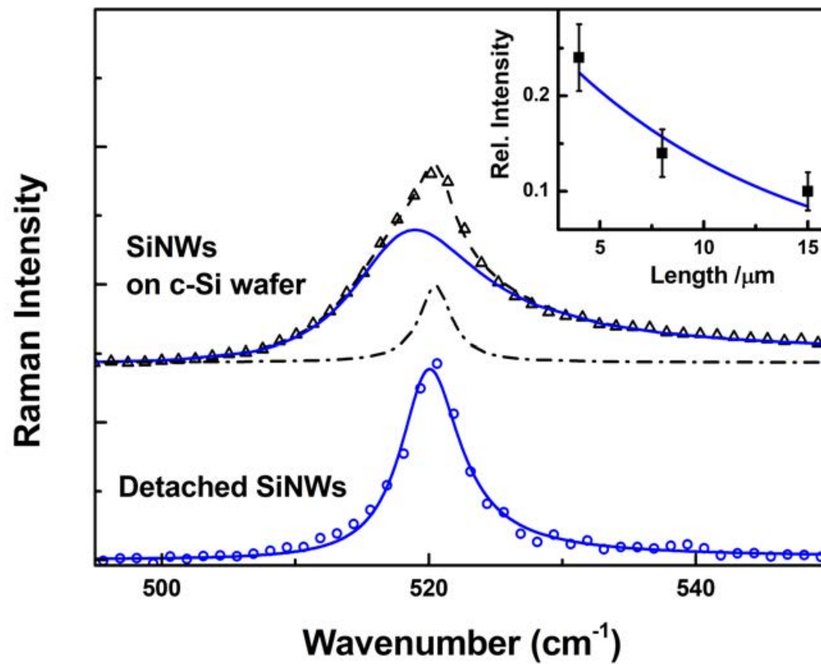

Figure 4.14: Raman spectra for SiNWs array on c-Si substrate (triangles) and detached SiNWs (circles). SiNWs length is of 15 μm. Solid lines represent fits of the spectra by Eq.(4.13). Contribution of c-Si substrate and fit of the total Raman spectrum of SiNWs on c-Si substrate are given by dash-dotted and dashed lines, correspondingly. The inset shows dependence of the relative integrated intensity of c-Si substrate peak in the total Raman spectrum for doped SiNWs on nanowire's length, solid line represents the fit of this dependence with Eq.(4.14). Laser wavelength is 632.8 nm.

The higher experimental values of the light penetration depth in SiNWs arrays indicate an effect of the strong light scattering in SiNWs arrays, that agrees well with the enhanced Raman intensity for low doped SiNWs (see Fig. 4.12). For highly-doped SiNWs arrays (see Fig. 4.13), the absence of c-Si substrate contribution to the Raman spectra allows us to estimate the effective light penetration depth to be below 8 μm.

4.2.2 Dependence of Fano effect on free charge carrier concentration

Modification of the spectral shape of the Raman spectrum of doped SiNWs allows us to estimate the free hole concentration. The peak half-width is the most convenient parameter for this purpose, since it does not depend on the laser wavelength and can be accurately determined for all hole concentrations. Other parameters such as $\overline{\Omega}$ and $1/q$ are not entirely suitable for low hole concentrations due to a high inaccuracy of their determination [160, 161].

The theoretical dependence of the Fano peak half-width on the free hole concentration in c-Si can be determined as follows. It was shown that Γ is proportional to the combined density

Cette thèse est accessible à l'adresse : http://theses.insa-lyon.fr/publication/2019LYSEI129/these.pdf
© [S. Rodichkina], [2019], INSA de Lyon, tous droits réservés

of states for the continuum of inter-valence-band transitions at the Fermi energy ($\rho(\mu)$), and the latter parameter contains all the information about the carrier concentration dependence of Γ (see for details Ref. [137]). Under the assumption of parabolic valence bands, $\rho(\mu)$ is proportional to $(N_h - N_l)/\mu$, where N_h and N_l are the number of carriers per unit volume in the upper and lower valence bands, respectively, μ is the Fermi energy. Using the density of states per unit volume for the parabolic isotropic energy bands in the three-dimensional case and considering that the total number of carriers $N = N_l + N_h$, one can obtain $\mu \propto N^{2/3}$, $N_{l,h} \propto N$ and $\rho(\mu) \propto N^{1/3}$. Thus, the dependence of Γ on N in p-type Si can be approximated by the following expression:

$$\Gamma = C_1 + C_2 N^{1/3}, \tag{4.15}$$

where $C_{1,2}$ are the coefficients, which can be found experimentally using the Raman spectra for p-type Si with the different hole concentration measured in the same conditions.

Accordingly to Ref. [137], the discussed determination of N is valid when μ is close to $\hbar\Omega$. Therefore, Eq. (4.15) is correct in the certain range of carrier concentration, e.g. for p-type c-Si at $T = 77$ K it is valid in the range of $N = 6 \cdot 10^{18} \div 1.6 \cdot 10^{20}$ cm^{-3}, while it can not be applied for $N = 4 * 10^{20}$ cm^{-3} [137]. At $T = 300$ K, since the Fermi energy in p-type Si with the given N decreases with the temperature [174], Eq. (4.15) is expected to be valid for higher concentrations. Using the dependence of the Fermi energy on the hole concentration in p-type Si at $T = 300$ K [170], one can see that $\mu = \hbar\Omega = 65$ meV corresponds to $N = 7 \cdot 10^{19}$ cm^{-3}, therefore we expect Eq. (4.15) to be valid for N of the order of $10^{19} \div 10^{20}$ cm^{-3}.

Eq. (4.15), established for c-Si, can be applied to Si nanostructures of different morphology with a diameter of more than 10 nm, for which there is no effect of the phonon confinement for the Raman scattering.

Fig. 4.15 (open points) shows the experimental dependence of the Fano peak half width on the free hole concentration for c-Si and its fit with Eq. (4.15). One can see from the figure, that Eq. (4.15) fits well the experimental data for the carrier concentration range of $N = (0.7 \div 40) \cdot 10^{19}$ cm^{-3}. However, outside this range, especially at low hole concentrations, it can be invalid.

In order to determine the free hole concentration in SiNWs, Raman spectra of SiNWs/c-Si structures were fitted by the Fano and Lorentzian peaks, corresponding to SiNWs and c-Si substrate, respectively (see Fig. 4.14). The half width of the Fano peak was used to determine the free hole concentration by Eq. (4.15), the obtained values for different SiNWs samples are

Cette thèse est accessible à l'adresse : http://theses.insa-lyon.fr/publication/2019LYSEI129/these.pdf
© [S. Rodichkina], [2019], INSA de Lyon, tous droits réservés

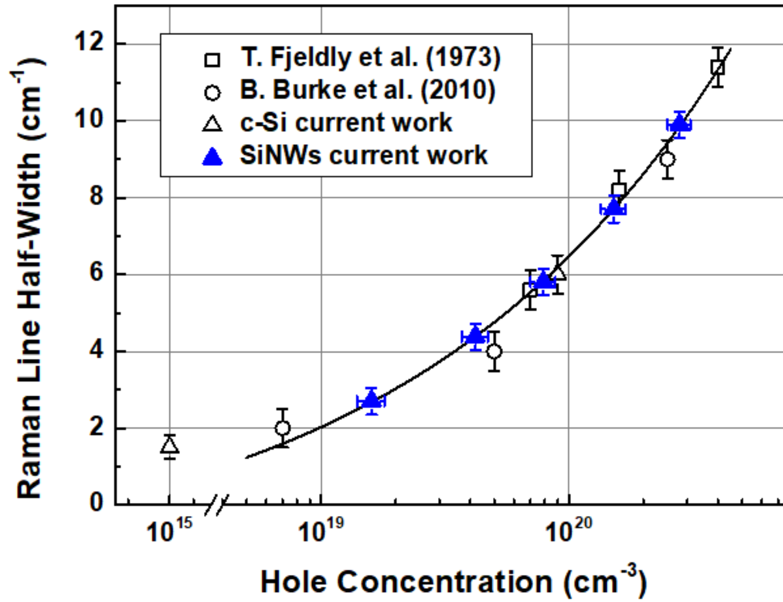

Figure 4.15: Dependence of the Raman line half-width (Γ) on the free hole concentration for c-Si (open squares, circles and triangles) and SiNWs (blue triangles). Line is a fit by Eq.(4.15) with $C_1 = -1.8$ cm^{-1} and $C_2 = 3.8$.

shown in Fig. 4.15 (blue triangles). As can be seen for the figure, the hole concentration values in SiNWs as high as $N = 10^{19} \div 10^{20}$ cm^{-3} can be obtained by the used spin-on doping method. It should be noted that the determined concentration values correspond to the upper parts of SiNWs arrays with a thickness of about d_{eff}, probed by the laser radiation with a given wavelength (see Sec. 4.2.1).

4.2.3 In-depth profiles of doping level for SiNWs arrays

A comprehensive characterization of SiNWs requires the determination of the free hole concentration in-depth profile. Such profiles for SiNWs arrays are useful for optimization of SiNWs-based solar cells and thermoelectric devices. Secondary ion mass spectrometry (SIMS) technique is usually used to profile the dopant concentration in SiNWs with spatial resolution of ~ 1 nm [55]. The main obstacle in using SIMS for SiNWs characterization is that it measures the total dopant concentration in SiNWs instead of free carrier concentration [175], which is responsible for the electrical conductivity of nanowires. The values of the dopant and free charge carrier concentration in SiNWs can significantly differ due to a dielectric mismatch between the wire interior and the surrounding air, as well as due to surface trap states (see Sec. 1.4). Thus, the

Cette thèse est accessible à l'adresse : http://theses.insa-lyon.fr/publication/2019LYSEI129/these.pdf
© [S. Rodichkina], [2019], INSA de Lyon, tous droits réservés

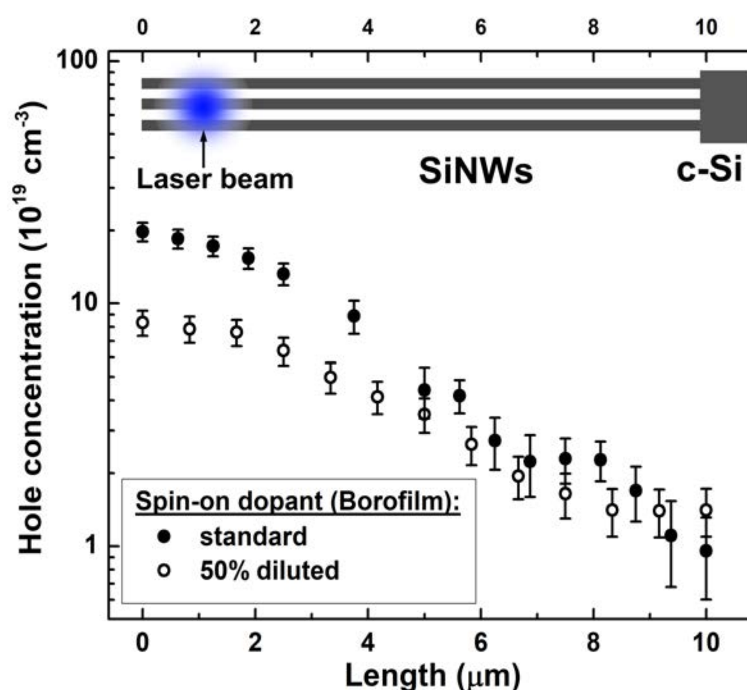

Figure 4.16: Profiles of the free charge carrier concentration in arrays of doped SiNWs (length of 10 μm). The doping was done using the standard spin-on dopant (solid circles) and 50% diluted one with acetone (open circles). The inset illustrates the Raman mapping technique.

micro-Raman spectroscopy, where the spatial resolution below 1 μm can be achieved, is a very useful non-destructive technique to study the free carrier concentration profile in SiNWs. Such a profile for SiNWs (SiNWs-C series) was obtained by mapping the cross section of SiNWs/c-Si structure, as shown in Fig. 4.16. The spatial resolution of the method is determined by the laser beam diameter, which in our case was about 2 μm. The figure shows profiles of free carrier concentration for SiNWs samples, doped using the standard spin-on dopant and 50 % diluted one with acetone. The decrease in the free carrier concentration toward the SiNW/c-Si interface can be seen, and it is explained by limited penetration of the doping agents into the layer depth. The dilution of the spin-on dopant leads to a decrease in the absolute value of N, while its profile does not change significantly.

4.3 Comparison of IR-ATR and Raman techniques

This section describes the comparison of the IR-ATR and Raman scattering techniques for determination of free charge carrier concentration in p- and n-type SiNWs arrays.

Cette thèse est accessible à l'adresse : http://theses.insa-lyon.fr/publication/2019LYSEI129/these.pdf
© [S. Rodichkina], [2019], INSA de Lyon, tous droits réservés

4.3.1 p-type SiNWs arrays

Fig. 4.11 shows the experimental ATR spectra and their fit for p-type highly-doped SiNWs (SiNWs-A series) of different length. The free hole concentration in SiNWs was determined by fitting of the ATR spectra using the anisotropic effective medium approximation and Drude model for free charge carriers, modified to describe the additional scattering of free charge carriers by the surface of Si nanocrystals (see Sec. 4.1.3). Fig. 4.17 shows the one-phonon Raman spectra for the same SiNWs samples. The Raman spectra for SiNWs arrays on c-Si substrate were deconvoluted to the asymmetric Fano peak and Lorentzian peak, corresponding to the doped SiNWs and c-Si substrate, respectively, the excitation depth in SiNWs is estimated of about 10 μm for 632.8 nm excitation (see Sec. 4.2.1). The free hole concentration in SiNWs was determined using the dependence of half-width of the Fano peak on free hole concentration for c-Si (see Sec. 4.2.2).

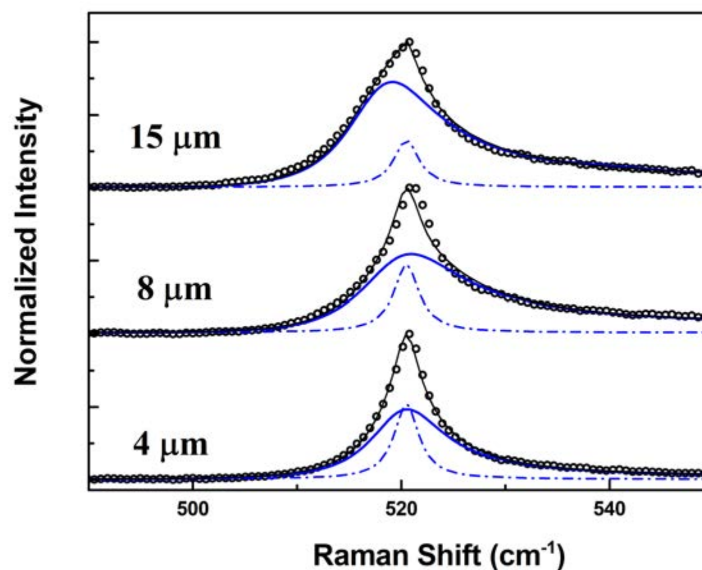

Figure 4.17: Normalized Raman spectra for SiNWs with different length (circles). Blue lines correspond to the Raman peaks for doped SiNWs (solid lines) and c-Si substrate (dash-dotted lines). Black lines show the total fit of the Raman spectra for SiNWs samples. Excitation wavelength is of 632.8 nm.

The free hole concentrations in SiNWs, which are determined from both the IR-ATR data and Raman spectra, are summarized in Table 4.4. The same order of free hole concentration estimated according to IR-ATR and Raman measurements indicates that optical methods are well applicable for an express-diagnostics of the electrical properties of SiNWs. It can be seen from the table that the IR-ATR spectroscopy underestimates the values of N about 4 times in comparison with

Cette thèse est accessible à l'adresse : http://theses.insa-lyon.fr/publication/2019LYSEI129/these.pdf
© [S. Rodichkina], [2019], INSA de Lyon, tous droits réservés

the Raman results. This difference can be associated with the porous morphology of the top of SiNWs (see Sec. 3.1.1). Since the SiNWs diameter is smaller at SiNWs tips, the actual porosity of SiNWs layer in contact with ATR crystal is higher than that measured by SEM. This result is particularly important for SiNWs, fabricated by Ag-assisted MACE, for which SiNWs with rough surface are usually obtained (see Sec. 1.1). SiNWs fabricated, for example, by Au-assisted MACE or reactive-ion etching usually exhibit no diameter variation along nanowires [176, 177], and the IR-ATR method should give more accurate results for such SiNWs arrays. The Raman scattering method in application to SiNWs does not have such a limitation, since the Raman peak for SiNWs with diameter more than 10 nm is independent of their shape and porosity of SiNWs array. Thus, for MACE-SiNWs the values of the free hole concentration obtained by the Raman spectroscopy method are more reliable. It is interesting to compare the values of N, obtained by IR-ATR technique assuming higher porosity at SiNWs tips ($p = 0.9$) and Raman technique. In such case, the value of $N = 4.6 * 10^{19}$ cm^{-3} for 4 μm SiNWs, obtained using IR-ATR method, is close to that obtained using Raman spectroscopy. The difference between the values of N determined using IR-ATR and Raman methods increases with the length of SiNWs, and for 15 μm SiNWs the values of N are of $4.6 * 10^{19}$ cm^{-3} and $N = 7.9 * 10^{19}$ cm^{-3} for the IR-ATR and Raman methods, correspondingly. This fact is consistent with our explanation of the inaccuracy of the IR-ATR method due to porous tips of SiNWs, since the porosity of SiNWs tips increases during the etching.

Table 4.4: Free charge carrier concentration in p-type SiNWs of different length obtained from the modeling of the IR-ATR spectra of SiNWs considering the anisotropic effective medium and $g_1 \neq 0$, as well as from the Raman spectra using the Fano peak half-width.

Length (μm)	**Porosity** (from SEM)	$\boldsymbol{N}$ (10^{19} cm^{-3}) IR-ATR	$\boldsymbol{N}$ (10^{19} cm^{-3}) Raman
4		1.4	4.2
8	0.75	1.9	8.3
15		1.2	7.9

4.3.2 n-type SiNWs arrays

Fig. 4.18 (a) shows the ATR spectra of n-type doped SiNWs with different length (SiNWs-B series). The ATR spectra of n-type SiNWs are similar to those for p-type SiNWs, which demonstrates that the IR-ATR method is not sensitive to the type of free charge carriers in SiNWs. Accordingly to Eqs. (4.6)-(4.11), (4.3)-(4.5), the modeling of ATR spectra for n- and p-type

Cette thèse est accessible à l'adresse : http://theses.insa-lyon.fr/publication/2019LYSEI129/these.pdf
© [S. Rodichkina], [2019], INSA de Lyon, tous droits réservés

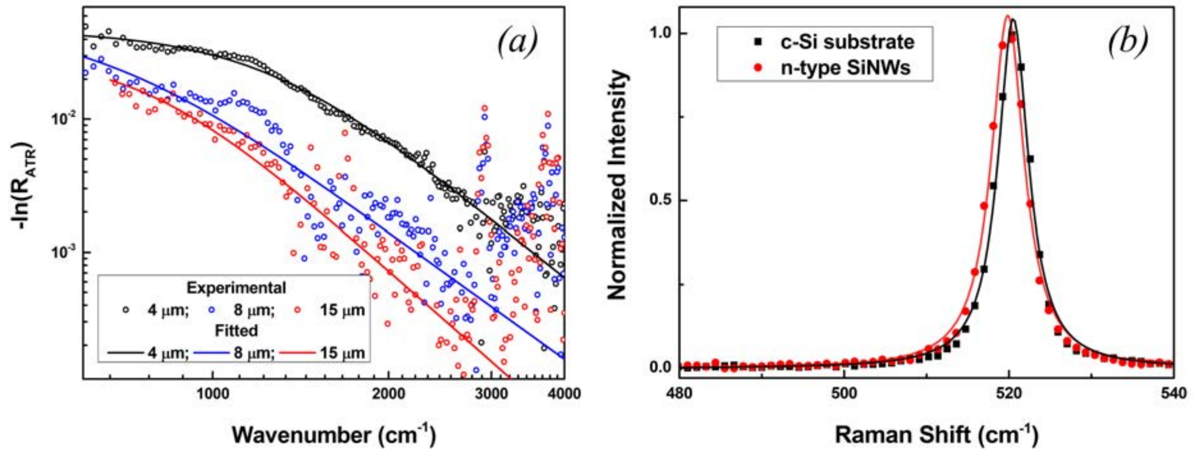

Figure 4.18: (a) Experimental spectra (points) and fitting (lines) of the ATR signal ($-ln(R_{ATR})$) for n-type SiNWs with different length. The fitting was done using Eqs. (4.6)-(4.11), (4.3)-(4.5) considering $g_1 \neq 0$. (b) Normalized Raman spectra for highly-doped n-type SiNWs and of initial c-Si substrate.

SiNWs differs only in the effective mass of charge carriers, which, in turn, is not large. The ATR spectra for n-type SiNWs were fitted using the anisotropic model with $g_1 \neq 0$, and one can see from Fig. 4.18 (a) that, unlike for p-type SiNWs (see Fig. 4.11), the fit is good in the entire studied range. Note, that the model with $g_1 = 0$ gives worse approximation, which is related to the surface scattering of charge carriers in SiNWs. The determined free electron concentration in n-type SiNWs is of the order of 10^{18} cm^{-3}, while the real values of N are several times higher because of the low porosity of SiNWs tips, as it was established in the previous section. The good fit of the ATR spectra for moderately-doped n-type SiNWs at high wavenumbers, in contrast to highly-doped p-type SiNWs, can be associated with lower values of N. Indeed, the conditions of total reflectance are broken for doped SiNWs due to free carrier absorption. The energy flux along z-axis for the transmitted light wave for doped SiNWs is not equal to zero, and the latter is scattered and absorbed in the SiNWs array. The light scattering in SiNWs array increases with the energy flux along z-axis for transmitted wave, which in turn increases with the free charge carrier concentration in SiNWs. This mechanism is not described in the model Eqs. (4.6)-(4.11), (4.3)-(4.5), which considers SiNWs arrays within the effective medium approximation. At that, the increase in free charge carrier concentration leads to the increase in free carrier absorption, that suppresses the light scattering in SiNWs array by decreasing the light penetration depth. For studied SiNWs, the high free charge carrier concentration promotes the effect of light scattering in the ATR spectra (see Fig. 4.11). It is important to note the minor influence of the light scattering on ATR spectra of SiNWs, because the absolute discrepancy between the experimental spectra and fits is small, and the effective medium approximation

Cette thèse est accessible à l'adresse : http://theses.insa-lyon.fr/publication/2019LYSEI129/these.pdf
© [S. Rodichkina], [2019], INSA de Lyon, tous droits réservés

describes well the ATR spectra at low wavenumbers.

The difference in the free charge carrier concentrations in n- and p-type SiNWs can be explained by the use of initially low p-type doped SiNWs. The free electron concentration in n-type SiNWs has been increased by increasing the amount of the dopant solution deposited at SiNWs surface. For this, the spin-coating deposition and drying of the dopant solution were applied several times before RTA annealing. However, after the doping procedure, the residual polymer film at the surface of SiNWs was formed, which could not be removed by HF. This film influences the dielectric constant of SiNWs sample, thus the highly-doped n-type SiNWs sample was studied only by Raman spectroscopy.

Fig. 4.18 (b) shows the one-phonon Raman spectra for n-type highly-doped SiNWs and low-doped c-Si substrate. It can be seen that n-type SiNWs exhibit a slightly asymmetric Fano-type peak with an anti-resonance at high wavenumber side, and the following conclusions can be made. Firstly, the antiresonance at the high-wavenumber side of the Raman peak is consistent with n-type doping of SiNWs [159], while p-type doped SiNWs exhibit the antiresonance at the low-wavenumber side of Raman peak [137]. Thus, the Raman scattering technique allows us to distinguish the type of free charge carriers in SiNWs. Secondly, it is known that the Fano resonance in n-type c-Si, and consequently in n-type SiNWs, can occur only if $N > 5 * 10^{19}$ cm^{-3} [159, 160]. High threshold of the free charge carrier concentration, required to observe the Fano effect in n-type SiNWs, in contrast to p-type SiNWs, is explained by the difference in the band structures of conduction and valence electron bands in Si, so that for n-type SiNWs the overlap of energies between the one-phonon and inter-conduction-band electron transitions takes place only if the Fermi level is above a rather high critical value [159, 160]. Therefore, one can conclude the high doping level in investigated highly-doped SiNWs above $N = 5 * 10^{19}$ cm^{-3}. Thirdly, it is important to highlight that the Fano peak half-width for n-type SiNWs, as well as the other peak parameters, almost coincide with those for Lorentzian c-Si peak, that does not allow the precise determination of the free electron concentration in SiNWs by Raman spectroscopy. This fact is related to the smaller electron-phonon interaction matrix element in the case of n-type SiNWs than for p-type SiNWs [159]. Overall, the Raman scattering technique in the case of n-type SiNWs allows us to probe values $N > 5 * 10^{19}$ cm^{-3}, but the precise determination of N is complicated.

Cette thèse est accessible à l'adresse : http://theses.insa-lyon.fr/publication/2019LYSEI129/these.pdf
© [S. Rodichkina], [2019], INSA de Lyon, tous droits réservés

4.4 Conclusions to Chapter 4

a) Infrared spectroscopy of por-Si and SiNWs arrays

The free charge carrier concentration in p- and n-type SiNWs was determined using the IR spectroscopy in attenuated total reflectance mode. The specular reflectance spectra for por-Si and SiNWs with diameter 100-300 nm were strongly affected by the light scattering by nanocrystals. Therefore, they could hardly be described theoretically due to unknown spectral dependence of optical losses due to light scattering. The IR-ATR spectra for SiNWs were fitted using both the isotropic and anisotropic effective medium approximation and Drude model for free charge carriers, modified to consider the additional charge carrier scattering by nanocrystal boundaries. The values of free charge carrier concentration in SiNWs, obtained using the isotropic effective medium model, were found to be 2-3 times higher than those, obtained using the anisotropic effective medium model, which was explained by the different effective dielectric constants of SiNWs in the case of anisotropic and isotropic models. The anisotropic effective medium model is more appropriate for SiNWs, while the isotropic one is suitable for por-Si layers. The estimated light penetration depth in highly-doped por-Si and SiNWs is of 0.1-1 μm. The free charge carrier concentrations in the p- and n-type doped Si nanocrystals of the top layer of por-Si and SiNWs of the order of $10^{18} \div 10^{20}$ cm^{-3} were measured. The error bars for the IR-ATR method are estimated of about 20 %. The obtained values of N for MACE-SiNWs can be underestimated, because the porosity at SiNWs tips in contact with ATR crystal is higher than the average porosity of SiNWs array.

b) Raman scattering spectroscopy of p-type doped SiNWs arrays

The Raman scattering spectroscopy was applied to determine the free charge carrier concentration and in-depth doping level profiles in p-type doped SiNWs arrays. The strong modification of the one-phonon Raman line for SiNWs after the p-type doping was observed and explained by the Fano resonance between the one-phonon and electron Raman scattering. The free hole concentration in SiNWs was determined in the range of $N = 10^{19} \div 10^{20}$ cm^{-3}, using the Fano peak half-width. The error bars of the Raman technique are about 10 %. The presented Raman technique is suitable for Si nanostructures of various morphology with the size of nanocrystallites more than 10 nm, for which the phonon confinement is negligible. The micro-Raman mapping was shown to be an efficient technique to determine the in-depth profiles of

Cette thèse est accessible à l'adresse : http://theses.insa-lyon.fr/publication/2019LYSEI129/these.pdf
© [S. Rodichkina], [2019], INSA de Lyon, tous droits réservés

free hole concentration in SiNWs arrays. For n-type SiNWs, the free electron concentration in the range of $N = 10^{19} \div 10^{20}$ cm^{-3} could not be precisely determined due to the weaker Fano effect, than for p-type SiNWs, and the Raman spectroscopy allowed us only to distinguish the high doping level above $5 * 10^{19}$ cm^{-3}.

c) Spin-on doping of SiNWs arrays

Initial SiNWs arrays were fabricated by MACE of p-type c-Si substrates, had the porosity of about 75 %, typical nanowire diameter of 100 nm, length of 4-15 μm and initial free hole concentration of $10^{14} \div 10^{15}$ cm^{-3}. The standard spin-on doping procedure (see. Sec. 2.1.2) was found to be highly efficient for the post-fabrication doping of such SiNWs, and the high free hole concentrations of the order of 10^{19} and 10^{20} cm^{-3} were achieved for n- and p-type doping, correspondingly. The obtained doping levels in SiNWs are rather close to the optimal doping level of $\approx 10^{21}$ cm^{-3} for thermoelectric applications (see Sec. 1.5). For p-type SiNWs, the observed maximum free hole concentration of about $2 * 10^{20}$ cm^{-3} is close to the boron solubility limit of $4 * 10^{20}$ cm^{-3} at the used annealing temperature (see Sec. 1.2.3). The lower effectiveness of the standard SOD doping procedure in the case of n-type doping was explained by the use of initial p-type SiNWs, and applying the SOD procedure several times, the free electron concentration in SiNWs of the order of 10^{20} cm^{-3} were achieved. Therefore, to obtain more efficient n-type doping, initial n-type MACE-SiNWs should be used.

Despite the high free charge carrier concentration at the top of SiNWs array, the in-depth profiles of the free charge carrier concentration in SiNWs array after the standard SOD procedure were strongly inhomogeneous. The inhomogeneous doping level along SiNWs arrays reduces their electrical conductivity. In this regard, Chapter 5 is devoted to the investigation of the SOD procedure parameters on in-depth profiles of doping level in SiNWs arrays.

Cette thèse est accessible à l'adresse : http://theses.insa-lyon.fr/publication/2019LYSEI129/these.pdf
© [S. Rodichkina], [2019], INSA de Lyon, tous droits réservés

Chapter 5
In-depth doping of silicon nanowire arrays

Post-fabrication doping of MACE-SiNWs arrays, which consists in the spin-coating of the commercial spin-on dopant solution on tops of SiNWs and following annealing at about 1000 ^{0}C, leads to the strongly inhomogeneous in-depth profile of the doping level of SiNWs (see Chapter 4), that reduces the electrical conductivity of SiNWs. At that, the free charge carrier concentration in the upper part of SiNWs after the additional doping is of the order of $10^{19} \div 10^{20}$ cm^{-3}. In this section we investigate the influence of the parameters of the post-fabrication doping procedure, such as the dilution degree of spin-on dopant (SOD) solution, annealing time and temperature on the in-depth profiles of the free charge carrier concentration in SiNWs arrays, as well as the influence of SiNWs morphology on the doping efficiency.

5.1 Influence of doping procedure parameters

A description of the applied SOD doping procedure can be found in Sec. 2.1.2. The standard SOD doping procedure included the spin-coating of the commercial Borofilm (Emulsitone Chemicals, LLC) dopant solution and annealing by RTA for 15 s with a maximum temperature of about 950 ^{0}C. The profiles of free charge carrier concentration along SiNWs were measured using the Raman spectroscopy, the laser spot diameter was about 2 μm and the wavelength was of 473 nm.

5.1.1 Dilution of dopant solution

Fig. 5.1 (black points) shows the in-depth profile of the free hole concentration in SiNWs arrays (SiNWs-C series) obtained using the standard SOD doping procedure. It can be seen from the figure, that the free hole concentration at SiNWs tips is of about $2 * 10^{20}$ cm^{-3}, that is close to the boron solubility limit in Si at the annealing temperature (about $4 * 10^{20}$ cm^{-3} at 1100 ^{0}C [16]).

Cette thèse est accessible à l'adresse : http://theses.insa-lyon.fr/publication/2019LYSEI129/these.pdf
© [S. Rodichkina], [2019], INSA de Lyon, tous droits réservés

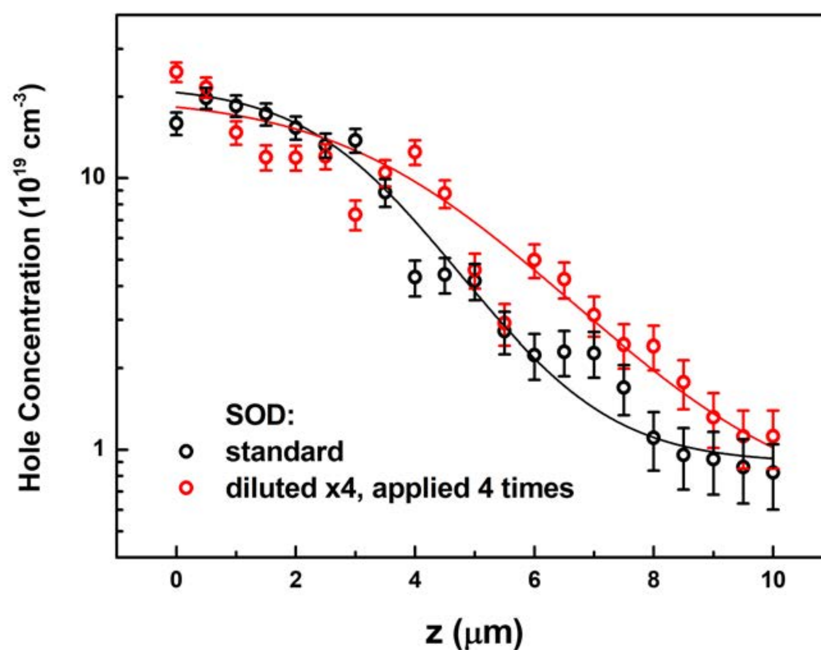

Figure 5.1: In-depth profile of the free hole concentration in SiNWs array after the additional doping using the standard spin-on dopant (black points) and one, fourfold diluted with ethanol, applied to SiNWs four times before the annealing (red points). The RTA annealing for 15 s with a maximum temperature of about 950 ^{0}C was used for both samples. The lines are to guide the eye, z is the depth coordinate with $z = 0$ at SiNWs top and $z = L$ at SiNWs/c-Si interface.

The free hole concentration profile along SiNWs is strongly inhomogeneous, and the depth of the doped layer can be estimated of about 3 μm, that can correspond to the penetration depth of dopant solution into SiNWs arrays. At the depth of more than 6 μm the doping level in SiNWs is insignificant ($N < 2 * 10^{19}$ cm^{-3}). The inhomogeneous free charge carrier concentration profile indicates the difficult penetration of the dopant solution deep into pores of SiNWs array, which is related to the high viscosity of the dopant solution and short solvent evaporation time.

In order to reduce the viscosity of the dopant solution, the latter can be dissolved in various solvents, such as ethanol, acetone, isopropanol. Fig. 5.1 (red points) shows the free hole concentration profile for doped SiNWs, obtained using a fourfold diluted dopant solution and four spin-coating and pre-baking procedures. It can be seen from the figure, that the free hole concentration at the top of SiNWs is the same for undiluted and diluted SOD. The dissolution of the dopant solution slightly enhances the doping profile in SiNWs. For the diluted SOD, the depth of the doped layer is estimated of about 5 μm, while for the undiluted SOD it was of about 3 μm. At $z > 8$ μm, the free hole concentration is less than $2 * 10^{19}$ cm^{-3}. Despite the lower viscosity of the diluted doping solution, the short solvent evaporation time seems to prevent the effective penetration of the doping solution deep into pores of SiNWs array.

Cette thèse est accessible à l'adresse : http://theses.insa-lyon.fr/publication/2019LYSEI129/these.pdf
© [S. Rodichkina], [2019], INSA de Lyon, tous droits réservés

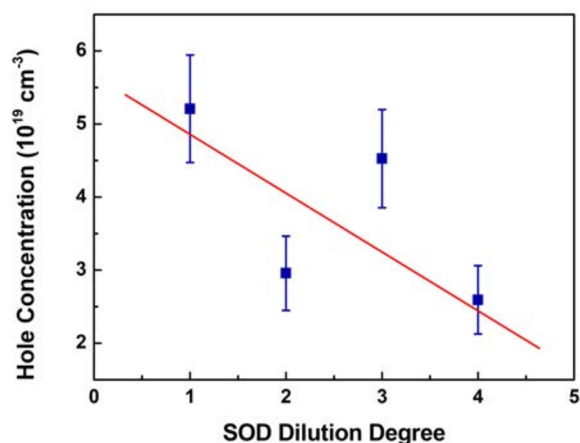

Figure 5.2: Free hole concentration in the top layer of SiNWs array for diluted SOD solution (acetone) as a function of the dissolution degree. The annealing temperature was about 900 ^{0}C. The line is to guide the eye.

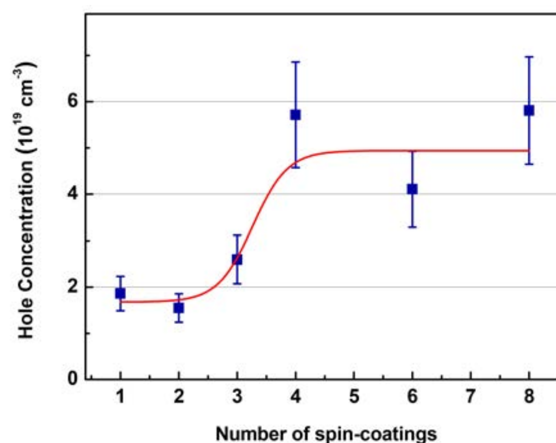

Figure 5.3: Dependence of the free hole concentration for the top layer of SiNWs array on the number of spin-coating and pre-baking procedures. SOD fourfold diluted with acetone was used. The annealing temperature was about 900 ^{0}C. The line is to guide the eye.

The influence of the dissolution of SOD on the resulting free hole concentration at tops of SiNWs is shown in Fig. 5.2. The depth of the investigated layer of SiNWs array can be estimated about 1 μm, that represents the light penetration depth in silicon for the light wavelength of 473 nm [172]. From the figure one can see that the increase in the dissolution degree of SOD in general leads to the decrease in the free charge carrier concentration at tops of SiNWs. This fact can be explained by a lower concentration of dopant agents in dissolved SOD, that limits the resulting free hole concentration in SiNWs after the dopant diffusion. However, the absence of the clear trend indicates that the penetration of polymer molecules containing dopants deep into SiNWs arrays depends on a number of various factors, such as the concentration of dopants in SOD, viscosity and evaporation time of SOD solution, which can not be precisely controlled experimentally.

Fig. 5.3 shows the free hole concentration in SiNWs as a function of the number of spin-coating and pre-baking procedures. Initially, Borofilm solution diluted four times with acetone was used. A decrease in the free charge carrier concentration in SiNWs obtained using the diluted SOD was observed compared to that for undiluted SOD (see Fig. 5.2). Then, the spin-coating and pre-baking procedures were applied several times to SiNWs samples, followed by the same RTA annealing. As can be seen from the figure, initially the free hole concentration in SiNWs increases with the number of spin-on deposition procedures, which is explained by the thicker SOD layer at SiNWs tips. After four depositions, subsequent SOD deposition does

Cette thèse est accessible à l'adresse : http://theses.insa-lyon.fr/publication/2019LYSEI129/these.pdf
© [S. Rodichkina], [2019], INSA de Lyon, tous droits réservés

not change the resulting doping level in SiNWs, and the maximum free hole concentration in SiNWs, obtained using several deposits of diluted SOD, is well consistent with that in the case of a single deposition of undiluted SOD. This fact indicates that the diffusion of boron into SiNWs is limited by the boron concentration at SOD/Si interface during the annealing, which, for spin-coated SOD layers, is already maximal in the case of undiluted SOD and can not be significantly increased by additional spin-coating of SOD. Note, that the annealing temperature used was about $T = 900\ ^0$C.

5.1.2 Thickness of dopant layer

Fig. 5.4 shows the comparison of the doping profiles in SiNWs arrays, obtained using the standard (spin-coated) and thick layer of SOD and the short-time annealing (25 s, RTA) at about 1000 ^{0}C. The thick layer of SOD was obtained by applying SOD to SiNWs without spin-coating procedure. It can be seen from the figure that the large thickness of SOD layer leads to a significant enhancement of the doping profile in SiNWs, and the free hole concentrations in SiNWs array more than 10^{20} cm^{-3} are observed up to the depth of $z = 10\ \mu$m. The high values of

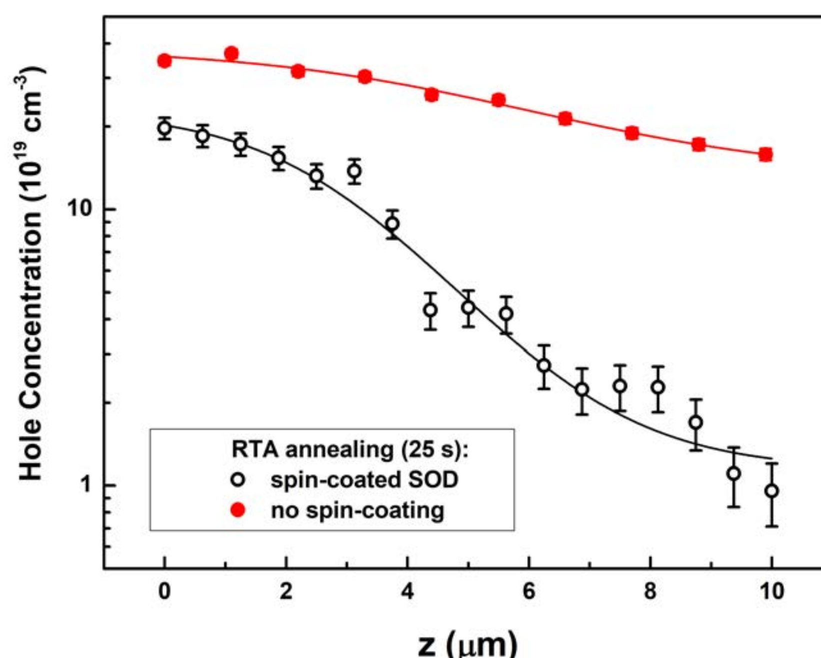

Figure 5.4: In-depth profile of the free hole concentration in SiNWs array after the additional doping using the thin (open circles) and thick (solid circles) layer of deposited spin-on dopant, obtained by using the spin-coating procedure and without it, correspondingly. The annealing was performed for 25 s using the RTA device with maximal temperature of about 1000 ^{0}C. The lines are to guide the eye.

Cette thèse est accessible à l'adresse : http://theses.insa-lyon.fr/publication/2019LYSEI129/these.pdf
© [S. Rodichkina], [2019], INSA de Lyon, tous droits réservés

free hole concentration at big depth in SiNWs array are explained by the evaporation of deposited SOD during the annealing [178] and by the increase in the amount of evaporated dopants with the thickness of SOD layer. The increase in the free hole concentration at SiNWs tips ($z = 0$) in the case of thick SOD layer compared to the case of standard spin-coated SOD layer for the same annealing conditions can be explained by the higher boron concentration at SOD/ Si interface during the annealing due to significantly higher amount of dopants in thick SOD layer. The free hole concentration at SiNWs tips of about $3.5 * 10^{20}$ cm^{-3}, obtained using thick SOD layer, seems to correspond to the boron solubility limit for the given annealing temperature (about $4 * 10^{20}$ cm^{-3} at 1100 ^{0}C [16]).

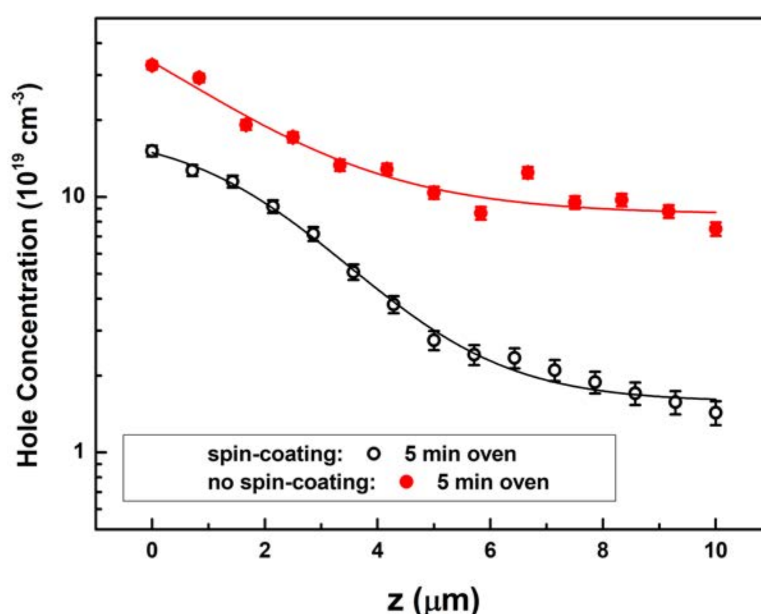

Figure 5.5: In-depth profile of the free hole concentration in SiNWs array after the additional doping using the thin (open circles) and thick (solid circles) layer of deposited spin-on dopant, obtained by using the spin-coating procedure and without it, correspondingly. The annealing was performed for 5 min using the oven at about 1000 ^{0}C. The lines are to guide the eye.

Fig. 5.5 shows the comparison of the doping profiles in SiNWs arrays, obtained using standard and thick layer of SOD and long-time annealing (5 min) in an oven at about 1000 ^{0}C. Similarly to the case of short-time RTA annealing, the inhomogeneous doping profile is observed for SiNWs after spin-coating of SOD, while the thick layer of SOD, deposited without spin-coating procedure, results in more homogeneous doping profile. Also, the free hole concentration at tops of SiNWs is higher in the case of thick SOD layer than in the case of standard spin-coated SOD layer. The free hole concentration both at SiNWs tips and in the depth of SiNWs array is higher in the case of RTA annealing than in the case of the oven annealing.

Thus, Figs. 5.4 and 5.5 show, that the increase in the annealing time does not improve

Cette thèse est accessible à l'adresse : http://theses.insa-lyon.fr/publication/2019LYSEI129/these.pdf
© [S. Rodichkina], [2019], INSA de Lyon, tous droits réservés

the doping profile in SiNWs. Moreover, more pronounced decrease in N with the depth of SiNWs array in the case of the oven heating can be associated with the slower increase in SiNWs temperature during the oven heating, that leads to the stronger formation of silicon oxide and silicon nitride on SiNWs surface during the annealing, which inhibit the boron diffusion in SiNWs. At that, the difference in the in-depth doping profiles of SiNWs arrays for RTA and oven annealing is not significant, and the free hole concentrations of more than 10^{20} cm^{-3} are observed to the depth of 10 μm in both cases. The depth of highly-doped layer of SiNWs array, at which $N > 2 * 10^{19}$ cm^{-3}, can be estimated of about 18 μm in the case of thick SOD layers.

5.1.3 Annealing time and temperature

Fig. 5.6 (a) shows the dependence of the free hole concentration at tops of SiNWs SiNWs after the doping on the maximal oven temperature during the RTA annealing. For the experiment, standard Borofilm solution and one, diluted three times with isopropanol, were used. The error bars are associated with both the determination of N from Raman spectra and averaging of N values between several sample points. One can see that the free hole concentration in SiNWs increases with the annealing temperature up to about $T = 950$ ^{0}C (1223 K, RTA annealing time of 15 s), and for higher annealing temperatures it remains constant within the experimental error. The maximal free hole concentration in SiNWs, obtained using spin-coated SOD layers, is of about $1 * 10^{20}$ cm^{-3}, and for thick SOD layers, obtained without spin-coating of SOD, it is of

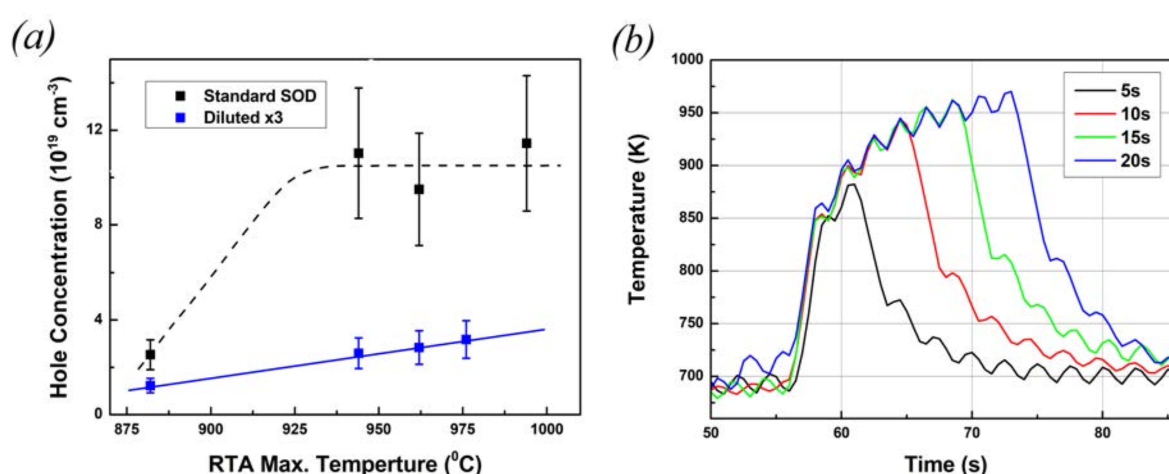

Figure 5.6: (a) Free hole concentration for the top layer of SiNWs array as a function of maximal temperature in the RTA chamber for the standard SOD (black squares) and one diluted 3 times with isopropanol (blue squares). Blue line shows the linear fit of the corresponding dependence, black dashed line is to guide the eye. (b) Temperature in the RTA chamber as a function of time for the different annealing time.

Cette thèse est accessible à l'adresse : http://theses.insa-lyon.fr/publication/2019LYSEI129/these.pdf
© [S. Rodichkina], [2019], INSA de Lyon, tous droits réservés

about $3.5 * 10^{20}$ cm^{-3}. For the diluted SOD, a linear increase of the free hole concentration in SiNWs with the annealing temperature is observed. As it can be seen from the time temperature profiles for the RTA chamber, shown in Fig. 5.6 (b), the maximal temperature in the RTA chamber is maintained for $t = 1 - 3$ s. Considering that the boron diffusivity in Si in the studied temperature range is of the order of $D_{\text{diff}} = 10^{-15}$ cm^2/s [35], the radial thickness of the doped part of a nanowire, estimated as $2\sqrt{D_{\text{diff}}t}$, is of the order of 100 nm, which corresponds to SiNWs diameter. One can conclude that the resulting doping level in SiNWs is determined mainly by the maximum RTA temperature, and the time temperature profile for the RTA chamber can be not taken into account. The observed dependencies of N on maximal annealing temperature can be understood considering that boron diffusion in Si is influenced by temperature [16], boron concentration in SOD layer at SOD/Si interface, SiNWs surface silicon oxide layer and surface roughness [55], and that it is limited by boron solubility limit [16].

It is important to note that the high temperature annealing of SiNWs at $900-1000$ ^{0}C did not influence their morphology and crystallinity (see Sec. 3.1.2).

5.2 Influence of SiNWs surface roughness on doping efficiency

The identical doping procedure, applied to different SiNWs samples, can lead to the free hole concentration in SiNWs in a range of $N = 10^{19} \div 10^{20}$ cm^{-3}. To study the effect of the morphology of SiNWs on the resulting doping level of SiNWs, SiNWs with different surface roughness were fabricated by varying the concentrations of HF and H_2O_2. At first, we confirmed the absence of a systematic dependence of the efficiency of the doping on the diameter and length of nanowires for investigated SiNWs. Also, in order to exclude the strong influence of the oxide layer on SiNWs walls on the doping efficiency [55], we removed it in HF prior the doping procedure. Considering the above facts, one can assume the major effect of por-Si shell at the walls of SiNWs (surface roughness), which is formed during the MACE and can strongly prevent the diffusion of doping atoms into the core of SiNWs.

To study the por-Si shell of SiNWs one can use the photoluminescence (PL) spectroscopy. Fig. 5.7 (a) shows the PL spectrum for non-doped SiNWs sample, here the PL signal corresponds to the por-Si layer on SiNWs walls, since the SiNWs core diameter (~ 100 nm) is too large for the quantum confinement of electrons. The PL maximum at about 1.9 eV corresponds to the nanocrystal size of about 2 nm [134]. SiNWs samples with different por-Si layer thickness

Cette thèse est accessible à l'adresse : http://theses.insa-lyon.fr/publication/2019LYSEI129/these.pdf
© [S. Rodichkina], [2019], INSA de Lyon, tous droits réservés

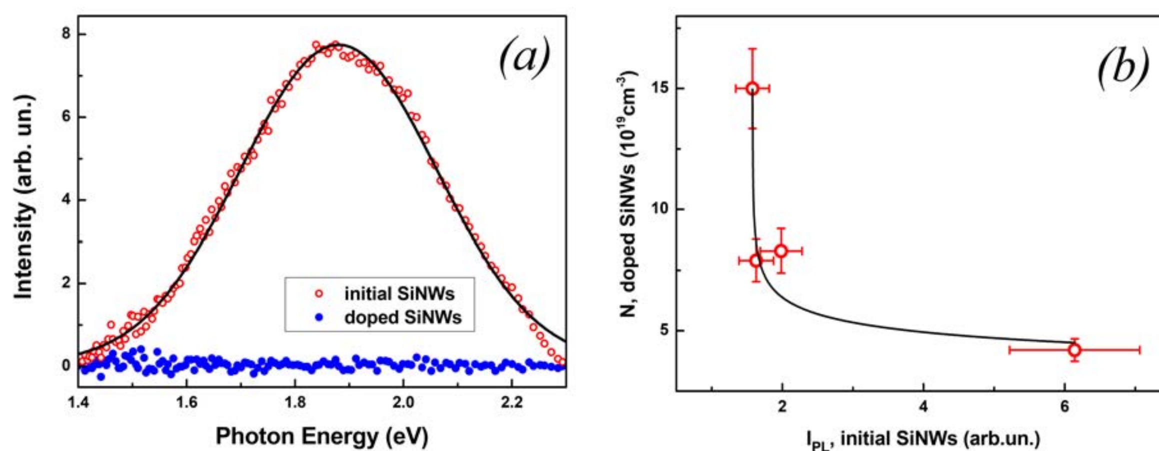

Figure 5.7: (a) Photoluminescence spectra of initial (red circles) and doped (blue) SiNWs, the line shows the Gauss fit of PL spectrum for doped SiNWs, (b) Dependence of the free hole concentration in doped SiNWs on the PL intensity of initial ones. The line is a guide for eye.

exhibit the same line shape of the spectra, that indicates the similar morphology of por-Si at the walls of these SiNWs. The integrated intensity of PL spectra for SiNWs sample is proportional to the volume of por-Si, irradiated by the excitation light. Considering the same light penetration depth for initial SiNWs samples, different integrated PL intensity for these samples can be attributed to a different thickness of por-Si layer on the walls of SiNWs. After the doping of SiNWs, the quenching of PL is observed, which implies the high free charge carrier concentration in nanocrystals of the por-Si layer, that enhances the non-radiative Auger recombination.

Fig. 5.7 (b) demonstrates the correlation between the doping level of SiNWs after the additional doping and the integrated PL intensity for the non-doped SiNWs, where the latter increases due to an increase in the por-Si layer thickness on SiNWs walls. The observed dependence confirms that the doping efficiency of SiNWs strongly increases with reducing the por-Si shell thickness at SiNWs walls.

5.3 Conclusions to Chapter 5

Post-fabrication doping method for SiNWs arrays, which consists in the spin-coating of the spin-on dopant solution on tops of SiNWs and following annealing at about 950 ^{0}C, leads to the strongly inhomogeneous doping profiles along SiNWs. While the high free hole concentration at tops of SiNWs about $2 * 10^{20}$ cm^{-3} was observed, the depth of the homogeneously doped layer in the upper part of SiNWs array was estimated about 3 μm, and the doping level less than $2 * 10^{19}$ cm^{-3} was observed at the depth of 6 μm. Dissolution of the dopant solution led

Cette thèse est accessible à l'adresse : http://theses.insa-lyon.fr/publication/2019LYSEI129/these.pdf
© [S. Rodichkina], [2019], INSA de Lyon, tous droits réservés

to a slight increase in the depth of the homogeneously doped layer to 5 μm. The increase in the annealing temperature above 950 ^{0}C and in the annealing time above 15 s did not lead to an increase in the free hole concentration in SiNWs, because the boron diffusion into SiNWs is limited by the boron concentration at SOD/Si interface and boron solubility limit, as well as to the enhancement of the doping level profile. The almost homogeneous in-depth doping profile in SiNWs arrays was obtained using the thick dopant layers, deposited on the top of SiNWs array without spin-coating, that was associated with the evaporation of the dopant layer during the annealing. In this case, the free hole concentration in SiNWs above 10^{20} cm^{-3} was observed to the depth of 10 μm. The obtained results show that the SOD doping technique is useful to obtain homogeneously doped SiNWs arrays for nano-electronic, thermoelectric and sensor applications.

Cette thèse est accessible à l'adresse : http://theses.insa-lyon.fr/publication/2019LYSEI129/these.pdf
© [S. Rodichkina], [2019], INSA de Lyon, tous droits réservés

Chapter 6
Electrical and thermal transport in silicon nanowires

Thermoelectric applications require the materials to have good electrical and poor thermal transport (see Sec.1.5). In this chapter we estimate the electrical and thermal conductivity of highly-doped SiNWs arrays to evaluate their potential as a thermoelectric material.

6.1 Electrical resistivity of SiNWs

The standard four-probe electrical resistivity measurements for individual SiNWs (see Sec. 1.4) are not suitable for SiNWs arrays. In this section the electrical resistivity of nanowires in SiNWs array is estimated using the profiles of the free hole concentration (see Chap. 5) and bulk c-Si mobility values for free charge carriers in SiNWs. The obtained results are compared with the results of direct two-probe electrical measurements for SiNWs arrays.

6.1.1 Estimation based on the free hole concentration

Numerous studies have shown that the free charge carrier mobility in moderately- and highly-doped SiNWs ($N > 10^{18}$ cm^{-3}) with diameter more than 20 nm is the same as in bulk c-Si (see Sec. 1.4.3). A minor role of the surface scattering of charge carriers was explained by their small mean free path with respect to the nanowire diameter due to the impurity scattering. Note, that at the same time the phonon transport along SiNWs is significantly suppressed by the surface scattering of phonons (see Sec. 1.3). At that, the electrical conductivity of SiNWs with ($N > 10^{18}$ cm^{-3}) and diameter of 20-70 nm was shown to differ from the bulk values for the same impurity concentrations due to the effect of donor deactivation in SiNWs and surface depletion of charge carriers due to interface states (see Sec. 1.4.2). In our case, both the IR-ATR and Raman spectroscopy techniques determine the free charge carrier concentration, and not the concentration of dopant atoms (see Sec. 4.3), so that the effects of donor deactivation and

Cette thèse est accessible à l'adresse : http://theses.insa-lyon.fr/publication/2019LYSEI129/these.pdf
© [S. Rodichkina], [2019], INSA de Lyon, tous droits réservés

interface states in SiNWs can be not taken into account. Thus, the electrical conductivity of SiNWs with diameter more than 20 nm can be calculated using the bulk free charge carrier mobility as $\sigma = eN\mu$, where N is the determined free charge carrier concentration, e is the electron charge and μ is the free charge carrier mobility in c-Si. The dependence of the c-Si resistivity on free charge carrier concentration is shown in Fig. 1.30.

The obtained values of the free charge carrier concentration for highly-doped p-type SiNWs are in the range of $0.5 - 27 * 10^{19}$ cm^{-3} (see Fig. 4.15), and the estimated electrical resistivity of SiNWs is in the range of 0.5-17 mΩ*cm. For n-type SiNWs, N is in the range of $0.5 - 5 * 10^{19}$ cm^{-3} (see Fig. 4.18), and the estimated electrical resistivity is in the range of 1.5-10 mΩ*cm.

The average electrical conductivity of SiNWs can be obtained using the profiles of free hole concentration along SiNWs. For example, using the doping level profiles given in Fig. 5.4, one can obtain, that the average electrical resistivity of SiNWs after the standard SOD doping procedure is of about 4 mΩ*cm. SOD doping procedure using thick dopant layer results in average ρ of SiNWs of about 1 mΩ*cm. The electrical resistivity of SiNWs is quite low, and close values have been measured experimentally for individual SiNWs (see Sec. 1.4.2).

6.1.2 Two-probe electrical measurements

The values of the electrical resistivity of por-Si and SiNWs obtained using the optical methods can be verified by direct electrical measurements. Note, that the samples present nanostructured layers on c-Si substrate.

Fig. 6.1 (a,b) shows the results of measurements of the lateral electrical conductivity for por-Si by the two-probe and four-probe methods. Both figures show a significant decrease in the electrical resistance of por-Si layers after the additional doping. This fact can be attributed to the drop of the contact resistance between por-Si and electrodes after the doping, as well as to the decrease in por-Si resistivity. While these observed data clearly indicate the high doping level in doped por-Si samples, the electrical resistivity of por-Si can not be evaluated because of the geometry of the measurements (see Fig. 6.1 (d)) and unknown substrate contribution. Note, that in the case of por-Si the electrical resistivity can not be directly evaluated from the free charge carrier concentration because of unknown free charge carrier mobility.

Fig. 6.1 (c) shows the dependence of the electrical resistance of por-Si layer on the distance between electrodes (d). In the configuration used, the measured resistance is $R = 2R_{\text{por-Si}} + R_{\text{c-Si}} + R_{\text{bar}}$, where $R_{\text{por-Si}}$ is a vertical resistance of a por-Si layer, $R_{\text{c-Si}}$ is a resistance of c-Si

Cette thèse est accessible à l'adresse : http://theses.insa-lyon.fr/publication/2019LYSEI129/these.pdf
© [S. Rodichkina], [2019], INSA de Lyon, tous droits réservés

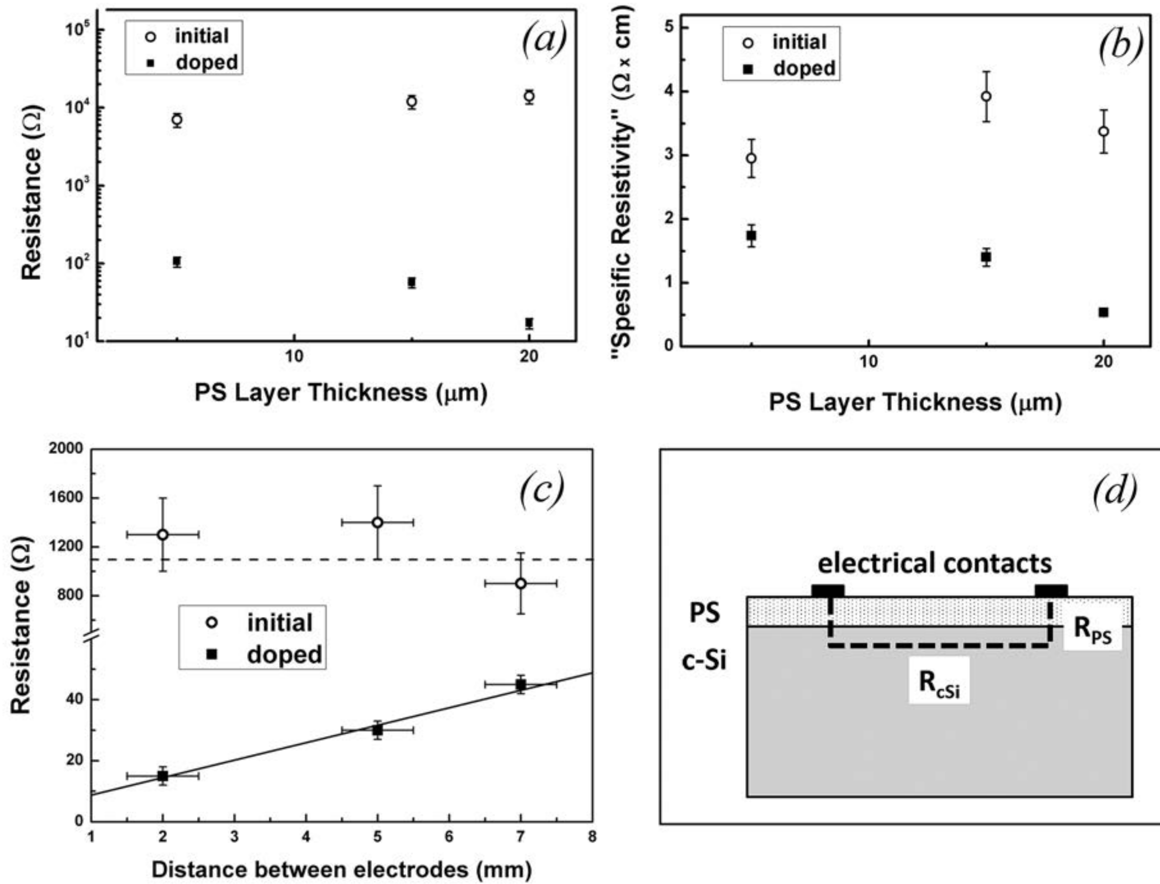

Figure 6.1: (a) Electrical resistance of the initial and additionally doped samples versus thickness of the PS layer; (b) "specific resistivity" of the initial ad additionally doped PS/c-Si structures measured by the standard 4-probe setup versus thickness of the PS layer. (c) Dependence of the electrical resistance on the distance between electrodes (d) for 5μm sample. (d) Schematic illustration of the configuration used for electrical measurements.

wafer between the electrodes, as it is indicated in Fig. 6.1 (d), R_{bar} is the contact resistance due to the Schottky barriers between metal electrode and Si nanostructures. Accordingly to the measurement geometry (see Fig. 6.1 (d)), $R_{\text{por-Si}}$ and R_{bar} should be independent of d, while $R_{\text{c-Si}}$ should be proportional to d. Therefore, the dependence of por-Si sample resistance on the distance between electrodes, shown in Fig. 6.1 (c), allows us to distinguish the contribution of $R_{\text{c-Si}}$. Accordingly to Fig. 6.1 (c), for the initial sample $R \approx 2R_{\text{por-Si}} + R_{\text{bar}}$ since R does not depend on d. For the doped sample, assuming the negligible contribution of R_{bar}, $R_{\text{por-Si}}$ can be estimated as $R_{\text{por-Si}} = R(d \to 0) = 10\,\Omega$, which is comparable with the substrate resistance. Our estimation of the effective specific resistivity of substrate from the tilt of $R(d)$ dependence gives $1\Omega{*}$cm, which is close to the initial substrate value. The significant drop of $(2R_{\text{por-Si}} + R_{\text{bar}})$ from 1 kΩ to 10 Ω after the performed phosphorous doping, which is independent of the substrate resistance $R_{\text{c-Si}}$, indicates that the doped por-Si began to be a degenerate semiconductor.

Cette thèse est accessible à l'adresse : http://theses.insa-lyon.fr/publication/2019LYSEI129/these.pdf
© [S. Rodichkina], [2019], INSA de Lyon, tous droits réservés

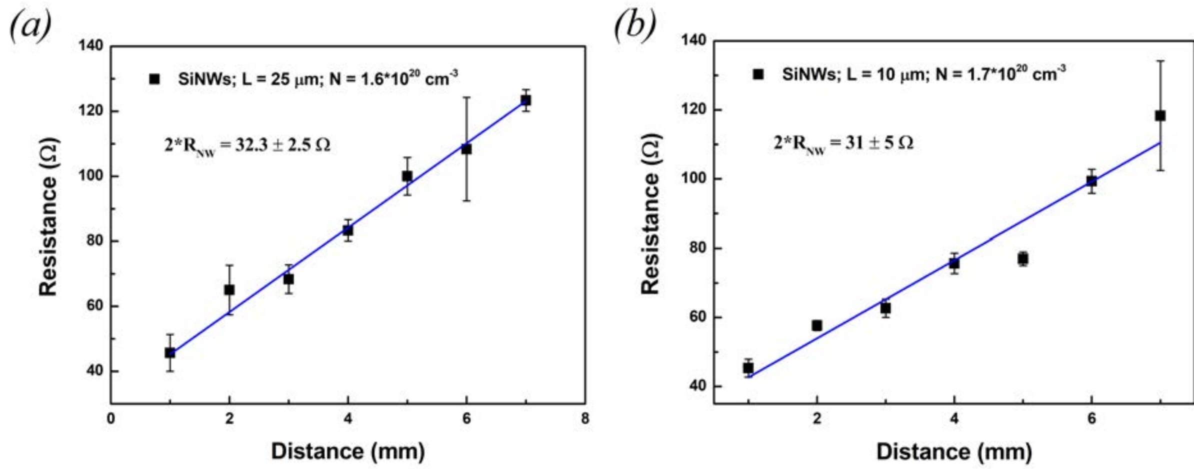

Figure 6.2: (a) Dependence of the electrical resistance on the distance between electrodes for doped SiNWs samples with length of 25 and 10 μm. Electrical contact area is of 2 and 1.4 mm^2 for 25 and 10 μm sample, correspondingly. The free hole concentration in both samples, determined using the Raman spectroscopy, is of about $1.6 * 10^{20}$ cm^{-3}.

Let us consider the results of the electrical resistance measurements for low- and highly-doped SiNWs (SiNWs-C series) samples with nanowire length of 10 and 25 μm. The sample were additionally doped using the standard SOD doping procedure and have doping level profile along nanowires as shown in Fig. 5.4. The electrical resistance of SiNWs samples was measured as a function of the distance between electrodes (d). The resistance of low-doped (initial) SiNWs samples is independent of d and is of 2.1 ± 0.3 and 8 ± 1 $M\Omega$ for 25 and 10 μm SiNWs sample, correspondingly. The different values of the resistance for undoped SiNWs with different length and por-Si can be explained by the different silicon oxide layer for these samples. Fig. 6.2 shows the linear dependence of the resistance of highly-doped SiNWs samples on d for both 10 and 25 μm samples, which it was fit accordingly to $R = 2R_{NW} + r_{\text{c-Si}} * d$, where R_{NW} is the resistance of SiNWs layer and $r_{\text{c-Si}}$ is the specific resistivity of c-Si wafer divided to its cross-section area (see Fig. 6.1 (d)). The decrease in SiNWs sample resistance after the doping is explained mainly by the drop of contact resistance. The values of R_{NW}, determined for doped SiNWs using the electrical measurements, are of 16.2 ± 1.3 and 15 ± 3 Ω for 25 and 10 μm SiNWs sample, correspondingly.

The electrical resistivity of SiNWs was calculated as $\rho = R_{NW} * S_{\text{contact}} * (1-p)/L$, where S_{contact} is the area of electrical contact between electrode and SiNWs sample, L is the SiNWs length, $(1-p)$ is the volume fraction of Si in SiNWs array. The electrical resistivity is estimated to be of 5 and 3 mΩ*cm for 10 and 25 μm SiNWs sample, correspondingly. The free hole

Cette thèse est accessible à l'adresse : http://theses.insa-lyon.fr/publication/2019LYSEI129/these.pdf
© [S. Rodichkina], [2019], INSA de Lyon, tous droits réservés

concentration in the top layer of SiNWs for both samples was of about $1.6 * 10^{20}$ cm^{-3}, and the corresponding bulk value of electrical resistivity is of about 1 mΩ*cm, which is close to the obtained values. Considering the free hole concentration profile in 10 μm SiNWs (see Sec. 4.2.3), one can obtain the average electrical resistivity of 4 mΩ*cm, which is close to the value of 5 mΩ*cm, obtained by electrical measurements. The difference in the values of the electrical resistivity of SiNWs, obtained using the electrical and optical measurements, is mainly related to the unknown real contact area between electrode and SiNWs and distance between electrode and c-Si, which can lead to the systematical error in the electrical measurements.

The obtained results show that the values of the free hole concentration in SiNWs, obtained using the Raman spectroscopy, as well as the assumption of bulk-like electrical transport in SiNWs with diameter of 50-100 nm, are reasonable and can be used for the express-diagnostics of electrical properties of SiNWs arrays.

6.2 Thermal conductivity of SiNWs

This section describes the contactless characterization of thermal conductivity of SiNWs arrays by using the Raman spectroscopy. The method is based on solving the heat equation for SiNWs under photo-induced heating, where the latter is determined from the one-phonon Raman peak parameters. The thermal conductivity of low- and highly-doped SiNWs is compared and discussed in view of thermoelectric applications of SiNWs arrays.

6.2.1 Thermal conductivity by Raman spectroscopy

a) Temperature dependence of the Raman peak for c-Si

Fig. 6.3 shows the Raman spectra of low-doped c-Si wafer at different temperature from 300 to 900 K. One can see from the figure, that as the temperature of c-Si increases, its Raman peak shifts to lower phonon frequencies and broadens. The downshift of the phonon frequency of c-Si with temperature is explained by a thermal expansion of its lattice and, consequently, weakening of the interaction force between Si atoms. The increase in the peak width, which can be interpreted as phonon damping constant [164], with temperature can be explained by the increase in the number of phonons in c-Si, which leads to the enhancement of the phonon-phonon scattering. The integrated intensity of the Raman peak for c-Si decreases with temperature. This fact was attributed to the decrease in the one-phonon Raman tensor for c-Si, which describes the

Cette thèse est accessible à l'adresse : http://theses.insa-lyon.fr/publication/2019LYSEI129/these.pdf
© [S. Rodichkina], [2019], INSA de Lyon, tous droits réservés

probability of the Raman scattering, with temperature due to the temperature increase in light absorption coefficient of c-Si [179, 180].

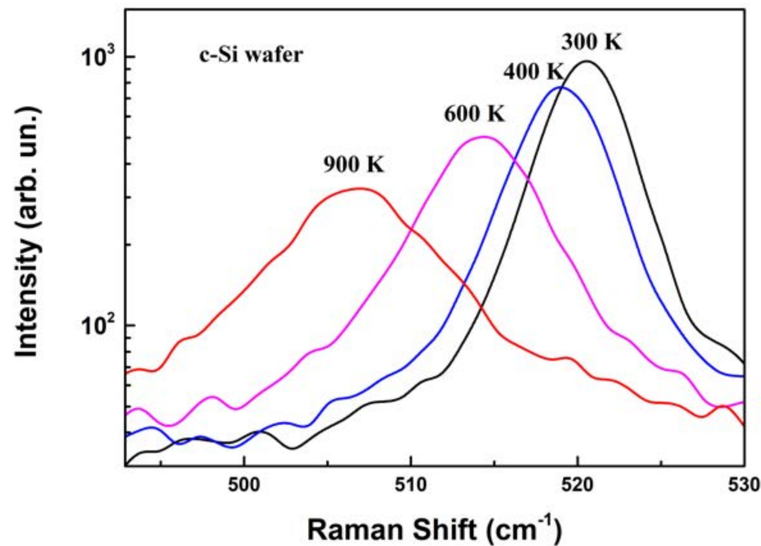

Figure 6.3: Raman spectra of low doped c-Si wafer under oven heating at different temperatures.

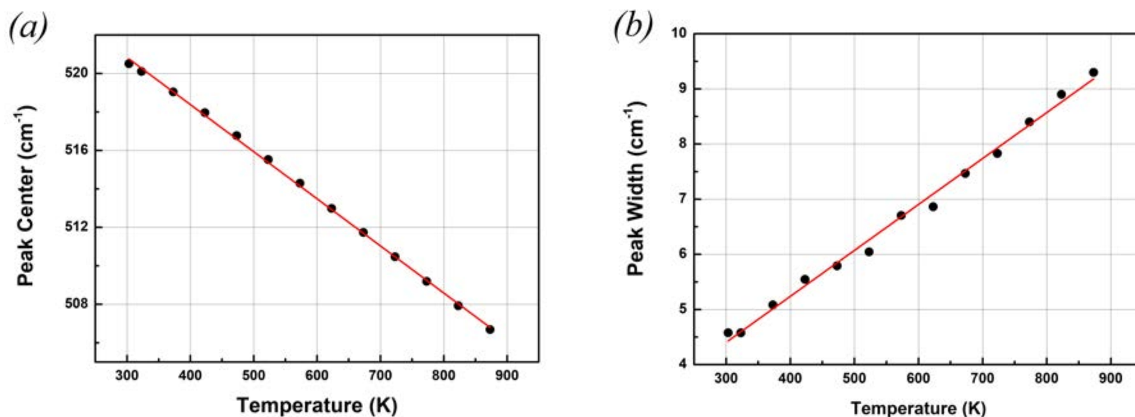

Figure 6.4: Dependence of the spectral position (a) and width (b) of the Raman peak for low doped c-Si on temperature. The red lines in (a,b) show the linear fit of the corresponding dependencies. The linear fits are given by: $\Omega = 528.2\ [\mathrm{cm}^{-1}] - 0.025\ [\mathrm{cm}^{-1}/\mathrm{K}] * T$; $\Gamma = 1.9\ [\mathrm{cm}^{-1}] + 0.0083\ [\mathrm{cm}^{-1}/\mathrm{K}] * T$, where T is the absolute temperature given in [K].

Fig. 6.4 shows the dependence of the spectral position and width of the Raman peak for low-doped c-Si on temperature, obtained from the fit of the Raman peaks by Lorentzian function. In accordance with the above, the spectral peak position linearly decreases with temperature, and the peak width linearly increases with temperature. It is important to note,

Cette thèse est accessible à l'adresse : http://theses.insa-lyon.fr/publication/2019LYSEI129/these.pdf
© [S. Rodichkina], [2019], INSA de Lyon, tous droits réservés

that the non-linear temperature dependence was reported both for spectral peak position and peak width for c-Si for a wide temperature range, and it was explained by a contribution of both cubic and quartic anharmonic terms of the c-Si vibrational Hamiltonian [164]. For a smaller temperature range studied in this work, the above dependencies can be approximated by a line, and the linear approximation will be used further to determine the temperature of c-Si and SiNWs from the Raman peak parameters because of the simplicity. The linear fits are given by: $\Omega = 528.2\ [\mathrm{cm}^{-1}] - 0.025\ [\mathrm{cm}^{-1}/\mathrm{K}] * T$; $2\Gamma = 1.9\ [\mathrm{cm}^{-1}] + 0.0083\ [\mathrm{cm}^{-1}/\mathrm{K}] * T$, where Ω is the phonon frequency in c-Si, 2Γ is the spectral width, T is the absolute temperature. Note that to determine the temperature of c-Si, one can also use the ratio of the Raman Stokes/anti-Stokes peak intensities: $I_S/I_{AS} = exp(\hbar\Omega/k_BT)$, where k_B is the Boltzmann's constant. The latter equation directly follows from $I_S \propto (N_{ph}+1)$ and $I_{AS} \propto N_{ph}$, where N_{ph} is a phonon mode occupation number at a given temperature.

b) Photo-induced heating of SiNWs arrays

In order to determine the thermal conductivity of SiNWs using the Raman spectroscopy, one should: (a) determine the magnitude of photo-induced heating of SiNWs (ΔT) at different excitation laser intensities and (b) correlate the SiNWs heating and thermal conductivity coefficient using the appropriate modeling of thermal transport in SiNWs sample. Strong laser-induced heating of SiNWs should be avoided in order to exclude the variation of the thermal conductivity coefficient with temperature. For the temperature-independent thermal conductivity, a linear dependence of photo-induced heating of SiNWs on the laser intensity should be observed due to the linear heat conduction equation.

Fig. 6.5 shows the one-phonon Raman spectra of SiNWs at different excitation laser intensity. The shift and broadening of the Raman peak for SiNWs with increasing laser intensity is observed, similar to that observed for oven heated c-Si (see Fig. 6.3). However, in the case of photoexcited SiNWs, the observed modification of the spectrum is related not solely to the photo-induced heating of SiNWs, but also to the mechanical stresses induced by the temperature gradient along SiNWs (see Sec. 3.2). The inset in Fig. 6.5 shows that the dependence of integrated Raman peak intensity for SiNWs on the laser intensity is linear. This fact implies that the thermal conductivity of SiNWs is constant in the studied range of photo-induced heating, and the linear heat equation can be used for thermal conductivity calculations. The decrease of the Raman tensor for c-Si with temperature, which could lead to the decrease in integrated Raman peak intensity for SiNWs, is

Cette thèse est accessible à l'adresse : http://theses.insa-lyon.fr/publication/2019LYSEI129/these.pdf
© [S. Rodichkina], [2019], INSA de Lyon, tous droits réservés

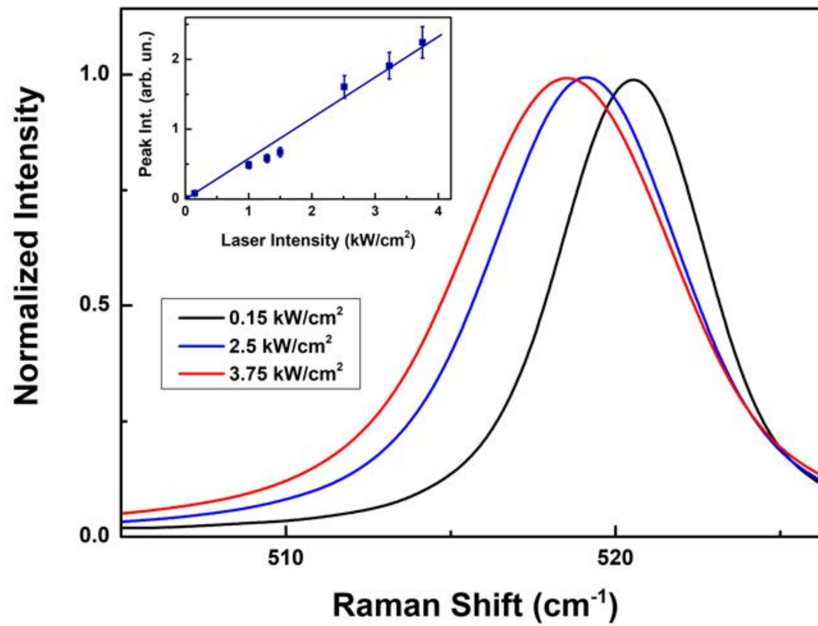

Figure 6.5: Normalized Raman spectra for SiNWs at low laser intensities. The inset shows the dependence of integrated Raman peak intensity for SiNWs on the laser intensity.

negligible for the observed photo-induced heating.

Fig. 6.6 shows the values of the photo-induced heating for SiNWs, determined from their Raman spectra (see Fig. 6.5) using the temperature dependence of the c-Si Raman peak position (blue squares) and peak width (red squares). The heating of SiNWs determined from Γ is about 2.5 higher than the one determined from Ω. As it was mentioned above, the observed discrepancy is explained by an influence of an average compressive mechanical stress in SiNWs, caused by temperature gradient in photoexcited SiNWs. Both the hydrostatic and uniaxial compression are known to lead to the increase in phonon frequency Ω in c-Si, while tensile stresses lead to the decrease in Ω [138]. At that, no influence of uniaxial compression on the Raman peak width Γ for c-Si was reported [138]. Therefore, more precise values of the photo-induced heating of SiNWs are obtained using the Raman peak width Γ, and commonly used Raman peak position Ω [144, 160] can lead to the underestimation of the SiNWs photo-induced heating.

In order to determine the photo-induced heating of SiNWs from the intensity ratio of Stokes/ anti-Stokes Raman peaks for SiNWs, one can use the modified formula, $I_S/I_{AS} = C exp(\hbar\Omega/k_B T)$, where the intensity coefficient C arises due to the different light scattering in SiNWs array for Stokes and anti-Stokes frequencies. For MACE-SiNWs, C was estimated to be about 12. The photoexcitation-induced mechanical stresses in SiNWs should not influence the I_S/I_{AS} ratio since the phonon occupation number does not directly depend on mechanical stress, and the change in I_S/I_{AS} due to the phonon frequency shift, caused by stress, is insignificant compared to that

Cette thèse est accessible à l'adresse : http://theses.insa-lyon.fr/publication/2019LYSEI129/these.pdf
© [S. Rodichkina], [2019], INSA de Lyon, tous droits réservés

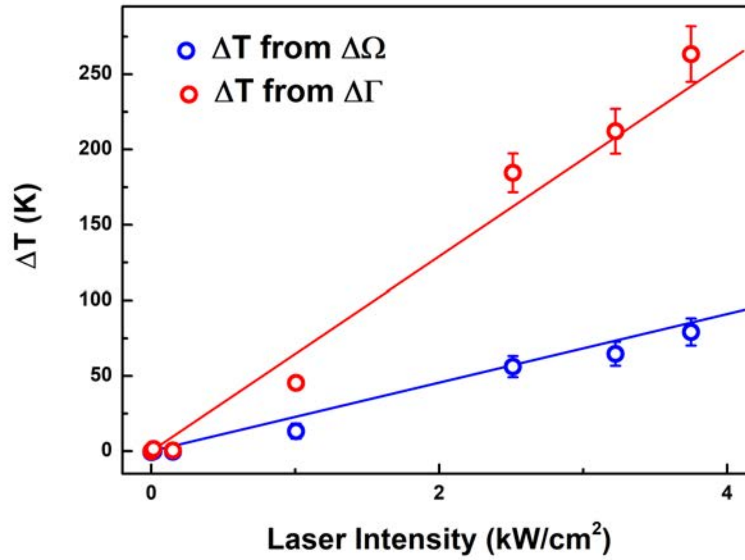

Figure 6.6: Heating of SiNWs at the center of the laser spot, calculated from the Raman peak position (blue rectangles) and width (red rectangles) as a function of excitation laser intensity.

one due to heating of SiNWs. The heating of SiNWs determined from I_S/I_{AS} is about 1.6 times higher than the one determined from Ω, and 1.5 lower than than the one determined from Γ. The discrepancy can be related in the temperature dependence of C due to temperature change in the absorbance coefficient and light scattering in SiNWs array. At that, both the line width of the Raman peak and Stokes/anti-Stokes intensity ratio are influenced by the inhomogeneous heating along SiNWs.

c) Heat equation for SiNWs array under photoexcitation

To determine the effective thermal conductivity coefficient of SiNWs from the photo-induced heating one can use the three-dimensional steady-state heat equation, given by

$$-k_{\text{eff}}\nabla^2\Delta T(r,z) = \rho_{heat}(r,z), \tag{6.1}$$

with $\rho_{heat} = 0$, where $\Delta T = T - 300$ [K] is the heating of SiNWs, k_{eff} is the effective thermal conductivity of SiNWs array and ρ_{heat} is the density of heat sources, r and z are the radial and axial coordinates, correspondingly. z-axis is directed along SiNWs with $z = 0$ at SiNWs/c-Si interface and $z = L$ at SiNWs tips, where L is the length of SiNWs. The following boundary conditions were used:

(a) $T|_{z=0} = 300$ [K] for $0 \leq r < \infty$, i.e. the c-Si substrate works as a heat sink, and its

Cette thèse est accessible à l'adresse : http://theses.insa-lyon.fr/publication/2019LYSEI129/these.pdf
© [S. Rodichkina], [2019], INSA de Lyon, tous droits réservés

temperature is equal to that of an ambient,

(b) SiNWs are heated by the laser, which has the heat flux equal to the laser intensity: $-k_{\text{eff}}\, d(\Delta T)/dz|_{z=L} = I_L$ for $r \leq D_L$, where I_L and D_L are the laser intensity and focused beam diameter, correspondingly. This boundary condition corresponds to the case when all the laser light is absorbed at SiNWs tips ($z = L$).

(c) Non-heated top surface of SiNWs is thermally insulated: $-k_{\text{eff}}\, d(\Delta T)/dz|_{z=L} = 0$ for $r > D_L$.

The boundary condition (b) assumes that all the laser light is absorbed in at SiNWs tips, and it does not take into account the light penetration depth in SiNWs. This assumption is the most correct for a visible light with short wavelength, for which the light penetration depth in c-Si is the smallest, and the light scattering in SiNWs does not significantly affect it. For example, the light penetration depth in c-Si for 473 nm light is below 1 μm, which is much less than SiNWs length of ~ 10 μm.

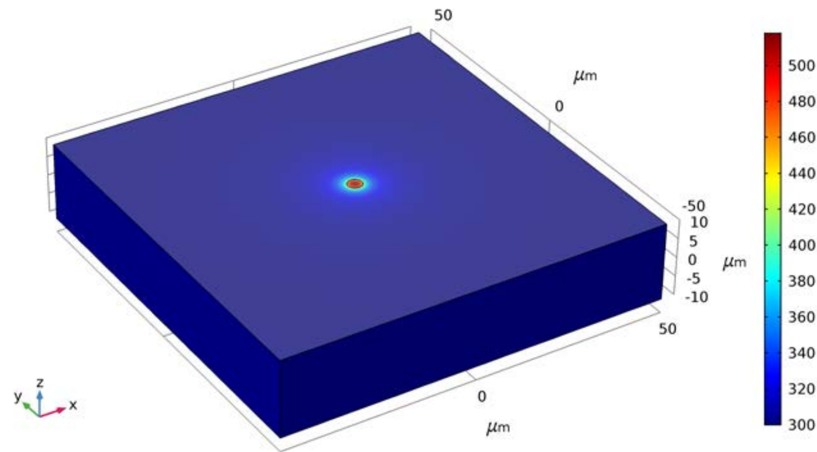

Figure 6.7: Illustration of the theoretical model used for calculations of the temperature distribution in SiNWs. The color indicates the SiNWs temperature, accordingly to the scale on the right.

The set problem was solved by the finite element analysis method. For the calculations, instead of the infinite layer, the block of the size of 100*100 μm was used, which has the isotropic thermal conductivity coefficient equal to k_{eff}. The size of the block was chosen to be much larger than temperature dissipation region, and the increase in the box size did not change the calculated temperature profile. Therefore, the influence of side borders of the box on the results of calculation can be excluded. The SiNWs sample used for simulations is illustrated in Fig. 6.7, where the color corresponds the calculated SiNWs temperature, with the scale bar in the right. As can be seen from the figure, the heating of SiNWs significantly differs from zero

Cette thèse est accessible à l'adresse : http://theses.insa-lyon.fr/publication/2019LYSEI129/these.pdf
© [S. Rodichkina], [2019], INSA de Lyon, tous droits réservés

for $r < 8\ \mu$m, which is much smaller than the box size.

Another approach to determine the thermal conductivity coefficient of SiNWs is to use the one-dimensional heat equation. This approach is consequential for SiNWs arrays because their lateral thermal transport is strongly suppressed. For example, the lateral thermal conductivity of MACE-SiNWs array was estimated of 0.01-0.03 W/(m*K), close to air thermal conductivity of 0.025 W/(m*K), while the thermal conductivity along SiNWs was of 4-6 W/(m*K) [8]. Considering the similar boundary conditions for one-dimensional heat transport in SiNWs array along z-axis (see Eq. (6.1)), the photo-induced heating of SiNWs is given by: $\Delta T = I_L L / k_{eff}$. Fig. 6.8 shows the experimental dependence of SiNWs photo-induced heating on their length and its fit in the cases of 1D and 3D heat transport. In 1D case, the linear dependence of photo-induced heating on SiNWs length is observed, while in 3D case the heating approaches a constant value for $L > 10\ \mu$m. One can observe that three-dimensional heat equation gives a much better qualitative description of the dependence of photo-induced SiNWs heating on their length. The reason can be that the thermal transport in individual SiNWs is strongly affected by the surface roughness scattering (see Sec. 1.3)) and can not be described by one-dimensional model.

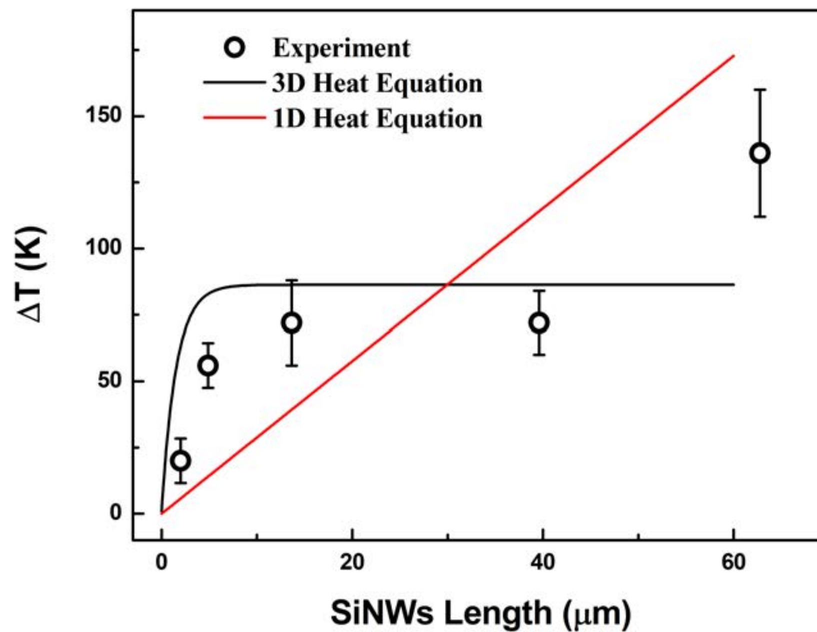

Figure 6.8: Experiment dependence (circles) of the photo-induced heating of SiNWs on their length. Lines show the fits of the experimental dependence, calculated assuming the three-dimensional (black line) and one-dimensional (red line) heat transport in SiNWs array.

The effective thermal conductivity coefficient of SiNWs array, determined using the Raman peak position Ω and peak width Γ, is of 0.8 and 0.27 W/(m·K), correspondingly. In regard with

Cette thèse est accessible à l'adresse : http://theses.insa-lyon.fr/publication/2019LYSEI129/these.pdf
© [S. Rodichkina], [2019], INSA de Lyon, tous droits réservés

the above, the value of $k_{\text{eff}} = 0.27$ W/(m·K), determined using Γ seems more reasonable. Thermal conductivity coefficient along SiNWs, estimated as $k_{NW} = k_{\text{eff}}/(1-p)$, is of 1.1 W/(m·K). This value corresponds well to the values of thermal conductivity coefficient of individual low-doped MACE-SiNWs, measured by direct methods, which are of 2-8 W/(m·K) for SiNWs diameter of 50-100 nm (see Sec. 1.3). In our case, lower values of thermal conductivity are mainly related to the fact that an isotropic heat transport in SiNWs array was considered, and in order to precisely determine the thermal conductivity along SiNWs, the anisotropy of the heat transport in SiNWs array should be considered.

6.2.2 Thermal conductivity of low- and highly-doped SiNWs

The insets in Fig. 6.9 show the Raman spectra for initial and doped SiNWs with increasing laser power and their fits with the Fano resonance function, given by Eq. (4.13). Lorentzian peak for undoped SiNWs is described by Eq.(4.13) with $q = \infty$. As the laser power increases, the low-frequency shift and broadening of the Raman peak both for undoped and doped SiNWs are observed, as well as the decrease in the asymmetry of the Raman peak for doped SiNWs. The modification of the Raman peak with increasing laser power is explained by the photo-induced heating for both undoped and doped SiNWs. The effect of photoexcitation on the Raman peak parameters for undoped SiNWs was discussed in detail in the previous section. For doped SiNWs, the effect of photoexcitation on the Fano resonance should also be taken into account, which consists in the change in the electron and phonon concentration and electron-phonon interaction in SiNWs under photo-induced heating. The photogeneration of electron-hole pairs was neglected. The effect of photoexcitation on free charge carriers in SiNWs will be discussed below in more detail.

The broadening of the Raman peak (ΔΓ) was calculated as the difference in half-width Γ for a given laser power and low laser power, which does not cause SiNWs heating. The Raman peak broadening values were used to calculate the heating of SiNWs using the temperature dependence of Raman peak width for c-Si (see Fig. 6.4 (b)). For undoped SiNWs, the Raman peak broadening is directly related to the photo-induced heating, because the width of the Raman peak for SiNWs does not depend on mechanical stresses in SiNWs (see Sec. 6.2.1). For doped SiNWs, the determined heating can be systematically overestimated, because the broadening of the Raman peak with increasing temperature is related not only to the enhancement of phonon-phonon scattering, but also of phonon-electron and phonon-impurity scattering.

Cette thèse est accessible à l'adresse : http://theses.insa-lyon.fr/publication/2019LYSEI129/these.pdf
© [S. Rodichkina], [2019], INSA de Lyon, tous droits réservés

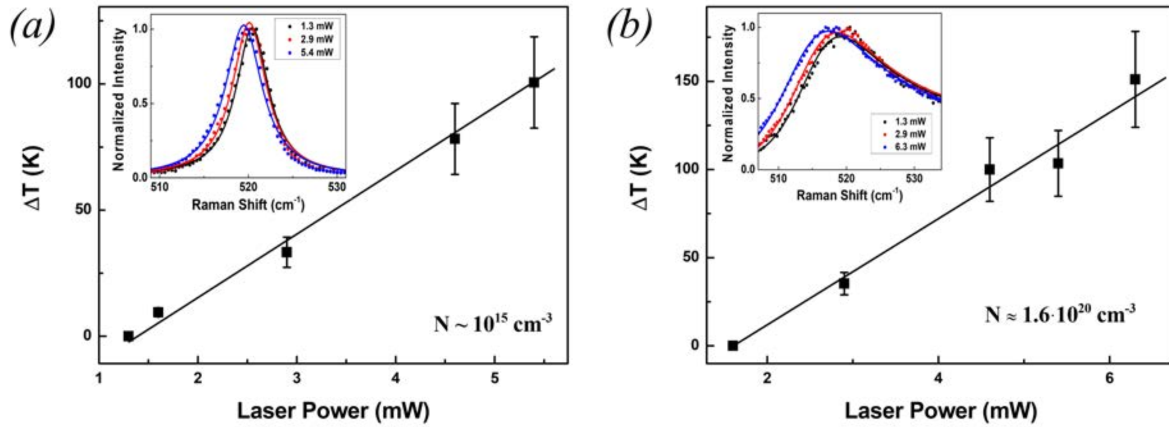

Figure 6.9: Heating of SiNWs, determined from the broadening of the one-phonon Raman peak, as a function of the laser power for (a) initial and (b) doped SiNWs. Lines show the linear fits of the above dependencies. Insets: (points) Raman spectra of SiNWs at different laser power, (lines) fit of the Raman spectra with Fano resonance function. The free hole concentration in doped SiNWs is of 15.7 ± 0.7 cm^{-3}. Laser wavelength is 632.8 nm.

It is interesting to analyze the change in the free hole concentration in SiNWs with increasing photo-excitation, which can be caused by a photogeneration of electron-hole (e-h) pairs, as well as by free charge carrier transport in SiNWs due to the electron thermal conductivity. The Fano effect for electrons in SiNWs can be observed only for free electron concentrations above $5 * 10^{19}$ cm^{-3} and is much weaker than the Fano effect for holes (see Sec. 4.3), and the photogeneration of e-h pairs would lead to the observation of Fano effect for holes. Since the Raman peak shape for low-doped SiNWs can be described by Lorentzian function ($q = \infty$) at all photoexcitation levels used, one can conclude that the concentration of e-h pairs in photoexcited SiNWs is less than 10^{19} cm^{-3}, much lower than the doping level of doped SiNWs ($\sim 10^{19}$ cm^{-3}). The decrease in the Raman peak asymmetry with increasing laser power for doped SiNWs can be explained by the change in relative probability of one-phonon and electron Raman scattering with temperature. Indeed, a linear decrease in $1/q$ with temperature was reported for oven-heated boron-doped c-Si with $N = 1.4 * 10^{20}$ cm^{-3}, studied under 708 nm excitation [160]. In our case, the free hole concentration in SiNWs is of $N = 1.6 * 10^{20}$ cm^{-3} and the laser wavelength is 632.8 nm. The slopes of the temperature dependence of $1/q$, normalized to $1/q$ values at $T = 300$ K, for c-Si and investigated SiNWs are of $-1.4 * 10^{-3}$ and $-1.0 * 10^{-3}$ 1/K, correspondingly, which are close to each other. Since the free hole concentration in c-Si does not change with temperature because all the impurity atoms are activated, one can conclude no change in free hole concentration in highly-doped SiNWs under used photoexcitation.

Fig. 6.9 (a,b) shows the photo-induced heating for low- and highly-doped SiNWs arrays,

Cette thèse est accessible à l'adresse : http://theses.insa-lyon.fr/publication/2019LYSEI129/these.pdf
© [S. Rodichkina], [2019], INSA de Lyon, tous droits réservés

determined from the broadening of the Raman peak, as a function of excitation power. The linear dependence of ΔT on laser power is observed, which is in accordance with the heat conductivity equation Eq. (6.1). The slopes of the lines for low- and highly-doped SiNWs are close to each other, which that thermal conductivity of SiNWs is almost independent of the doping level up to $\sim 10^{20}$ cm^{-3}. One can expect the decrease in thermal conductivity of SiNWs for higher photo-induced heating due to decrease in both lattice and electron thermal conductivity because of enhanced phonon and electron scattering [29, 181].

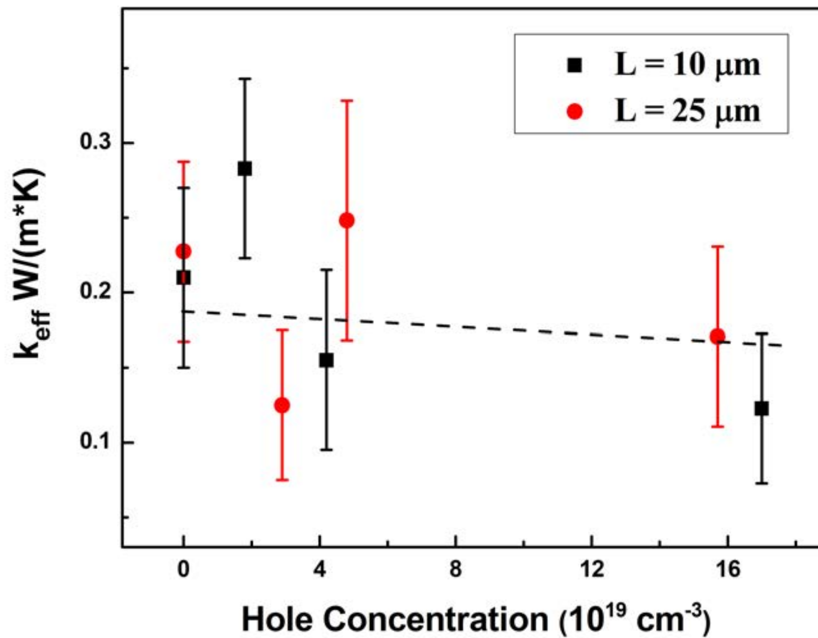

Figure 6.10: Effective thermal conductivity coefficient of SiNWs array as a function of the free hole concentration. SiNWs length is 10 and 25 μm. Lines show the least squares linear fit of the above dependence.

The effective thermal conductivity coefficient for SiNWs arrays was determined from the slope of the dependence of photo-induced heating on laser intensity by solving the heat conductivity equation (Eq. (6.1)). The obtained values of k_{eff} were averaged over several points of SiNWs sample. Fig. 6.10 shows the effective thermal conductivity coefficient of SiNWs arrays as a function of the free hole concentration for SiNWs with length of 10 and 25 μm. No difference in the thermal conductivity between low- and highly-doped SiNWs is observed within the experimental error. The determined k_{eff} for SiNWs arrays is of about 0.2 W/(m*K), and the thermal conductivity of SiNWs, estimated as $k_{NW} = k_{\mathrm{eff}}/(1-p)$, is of about 0.8 W/(m*K). Similar results were obtained by direct measurements of individual low- and highly-doped MACE-SiNWs, which shown a slight decrease in the thermal conductivity for a nanowire with diameter of 50 nm after the doping to the level of $N \sim 10^{19}$ cm^{-3} (see Sec. 1.3). Considering the

Cette thèse est accessible à l'adresse : http://theses.insa-lyon.fr/publication/2019LYSEI129/these.pdf
© [S. Rodichkina], [2019], INSA de Lyon, tous droits réservés

same electron transport in SiNWs and c-Si (see Sec. 6.1), the hole thermal conductivity in SiNWs with $N \sim 10^{20}$ cm^{-3}, calculated using the Wiedemann-Franz law, is of about 0.5 W/(m*K), which is close to $k_{NW} \approx 0.80$ W/(m*K) and to the error bars of k_{NW} of about 0.25 W/(m*K). The absence of the considerable trend in k_{eff} with increasing free hole concentration for SiNWs can be explained by the simultaneous effect of the electron contribution to the thermal conductivity and phonon-impurity and phonon-electron scattering (see Sec. 1.3). Note, that the values of k_{NW} are underestimated because the anisotropy of the heat transport was not taken into account. An inhomogeneous doping level profile along SiNWs and nonzero light penetration depth, which have not been taken into account, can also influence the determined values of thermal conductivity of SiNWs.

The values of photo-induced heating for 10 and 25 μm SiNWs are close to each other, which is in agreement with the results of 3D thermal transport modeling (see Fig. 6.8). The same photo-induced heating for SiNWs with different length > 10 μm indicates that in-depth temperature decrease in SiNWs due to thermal conductivity takes place at depth less than 10 μm, and the c-Si substrate does not influence thermal transport in SiNWs array. This fact can be explained by the influence of surface roughness scattering in SiNWs. The observed thermal transport behaviour shows the fundamental limit in SiNWs length for thermoelectric devices, since no temperature gradient exists in SiNWs array at depth more than 10 μm, and no thermoelectric effect occurs.

6.3 Conclusions to Chapter 6

a) Electrical resistivity of MACE-SiNWs

The electrical resistivity of SiNWs was determined using (i) the free hole concentration values, measured by the optical methods and (ii) two-probe electrical measurements of SiNWs arrays at different distances between the electrical contacts. To compare the results of both techniques, the average electrical resistivity of SiNWs using the doping level profile along nanowires was calculated. The obtained values are close to each other, which indicates that the free hole mobility in highly-doped SiNWs arrays is close to the corresponding bulk Si values for the given free hole concentration. The absence of the influence of SiNWs surface on the free hole mobility is explained by the high scattering rate of holes by impurity atoms, which limits the electron transport in SiNWs.

The electrical resistivity of highly-doped SiNWs, obtained using the standard SOD doping

Cette thèse est accessible à l'adresse : http://theses.insa-lyon.fr/publication/2019LYSEI129/these.pdf
© [S. Rodichkina], [2019], INSA de Lyon, tous droits réservés

procedure, is about 1 mΩ*cm at the top of SiNWs, and the average value along SiNWs is about 4 mΩ*cm. The average electrical resistivity of SiNWs, obtained using the SOD doping procedure with thick dopant layers, is about 1 mΩ*cm, that is essential for application of SiNWs in nano-electronic, thermoelectric and sensor devices.

b) Thermal conductivity of MACE-SiNWs

Thermal conductivity of SiNWs array was determined by solving the heat equation, where the values of photo-induced heating were determined using the broadening of the one-phonon Raman peak. The thermal conductivity coefficient is of $k_{NW} \approx 1.0$ W/(m*K) for both low- and highly-doped SiNWs. This fact is important for thermoelectric applications of highly-doped SiNWs, because the doping does not increase the SiNWs thermal conductivity. Our analysis shows that the heat transport along SiNWs is strongly influenced by SiNWs surface and can not be described by one-dimensional heat equation. The same values of photo-induced heating observed for SiNWs with length more than 10 μm indicate that the temperature gradient in SiNWs exists up to the depth of about 10 μm, which represents the limiting length of nanowires in SiNWs arrays for thermoelectric devices.

c) Evaluation of the potential of highly-doped MACE-SiNWs for thermoelectric applications

Highly-doped MACE-SiNWs, obtained using the standard SOD procedure, exhibit the electrical resistivity of about 4 mΩ*cm and thermal conductivity of about 1 W/(m*K) at room temperature. One can estimate their thermoelectric potential, using the reported value of $S = 0.24$ mV/K for MACE-SiNWs with electrical resistivity of 1.7 mΩ*cm (see Sec. 1.5). Thus, the average ZT of nanowires in SiNWs array can be estimated of about 0.5.

One can take into account that (i) highly-doped SiNWs arrays with homogeneous doping level exhibit $\rho = 1$ mΩ*cm, (ii) more reasonable value of the thermal conductivity of 1.6 W/(m*K), measured by direct method for highly-doped individual SiNWs with $\rho = 1.7$ mΩ*cm. Thus, ZT of MACE-SiNWs arrays, additionally doped using the SOD doping procedure, lies in the range of 0.5 - 1.7, that makes such SiNWs promising for thermoelectric applications.

Cette thèse est accessible à l'adresse : http://theses.insa-lyon.fr/publication/2019LYSEI129/these.pdf
© [S. Rodichkina], [2019], INSA de Lyon, tous droits réservés

General conclusions

In this work the electrical and thermal properties of SiNWs arrays, formed by metal-assisted chemical etching of low-doped crystalline silicon wafers followed by thermo-diffusional doping with p- and n-type impurities, were investigated in view of their thermometric applications, and the following main results were obtained:

1. Arrays of crystalline SiNWs with porosity of 75%, typical nanowire diameter of 100 nm and length of 10 μm, and initial concentration of boron impurities $\sim 10^{15}$ cm^{-3}, were homogeneously doped with boron impurities to the level above 10^{20} cm^{-3} for entire length of SiNWs, using the thermal diffusion of boron atoms. SiNWs, formed by metal-assisted chemical etching of low p-type doped c-Si substrates with the electrical resistivity ~ 10 Ω*cm, had bulk core/rough surface morphology and nearly uniform diameter along the nanowires. Post-fabrication doping of SiNWs was performed by using the thermal diffusion of boron (p-type) or phosphorus (n-type) impurities from commercial spin-on dopant solutions, and the doping levels in Si nanocrystals $\sim 10^{20}$ cm^{-3} were obtained. The doping procedure, which includes high-temperature annealing at about 1000 ^{0}C does not influence the morphology and crystallinity of SiNWs.
2. The Raman spectroscopy can be used to as an efficient method to monitor the crystalline structure of SiNWs. It was found that SiNWs, excited with visible laser radiation with intensity above 10 kW/cm^2 exhibit structural transformation form cubic to hexagonal diamond lattice. The effect can be monitored as the shift and splitting of the one-phonon Raman line of SiNWs with increasing photoexcitation, where the Raman peak for hex-Si phase is centered around 490-505 cm^{-1}. Formation of the hex-Si phase in SiNWs is favoured by strong mechanical stresses caused by temperature gradient along SiNWs, which can be observed as a singlet-doublet splitting of the Raman peaks for LO and TO phonons. The formation of hex-Si phase in SiNWs under intense photoexcitation can be additionally proved by the PL method as the huge increase in the PL intensity at laser intensities above 10 kW/cm^2, which correlates with the appearance of the Raman peak for

Cette thèse est accessible à l'adresse : http://theses.insa-lyon.fr/publication/2019LYSEI129/these.pdf
© [S. Rodichkina], [2019], INSA de Lyon, tous droits réservés

hex-Si. The spectral position of PL band at about 1.5 eV is close to the direct band gap transition in the stressed hex-Si.

3. Infrared spectroscopy in attenuated total reflectance mode was applied to probe the free charge carrier concentration in p- and n-type highly-doped SiNWs and por-Si in the range of $10^{18} \div 10^{20}$ cm^{-3}. To describe the IR-ATR spectra of SiNWs, the theoretical model based on anisotropic effective medium approximation and Drude model for free charge carriers was developed. The Drude model was modified to describe the additional scattering of free charge carriers by the surface of Si nanocrystals. IR-ATR method was shown to underestimate the values of free charge carrier concentration for MACE-SiNWs due to the rough morphology of SiNWs tips.
4. Raman scattering spectroscopy was applied to precisely probe the free charge carrier in p-type highly-doped SiNWs in the range of $10^{19} \div 10^{20}$ cm^{-3}. One-phonon Raman spectra of the boron-doped SiNWs are strongly modified due to the Fano effect, that allows us to determine the free hole concentration in SiNWs using the Fano peak half-width. The micro-Raman mapping was used to determine the in-depth profiles of the free hole concentration in SiNWs arrays. For n-type SiNWs, the Fano modification of the Raman peak is much smaller than for p-type ones, and it can be observed only for doping levels of SiNWs above $5 * 10^{19}$ cm^{-3}.
5. Post-fabrication doping method which consists in the spin-coating of the spin-on dopant solution on tops of SiNWs and following annealing, leads to the strongly inhomogeneous in-depth doping profiles in SiNWs arrays. The doping levels less than $2 * 10^{19}$ cm^{-3} are observed at the depth of 6 μm. Dissolution of spin-on dopant slightly increases the doping depth to 8 μm. The increase in the annealing temperature above 950 ^{0}C, as well as in the annealing time above 25s, does not enhance the doping profile in SiNWs, because the boron diffusion into SiNWs is limited by the boron concentration in the dopant layer and boron solubility limit. The almost homogeneous in-depth doping profile in SiNWs arrays were obtained using the thick dopant layers, deposited without spin-coating, and the free hole concentration in SiNWs above 10^{20} cm^{-3} is observed up to the depth of 10 μm.
6. The free hole mobility in highly-doped SiNWs arrays is close to the corresponding bulk Si values for the given free hole concentration. The values of the electrical resistivity of SiNWs, estimated using the two-point probe technique at different distances between the electrical contacts, are close to the ones, calculated using the free hole concentration

Cette thèse est accessible à l'adresse : http://theses.insa-lyon.fr/publication/2019LYSEI129/these.pdf
© [S. Rodichkina], [2019], INSA de Lyon, tous droits réservés

profile of SiNWs and bulk mobility values. The absence of the influence of SiNWs surface on the free hole mobility is explained by the high scattering rate of holes by impurity atoms, which limits the electron transport in SiNWs. The values of electrical resistivity for highly-doped SiNWs are about 1-5 mΩ*cm, which is essential for application of SiNWs in nano-electronic, thermoelectric and sensor devices.

7. Raman scattering spectroscopy was applied to probe the effective thermal conductivity coefficient of SiNWs arrays. The latter was determined by solving the three-dimensional heat equation, where the values of photo-induced heating can be determined using the broadening of the one-phonon Raman peak. The thermal conductivity coefficient along SiNWs is estimated of about 1.0 ± 0.3 W/(m*K), and it is independent of the p-type doping level in SiNWs up to $2 * 10^{20}$ cm^{-3} withing the experimental error. The electron thermal conductivity of SiNWs with $N \approx 10^{20}$ cm^{-3}, estimated using the bulk hole mobility, is of 0.5 W/(m*K). The determined values of SiNWs thermal conductivity can be underestimated due to use of isotropic heat transport model. The same values of photo-induced heating observed for SiNWs with length more than 10 μm indicate that the temperature gradient in SiNWs exists up to the depth of about 10 μm, which represents the limiting length of nanowires in SiNWs arrays for thermoelectric devices.

The observed high electrical and low thermal conductivity of highly-doped SiNWs arrays, which were fabricated using the simple and low-cost methods, shows that SiNWs arrays represent a promising material for thermoelectric applications.

Cette thèse est accessible à l'adresse : http://theses.insa-lyon.fr/publication/2019LYSEI129/these.pdf
© [S. Rodichkina], [2019], INSA de Lyon, tous droits réservés

Appendix A

Derivation of Fresnel equations for an anisotropic medium

Let us consider the macroscopic Maxwell's equations [153] and constitutive relations for a continuous medium:

$$\mathbf{D} = \varepsilon\mathbf{E}; \mathbf{B} = \mathbf{H}, \tag{6.2}$$

where $\mathbf{E}$ is the electrical field, $\mathbf{B}$ is the magnetic field, $\mathbf{D}$ is the displacement field, $\mathbf{H}$ is the magnetizing field and ε is the tensor of dielectric constant of the medium. For an uniaxial anisotropic medium and the chosen coordinate set, Eqs. (6.2) take the following form, since z-axis coincides with the optical axis of crystal

$$\mathbf{D} = \begin{pmatrix} \varepsilon_{\perp} & & \\ & \varepsilon_{\perp} & \\ & & \varepsilon_{\parallel} \end{pmatrix} \mathbf{E} \tag{6.3}$$

For the ordinary and extraordinary rays, one can obtain (i) the relations between the refraction index and dielectric constant:

$$n_o^2 = \varepsilon_{\perp} \tag{6.4}$$

$$\frac{n_{z_e}^2}{\varepsilon_{\perp}} + \frac{n_{x_e}^2 + n_{y_e}^2}{\varepsilon_{\parallel}} = 1, \tag{6.5}$$

where $\mathbf{n}$ is determined by $\mathbf{k} = \omega\mathbf{n}/\mathbf{c}$, $\mathbf{k}$ is the light wave vector, ω is the light frequency, c is the speed of light in vacuum.

(ii) The ordinary wave is polarized perpendicular to the optical axis of the medium, and the extraordinary wave is polarized in plane of $\mathbf{k}$ and optical axis (xz-plane).

At reflection, the following relations for wave vectors of incident, reflected and transmitted waves can be obtained:

$$n_{x0} = n_{x1} = n_{x2} \tag{6.6}$$

Cette thèse est accessible à l'adresse : http://theses.insa-lyon.fr/publication/2019LYSEI129/these.pdf
© [S. Rodichkina], [2019], INSA de Lyon, tous droits réservés

$$n_{y0} = n_{y1} = n_{y2} \tag{6.7}$$

$$n_{z2_o} = \sqrt{\varepsilon_{\perp} - n_{x0}^2} \tag{6.8}$$

$$n_{z2_e} = \sqrt{\varepsilon_{\perp} - \frac{\varepsilon_{\perp}}{\varepsilon_{\parallel}} n_{x0}^2} \tag{6.9}$$

For the electromagnetic field, the continuity conditions for the components $E_{x,y}$ and $H_{x,y}$ are satisfied.

Therefore, in the considered case, the transmitted wave for the s-polarized incident wave represents an ordinary wave, and for p-polarized incident wave the transmitted wave is an extraordinary wave.

– *s-polarized incident wave*

The continuity conditions for E_y and H_x:

$$E_{0y} + E_{1y} = E_{2y} \tag{6.10}$$

$$H_{0x} + H_{1y} = H_{2x} \tag{6.11}$$

Considering that $\mathbf{H} = [\mathbf{nE}]$, one obtains

$$E_0 + E_1 = E_2 \tag{6.12}$$

$$n_{z0}E_0 - n_{z0}E_1 = n_{z2}E_2 \tag{6.13}$$

The electric field of the reflected and transmitted wave is

$$E_1 = \frac{n_{z0} - n_{z2}}{n_{z0} + n_{z2}} E_0 \tag{6.14}$$

$$E_2 = \frac{2n_{z0}E_0}{n_{z0} + n_{z2}} \tag{6.15}$$

– *p-polarized incident wave*

The continuity conditions for H_y and E_x:

$$H_{y0} + H_{y1} = H_{y2} \tag{6.16}$$

Cette thèse est accessible à l'adresse : http://theses.insa-lyon.fr/publication/2019LYSEI129/these.pdf
© [S. Rodichkina], [2019], INSA de Lyon, tous droits réservés

$$E_{x0} + E_{x1} = E_{x2} \tag{6.17}$$

Considering that $\mathbf{D} = -[\mathbf{nH}]$, one obtains

$$E_x = \frac{D_x}{\varepsilon_\perp} = \frac{n_z H_y}{\varepsilon_\perp} \tag{6.18}$$

and

$$H_0 + H_1 = H_2 \tag{6.19}$$

$$\frac{n_{z0} H_0}{\varepsilon_{Ge}} - \frac{n_{z0} H_1}{\varepsilon_{Ge}} = \frac{n_{z2} H_2}{\varepsilon_\perp} \tag{6.20}$$

The magnetic field of the reflected and transmitted wave is

$$H_1 = \frac{\varepsilon_\perp cos\theta - n_{z2} n_{Ge}}{\varepsilon_\perp cos\theta + n_{z2} n_{Ge}} H_0 \tag{6.21}$$

$$H_2 = \frac{2\frac{n_{z0}}{\varepsilon_{Ge}} H_0}{\frac{n_{z0}}{\varepsilon_{Ge}} + \frac{n_{z2}}{\varepsilon_\perp}} \tag{6.22}$$

If $\varepsilon_\perp = \varepsilon_2$, the formula for H_1 coincides with the corresponding formula for opaque isotropic medium.

The reflectance coefficients are obtained as $R_s = |E_1/E_0|^2$ and $R_p = |H_1/H_0|^2$. Finally, the reflectance coefficients $R_{s,p}$ can be expressed in the following way:

$$R_s = \left| \frac{\frac{\omega}{c} n_{Ge} cos\theta - k_{zo}}{\frac{\omega}{c} n_{Ge} cos\theta + k_{zo}} \right|^2 \tag{6.23}$$

$$R_p = \left| \frac{\frac{\omega}{c} \varepsilon_\perp cos\theta - n_{Ge} k_{ze}}{\frac{\omega}{c} \varepsilon_\perp cos\theta + n_{Ge} k_{ze}} \right|^2, \tag{6.24}$$

where

$$k_{zo} = \frac{\omega}{c} \sqrt{\varepsilon_\perp - n_{Ge}^2 sin^2\theta} \tag{6.25}$$

$$k_{ze} = \frac{\omega}{c} \sqrt{\varepsilon_\perp - \frac{\varepsilon_\perp}{\varepsilon_\parallel} n_{Ge}^2 sin^2\theta}. \tag{6.26}$$

Cette thèse est accessible à l'adresse : http://theses.insa-lyon.fr/publication/2019LYSEI129/these.pdf
© [S. Rodichkina], [2019], INSA de Lyon, tous droits réservés

Bibliography

[1] S. Misra, L. Yu, W. Chen, M. Foldyna, and P. R. Cabarrocas, "A review on plasma-assisted vls synthesis of silicon nanowires and radial junction solar cells," *Journal of Physics D: Applied Physics*, vol. 47, no. 39, p. 393001, 2014.

[2] Z. R. Smith, R. L. Smith, and S. D. Collins, "Mechanism of nanowire formation in metal assisted chemical etching," *Electrochimica Acta*, vol. 92, pp. 139–147, 2013.

[3] J. Wang, Y. Hu, H. Zhao, H. Fu, Y. Wang, C. Huo, and K.-Q. Peng, "Oxidant concentration modulated metal/silicon interface electrical field mediates metal-assisted chemical etching of silicon," *Advanced Materials Interfaces*, vol. 5, no. 23, p. 1801132, 2018.

[4] Y. Liu, W. Sun, Y. Jiang, and X.-Z. Zhao, "Fabrication of bifacial wafer-scale silicon nanowire arrays with ultra-high aspect ratio through controllable metal-assisted chemical etching," *Materials Letters*, vol. 139, pp. 437–442, 2015.

[5] Y. Qu, L. Liao, Y. Li, H. Zhang, Y. Huang, and X. Duan, "Electrically conductive and optically active porous silicon nanowires," *Nano letters*, vol. 9, no. 12, pp. 4539–4543, 2009.

[6] J. M. Weisse, A. M. Marconnet, D. R. Kim, P. M. Rao, M. A. Panzer, K. E. Goodson, and X. Zheng, "Thermal conductivity in porous silicon nanowire arrays," *Nanoscale research letters*, vol. 7, no. 1, p. 554, 2012.

[7] A. I. Hochbaum, R. Chen, R. D. Delgado, W. Liang, E. C. Garnett, M. Najarian, A. Majumdar, and P. Yang, "Enhanced thermoelectric performance of rough silicon nanowires," *Nature*, vol. 451, no. 7175, pp. 163–167, 2008.

[8] M. Isaiev, O. Didukh, T. Nychyporuk, V. Timoshenko, and V. Lysenko, "Anisotropic heat conduction in silicon nanowire network revealed by raman scattering," *Applied Physics Letters*, vol. 110, no. 1, p. 011908, 2017.

Cette thèse est accessible à l'adresse : http://theses.insa-lyon.fr/publication/2019LYSEI129/these.pdf
© [S. Rodichkina], [2019], INSA de Lyon, tous droits réservés

[9] M. Dutta, L. Thirugnanam, and N. Fukata, "Si nanowire solar cells: Principles, device types, future aspects, and challenges," in *Advances in Silicon Solar Cells*, pp. 299–329, Springer, 2018.

[10] B. M. Kayes, M. A. Filler, M. C. Putnam, M. D. Kelzenberg, N. S. Lewis, and H. A. Atwater, "Growth of vertically aligned si wire arrays over large areas (> 1 cm 2) with au and cu catalysts," *Applied Physics Letters*, vol. 91, no. 10, p. 103110, 2007.

[11] S. Wippermann, Y. He, M. Vörös, and G. Galli, "Novel silicon phases and nanostructures for solar energy conversion," *Applied Physics Reviews*, vol. 3, no. 4, p. 040807, 2016.

[12] J. Tang, J. L. Maurice, F. Fossard, I. Florea, W. Chen, E. V. Johnson, M. Foldyna, L. Yu, and P. Rocai Cabarrocas, "Natural occurrence of the diamond hexagonal structure in silicon nanowires grown by a plasma-assisted vapour-liquid-solid method," *Nanoscale*, vol. 9, no. 24, pp. 8113–8118, 2017.

[13] Y. Gogotsi, C. Baek, and F. Kirscht, "Raman microspectroscopy study of processing-induced phase transformations and residual stress in silicon," *Semicond. Sci. Technol.*, vol. 14, no. 10, pp. 936–944, 1999.

[14] C. Kendrick, M.-W. Kuo, J. Li, H. Shen, T. S. Mayer, and J. M. Redwing, "Uniform p-type doping of silicon nanowires synthesized via vapor-liquid-solid growth with silicon tetrachloride," *Journal of Applied Physics*, vol. 122, no. 23, p. 235101, 2017.

[15] N. Fukata, R. Takiguchi, S. Ishida, S. Yokono, S. Hishita, and K. Murakami, "Recrystallization and reactivation of dopant atoms in ion-implanted silicon nanowires," *Acs Nano*, vol. 6, no. 4, pp. 3278–3283, 2012.

[16] S. W. Jones, "Diffusion in silicon," *IC Knowledge LLC*, pp. 23–61, 2008.

[17] F. A. Trumbore, "Solid solubilities of impurity elements in germanium and silicon," *Bell System Technical Journal*, vol. 39, no. 1, pp. 205–233, 1960.

[18] V. Boeisenko and S. Yudin, "Steady-state solubility of substitutional impurities in silicon," *physica status solidi (a)*, vol. 101, no. 1, pp. 123–127, 1987.

[19] F. A. Trumbore, "Solid solubilities of impurity elements in germanium and silicon," *Bell System Technical Journal*, vol. 39, no. 1, pp. 205–233, 1960.

Cette thèse est accessible à l'adresse : http://theses.insa-lyon.fr/publication/2019LYSEI129/these.pdf
© [S. Rodichkina], [2019], INSA de Lyon, tous droits réservés

[20] M. Nolan, T. Perova, R. Moore, and H. Gamble, "Boron diffusion from a spin-on source during rapid thermal processing," *Journal of non-crystalline solids*, vol. 254, no. 1-3, pp. 89–93, 1999.

[21] S. Ingole, P. Aella, P. Manandhar, S. Chikkannanavar, E. Akhadov, D. Smith, and S. Picraux, "Ex situ doping of silicon nanowires with boron," *Journal of Applied Physics*, vol. 103, no. 10, p. 104302, 2008.

[22] J. Zou and A. Balandin, "Phonon heat conduction in a semiconductor nanowire," *J. Appl. Phys.*, vol. 89, no. 5, pp. 2932–2938, 2001.

[23] J. Zhou, B. Liao, B. Qiu, S. Huberman, K. Esfarjani, M. S. Dresselhaus, and G. Chen, "Ab initio optimization of phonon drag effect for lower-temperature thermoelectric energy conversion," *Proc. Natl. Acad. Sci.*, vol. 112, no. 48, pp. 14777–14782, 2015.

[24] D. Li, Y. Wu, P. Kim, L. Shi, P. Yang, and A. Majumdar, "Thermal conductivity of individual silicon nanowires," *Appl. Phys. Lett.*, vol. 83, no. 14, pp. 2934–2936, 2003.

[25] D. Lacroix, K. Joulain, D. Terris, and D. Lemonnier, "Monte Carlo simulation of phonon confinement in silicon nanostructures: Application to the determination of the thermal conductivity of silicon nanowires," *Appl. Phys. Lett.*, vol. 89, no. 10, 2006.

[26] P. Chantrenne, J. L. Barrat, X. Blase, and J. D. Gale, "An analytical model for the thermal conductivity of silicon nanostructures," *J. Appl. Phys.*, vol. 97, no. 10, pp. 1–8, 2005.

[27] S. Volz, D. Lemonnier, and J. Saulnier, "Microscale thermophys. eng," 2001.

[28] N. Mingo, "Calculation of si nanowire thermal conductivity using complete phonon dispersion relations," *Phys. Rev. B*, vol. 68, p. 113308, 2003.

[29] C. J. Glassbrenner and G. A. Slack, "Thermal conductivity of silicon and germanium from 3K to the melting point," *Phys. Rev.*, vol. 134, no. 4A, 1964.

[30] A. Stranz, J. Kähler, A. Waag, and E. Peiner, "Thermoelectric properties of high-doped silicon from room temperature to 900 K," *J. Electron. Mater.*, vol. 42, no. 7, pp. 2381–2387, 2013.

Cette thèse est accessible à l'adresse : http://theses.insa-lyon.fr/publication/2019LYSEI129/these.pdf
© [S. Rodichkina], [2019], INSA de Lyon, tous droits réservés

[31] P. Martin, Z. Aksamija, E. Pop, and U. Ravaioli, “Impact of phonon-surface roughness scattering on thermal conductivity of thin Si nanowires,” *Phys. Rev. Lett.*, vol. 102, no. 12, pp. 1–4, 2009.

[32] Ioffe Institute (Russia) official website, “`http://www.ioffe.ru/SVA/NSM/Semicond/Si/electric.html`,” accessed 30/08/2019.

[33] W. R. Thurber, *The relationship between resistivity and dopant density for phosphorus- and boron-doped silicon*, vol. 400. US Department of Commerce, National Bureau of Standards, 1981.

[34] V. Schmidt, J. V. Wittemann, and U. Gosele, “Growth, Thermodynamics, and Electrical Properties of Silicon Nanowires.,” *Chem. Rev. (Washington, DC, United States)*, vol. 110, no. 1, pp. 361–388, 2010.

[35] S. Jin, M. V. Fischetti, and T. W. Tang, “Modeling of electron mobility in gated silicon nanowires at room temperature: Surface roughness scattering, dielectric screening, and band nonparabolicity,” *J. Appl. Phys.*, vol. 102, no. 8, 2007.

[36] V. A. Fonoberov and A. A. Balandin, “Giant enhancement of the carrier mobility in silicon nanowires with diamond coating,” *Nano Lett.*, vol. 6, no. 11, pp. 2442–2446, 2006.

[37] I. Park, Z. Li, A. P. Pisano, and R. S. Williams, “Top-down fabricated silicon nanowire sensors for real-time chemical detection,” *Nanotechnology*, vol. 21, no. 1, 2010.

[38] J. Kim, Y. Hyun, Y. Park, W. Choi, S. Kim, H. Jeon, T. Zyung, and M. Jang, “Seebeck Coefficient Characterization of Highly Doped <I>n</I>- and <I>p</I>-Type Silicon Nanowires for Thermoelectric Device Applications Fabricated with Top-Down Approach,” *J. Nanosci. Nanotechnol.*, vol. 13, no. 9, pp. 6416–6419, 2013.

[39] G. Pennelli, “Review of nanostructured devices for thermoelectric applications,” *Beilstein J. Nanotechnol.*, vol. 5, no. 1, pp. 1268–1284, 2014.

[40] M. T. Björk, H. Schmid, J. Knoch, H. Riel, and W. Riess, “Donor deactivation in silicon nanostructures,” *Nat. Nanotechnol.*, vol. 4, no. 2, pp. 103–107, 2009.

[41] G. Gadea, M. Pacios, Á. Morata, and A. Tarancón, “Silicon-based nanostructures for integrated thermoelectric generators,” *Journal of Physics D: Applied Physics*, vol. 51, no. 42, p. 423001, 2018.

Cette thèse est accessible à l'adresse : http://theses.insa-lyon.fr/publication/2019LYSEI129/these.pdf
© [S. Rodichkina], [2019], INSA de Lyon, tous droits réservés

[42] N. F. Hinsche, I. Mertig, and P. Zahn, "Effect of strain on the thermoelectric properties of silicon: an ab initio study," *Journal of Physics: Condensed Matter*, vol. 23, no. 29, p. 295502, 2011.

[43] M. Raya-Moreno, H. Aramberri, J. A. Seijas-Bellido, X. Cartoixà, and R. Rurali, "Thermal conductivity of hexagonal si and hexagonal si nanowires from first-principles," *Applied Physics Letters*, vol. 111, no. 3, p. 032107, 2017.

[44] P. Yu, J. Wu, S. Liu, J. Xiong, C. Jagadish, and Z. M. Wang, "Design and fabrication of silicon nanowires towards efficient solar cells," *Nano Today*, vol. 11, no. 6, pp. 704–737, 2016.

[45] C. Wood, "Materials for thermoelectric energy conversion," *Reports on progress in physics*, vol. 51, no. 4, p. 459, 1988.

[46] Z. Huang, N. Geyer, P. Werner, J. De Boor, and U. Gösele, "Metal-assisted chemical etching of silicon: A review," *Adv. Mater.*, vol. 23, no. 2, pp. 285–308, 2011.

[47] C.-M. Hsu, S. T. Connor, M. X. Tang, and Y. Cui, "Wafer-scale silicon nanopillars and nanocones by langmuir–blodgett assembly and etching," *Applied Physics Letters*, vol. 93, no. 13, p. 133109, 2008.

[48] E. Garnett and P. Yang, "Light trapping in silicon nanowire solar cells," *Nano letters*, vol. 10, no. 3, pp. 1082–1087, 2010.

[49] W. Chen and H. Ahmed, "Fabrication of high aspect ratio silicon pillars of< 10 nm diameter," *Applied physics letters*, vol. 63, no. 8, pp. 1116–1118, 1993.

[50] V. Auzelyte, H. Solak, Y. Ekinci, R. MacKenzie, J. Vörös, S. Olliges, and R. Spolenak, "Large area arrays of metal nanowires," *Microelectronic Engineering*, vol. 85, no. 5-6, pp. 1131–1134, 2008.

[51] R. Wagner and W. Ellis, "Vapor-liquid-solid mechanism of single crystal growth," *Applied physics letters*, vol. 4, no. 5, pp. 89–90, 1964.

[52] A. M. Morales and C. M. Lieber, "A laser ablation method for the synthesis of crystalline semiconductor nanowires," *Science*, vol. 279, no. 5348, pp. 208–211, 1998.

Cette thèse est accessible à l'adresse : http://theses.insa-lyon.fr/publication/2019LYSEI129/these.pdf
© [S. Rodichkina], [2019], INSA de Lyon, tous droits réservés

[53] P. Das Kanungo, N. Zakharov, J. Bauer, O. Breitenstein, P. Werner, and U. Goesele, "Controlled in situ boron doping of short silicon nanowires grown by molecular beam epitaxy," *Applied Physics Letters*, vol. 92, no. 26, p. 263107, 2008.

[54] K.-Q. Peng, Y.-J. Yan, S.-P. Gao, and J. Zhu, "Synthesis of large-area silicon nanowire arrays via self-assembling nanoelectrochemistry," *Advanced materials*, vol. 14, no. 16, pp. 1164–1167, 2002.

[55] J. S. Sadhu, H. Tian, T. Spila, J. Kim, B. Azeredo, P. Ferreira, and S. Sinha, "Controllable doping and wrap-around contacts to electrolessly etched silicon nanowire arrays," *Nanotechnology*, vol. 25, no. 37, 2014.

[56] M. S. Gudiksen, L. J. Lauhon, J. Wang, D. C. Smith, and C. M. Lieber, "Growth of nanowire superlattice structures for nanoscale photonics and electronics," *Nature*, vol. 415, no. 6872, p. 617, 2002.

[57] Y. Cui, X. Duan, J. Hu, and C. M. Lieber, "Doping and electrical transport in silicon nanowires," *The Journal of Physical Chemistry B*, vol. 104, no. 22, pp. 5213–5216, 2000.

[58] T. Shimizu, T. Xie, J. Nishikawa, S. Shingubara, S. Senz, and U. Gösele, "Synthesis of vertical high-density epitaxial si (100) nanowire arrays on a si (100) substrate using an anodic aluminum oxide template," *Advanced Materials*, vol. 19, no. 7, pp. 917–920, 2007.

[59] S. Hofmann, C. Ducati, R. Neill, S. Piscanec, A. Ferrari, J. Geng, R. Dunin-Borkowski, and J. Robertson, "Gold catalyzed growth of silicon nanowires by plasma enhanced chemical vapor deposition," *Journal of Applied Physics*, vol. 94, no. 9, pp. 6005–6012, 2003.

[60] B. Fuhrmann, H. S. Leipner, H.-R. Höche, L. Schubert, P. Werner, and U. Gösele, "Ordered arrays of silicon nanowires produced by nanosphere lithography and molecular beam epitaxy," *Nano letters*, vol. 5, no. 12, pp. 2524–2527, 2005.

[61] J. Weiss, "The catalytic decomposition of hydrogen peroxide on different metals," *Transactions of the Faraday Society*, vol. 31, pp. 1547–1557, 1935.

[62] H. Fang, Y. Wu, J. Zhao, and J. Zhu, "Silver catalysis in the fabrication of silicon nanowire arrays," *Nanotechnology*, vol. 17, no. 15, p. 3768, 2006.

Cette thèse est accessible à l'adresse : http://theses.insa-lyon.fr/publication/2019LYSEI129/these.pdf
© [S. Rodichkina], [2019], INSA de Lyon, tous droits réservés

[63] Z. R. Smith, R. L. Smith, and S. D. Collins, “Mechanism of nanowire formation in metal assisted chemical etching,” *Electrochimica Acta*, vol. 92, pp. 139–147, 03 2013.

[64] K. W. Kolasinski, “Electron transfer during metal-assisted and stain etching of silicon,” *Semiconductor Science and Technology*, vol. 31, no. 1, p. 014002, 2015.

[65] X. Li, “Metal assisted chemical etching for high aspect ratio nanostructures: A review of characteristics and applications in photovoltaics,” *Current Opinion in Solid State and Materials Science*, vol. 16, no. 2, pp. 71–81, 2012.

[66] S. Yae, Y. Morii, N. Fukumuro, and H. Matsuda, “Catalytic activity of noble metals for metal-assisted chemical etching of silicon,” *Nanoscale research letters*, vol. 7, no. 1, p. 352, 2012.

[67] K. Balasundaram, J. S. Sadhu, J. C. Shin, B. Azeredo, D. Chanda, M. Malik, K. Hsu, J. A. Rogers, P. Ferreira, S. Sinha, *et al.*, “Porosity control in metal-assisted chemical etching of degenerately doped silicon nanowires,” *Nanotechnology*, vol. 23, no. 30, p. 305304, 2012.

[68] S.-l. Wu, T. Zhang, R.-t. Zheng, and G.-a. Cheng, “Facile morphological control of single-crystalline silicon nanowires,” *Applied Surface Science*, vol. 258, no. 24, pp. 9792–9799, 2012.

[69] C. Chiappini, X. Liu, J. R. Fakhoury, and M. Ferrari, “Biodegradable porous silicon barcode nanowires with defined geometry,” *Advanced functional materials*, vol. 20, no. 14, pp. 2231–2239, 2010.

[70] C. Chartier, S. Bastide, and C. Lévy-Clément, “Metal-assisted chemical etching of silicon in HF-H2O2,” *Electrochim. Acta*, vol. 53, no. 17, pp. 5509–5516, 2008.

[71] N. Geyer, N. Wollschläger, B. Fuhrmann, A. Tonkikh, A. Berger, P. Werner, M. Jungmann, R. Krause-Rehberg, and H. S. Leipner, “Influence of the doping level on the porosity of silicon nanowires prepared by metal-assisted chemical etching,” *Nanotechnology*, vol. 26, no. 24, p. 245301, 2015.

[72] A. I. Hochbaum, D. Gargas, Y. J. Hwang, and P. Yang, “Single crystalline mesoporous silicon nanowires,” *Nano letters*, vol. 9, no. 10, pp. 3550–3554, 2009.

Cette thèse est accessible à l'adresse : http://theses.insa-lyon.fr/publication/2019LYSEI129/these.pdf
© [S. Rodichkina], [2019], INSA de Lyon, tous droits réservés

[73] V. Paillard, P. Puech, M. Laguna, R. Carles, B. Kohn, and F. Huisken, "Improved one-phonon confinement model for an accurate size determination of silicon nanocrystals," *Journal of Applied Physics*, vol. 86, no. 4, pp. 1921–1924, 1999.

[74] Y. M. Niquet, A. Lherbier, N. H. Quang, M. V. Fernández-Serra, X. Blase, and C. Delerue, "Electronic structure of semiconductor nanowires," *Phys. Rev. B - Condens. Matter Mater. Phys.*, vol. 73, no. 16, 2006.

[75] Y.-H. Park, J. Kim, H. Kim, I. Kim, K.-Y. Lee, D. Seo, H.-J. Choi, and W. Kim, "Thermal conductivity of vls-grown rough si nanowires with various surface roughnesses and diameters," *Applied Physics A*, vol. 104, no. 1, p. 7, 2011.

[76] Y. Wu, H. Yan, M. Huang, B. Messer, J. H. Song, and P. Yang, "Inorganic semiconductor nanowires: rational growth, assembly, and novel properties," *Chemistry–A European Journal*, vol. 8, no. 6, pp. 1260–1268, 2002.

[77] F. Wang and Y. R. Shen, "General properties of local plasmons in metal nanostructures," *Phys. Rev. Lett.*, vol. 97, p. 206806, 2006.

[78] J. Lim, K. Hippalgaonkar, S. C. Andrews, A. Majumdar, and P. Yang, "Quantifying surface roughness effects on phonon transport in silicon nanowires," *Nano letters*, vol. 12, no. 5, pp. 2475–2482, 2012.

[79] M. K. Jangid, A. S. Lakhnot, A. Vemulapally, F. J. Sonia, S. Sinha, R. O. Dusane, and A. Mukhopadhyay, "Crystalline core/amorphous shell structured silicon nanowires offer size and structure dependent reversible na-storage," *Journal of Materials Chemistry A*, vol. 6, no. 8, pp. 3422–3434, 2018.

[80] J. Niu, J. Sha, and D. Yang, "Temperature dependence of the first-order raman scattering in silicon nanowires," *Scripta materialia*, vol. 55, no. 2, pp. 183–186, 2006.

[81] Z. Cui, "Band gap engineering of wurtzite silicon by uniaxial pressure," *International Journal of Innovative Research in Computer Science Technology*, vol. 5, pp. 230–233, 2017.

[82] F. J. Lopez, U. Givan, J. G. Connell, and L. J. Lauhon, "Silicon nanowire polytypes: identification by raman spectroscopy, generation mechanism, and misfit strain in homostructures," *Acs Nano*, vol. 5, no. 11, pp. 8958–8966, 2011.

Cette thèse est accessible à l'adresse : http://theses.insa-lyon.fr/publication/2019LYSEI129/these.pdf
© [S. Rodichkina], [2019], INSA de Lyon, tous droits réservés

[83] X. Liu and D. Wang, “Kinetically-induced hexagonality in chemically grown silicon nanowires,” *Nano Res.*, vol. 2, no. 7, pp. 575–582, 2009.

[84] G. Weills, G. Sagonll, and J. M. Bessons, “Characterization of Si III and Si IV metastable phases,” *Sites J. 20Th Century Contemp. French Stud.*, vol. 4, pp. 280–282, 1989.

[85] T. Akiyama, K. Nakamura, and T. Ito, “Stacking sequence preference of pristine and hydrogen-terminated si nanowires on si (111) substrates,” *Physical Review B*, vol. 74, no. 3, p. 033307, 2006.

[86] R. E. Algra, M. Hocevar, M. A. Verheijen, I. Zardo, G. G. Immink, W. J. van Enckevort, G. Abstreiter, L. P. Kouwenhoven, E. Vlieg, and E. P. Bakkers, “Crystal structure transfer in core/shell nanowires,” *Nano letters*, vol. 11, no. 4, pp. 1690–1694, 2011.

[87] H. I. T. Hauge, M. A. Verheijen, S. Conesa-Boj, T. Etzelstorfer, M. Watzinger, D. Kriegner, I. Zardo, C. Fasolato, F. Capitani, P. Postorino, S. Kölling, A. Li, S. Assali, J. Stangl, and E. P. A. M. Bakkers, “Hexagonal Silicon Realized,” *Nano Lett.*, vol. 15, no. 9, pp. 5855–5860, 2015.

[88] P. J. Newby, B. Canut, J. M. Bluet, S. Gomès, M. Isaiev, R. Burbelo, K. Termentzidis, P. Chantrenne, L. G. Fréchette, and V. Lysenko, “Amorphization and reduction of thermal conductivity in porous silicon by irradiation with swift heavy ions,” *J. Appl. Phys.*, vol. 114, no. 1, 2013.

[89] S. Rodichkina, L. Osminkina, M. Isaiev, A. Pavlikov, A. Zoteev, V. Georgobiani, K. Gonchar, A. Vasiliev, and V. Y. Timoshenko, “Raman diagnostics of photoinduced heating of silicon nanowires prepared by metal-assisted chemical etching,” *Applied Physics B*, vol. 121, no. 3, pp. 337–344, 2015.

[90] A. K. Shukla and S. Dixit, “Raman study of phase transformation from diamond structure to wurtzite structure in the silicon nanowires,” *J. Phys. D. Appl. Phys.*, vol. 49, no. 28, p. 285304, 2016.

[91] V. Yukhymchuk, V. Dzhagan, M. Y. Valakh, V. Klad’ko, O. Gudymenko, V. Yefanov, and D. Zahn, “In situ photoluminescence/raman study of reversible photo-induced structural transformation of nc-si,” *Materials Research Express*, vol. 1, no. 4, p. 045905, 2014.

Cette thèse est accessible à l'adresse : http://theses.insa-lyon.fr/publication/2019LYSEI129/these.pdf
© [S. Rodichkina], [2019], INSA de Lyon, tous droits réservés

[92] E. Arduca and M. Perego, "Doping of silicon nanocrystals," *Materials Science in Semiconductor Processing*, vol. 62, pp. 156–170, 2017.

[93] J. Wallentin and M. T. Borgström, "Doping of semiconductor nanowires," *Journal of Materials Research*, vol. 26, no. 17, pp. 2142–2156, 2011.

[94] F. Zhuge, T. Yanagida, N. Fukata, K. Uchida, M. Kanai, K. Nagashima, G. Meng, Y. He, S. Rahong, X. Li, *et al.*, "Modulation of thermoelectric power factor via radial dopant inhomogeneity in b-doped si nanowires," *Journal of the American Chemical Society*, vol. 136, no. 40, pp. 14100–14106, 2014.

[95] K.-K. Lew, L. Pan, T. E. Bogart, S. M. Dilts, E. C. Dickey, J. M. Redwing, Y. Wang, M. Cabassi, T. S. Mayer, and S. W. Novak, "Structural and electrical properties of trimethylboron-doped silicon nanowires," *Applied Physics Letters*, vol. 85, no. 15, pp. 3101–3103, 2004.

[96] Y. H. Lee and M.-M. Chen, "Silicon doping effects in reactive plasma etching," *Journal of Vacuum Science & Technology B: Microelectronics Processing and Phenomena*, vol. 4, no. 2, pp. 468–475, 1986.

[97] J. D. Plummer and P. B. Griffin, "Material and process limits in silicon vlsi technology," *Proceedings of the IEEE*, vol. 89, no. 3, pp. 240–258, 2001.

[98] N. Clement, D. Tonneau, H. Dallaporta, V. Bouchiat, D. Fraboulet, D. Mariole, J. Gautier, and V. Safarov, "Electronic transport properties of single-crystal silicon nanowires fabricated using an atomic force microscope," *Physica E: Low-dimensional Systems and Nanostructures*, vol. 13, no. 2-4, pp. 999–1002, 2002.

[99] A. Slaoui, L. Ventura, A. Lachiq, R. Monna, and J. Muller, "Rapid isothermal annealing of doped and undoped spin-on glass films," *MRS Online Proceedings Library Archive*, vol. 387, 1995.

[100] S. Teh and D. Chuah, "Diffusion profile of spin-on dopant in silicon substrate," *Solar energy materials*, vol. 19, no. 3-5, pp. 237–247, 1989.

[101] Emulsitone Chemicals, LLC official website, "`http://www.emulsitone.com/index.htm`," accessed 30/08/2019.

Cette thèse est accessible à l'adresse : http://theses.insa-lyon.fr/publication/2019LYSEI129/these.pdf
© [S. Rodichkina], [2019], INSA de Lyon, tous droits réservés

[102] W. Zagozdzon-Wosik, P. Grabiec, and G. Lux, “Fabrication of submicron junctions-proximity rapid thermal diffusion of phosphorus, boron, and arsenic,” *IEEE Transactions on Electron Devices*, vol. 41, no. 12, pp. 2281–2290, 1994.

[103] S. K. Ghandhi, *VLSI fabrication principles: silicon and gallium arsenide*. John Wiley & Sons, 2008.

[104] D. T. Morelli, J. P. Heremans, and G. A. Slack, “Estimation of the isotope effect on the lattice thermal conductivity of group IV and group III-V semiconductors,” *Phys. Rev. B - Condens. Matter Mater. Phys.*, vol. 66, no. 19, pp. 1953041–1953049, 2002.

[105] H. B. Casimir, “Note on the conduction of heat in crystals,” *Physica*, vol. 5, no. 6, pp. 495–500, 1938.

[106] R. Chen, A. I. Hochbaum, P. Murphy, J. Moore, P. Yang, and A. Majumdar, “Thermal Conductance of Thin Silicon Nanowires,” *Phys. Rev. Lett.*, vol. 101, no. 10, pp. 1–4, 2008.

[107] A. McConnell and K. E. Goodson, “Thermal conduction in silicon micro-and nanostructures,” *Annual review of heat transfer*, vol. 14, 2005.

[108] J. Sadhu and S. Sinha, “Room-temperature phonon boundary scattering below the Casimir limit,” *Phys. Rev. B - Condens. Matter Mater. Phys.*, vol. 84, no. 11, pp. 1–6, 2011.

[109] G. L. Pearson and J. Bardeen, “Electrical properties of pure silicon and silicon alloys containing boron and phosphorus,” *Physical Review*, vol. 75, no. 5, p. 865, 1949.

[110] F. Morin and J. Maita, “Electrical properties of silicon containing arsenic and boron,” *Physical Review*, vol. 96, no. 1, p. 28, 1954.

[111] M. Diarra, Y. M. Niquet, C. Delerue, and G. Allan, “Ionization energy of donor and acceptor impurities in semiconductor nanowires: Importance of dielectric confinement,” *Phys. Rev. B - Condens. Matter Mater. Phys.*, vol. 75, no. 4, pp. 1–4, 2007.

[112] E. B. Ramayya, D. Vasileska, S. M. Goodnick, and I. Knezevic, “Electron transport in silicon nanowires: The role of acoustic phonon confinement and surface roughness scattering,” *J. Appl. Phys.*, vol. 104, no. 6, 2008.

[113] C. Jacoboni, C. Canali, G. Ottaviani, and A. A. Quaranta, “A review of some charge transport properties of silicon,” *Solid-State Electronics*, vol. 20, no. 2, pp. 77–89, 1977.

Cette thèse est accessible à l'adresse : http://theses.insa-lyon.fr/publication/2019LYSEI129/these.pdf
© [S. Rodichkina], [2019], INSA de Lyon, tous droits réservés

[114] G. Pennelli and M. MacUcci, "Optimization of the thermoelectric properties of nanostructured silicon," *J. Appl. Phys.*, vol. 114, no. 21, 2013.

[115] A. I. Hofmann, R. Kroon, and C. Müller, "Doping and processing of organic semiconductors for plastic thermoelectrics," in *Handbook of Organic Materials for Electronic and Photonic Devices*, pp. 429–449, Elsevier, 2019.

[116] G. A. Slack, D. Rowe, *et al.*, *CRC handbook of thermoelectrics*. CRC press Boca Raton, FL, 1995.

[117] Y. Mishima, Y. Kimura, and S. W. Kim, "Enhancement of thermoelectric figure of merit through nanostructural control on intermetallic semiconductors toward high-temperature applications," in *Nanomaterials: Research Towards Applications*, vol. 161, p. 383, Elsevier, 2006.

[118] A. V. Dmitriev and I. P. Zvyagin, "Current trends in the physics of thermoelectric materials," *Physics-Uspekhi*, vol. 53, no. 8, p. 789, 2010.

[119] V. Y. Timoshenko, K. A. Gonchar, L. A. Golovan, A. I. Efimova, V. A. Sivakov, A. Dellith, and S. H. Christiansen, "Photoluminescence and raman scattering in arrays of silicon nanowires," *Journal of Nanoelectronics and Optoelectronics*, no. 6, pp. 519–524, 2011.

[120] K. A. Gonchar, L. A. Osminkina, R. A. Galkin, M. B. Gongalsky, V. S. Marshov, V. Y. Timoshenko, M. N. Kulmas, V. V. Solovyev, A. A. Kudryavtsev, and V. A. Sivakov, "Growth, structure and optical properties of silicon nanowires formed by metal-assisted chemical etching," *Journal of Nanoelectronics and Optoelectronics*, vol. 7, no. 6, pp. 602–606, 2012.

[121] TESCAN official website, "`https://www.tescan.com/en-us/technology/sem/mira3`," accessed: 30/08/2019.

[122] Nanoscience Instruments official website, "`https://www.nanoscience.com/techniques/scanning-electron-microscopy`," accessed: 30/08/2019.

[123] University of Warwick official website, "`https://warwick.ac.uk/fac/sci/physics/current/postgraduate/regs/mpagswarwick/ex5/techniques/structural/sem3/`," accessed: 30/08/2019.

Cette thèse est accessible à l'adresse : http://theses.insa-lyon.fr/publication/2019LYSEI129/these.pdf
© [S. Rodichkina], [2019], INSA de Lyon, tous droits réservés

[124] AZO materials official website, "https://www.azom.com/article.aspx?ArticleID=14309," accessed: 30/08/2019.

[125] S. Bhattacharya, "Chapter 8 - electrical transport properties of ion-conducting glass nanocomposites," in *Glass Nanocomposites* (B. Karmakar, K. Rademann, and A. L. Stepanov, eds.), pp. 181 – 214, Boston: William Andrew Publishing, 2016.

[126] M. Nasrollahzadeh, S. M. Sajadi, M. Sajjadi, Z. Issaabadi, and M. Atarod, eds., *Chapter 6 - Plant-Mediated Green Synthesis of Nanostructures: Mechanisms, Characterization, and Applications*, vol. 28 of *Interface Science and Technology*. Elsevier, 2019.

[127] Science Direct official website, "https://www.sciencedirect.com/topics/pharmacology-toxicology-and-pharmaceutical-science/infrared-spectroscopy," accessed: 30/08/2019.

[128] Bruker official website, "https://www.bruker.com/fr/products/infrared-near-infrared-and-raman-spectroscopy/landing-pages/general/ir-tutorial.html," accessed: 30/08/2019.

[129] L. D. Landau and E. M. Lifshitz, *Electrodynamics of Continuous Media*. Pergamon Press, 1960.

[130] Horiba official website, "http://www.horiba.com/fr/scientific/products/raman-spectroscopy/raman-academy/raman-tutorial/," accessed 30/08/2019.

[131] G. Gilliland, "Photoluminescence spectroscopy of crystalline semiconductors," *Materials Science and Engineering: R: Reports*, vol. 18, no. 3-6, pp. 99–399, 1997.

[132] Horiba official website, "https://www.horiba.com/en_en/products/by-technique/molecular-spectroscopy/photoluminescence-pl-electroluminescence-el/," accessed 30/08/2019.

[133] D. Pendse and A. Chin, "Cathodoluminescence and transmission cathodoluminescence," 2001.

[134] X. Wen, P. Zhang, T. A. Smith, R. J. Anthony, U. R. Kortshagen, P. Yu, Y. Feng, S. Shrestha, G. Coniber, and S. Huang, "Tunability limit of photoluminescence in colloidal silicon nanocrystals," *Scientific reports*, vol. 5, p. 12469, 2015.

Cette thèse est accessible à l'adresse : http://theses.insa-lyon.fr/publication/2019LYSEI129/these.pdf
© [S. Rodichkina], [2019], INSA de Lyon, tous droits réservés

[135] Y. Singh, "Electrical resistivity measurements: a review," *International Journal of Modern Physics Conference Series*, vol. 22, pp. 745–756, 2013.

[136] V. Bonch-Bruevich and S. Kalashnikov, *Physics of semiconductors*. Nauka, Moscow, 1977.

[137] T. A. Fjeldly, F. Cerdeira, and M. Cardona, "Effects of free carriers on zone-center vibrational modes in heavily doped p-type Si. Optical Modes.," *Phys. Rev. B*, vol. 8, no. 10, pp. 4723–4733, 1973.

[138] E. Anastassakis, A. Cantarero, and M. Cardona, "Piezo-raman measurements and anharmonic parameters in silicon and diamond," *Phys. Rev. B*, vol. 41, pp. 7529–7535, 1990.

[139] V. Poborchii, T. Tada, and T. Kanayama *Jpn. J. Appl. Phys.*, vol. 51, no. 7(1), 2012.

[140] V. A. Volodin, V. A. Timofeev, A. R. Tuktamyshev, and A. I. Nikiforov, "Splitting of frequencies of optical phonons in tensile-strained germanium layers," *JETP Lett.*, vol. 105, no. 5, pp. 327–331, 2017.

[141] M. Yin and M. L. Cohen, "Theory of static structural properties, crystal stability, and phase transformations: Application to si and ge," *Physical Review B*, vol. 26, no. 10, p. 5668, 1982.

[142] C. Glynn, K.-M. Jones, V. Mogili, W. McSweeney, and C. O'Dwyer, "The nature of silicon nanowire roughness and thermal conductivity suppression by phonon scattering mechanisms," *ECS Journal of Solid State Science and Technology*, vol. 6, no. 3, pp. 3029–3035, 2017.

[143] E. Djoufac Woumfo, A. Elimbi, G. Panczer, R. Nyada Nyada, and D. Njopwouo, "Caracterisations physico-chimiques et mineralogiques des vertisols de garoua (Nord Cameroun)," *Ann. Chim. Sci. des Mater.*, vol. 31, no. 1, pp. 75–90, 2006.

[144] S. Périchon, V. Lysenko, B. Remaki, D. Barbier, and B. Champagnon, "Measurement of porous silicon thermal conductivity by micro-Raman scattering," *J. Appl. Phys.*, vol. 86, no. 8, pp. 4700–4702, 1999.

Cette thèse est accessible à l'adresse : http://theses.insa-lyon.fr/publication/2019LYSEI129/these.pdf
© [S. Rodichkina], [2019], INSA de Lyon, tous droits réservés

[145] A. Mujica, A. Rubio, A. Muñoz, and R. J. Needs, "High-pressure phases of group-IV, III-V, and II-VI compounds," *Rev. Mod. Phys.*, vol. 75, no. 3, pp. 863–912, 2003.

[146] T. T. Tran, J. Mathews, and J. S. Williams, "Materials Science in Semiconductor Processing Towards a direct band gap group IV Ge-based material," *Mater. Sci. Semicond. Process.*, vol. 92, no. July 2018, pp. 39–46, 2019.

[147] L. A. Osminkina, E. V. Kurepina, A. V. Pavlikov, V. Y. Timoshenko, and P. K. Kashkarov, "Interaction of infrared radiation with free carriers in mesoporous silicon," *Semiconductors*, vol. 38, no. 5, pp. 581–587, 2004.

[148] J. Humlíček and K. Vojtěchovský, "Infrared optical constants of n-type silicon," *Czech. J. Phys.*, vol. 38, no. 9, pp. 1033–1049, 1988.

[149] M. van Exter and D. Grischkowsky, "Carrier dynamics of electrons and holes in moderately doped silicon," *Phys. Rev. B*, vol. 41, no. 17, pp. 12140–12149, 1990.

[150] W. Theiß, "Optical properties of porous silicon," *Surf. Sci. Rep.*, vol. 29, no. 3-4, pp. 91–192, 1997.

[151] H. R. Philipp and E. A. Taft, "Optical constants of silicon in the region 1 to 10 ev," *Phys. Rev.*, vol. 120, no. 1, pp. 37–38, 1960.

[152] V. Y. Timoshenko, T. Dittrich, V. Lysenko, M. G. Lisachenko, and F. Koch, "Free charge carriers in mesoporous silicon," *Phys. Rev. B*, vol. 64, p. 085314, 2001.

[153] L. D. Landau, J. Bell, M. Kearsley, L. Pitaevskii, E. Lifshitz, and J. Sykes, *Electrodynamics of continuous media*, vol. 8. Elsevier, 2013.

[154] D. Schmidt and M. Schubert, "Anisotropic bruggeman effective medium approaches for slanted columnar thin films," *Journal of Applied Physics*, vol. 114, no. 8, p. 083510, 2013.

[155] N. J. Harrick, "Electric field strengths at totally reflecting interfaces," *J. Opt. Soc. Am.*, vol. 55, no. 7, p. 851, 1965.

[156] W. N. Hansen, "Expanded formulas for attenuated total reflection and the derivation of absorption rules for single and multiple ATR spectrometer cells," *Spectrochim Acta*, vol. 21, no. 4, pp. 815–833, 1965.

Cette thèse est accessible à l'adresse : http://theses.insa-lyon.fr/publication/2019LYSEI129/these.pdf
© [S. Rodichkina], [2019], INSA de Lyon, tous droits réservés

[157] V. A. Sivakov, F. Voigt, A. Berger, G. Bauer, and S. H. Christiansen, “Roughness of silicon nanowire sidewalls and room temperature photoluminescence,” *Phys. Rev. B*, vol. 82, p. 125446, 2010.

[158] B. G. Burke, J. Chan, K. A. Williams, Z. Wu, A. A. Puretzky, and D. B. Geohegan, “Raman study of Fano interference in p-type doped silicon,” *J. Raman Spectrosc.*, vol. 41, no. 12, pp. 1759–1764, 2010.

[159] M. Chandrasekhar, J. B. Renucci, and M. Cardona, “Effects of interband excitations on raman phonons in heavily doped $n-$Si,” *Phys. Rev. B*, vol. 17, pp. 1623–1633, 1978.

[160] V. Magidson and R. Beserman, “Fano-type interference in the raman spectrum of photoexcited si,” *Physical Review B*, vol. 66, no. 19, p. 195206, 2002.

[161] R. Beserman and T. Bernstein, “Raman scattering measurement of the free-carrier concentration and of the impurity location in boron-implanted silicon,” *Journal of Applied Physics*, vol. 48, no. 4, pp. 1548–1550, 1977.

[162] S. K. Saxena, R. Borah, V. Kumar, H. M. Rai, R. Late, V. G. Sathe, A. Kumar, P. R. Sagdeo, and R. Kumar, “Raman spectroscopy for study of interplay between phonon confinement and Fano effect in silicon nanowires,” *J. Raman Spectrosc.*, vol. 47, no. 3, pp. 283–288, 2016.

[163] U. Fano, “Effect of configuration Interaction on intensities and phase shifts,” *Phys. Rev.*, vol. 124, no. 6, pp. 1866–1878, 1961.

[164] M. Balkanski, R. F. Wallis, and E. Haro, “Anharmonic effects in light scattering due to optical phonons in silicon,” *Phys. Rev. B*, vol. 28, no. 4, pp. 1928–1934, 1983.

[165] D. A. Mamichev, K. A. Gonchar, V. Y. Timoshenko, G. K. Mussabek, V. E. Nikulin, and T. I. Taurbaev, “Enhanced raman scattering in multilayer structures of porous silicon,” *Journal of Raman Spectroscopy*, vol. 42, no. 6, pp. 1392–1395, 2011.

[166] L. A. Osminkina, K. A. Gonchar, V. S. Marshov, K. V. Bunkov, D. V. Petrov, L. A. Golovan, F. Talkenberg, V. A. Sivakov, and V. Timoshenko, “Optical properties of silicon nanowire arrays formed by metal-assisted chemical etching: evidences for light localization effect,” *Nanoscale Research Letters*, vol. 7, no. 1, p. 524, 2012.

Cette thèse est accessible à l'adresse : http://theses.insa-lyon.fr/publication/2019LYSEI129/these.pdf
© [S. Rodichkina], [2019], INSA de Lyon, tous droits réservés

[167] P. E. Schmid, "Optical absorption in heavily doped silicon," *Phys. Rev. B*, vol. 23, no. 10, pp. 5531–5536, 1981.

[168] H. Richter, Z. Wang, and L. Ley, "The one phonon raman spectrum in microcrystalline silicon," *Solid State Communications*, vol. 39, no. 5, pp. 625 – 629, 1981.

[169] I. Campbell and P. Fauchet, "The effects of microcrystal size and shape on the one phonon raman spectra of crystalline semiconductors," *Solid State Communications*, vol. 58, no. 10, pp. 739 – 741, 1986.

[170] T. A. Fjeldly, F. Cerdeira, and M. Cardona, "Effects of free carriers on zone-center vibrational modes in heavily doped p-type si. i. acoustical modes," *Physical Review B*, vol. 8, no. 10, pp. 4723–4733, 1973.

[171] F. Cerdeira, T. A. Fjeldly, and M. Cardona, "Interaction between electronic and vibronic raman scattering in heavily doped silicon," *Solid State Communications*, vol. 13, no. 3, pp. 325–328, 1973.

[172] M. A. Green, "Self-consistent optical parameters of intrinsic silicon at 300 k including temperature coefficients," *Solar Energy Materials and Solar Cells*, vol. 92, p. 1305–1310, 2008.

[173] S. Giordano, "Effective medium theory for dispersions of dielectric ellipsoids," *Journal of electrostatics*, vol. 58, no. 1-2, pp. 59–76, 2003.

[174] A. Grove, "Physics and technology of," *Semiconductor Devices*, pp. 226–227, 1967.

[175] S. Werner, U. Belledin, A. Kimmerle, A. Fallisch, A. Wolf, and D. Biro, "Doping-and carrier concentration profile characterisation of highly phosphorus-doped emitters," *25th Eur. Photovolt. Sol. Energy Conf. Exhib. / 5th World Conf. Photovolt. Energy Convers.*, no. June 2014, pp. 1942 – 1947, 2010.

[176] N. P. Dasgupta, C. Liu, S. Andrews, F. B. Prinz, and P. Yang, "Atomic layer deposition of platinum catalysts on nanowire surfaces for photoelectrochemical water reduction," *Journal of the American Chemical Society*, vol. 135, no. 35, pp. 12932–12935, 2013.

[177] K. Balasundaram, J. S. Sadhu, J. C. Shin, B. Azeredo, D. Chanda, M. Malik, K. Hsu, J. A. Rogers, P. Ferreira, S. Sinha, *et al.*, "Porosity control in metal-assisted chemical etching

Cette thèse est accessible à l'adresse : http://theses.insa-lyon.fr/publication/2019LYSEI129/these.pdf
© [S. Rodichkina], [2019], INSA de Lyon, tous droits réservés

of degenerately doped silicon nanowires," *Nanotechnology*, vol. 23, no. 30, p. 305304, 2012.

[178] M. Nolan, T. Perova, R. Moore, and H. Gamble, "Boron diffusion from a spin-on source during rapid thermal processing," *Journal of non-crystalline solids*, vol. 254, no. 1-3, pp. 89–93, 1999.

[179] A. Compaan, M. Lee, and G. Trott, "Phonon populations by nanosecond-pulsed raman scattering in si," *Physical Review B*, vol. 32, no. 10, p. 6731, 1985.

[180] G. Jellison Jr and F. Modine, "Optical absorption of silicon between 1.6 and 4.7 ev at elevated temperatures," *Applied Physics Letters*, vol. 41, no. 2, pp. 180–182, 1982.

[181] A. Stranz, J. Kähler, A. Waag, and E. Peiner, "Thermoelectric properties of high-doped silicon from room temperature to 900 k," *Journal of electronic materials*, vol. 42, no. 7, pp. 2381–2387, 2013.

Cette thèse est accessible à l'adresse : http://theses.insa-lyon.fr/publication/2019LYSEI129/these.pdf
© [S. Rodichkina], [2019], INSA de Lyon, tous droits réservés

FOLIO ADMINISTRATIF

THESE DE L'UNIVERSITE DE LYON OPEREE AU SEIN DE L'INSA LYON

NOM : RODICHKINA DATE de SOUTENANCE :10/12/2019
(avec précision du nom de jeune fille, le cas échéant)

Prénoms : Sofia

TITRE : Electrical and thermal properties of silicon nanowire arrays

NATURE : Doctorat Numéro d'ordre : 2019LYSEI129

Ecole doctorale : ED34 Matériaux

Spécialité : Matériaux

RESUME : This work aims to provide a reader with information on fabrication of highly-doped SiNWs arrays, their contactless diagnostics, thermal and electrical conductivity. The observed high electrical and low thermal conductivity of highly-doped SiNWs arrays, formed by metal-assisted chemical etching and additionally doped using the thermal diffusion of impurities from spin-on dopant solutions, shows that SiNWs arrays represent a promising material for thermoelectric applications.

MOTS-CLÉS : silicon nanowires, thermal conductivity, electrical conductivity, optical characterization, thermoelectricity

Laboratoire (s) de recherche : INL (INSA Lyon, France), LTP (MSU, Russie)

Directeur de thèse:
M. TIMOSHENKO Victor, Professeur des Universités, MSU (Russie)
M. LYSENKO Vladimir, Chargé de recherche, CNRS (France)

Président de jury :

Composition du jury :
M. LERONDEL Gilles, Professeur des Universités, Université de Technologie de Troyes (Rapporteur)
M. GAUTIER Gael, Professeur des Universités, Université de Tours (Rapporteur)
M. LE DANTEC Ronan, Professeur des Universités, Université de Savoie (Examinateur)
MME GOMES Séverine, Directrice de Recherche, CNRS (Examinatrice)

M. TIMOSHENKO Victor, Professeur des Universités, MSU, Russie (Directeur de thèse)
M. LYSENKO Vladimir, Chargé de recherche, CNRS (Directeur de thèse)
MME NYCHYPORUK Tetyana, Maître de conférences, INSA Lyon (Co-directrice de thèse)

Cette thèse est accessible à l'adresse : http://theses.insa-lyon.fr/publication/2019LYSEI129/these.pdf
© [S. Rodichkina], [2019], INSA de Lyon, tous droits réservés